CHARLES UNIVERSITY

FACULTY OF SCIENCE

Institute of Petrology and Structural Geology

Study program: Geology

Geodynamic evolution and post-collisional magmatic activity in the Arabian-Nubian Shield (East African Orogeny) and southwestern Moldanubian Zone (Central European Variscides)

Příspěvek ke geodynamickému vývoji a postkolizní magmatické aktivitě v jednotce Arabsko-Nubijského štítu (Východoafrické orogenní pásmo) a severozápadní části Moldanubika (Středoevropské variscidy)

Leta Alemayehu Megerssa, M.Sc.

Appendices to Dissertation

Prague 2022

Appendix 1

Journal of African Earth Sciences 162 (2020) 103695

Contents lists available at ScienceDirect

Journal of African Earth Sciences

journal homepage: www.elsevier.com/locate/jafrearsci

Emplacement and thermal effect of post-collisional Chewo Pluton (Arabian-Nubian Shield); implication for late East-African Orogeny

Leta Megerssa[a,b,*], Kryštof Verner[a,b], David Buriánek[b], Jiří Sláma[c]

[a] Institute of Petrology and Structural Geology, Faculty of Science, Charles University, Albertov 6, Prague, 128 43, Czech Republic
[b] Czech Geological Survey, Klárov 3, Prague, 11821, Czech Republic
[c] The Czech Academy of Sciences, Institute of Geology, Rozvojová 269, Prague, 6 16500, Czech Republic

ARTICLE INFO

Keywords:
Eastern African Orogen
Arabian-Nubian Shield
Pluton emplacement
Petrology
U/Pb dating

ABSTRACT

The Chewo pluton built by pyroxene-amphibole to amphibole-biotite monzodiorite and quartz monzonite is a typical post-collisional intrusive body emplaced into a low-grade Neoproterozoic Tambien Group belonging to the Tokar-Barka Terrane in the southern Arabian–Nubian Shield. The pluton shows a high-K calc-alkaline and metaluminous composition with significant enrichment in both LREE and LILE due to hybridization and magma mixing between crustal and mantle-derived melts. Estimated P-T conditions of quartz monzonite magma solidification at T: 703 ± 23 °C and P: 0.32 ± 0.08 GPa and thermal overprint in the pluton aureole at T: 200–755 °C and P: 0.28 ± 0.06 GPa indicate that the Chewo pluton intruded at a depth of between ca. 10–13 km. The Chewo Pluton was emplaced diapirically, which was driven by a local extension in the hinge of the large-scale asymmetric syncline during the last increments of regional deformation – orogen-perpendicular WNW(NW)-ESE(SE) compression. It indicates that the regional WNW(NW)-ESE(SE) shortening is the main geodynamic event of the East African Orogen in the upper-crustal Tokar-Barka Terrane resulting in the assembly of the eastern and western Gondwana continents. In concordance, the zircon U/Pb age of the Chewo pluton (618.1 ± 1.5 Ma) provides the upper limit for the regional deformation.

1. Introduction

A comprehensive study of petrogenesis, fabric pattern and emplacement mechanisms of post-orogenic granite plutons as well as their thermal aureoles in the context of the regional tectonometamorphic evolution allows an overall interpretation of the geodynamic scenario and magmatism at the final stages of orogenic processes (e.g. White and Chappell, 1983; Pearce et al., 1984; Whalen et al., 1987; Barbarin, 1999; Asrat et al., 2003). In the East African Orogen (EAO) individual stages of geodynamic evolution and the associated syn- to post-tectonic magmatic activity are among the issues of ongoing discussion (e.g. Tadesse et al., 1997; Alemu, 1998; Asrat et al., 2003; Jacobs and Thomas, 2004; Kusky et al., 2003; Hargrove et al., 2006; El-Bialy and Streck, 2009; Eyal et al., 2010; De Wall et al., 2011; Farahat and Azer, 2011; Greiling et al., 2014; Khalil et al., 2015; Azer et al., 2016; Dawaï et al., 2017).

The EAO was developed as a Neoproterozoic accretion-type orogen (ca. 850 to 540 Ma) involving the assemblage of oceanic arc/back-arc basin closures, continental fragments and suture zones (for a general review see Fritz et al., 2013). The northern part of the EAO was designated as the Arabian Nubian Shield (ANS; Fig. 1a and b) where four distinct phases of terrane accretion associated with a regional low- to high-grade metamorphism and widespread late-orogenic peraluminous to high-K calc-alkaline to alkaline magmatic event took place between~860 and 540 Ma (Abdelsalam and Stern, 1996; Fritz et al., 2013). A number of contrasting hypotheses are suggested with regard to the tectonic and metamorphic evolution of the ANS and post-tectonic magmatic activity including the timing of all these events (e.g. Ghebreab et al., 1999; Asrat et al., 2004; Sifeta et al., 2005; Alene et al., 2006; Eyal et al., 2010; Farahat and Azer, 2011; Miller et al., 2011; De Wall et al., 2011; Johnson, 2014).

This paper presents the results of field structural mapping, an analysis of anisotropy of magnetic susceptibility (AMS), petrological, geochemical and geochronological data from post-collisional Chewo Pluton and its host low-grade Tambien and Tsaliet groups to shed some light on the last stage of evolution for this part of the ANS. The study is based on the example from two classic areas – the Mai Kenetal and Chewo synclines both belonging to the southern part of the ANS (Tokar-Barka Terrane; Fig. 1c). Using a new petrological, geochemical, U–Pb and structural data an interpretation is given of the petrogenesis and

* Corresponding author. Institute of Petrology and Structural Geology, Faculty of Science, Charles University, Albertov 6, Prague, 128 43, Czech Republic.
E-mail address: MEGERSSAL@natur.cuni.cz (L. Megerssa).

https://doi.org/10.1016/j.jafrearsci.2019.103695
Received 4 June 2019; Received in revised form 25 October 2019; Accepted 31 October 2019
Available online 06 November 2019
1464-343X/

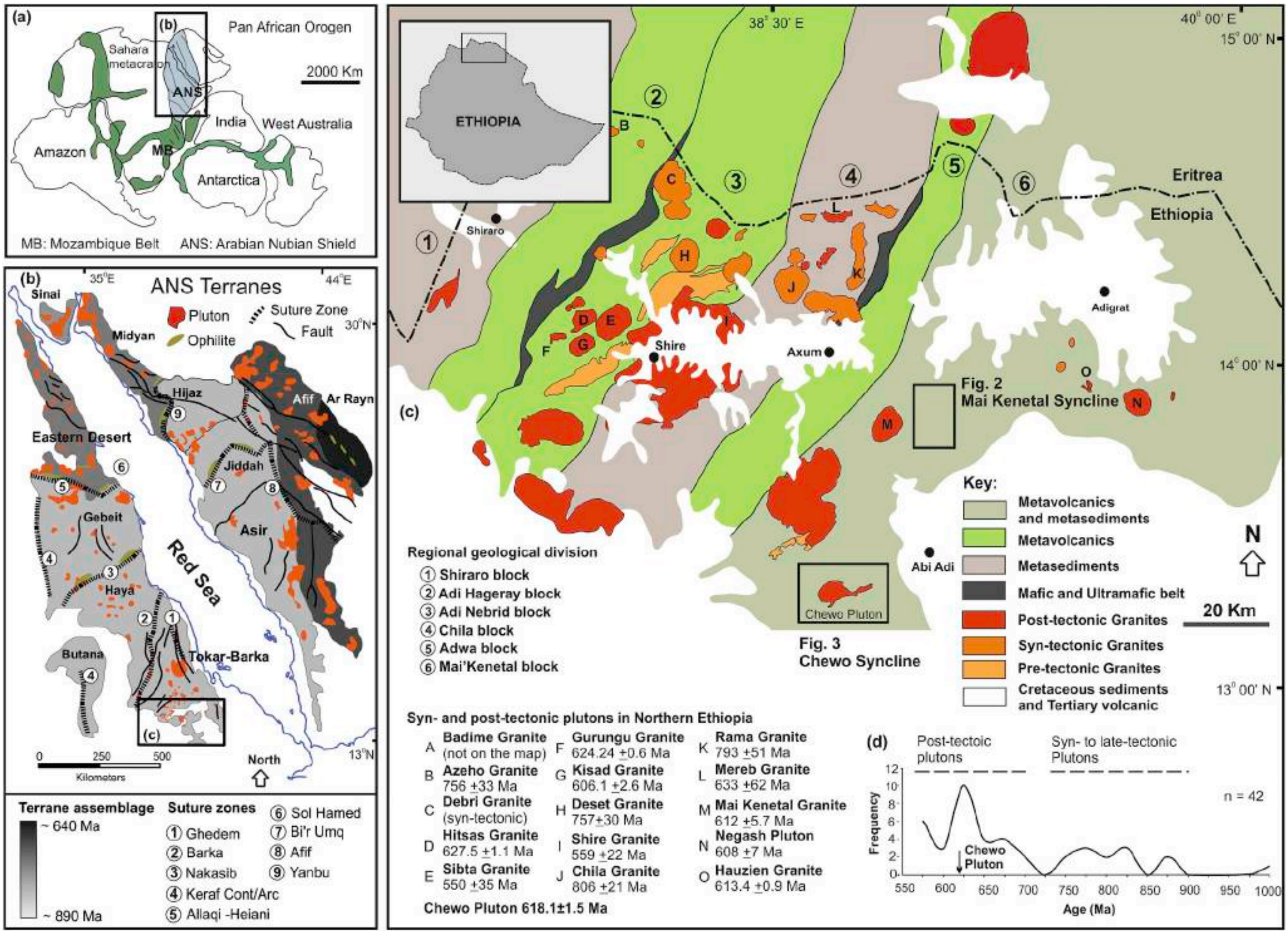

Fig. 1. (a) Sketch of Gondwana supercontinent assembly and position of ANS (after Fritz et al., 2013; Johnson, 2014), **(b)** Exposure of ANS terranes and related plutons (after Fritz et al., 2013), **(c)** Simplified geological map of the southernmost part of Tokar-Barka Terrane (after Avigad et al., 2007 and references therein), **(d)** Pluton age distribution in southernmost part of Tokar-Barka Terrane (for source see Table S5).

emplacement of the Chewo Pluton with a broad implication for the later stages geodynamic evolution of the ANS.

2. Geological setting

The Precambrian rocks exposed in northern Ethiopia constitute the southernmost part of the Tokar-Barka Terrane which is the earliest accreted segment among the ANS terrane assemblage (e.g. Fritz et al., 2013; Miller et al., 2011). These rocks predominantly portray NNE–SSW trending foliations and boundaries of individual lithologies (Fig. 1c; Tadesse, 1997; Tadesse et al., 1997; Teklay et al., 2001; Asrat et al., 2003; Alene et al., 2006; Avigad et al., 2007; Miller et al., 2011). The wider extent of the study area is built by the stratigraphically lowest Tsaliet Group overlaid by a metavolcano-sedimentary sequence of the Tambien Group (Hailu, 2000; Alene et al., 2006; Miller et al., 2011). The Tsaliet Group is composed of low-grade intermediate to felsic lava and welded tuffs, well-bedded lapilli tuffs and agglomerates and limestones deposited between 850 and 740 Ma (Beyth et al., 2003; Alene et al., 2006). The stratigraphically younger Tambien Group is prevalently composed of limestones, quartzitic dolomites and minor siliciclastic sediments (slates, phyllites and greywackes) deposited in intra-oceanic platform settings between 800 and 735 Ma (Sifeta et al., 2005; Alene et al., 2006; Avigad et al., 2007). Nevertheless, both lithological groups underwent several episodes of deformation up to the final closure of the intervening Mozambique Ocean at 630 Ma. These lithologies underwent pumpellyite-actinolite to lower-greenschist facies metamorphism and polyphase deformation followed by a thermal (contact) overprint around calc-alkaline plutons (Alene and Sacchi, 2000; Alene et al., 2006; Miller et al., 2003, 2011). Five deformation phases were outlined in the wider studied area (Tadesse, 1997): (a) a NW–SE oblique compression that resulted in the folding and thrusting of mafic and ultramafic belts; (b) the extension and formation of intra-orogenic basins with the deposition of sedimentary sequences of the Tambien Group; (c) left-lateral transpressional shearing; (d) ENE-WSW right-lateral brittle-ductile shearing and (e) a regional uplift associated with NW–SE trending kink-band folds, normal faults and extensional joints. Nevertheless, based on the reliable chemostratigraphic synthesis, deposition of the Tambien group in a marine arc-accretion platform setting (Miller et al., 2011) is maintained in this study. Several crustal blocks with differences in their lithological composition and structural record (Shiraro, Adi Nebrid, Adi Hageray, Adwa-Chila and Mai Kenetal blocks) were defined as in Fig. 1c (Tadesse, 1997; Tadesse et al., 2000). The intervening zone is occupied by steep shear zones of mafic and ultramafic rock assemblages (Tadesse, 1997; De Wall et al., 2011). At the later stages of the orogen, these Neoproterozoic low-grade rocks were intruded by several post-orogenic granitoid plutons of calc-alkaline to alkaline composition ranging in crystallization age from 640 to 580 Ma (Teklay et al., 2001; Miller et al., 2003; Asrat et al., 2004; Avigad et al., 2007; Johnson et al., 2011). The origin of these granitoids is interpreted as being triggered by the high heat flow in the context of the delamination of the sub-continental lithospheric mantle (e.g. Sylvester, 1989, 1998; Liégeois et al., 1998; Avigad and Gvirtzman,

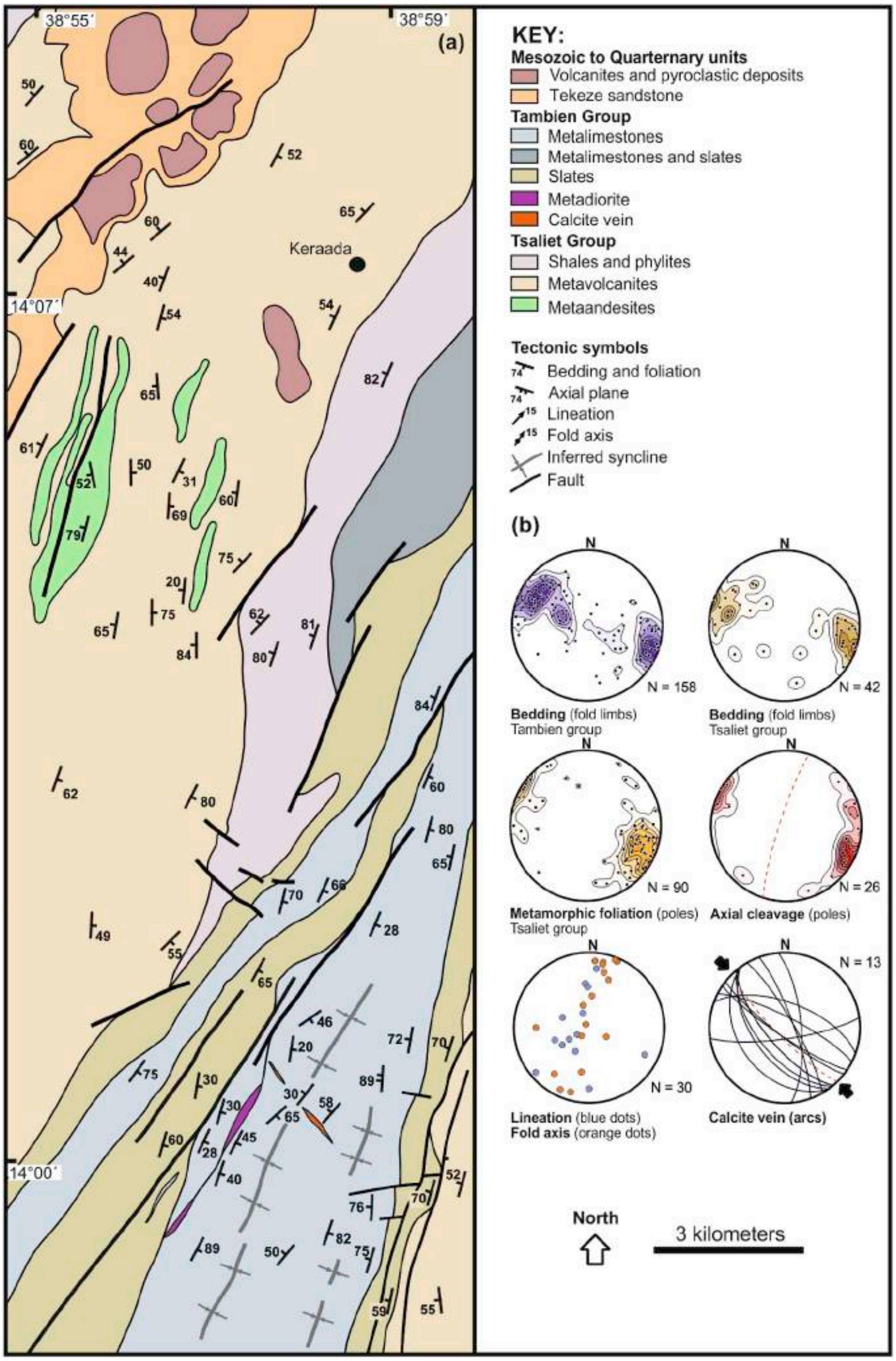

Fig. 2. (a) Simplified structural map of the Mai Kenetal Syncline, **(b)** Tectonic diagrams of field measurements (equal area lower hemisphere projection).

2009; Eyal et al., 2010; Fritz et al., 2013). The occurrence of plutons systematically decreases from the northern part of the ANS to the south (Johnson et al., 2011). The relatively older plutons~620–610 Ma exposed predominantly along the Keraf Suture (Al-Amar arc in north eastern ANS; Johnson et al., 2011) are coeval with latter stages of crustal accretion. A general overview of the distribution of the syn- to post-tectonic plutons and their crystallization ages in northern Ethiopia is shown in Fig. 1d. The main target of the study - the Chewo pluton represents a typical example of a post-collisional intrusive body emplaced into the central part of the upper-crustal Chewo Syncline belonging to the Tokar-Barka Terrane (Beyth, 1972; Tadesse, 1997; Miller et al., 2011). The pluton forms an elliptical body elongated along the northeast-southwest direction with the longer axis of~7 km and the shorter~5 km.

3. Structural pattern

The structural pattern of post-collisional Chewo Pluton and host low-grade metamorphic rocks (Tsaliet and Tambien groups) was investigated in the Mai Kenetal and Chewo synclines (Fig. 1c).

3.1. Low-grade volcano-sedimentary sequence (Mai Kenetal Syncline)

The western part of the Mai Kenetal Syncline (Alene et al., 2006) is formed by a low-grade volcano-sedimentary sequence of the Tambien and Tsaliet groups (Fig. 2a). The sedimentary bedding is mostly parallel

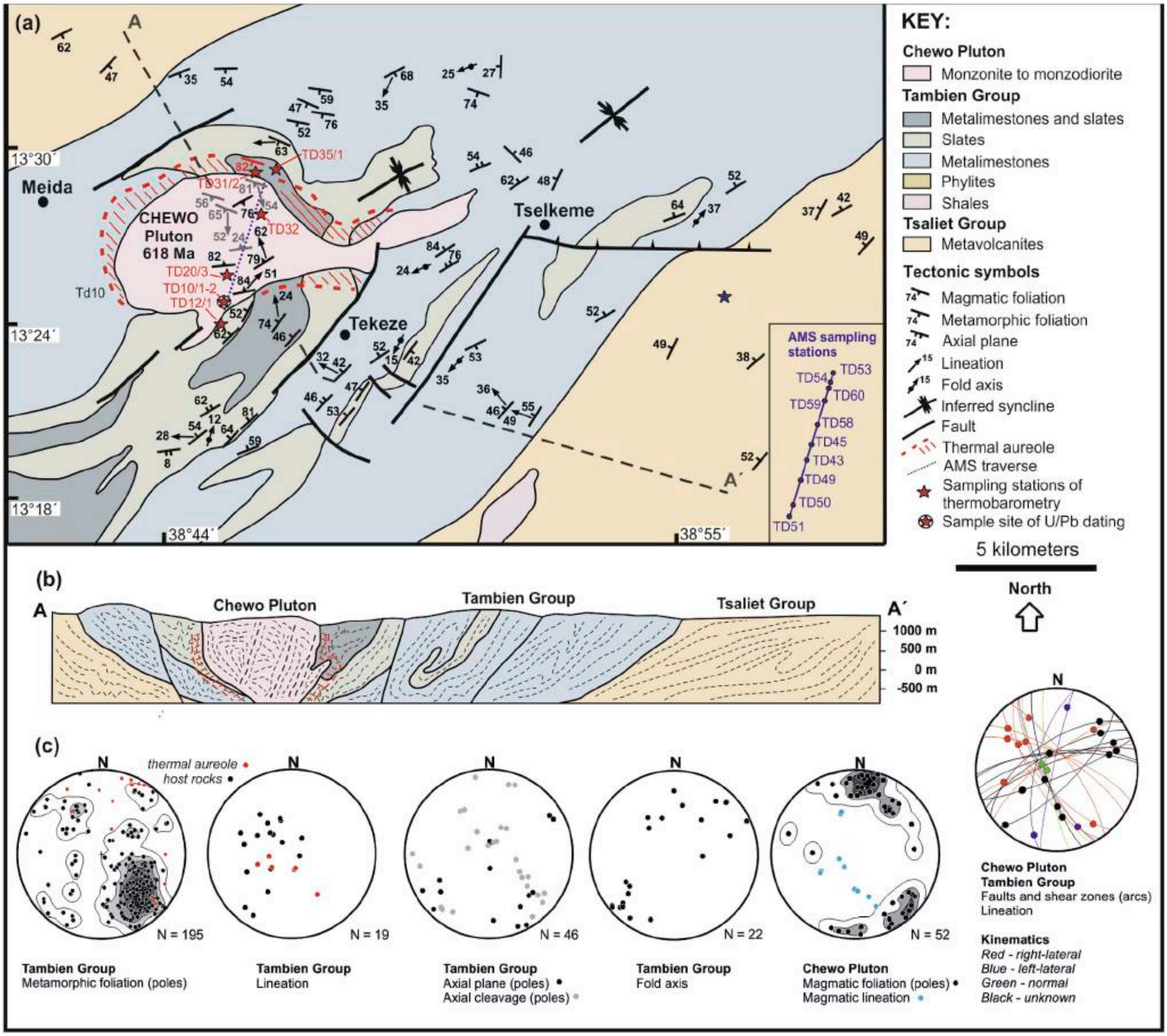

Fig. 3. (a) Simplified structural map of the Chewo Syncline and Chewo Pluton (modified after Hailu, 2000). **(b)** Schematic geological cross-section of the Chewo Syncline, **(c)** Tectonic diagrams of field measurements (equal area lower hemisphere projection). Locations of AMS sampling stations are shown in the lower right corner, along the NE–SW running traverse across the Chewo pluton.

to the metamorphic schistosity (Fig. 4a). Both planar fabrics were transposed into asymmetric, open to isoclinal fold structures, at a regional scale forming the NNE–SSW trending Mai Kenetal Syncline. The fold limbs dip steeply to WNW or ESE (Fig. 2b). The associated fold axes plunge gently to NNE or WSW and are mostly subparallel to weak mineral or stretching lineations. Well-developed axial cleavages dip steeply to WNW (Figs. 2b and 4b). In addition, carbonate or quartz veins (with a thickness up to 0.2 m) are mostly vertical, predominantly trending NW-SE (Fig. 2b). In some places the “en échelon” structures are apparent. In addition, superimposed kink-bands and open folds with subvertical E(ESE)–W(WNW) trending axial planes were systematically observed across the studied area. The brittle structures are mainly manifested as a series of major ca NE–SW trending right-lateral strike-slip faults and perpendicular NW–SE trending faults that partly offset the lithologies.

3.2. Low- to medium grade metasedimentary sequence (Chewo Syncline)

In the Tambien Group, relic sedimentary bedding and low-grade schistosity were folded into large-scale asymmetric tight to open folds forming a syncline on the regional scale (Figs. 3a, 4c and d). The fold limbs dip steeply to moderately to the NW or SE, often bearing mineral lineation plunging to SW to SSW (Fig. 3b and c). The corresponding axial cleavage planes dip steeply to NW. Furthermore, two generations of superimposed structures were detected: (a) a relatively older crenulation cleavage dipping gently to SW in response to weak subvertical shortening (Fig. 4e) and (b) kink-bands, open folds and the associated crenulation cleavage dipping steeply to NNE or SSW. In addition, two populations of steep calcite and quartz vein trending NE–SW and NW–SE often associated with faults and extensional joints were identified (Fig. 3c). Superimposed NE to SW and NW(NNW) to SE(SSE) trending faults and shear zones reveal a polyphase reactivation in different tectonic settings from a predominant right-lateral strike-slip to normal faulting in both directions (Figs. 3b and 4f).

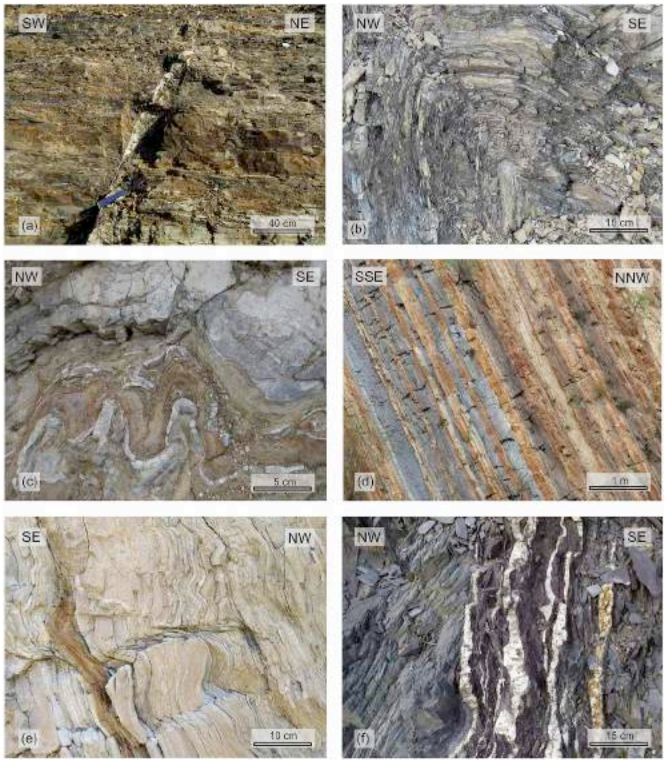

Fig. 4. Field photographs from the Mai Kenetal and Chewo synclines: **(a)** Relic sedimentary bedding parallel to the low-grade metamorphic schistosity. Systematic set of extensional joints (cracks) trending NW–SE often bearing quartz mineral infill. **(b)** Assymmetric close fold with ESE moderately dipping axial plane and parallel axial cleavage at the eastern margin of the Tambien Group. **(c)** Minor tight to open folds in heterogeneous limestones of the Tambien Group with steeply dipping axial plane reflecting regional NW–SE compression. **(d)** Steeply NW dipping bedding and parallel metamorphic schistosity in volcano-sedimentary rocks of Tambien Group. **(e)** Superimposed kink-band folds with gently NW dipping axial planes reflecting subvertical shortening during exhumation. **(f)** Partly discordant subvertical NE–SW trending shear zone with syntectonic calcite vein.

3.3. The Chewo Pluton and its thermal aureole

The Chewo pluton is characterized by the presence of medium- to coarse-grained quartz monzonite and quartz monzodiorite (Fig. 5a). In addition, host rock xenoliths (15–20 cm in size) and mafic microgranular enclaves (MME) were mapped along the pluton contacts (Figs. 5b and c). The structural and thermal aureole has been clearly preserved in a narrow zone (100–300 m). However, in the wider area of up to 2,000 m, sporadic evidences of the thermal/structural overprint have been found (extent of the aureole is shown in Figs. 3a and b). The pluton has partly discordant intrusive contacts to host low-grade Tambien Group. Intrusive contacts are mostly steep, dipping inward to the pluton. Two distinct fabrics were identified in the Chewo pluton. The relatively older fabric is defined by a melt induced planar preferred alignment of feldspar and biotite aggregates (M1) bearing no evidence of subsolidus deformation or post-magmatic alteration (Figs. 5b and 6a). This early magmatic foliation has a lower intensity and is mostly parallel to the pluton contacts. The orientation of this magmatic foliation changes moderately to gently NW to NE dipping in the central part of the pluton (Fig. 3a and c). A superimposed fabric (M2) reveals a transitional magmatic to high-temperature solid-state pattern mostly defined by relic crystallization-induced aggregates affected by crystal-plastic deformation (Figs. 5d and 6b). The solid-state deformation was localized mainly in quartz and feldspar crystals often forming a mosaic of small subgrains in pressure shadows, irregular and lobate grain boundaries and chessboard texture (Fig. 6b). This foliation dips steeply

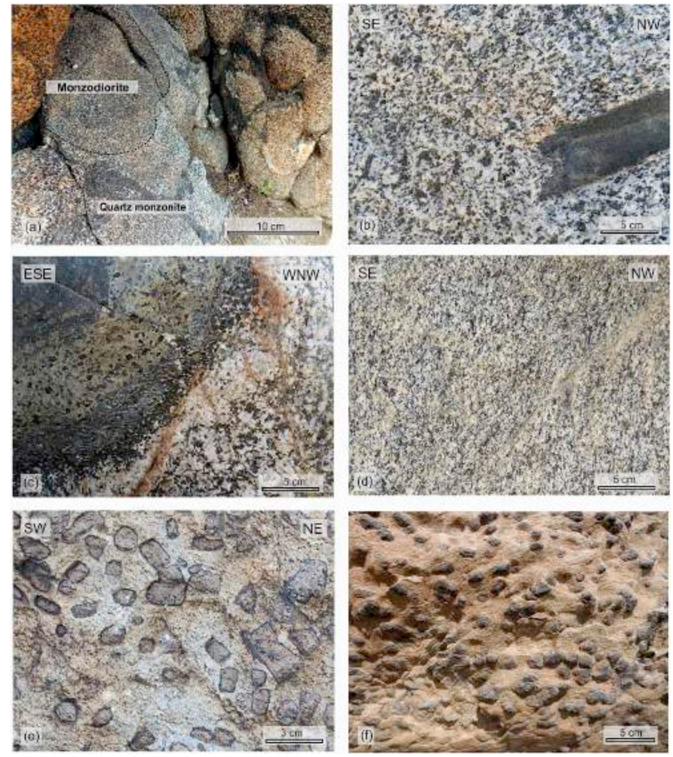

Fig. 5. Field photographs from the Chewo Pluton. **(a)** Contact between prevailing rock types - medium-grained quartz monzodiorite and medium to coarse grained quartz monzonite. **(b)** Relatively older magmatic fabric (M1) and host rock xenolith. **(c)** Mafic microgranular enclave (MME) within the quartz monzonite as the result of magma mingling. **(d)** A superimposed transitional magmatic to high-temperature solid-state fabric (M2). **(e,f)** Cordierite poikiloblasts in the schist from the contact aureole.

to NW to N or S (Fig. 3a and c) regardless of the location in the pluton. A heterogeneous re-working of original low-grade schistosity was found in the pluton aureole with presence of new cordiorite aggregates (Fig. 5e and f). The prevailing fabric in the contact aureole is contact-parallel foliation bearing steeply plunging stretching lineation, often with relics of asymmetrically folded regional schistosity.

4. Anisotropy of magnetic susceptibility (AMS)

The anisotropy of magnetic susceptibility (AMS) in the Chewo pluton was analysed from samples collected along a NE–SW transect (Table 1 and Fig. 3). The bulk magnetic susceptibility (km) ranges widely from 2.02×10^{-4} to 3.18×10^{-3} [SI]. Their distribution portrays two clusters with the majority having an average value of 1.3×10^{-3} SI indicating the predominant influence of paramagnetic minerals to magnetic anisotropy (Fig. 7a). Thermomagnetic analyses were carried out for 3 samples and reveal different values of bulk susceptibility (specimens TD60-3-3 from site TD60, TD45-2-3 from site TD45 and TD58-4-2 from site TD58; Fig. 7b). The heating and cooling thermomagnetic curves (Fig. 7b) are characterized by: (a) Curie points at 576 °C (TD60-3-3), at 580 °C (TD58-4-2) and at 581 °C (TD45-2-3) which indicates the presence of low-Ti magnetite (b) Increasing magnetic susceptibility at 400 °C (TD45-2-3), 420 °C (TD58-4-2) and 460 °C (TD63-3-3) indicating the Hopkinson effect and (c) increasing magnetic susceptibility between 160 and 370 °C (TD45-2-3), 180 and 380 °C (TD58-4-2), 190 and 400 °C (TD60-3-3) which could reflect the presence of minor single domain (SD) magnetite grains or secondary recrystallization to (Ti) maghemite as described by Archanjo et al. (1999) and Magee et al. (2012). The degree of anisotropy (P parameter) for both defined fabrics (M1 and M2) is relatively low, ranging from 1.069

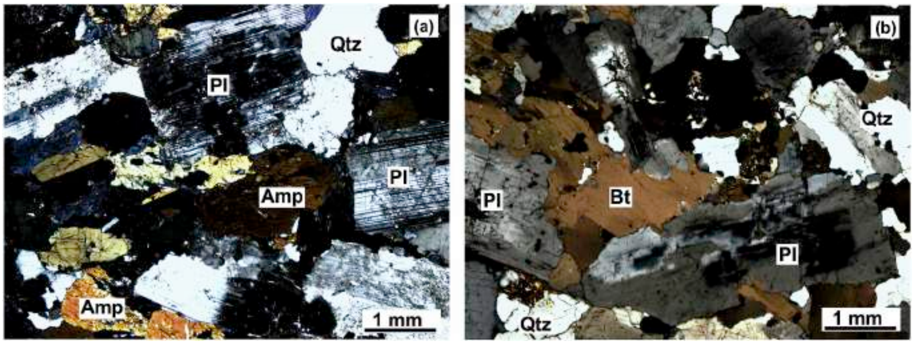

Fig. 6. Microphotographs of two defined fabrics in the Chewo Pluton. **(a)** M1 – melt-induced magmatic fabric with no evidence of crystal-plastic deformation and recrystallization. **(b)** M2 – transitional magmatic to low-intensity HT solid-state fabric with evidence of irregular and lobate grain boundaries, chessboard texture and minor subgrains in pressure shadows.

Table 1
The results of AMS analyses of the Chewo pluton. K1 and K3 are derived parameters of magnetic lineation and pole to magnetic foliation respectively. Km, T and Pj are bulk magnetic susceptibility, shape parameter and degree of anisotropy respectively. Samples are listed in order from NE to SW. (Dec: declination (azimuth), Inc: inclination (dip or plunge)).

Sampling stations	No. of Specimen	Km [10^{-6}]	Pj	T	K1 (Dec/Inc)	K3 (Dec/Inc)	East (°)	North (°)
TD53	15	459	1.06	0.665	189/35	053/45	38.77016	13.47344
TD54	12	964	1.085	0.589	199/13	303/46	38.75915	13.44878
TD60[a]	13	8,330	1.123	0.617	286/43	030/14	38.77433	13.37152
TD59	15	1,760	1.132	0.172	181/36	031/49	38.76405	13.39742
TD58[a]	17	1,570	1.1	−0.302	177/39	009/51	38.74310	13.35372
TD45[a]	9	2,830	1.053	0.384	265/01	356/17	38.73518	13.35350
TD48	18	1,320	1.115	−0.039	023/25	138/42	38.75063	13.39924
TD49	17	2,350	1.057	0.032	162/07	033/79	38.76456	13.46542
TD50	14	523	1.06	−0.054	099/51	356/10	38.75988	13.46280
TD51	10	278	1.066	0.463	010/74	140/10	38.76725	13.46693

[a] Also stations of specimens used for thermomagnetic analysis.

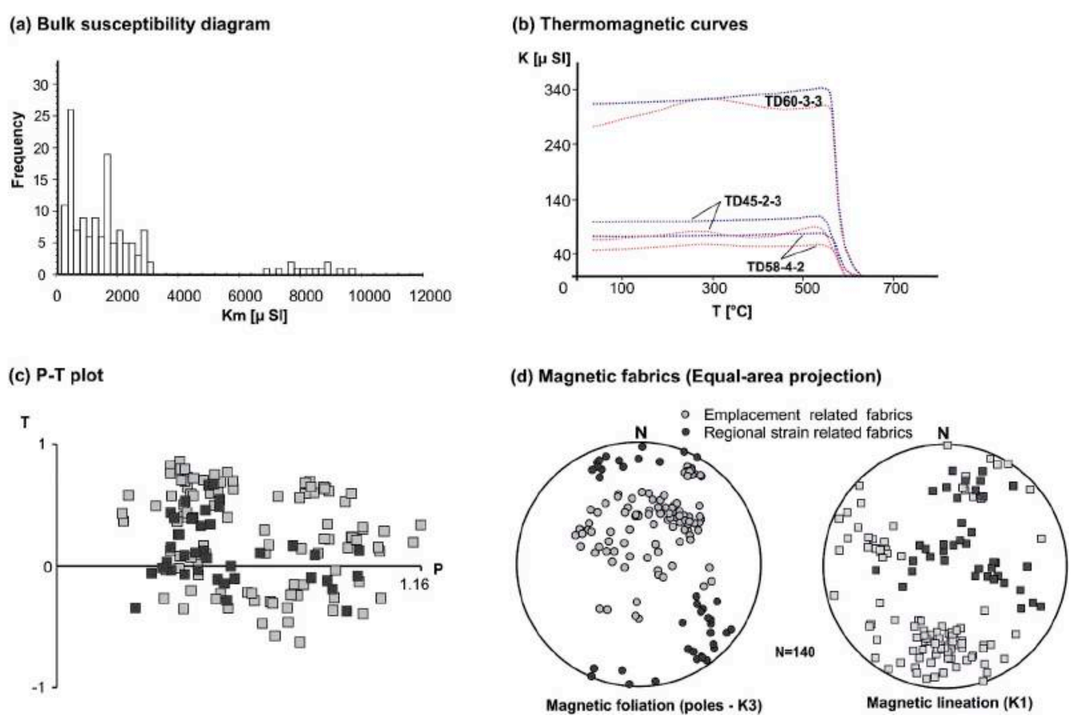

Fig. 7. AMS parameters in the Chewo Pluton. **(a)** Bulk magnetic susceptibility distribution, **(b)** Thermomagnetic heating and cooling curves, **(c)** P-T plot (P: degree of anisotropy, T: shape parameter), **(d)** Diagrams of magnetic foliations and lineations (equal area lower hemisphere projection). Location of the stations where the AMS samples were collected are shown in Fig. 3 and Table.1.

to 1.161 (Fig. 7c). The susceptibility ellipsoid shapes (T parameter) are almost evenly distributed between slightly prolate to oblate with values ranging from −0.64 to 0.86 (Fig. 7c). At localities with predominant magmatic foliation (M1) or where no apparent mesoscopic fabric was evident, the magnetic foliations dip gently to moderately towards the ~NW to ~NE bearing shallowly ~S to ~SSW or ~W plunging magnetic lineations (Fig. 7d). At the localities where the transitional magmatic to high-temperature fabric (M2) was found the magnetic foliation dips steeply to ~NW to ~N or ~S and magnetic lineation plunges steeply to moderately to ~N or ~E (Fig. 7d).

Table 2
Mineral assemblages of samples taken for geochemical and petrological analysis (accessory minerals in the parentheses and secondary minerals in italics). The abbreviations of mineral names are after Kretz (1983).

Samples	Longitude	Latitude	Rock name	Mineral composition
TD19/2	38.919841	13.438853	Bt schist	Qtz, Pl, Bt, (Ap), *Chl*
TD13/1	38.749572	13.415557	Bt schist	Qtz, Chl, Bt, Pl, (Opq, Mnz)
TD35/1	38.769615	13.472606	Crd-Bt schist	Qtz, Crd, Bt, Pl, (Opq), *Ms, Chl*
TD5/1	38.735180	13.353505	Bt hornfels	Bt, Pl, (Opq), *Chl, Ms*
TD12/1	38.746235	13.417976	Cdr-Bt hornfels	Bt, Qtz, Pl, Cdr, (Opq, Ap), Chl
TD14	38.746678	13.403810	Cdr-Bt hornfels	Qtz, Bt, Cdr, (Opq, Ap), *Chl*
TD31/2	38.764393	13.465182	Grt-Crd hornfels	Qtz, Pl, Bt, Sill, Cdr, Grt, (Ap, Opq) *Chl*
TD35/2	38.770196	13.473692	Crd-Bt hornfels	Qtz, Crd, Bt, Pl, Ms, Chl, (Opq)
TD12/2	38.746235	13.417976	Sill-Crd hornfels	Qtz, Pl, Bt, Sill, Cdr (Ap, Opq) *Chl*
TD5/2	38.735180	13.353505	Metatuff	Cal, Chl, Qtz, Bt (Opq)
TD9/1	38.764052	13.397421	Metatuff	Bt, Qtz, Pl, Cal, (Opq, Ap), Chl
TD5/3	38.735180	13.353505	Metamarle	Cal, Qtz, Chl
TD22	38.854678	13.364065	Marble	Cal (Qtz)
TD34	38.768136	13.469189	Marble	Cal, Phl, Mgs (Chl, Atg)
TD33	38.766895	13.466637	Bt orthogneiss	Pl, Bt, Qtz, (Tu, Ap, Mnz)
TD10/1	38.746133	13.421491	Amp hornfels	Amp, Px, Qtz, Pl, (Ap, Opq), Chl
TD10/5	38.746133	13.421491	Qtz monzonite	Qtz, Pl, Kfs, Amp, Bt, (Ap, Mnz)
TD48	38.751802	13.437849	Qtz monzonite	Pl, Amp, Bt, Qtz, (Ap, Opq), *Chl*
TD49	38.750718	13.431595	Qtz monzonite	Pl, Amp, Bt, Qtz, (Ap, Zr), *Chl*
TD50/1	38.750050	13.423495	Qtz monzonite	Pl, Amp, Bt, Qtz, (Ap, Zr, Opq), *Chl*
TD50/2	38.750050	13.423495	Qtz monzonite	Pl, Amp, Bt, Qtz, (Ap, Zr), *Chl*
TD51	38.750794	13.420740	Qtz monzonite	Pl, Amp, Bt, Qtz, (Ap, Zr, Opq)
TD53	38.764556	13.465420	Qtz monzonite	Pl, Amp, Bt, Qtz, (Ap, Opq), *Chl*
TD54	38.759875	13.462801	Qtz monzonite	Pl, Amp, Bt, Qtz, (Ap, Zr), *Chl*
TD58	38.759145	13.448776	Qtz monzonite	Pl, Amp, Bt, Qtz, (Ap, Zr, Opq), *Chl*
TD59	38.761875	13.456184	Qtz monzonite	Pl, Amp, Bt, Qtz, (Ap, Opq)
TD60	38.763173	13.460616	Qtz monzonite	Pl, Amp, Bt, Qtz, (Ap, Opq), *Chl*
TD32	38.766257	13.461212	Qtz monzonite	Pl, Amp, Bt, Px, Qtz, Kfs (Opq, Ap, Zr)
TD10/2	38.746133	13.421491	Monzodiorite	Amp, Pl, Bt, Qtz, (Ap, Opq, Ttn), Czo
TD10/3	38.746133	13.421491	Monzodiorite	Pl, Amp, Bt, Qtz, (Ap, Zr), *Chl*
TD10/4	38.746133	13.421491	Monzodiorite	Pl, Amp, Bt, Qtz, (Ap), *Chl, Czo*
TD10/6	38.746133	13.421491	Monzodiorite	Bt, Amp, Pl, Qtz, (Opq, Ap), *Chl*
TD45	38.752900	13.442419	Monzodiorite	Bt, Amp, Pl, Qtz, (Opq, Ap, Ttn), *Chl*
TD20/3	38.746424	13.427392	Monzodiorite	Pl, Qtz, Bt, Amp, Kfs, Ilm, Mgt (Ap, Ttn, Zr)

5. Petrology and mineral chemistry

5.1. The Chewo Pluton

Based on differences in mineral composition, textural features and whole-rock geochemistry, two principal magmatic suites are distinguished in the Chewo Pluton. All the rocks contain variable proportions of plagioclase, quartz, amphibole and biotite (Table 2). Locally present are also K-feldspar and clinopyroxene. Common accessories are titanite, apatite, ilmenite and magnetite (Table 2). The **quartz monzonite suite** representing the porphyritic to equigranular, medium-grained pyroxene-amphibole to amphibole-biotite quartz monzonite (Fig. 8a) is dominated by subhedral plagioclase (41–48 vol %), anhedral perthitic K-feldspar (5–14 vol %; Or_{84-85} Ab_{15-16}) and quartz (12–20 vol %). Plagioclase is oscillatory or occasionally patchily zoned with resorbed cores (Fig. 9a; An_{18-21}). Biotite flakes (10–20 vol %; Fig. 9b; $^{IV}Al = 2.29–2.30$ apfu, $X_{Fe} = 0.46–0.47$) are 0.1–0.3 mm in size and occur as individual crystals or aggregates associated with amphibole (10–17 vol %). Chemically homogenous diopside ($X_{Fe} = 0.26–0.27$) forms small (up to 1.5 mm) euhedral crystals (0–6 vol. %) which are rimmed by amphibole (Fig. 9c–d; magnesiohornblende to edenite; $Si = 6.65–7.00$ apfu, $X_{Mg} = 0.62–0.77$), biotite and quartz. Zircon and apatite are typical accessories in the quartz monzonite rocks. Also present, though rarely, are microgranular mafic enclaves (MME) up to 10 cm in diameter which consist of amphibole (35–45 vol %), biotite (30–40 vol %), plagioclase (10–26 vol %) and quartz (2–10 vol %). Typically the **monzodiorite suite** (Fig. 8b and c) is porphyritic to equigranular, medium-grained amphibole-biotite to biotite-amphibole monzodiorite to diorite in composition. It is characterized by a lower content of K-feldspar (0–5 vol. %) and quartz (1–7 vol. %) in comparison to the quartz monzonite suite. It also typically portrays a higher content of ferromagnesian minerals. Quartz and the rarely present K-feldspar occur as anhedral interstitial grains. Subhedral to euhedral plagioclase (49–65 vol %; Fig. 9a; An_{22-40}) is normally or oscillatory zoned. Plagioclase cores are often highly retrogressed to sericite, epidote, prehnite and calcite. Biotite (12–21 vol %; Fig. 9b; $^{IV}Al = 2.29–2.43$ apfu, $X_{Fe} = 0.45–0.53$) forms subhedral crystals 2–5 mm in length which is partly affected by a pervasive chloritization. The composition of subhedral amphibole crystals (13–19 vol %; Fig. 8c) ranges from pargasite through edenite to magnesiohornblende (Fig. 9c–d; $Si = 6.34–7.70$ apfu, $X_{Mg} = 0.59–0.79$). The Electron Microprobe Anaysis of typical amphiboles, feldspars and biotites from Chewo pluton are available in the supplementary material to this article (Tables S1–3).

5.2. Host Tambien Group

The rocks of the Tambien Group exposed in the Tekeze Dam area are represented by purple metasiltstone with metatuff, limestone (marble) and metasandstone layers. Limestones with thin siltstone bands are predominant in the footwall of this sedimentary sequence (Hailu, 2000; Alene et al., 2006; Swanson-Hysell et al., 2015). The metasiltstone in the Tambien Group display a strongly developed cleavage associated with the regional low grade metamorphism. The mineral assemblage in the metasiltstones is albite + quartz + chlorite ± white mica ± smectite group ± graphite ± calcite ± pyrite (Table 2). These rocks usually show well-defined slaty cleavage (S1) and primary sedimentary structures (S0) are locally preserved. The metasiltstone beds display small-scale lamination (Fig. 8d) with locally present layers or bodies of fine grained, sometimes laminated, metatuffs with the mineral assemblage: albite + chlorite + calcite ± clinozoisite ± titanite ± quartz ±

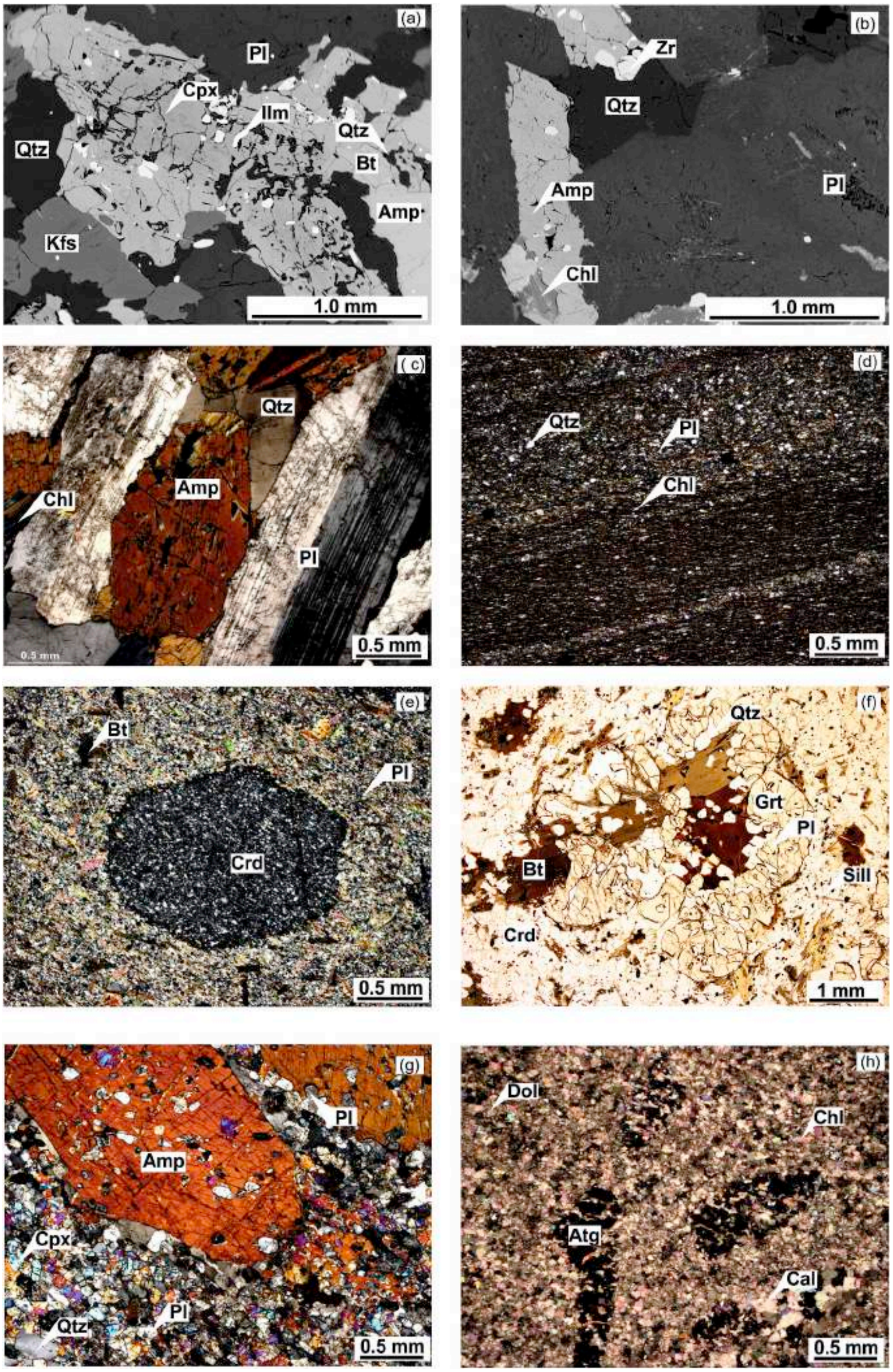

Fig. 8. Selected backscattered electron (BSE) and optical microscope images of the igneous rocks from the Chewo Pluton and metamorphic rocks its contact aureole. (**a)** Quartz monzonite (sample TD32) contain euhedral diopside crystals rimmed by the amphibole (BSE). (**b)** Monzodiorite (sample TD20) subhedral plagioclase is partially altered to sericite, epidote and prehnite (BSE). (**c)** Typical texture of the amphibole–biotite monzodiorite (XPL, sample TD10/2). (**d)** Laminated metasiltstone (XPL, sample TD19/2). (**e)** Cordierite poikiloblast in the schist from the contact aureole of the Chewo Pluton (XPL, sample TD12/1). (**f)** Garnet poikiloblast with abundant quartz and ilmenite inclusions from xenolith of the garnet-sillimanite-cordierite hornfels (PPL, sample TD31/2). (**g)** Euhedral amphibole porphyroblasts from xenolith of the amphibole hornfels (XPL, sample TD10/1). (**h)** Antigorite pseudomorph after forsterite in the marble from the contact aureole of the Chewo Pluton (XPL, sample TD34/1).

smectite group ± biotite (Table 2). Marbles beyond the contact aureole consist predominantly of fine to medium grained calcite with minor quartz and chlorite.

5.3. Thermal aureole of the Chewo Pluton

The contact aureole in the Tambien Group extends to ca. 2,000 m from the edge of the Chewo Pluton (Fig. 3a). Its outer limit is marked by the appearance of cordierite in metasiltstones (Fig. 5d,f). The list of samples location and associated mineral assemblages are shown in Table 2. Garnet in cordierite hornfels is present only within the ca. 7 m zone from the contact with the igneous rocks where garnet-sillimanite-cordierite and amphibole hornfels occur as xenoliths ranging in size from 20 to 130 cm in diameter. Cordierite schists are grey to greyish-green, fine-grained, foliated rocks with the assemblage cordierite + biotite + quartz ± white mica ± plagioclase ± smectite group ± magnetite ± ilmenite ± apatite ± monazite ± pyrite ± pyrhotite ± graphite. Superimposed metamorphic foliation (S2) is defined by an alignment of biotite and/or grain-flattening (mainly quartz grains). Flattening is also often visible on the inclusion-rich poikiloblasts of cordierite (Al = 3.85–4.01 apfu, X_{Fe} = 0.10–0.11). Poikiloblasts (Fig. 8e), up to 3 mm in diameter are partially or completely replaced by secondary minerals (mainly muscovite and chlorite). Anhedral quartz, subhedral plagioclase (Fig. 9a; $An_{35–37}$), sometimes fine-grained chlorite, white mica and/or smectite minerals group are present as the finer-grained matrix. Biotite (Fig. 9b;

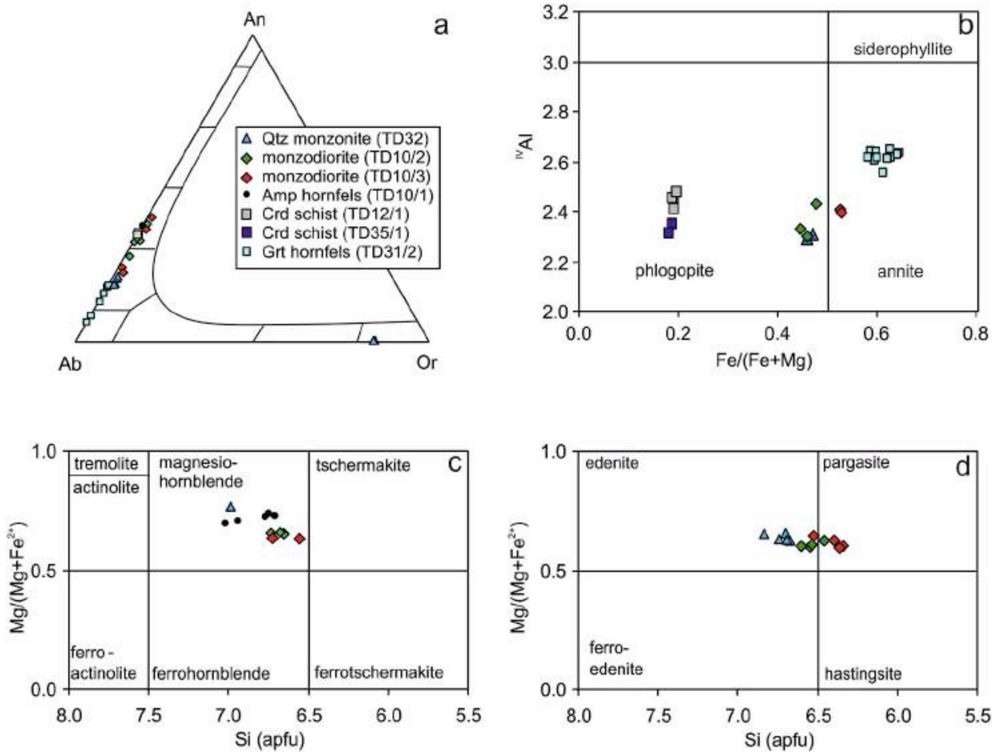

Fig. 9. Compositions of selected rock-forming minerals: (**a**) Ternary diagram Ab–An–Or for feldspar classification. (**b**) ^{IV}Al vs. Fe/(Fe + Mg) classification diagram of biotite. (**c** and **d**) Mg/(Mg + Fe^{2+}) vs. Si classification diagram for calcic amphiboles (Leake et al., 1997) $Ca_B \geq 1.5$, $(Na + K)_A < 0.5$, $Ca_A < 0.5$ (a) and $Ca_B \geq 1.5$, $(Na + K)_A \geq 0.5$, Ti < 0.5 (b) (The raw data is provided in Supplementary Tables S1–3).

^{IV}Al = 2.55–2.65 apfu, X_{Fe} = 0.58–0.58) occur as platy subhedral crystals that are up to 0.2 mm in length or 1 mm long porphyroblasts. Magnetite, ilmenite, apatite, monazite, pyrite, pyrhotite, graphite grains are present as accessory minerals.

The **garnet-silimanite-cordierite hornfels** is medium-grained, dark-brown to black, massive rock containing abundant cordierite and garnet poikiloblasts (Fig. 8f) within a matrix of biotite, sillimanite and quartz. Sillimanite is present as fibrolite or acicular crystal while cordierite (Al = 3.97–4.03 apfu, X_{Fe} = 0.43–0.47) occurs as anhedral poikiloblast up to 4 mm in size. Biotite (Fig. 9b; ^{IV}Al = 2.31–2.48 apfu, X_{Fe} = 0.18–0.20) crystals up to 2 mm in size are irregularly disseminated in the samples. Subhedral garnets are chemically relatively homogeneous ($Alm_{87–82}Prp_{11–14}Adr_{0–2}Sps_1Grs_{0–1}$) and occur as porphyroblast up to 3 mm in size. Subhedral plagioclase is normally zoned, with $An_{6–13}$ cores and $An_{16–18}$ rims (Fig. 9a). Ilmenite, magnetite and apatite grains are typical accessories in these rocks.

The **amphibole hornfels** are fine-grained to medium-grained rocks composed of amphibole, plagioclase and clinopyroxene (Fig. 8g). Amphibole (Fig. 9c–d; Si = 6.94–7.02 apfu, X_{Mg} = 0.70–0.74) forms poikilitic porphyroblasts commonly 3–10 mm long. Characteristic are up to 0.3 mm inclusions of the plagioclase (Fig. 9a; $An_{37–38}$), and diopside (X_{Fe} = 0.24–0.25). The matrix is a equigranular mosaic of diopside, plagioclase and quartz. Small flakes of chlorite and sericite are also present locally.

Medium-grained, equigranular **marble** dominated by calcite and, in some cases, forsterite plus secondary serpentine, with lesser phlogopite and/or chlorite, dolomite and/or quartz and accessory sulphides are present. Near the contact with the plutonic rocks (TD34) medium-grained, granular marble dominated by calcite (65 vol %) and dolomite (18 vol %) with minor magnesite, chlorite and antigorite and talc are present. Antigorite occurs as a fine grained pseudomorph after forsterite (Fig. 8h).

6. Thermobarometry and P-T modelling

The temperature and pressure conditions of the magma emplacement are calculated based on (a) the amphibole–plagioclase (edenite–richterite model) thermometry of Holland and Blundy (1994) and (b) amphibole–plagioclase barometry of Molina et al. (2015), which gave solidus temperature and pressure of 680–777 °C and 0.22–0.49 GPa respectively (Table 3a). A slightly narrower range of pressure estimates were obtained for the amphibole hornfels from the contact aureole (0.25–0.31 GPa; Table 3b). Applied barometry, based on the total Al content of amphibole (Anderson and Smith, 1995) for the igneous rocks, gave similar pressures (0.32–0.43 GPa). The pressure–temperature conditions of garnet-bearing hornfels were assessed with THERMOCALC 3.33 (Holland and Powell, 1998) in the average P–T (avPT) mode of Powell and Holland (2008). This method is based upon calculating an independent set of reactions between the mineral phases of an equilibrium assemblage and computing the average P–T from the intersection of all the reactions. Activities of the mineral phases used for the calculations were obtained using the AX software (Holland and Powell, 1998). The avPT calculations were made on the garnet-bearing hornfels (sample TD31/2; Table 2) with peak mineral assemblage: Bt + Cdr + Grt + Sill (Table 3b). The parageneses of the cordierite schists did not permit these calculations. In order to constrain the metamorphic temperatures in the contact aureole of the Chewo Pluton, the Ti content in biotite (Henry et al., 2005) was used. This geothermometer was calibrated for graphitic metapelites that contain ilmenite or rutile as a Ti-saturating phase. Garnet-sillimanite-cordierite hornfels form oval xenolith 50 cm in diameter which is situated close to the contact of monzodiorites with metasediments in the contact aureole. This hornfels is a typical member of the Tambien Group and is associated with marble. The content of X_{CO2} in the coexisting fluid has a relatively high influence on the pressure calculation for the mineral assemblage of hornfels (Table 3b). Therefore P-T conditions with wide fluid-composition range (X_{CO2} = 0.0–0.5) were calculated. However the P-T conditions calculated for the composition ambient fluid X_{CO2}~ 0.0 in the garnet-sillimanite-cordierite hornfels are found to be most reliable. Estimated temperatures 634 ± 78 °C and pressures 0.41 ± 0.09 GPa were obtained for this fluid composition. The results of Ti-in-biotite thermometer (Henry et al., 2005) from cordierite-biotite schists (601 ± 13 °C and 578 ± 24 °C, Table 3b) indicate a relatively low temperature gradient from the hot intrusive contact of Chewo

Table 3
P-T modelling of the Chewo pluton emplacement. (a) Modal compositions, mineralogy, PT conditions of the igneous rocks and amphibolite; modal compositions in vol. % (numbers in parentheses). (b) Mineralogy and PT conditions of the cordierite-biotite schists and hornfels (Sd = standard deviation; Corr = correlation coefficient; Sigfit = statistical consistency). Sample locations given in Fig. 3 and Table 2.

(a)

Rock	Amp-Bt quartz monzonite	Bt-Amp monzodiorite	Bt-Amp monzodiorite	Amp hornfels
Sample	TD32	TD20/3	TD10/2	TD10/1
Mineral assemblage	Pl (36), Qtz (26), Kfs (15), Bt (9), Amp (7), Px (6), Ilm, Mgt, Ap, Ttn, Zr	Pl (52), Qtz (17), Bt (16), Amp (14), Kfs (1) Ilm, Mgt, Ap, Ttn, Zr	Pl (58), Bt (18), Amp (15), Qtz (8), Ilm, Mag, Ap, Ttn	Pl (56), Amp (21), Qtz (12), Cpx (10), Ilm, Mag, Ap, Zr
Plagioclase (An)	19–21	22–40	28–34	37–38
Biotite (X_{Fe})	0.46–0.47	0.53	0.45–0.48	–
Biotite (^{IV}Al)	2.29–2.30	2.39–2.40	2.29–2.43	–
Clinopyroxene (X_{Fe})	0.26–0.27	–	–	0.24–0.25
Amphibole (X_{Mg})	0.62–0.77	0.66–0.63	0.59–0.79	0.70–0.74
Amphibole (Si)	6.65–7.00	6.46–6.72	6.34–7.70	6.94–7.02
Amp–Pl thermometry (Holland and Blundy, 1994); pressure according to Amp barometry (Molina et al., 2015)				
T (°C) ± 32 °C	680–726	687–777	717–775	666–755
Amp-Pl barometry (Molina et al., 2015); temperature according to Amp thermometry (Holland and Blundy, 1994)				
P (GPa)	0.28–0.36	0.22–0.43	0.24–0.49	0.25–0.31
Amp barometry (Anderson and Smith, 1995); temperature according to Amp-Pl thermometry (Holland and Blundy, 1994)				
P (GPa)	0.33–0.34	0.32–0.41	0.32–0.43	–

(b)

Rock	Grt-Sill-Cdr hornfels		Crd-Bt schist	Crd-Bt schist
Sample	TD31/2		TD35/1	TD12/1
Mineral assemblage	Qtz, Bt, Cdr, Grt, Sill, Pl, Mgt, Ilm, Ap		Qtz, Bt, Cdr, Ms, Sm-Chl, Mgt, Ap	Qtz, Bt, Cdr, Pl, Chl, Mgt, Ap, Mnz, Ilm
Biotite (X_{Fe})	0.58–0.64		0.18–0.19	0.19–0.20
Biotite (^{IV}Al)	2.55–2.65		2.31–2.35	2.41–2.48
Plagioclase (An)	6–18		–	35–36
Cordierite (X_{Fe})	0.43–0.47		0.10	0.11
Average PT calculations (THERMOCALC 3.33)				
aH_2O	1.0	0.5	–	–
T (°C)	634	631	–	–
Sd	78	77	–	–
P (GPa)	0.41	0.34	–	–
Sd	0.09	0.08	–	–
Corr	0.916	0.913	–	–
Sigfit	0.64	0.59	–	–
Ti-in-biotite geothermometer of Henry et al. (2005)				
T (°C)	560–657		588–614	555–602
Grt-Crd geothermometer of Dwivedi et al. (1998)				
T (°C)	637–701		–	–

Pluton to the low grade metasediments of the Tambien Group.

7. Major and trace element geochemistry

The chemical composition of rocks from the Chewo Pluton ranges from intermediate to acidic (SiO_2 = 52–63 wt %). Using the TAS (total alkalis versus silica) diagram (Middlemost, 1994) they are classified as monzodiorite and quartz monzonite (Fig. 10a). The rocks are predominantly subalkaline (Fig. 10a) where sodium prevails over potassium (K_2O/Na_2O = 0.27–0.92). Based on a K_2O versus SiO_2 plot (Fig. 10b; Peccerillo and Taylor, 1976) almost all the rocks studied (K_2O = 1.1–4.3 wt %) are classified as high-K calc-alkaline except one calc-alkaline monzodiorite (K_2O = 1.1 wt %). The metaluminous characteristics (A/CNK = 0.79–0.98; Fig. 10c) and relatively high mg# (molar 100 × MgO/(MgO + FeOt) = 50–62) are in good agreement with the rocks position in the B–A plot (Debon and Le Fort, 1983, Fig. 10d) which indicates the mineral assemblage Bt + Amp ± Cpx. The monzonite rocks are characterized by lower CaO/Na_2O (1.40–1.78) in comparison to monzodiorites (0.79–1.17). With regard to the major elements, the monzodiorites have higher Al_2O_3, MgO, CaO, TiO_2, FeO_t, and P_2O_5 than the quartz monzonites (Supplementary Table S4). The REE data plotted in chondrite-normalized (Boynton, 1984) spiderplot (Fig. 11a) show light rare earth element enriched patterns (Fig. 11a) with La_N/Yb_N ratios 6.8–15.6 and slightly negative to no Eu anomaly (Eu/Eu* = 0.8–1.0). The quartz monzonites and monzodiorites also have a similar REE pattern (103–163 ppm). In the primitive mantle-normalized (McDonough and Sun, 1995) spidergram (Fig. 11b), Chewo Pluton rocks are characterized by strong enrichment in the majority of

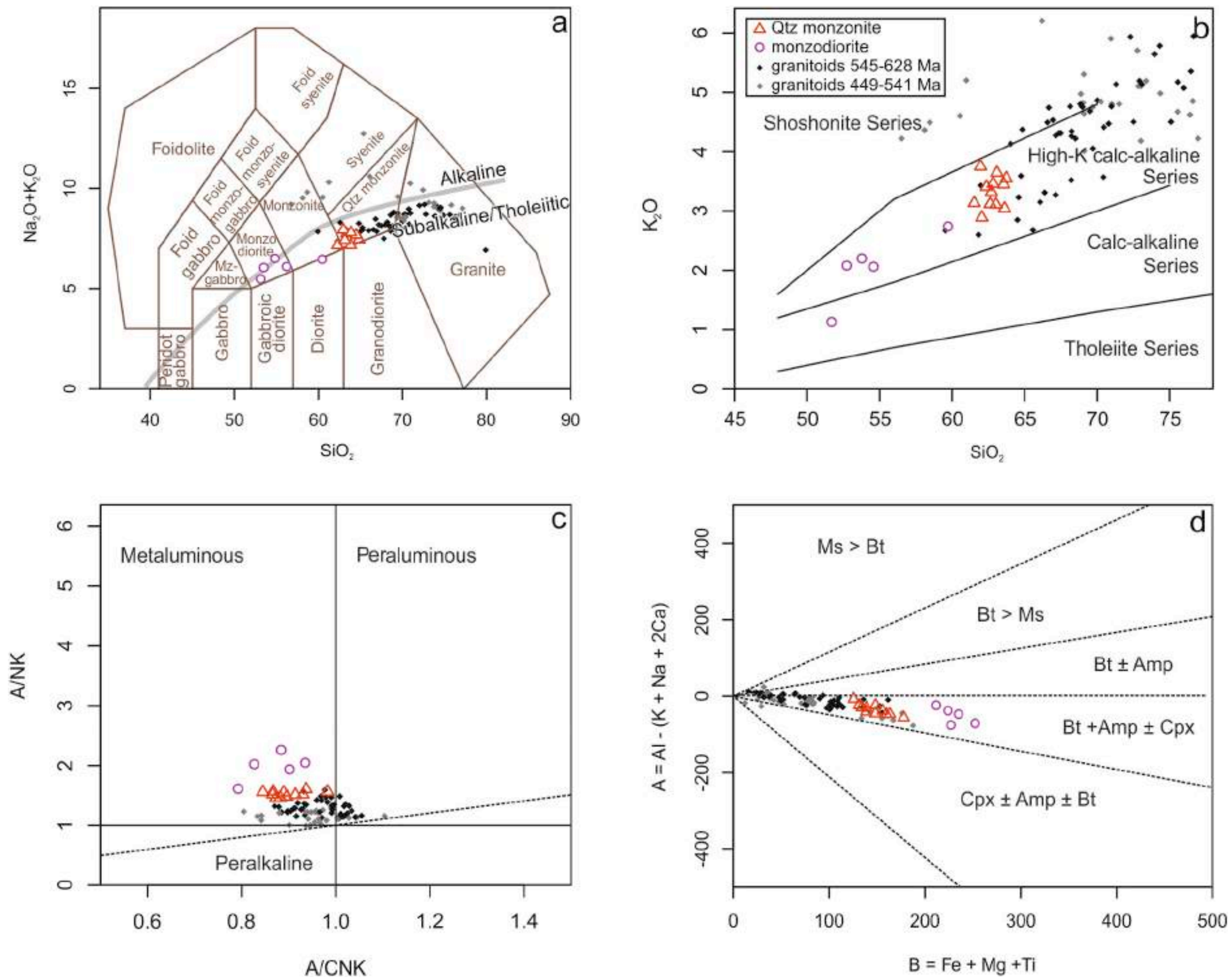

Fig. 10. Chemical classification of plutonic rocks from the Chewo Pluton: **(a)** Total alkali vs. silica (TAS) diagram (Middlemost, 1994; thick solid line shows boundary between alkaline and subalkaline rocks according to Le Bas et al., 1986). **(b)** K_2O vs. SiO_2 diagram with discriminating boundaries after Peccerillo and Taylor (1976). **(c)** A/NK vs. A/CNK diagram (after Shand, 1943). **(d)** B–A plot after Debon and Le Fort (1983). Ms = muscovite, Bt = biotite, Amp = amphibole, Cpx = clinopyroxene. Geochemical data for Neoproterozoic and Lower Paleozoic granitoids (545–628 and 449–541 Ma) in the southern part of the ANS from previous works (Tadesse et al. 1997, 2000; Ayalew et al., 1990; Asrat and Barbey, 2003; Miller et al., 2003; Asrat et al., 2004; Gebreyohannes, 2014).

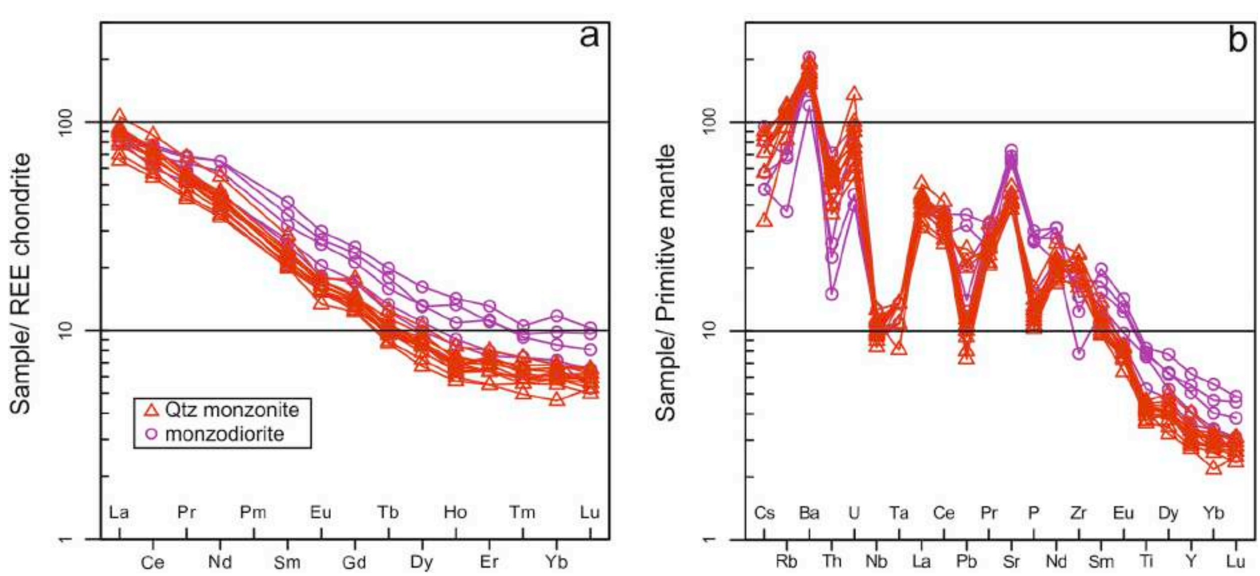

Fig. 11. (a) Chondrite-normalized REE patterns (normalization values from Boynton, 1984) and **(b)** Primitive mantle normalized multi-element patterns of igneous rocks from the Chewo Pluton (normalization values from McDonough and Sun, 1995).

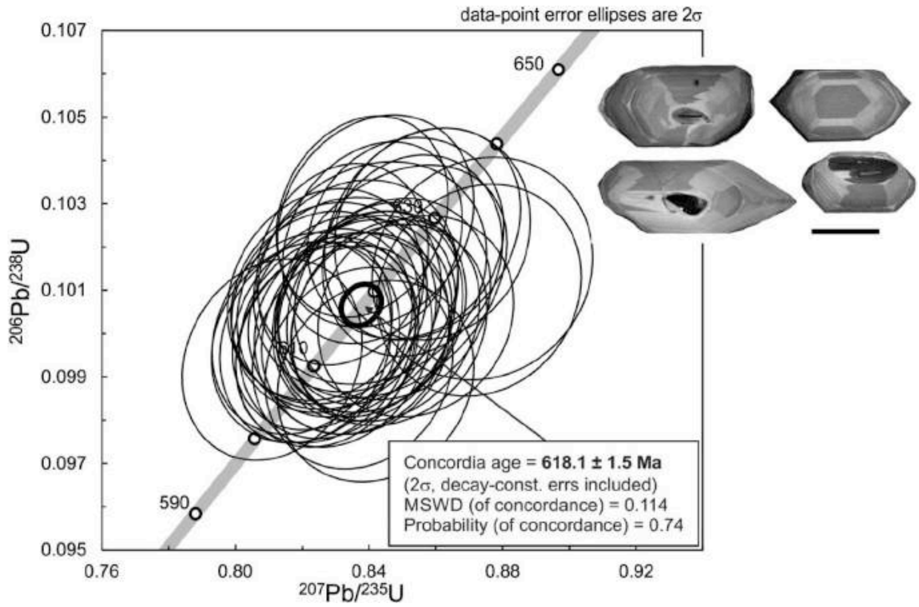

Fig. 12. Zircon weighted mean (concordia) age generated with the ISOPLOT program (v. 3.50, (Ludwig, 2003). Representative CL images of zircons from sample TD10/6. The scale bar represents 100 µm.

the large ion lithospheric elements (LILE) such as Ba, U, Sr, and the LREE (Light Rare Earth Elements), whereas normalized contents of Y and the HREE (Heavy Rare Earth Elements) are close to unity. Negative Th, Nb and Ta anomalies are also typical. The zircon saturation temperatures (Watson and Harrison, 1983) calculated from bulk-rock compositions, for quartz monzodiorite and monzodiorite (677–748 °C) are slightly lower in comparison to quartz monzonite (749–791 °C). Using the Harrison and Watson (1984) apatite saturation model, the temperatures for monzodiorite are 900–930 °C and 904–931 °C for quartz monzonite.

8. U/Pb geochronology

The zircons separated from sample TD10/6 (Table 2), taken from Chewo Pluton, that formed clear euhedral crystals and showed uniform bright sector zonation in CL (cathodoluminescence) were used for dating (Fig. 12). A Thermo-Finnigan Element 2 sector field ICP-MS coupled to a 193 nm ArF excimer laser (Resonetics Resolution M-50 LR) at Bergen University, Norway, was used to measure Pb/U and Pb isotopic ratios in zircons (Table 4). The apparent darker cores detected in most zircon grains gaveidentical U/Pb ages to the brighter “rims” and therefore cannot be considered as an inherited zircon population. More likely they all grew during a single magmatic event dated at 618.1 ± 1.5 Ma and the “cores” may simply represent the homogenous zircon formed during early stages of zircon crystallization. The oval shape of the “cores” may be due to the magmatic corrosion of the earlier zircon grains.

9. Discussion

Diverse polyphase deformation operating at low metamorphic grade and post-orogenic magmatism evolved along with interplay of multiple terrane accretion and back-arc basin development and closure in the ANS. The timing and extent of the deformation involved, especially near the end of the orogeny, are deciphered from the overprinting rock fabric, geochemical affinity and petrological and geochronological constraints discussed below.

9.1. Petrogenesis and magma source

According to the Rb versus Yb + Nb diagram (Pearce et al., 1984; Pearce, 1996) Neoproterozoic and Lower Paleozoic granitoids from the southern part of the ANS fall in the “post-collision granites” field (Fig. 13a). These granitoids can be divided into two groups based on whole-rock chemical compositions and age (Fig. 10; 13a,b). Neoproterozoic granitoids (545–682 Ma) are high-K calc-alkaline, whereas Cambro-Ordovician granitoids (449–510 Ma) indicate evolution from high-K calc-alkaline towards the alkaline series (Ayalew et al., 1990; Tadesse et al. 1997, 2000; Asrat and Barbey, 2003; Miller et al., 2003; Asrat et al., 2004; Gebreyohannes, 2014). In the Th/Yb versus Nb/Yb diagram (Pearce, 2008) it can be clearly seen that the samples of post-collisional granitoids from the southern part of the ANS generally trend from the mantle array (close to E-MORB) to the volcanic arc array (Fig. 13b). This trend indicates the crustal contamination of mantle-derived melts (Pearce, 2008). In the R1 – R2 diagram (Fig. 13c) the majority of the samples from Neoproterozoic and Lower Paleozoic granitoids in the southern part of the ANS fall into the syn-collision, late-orogenic and post-collisional uplift fields (Fig. 13c).

The major and trace element composition of the plutonic rocks from the Chewo Pluton area resemble Neoproterozoic post-collisional high-K calc-alkaline and metaluminous plutons in ANS (Figs. 10 and 13a-c; Alemu, 1998; Tadesse et al., 2000; Asrat et al., 2003, 2004; Avigad et al., 2007). The presence of mafic microgranular enclaves (MME), common resorbed Ca-rich plagioclase cores (e. g. Barbarin, 2005; Blundy and Sparks, 1992; Chen et al., 2005; Janoušek et al., 2004; Słaby and Martin, 2008) and the whole-rock chemical composition (Fig. 11b; variation in Th, U, Pb, Sr, P, Zr, Ti and REE) show that magma mixing and mingling between crustal and mantle-derived melts played an important role in the petrogenesis of the Chewo Pluton. The negative Nb as well as the positive Ba and Sr anomalies in the mantle normalized trace-element patterns (Fig. 11b) are a characteristic feature of most subduction-related granitoids (e.g. Pearce, 2008). According to Asrat et al. (2004) these ambiguities in the whole-rock chemical signatures of late Neoproterozoic granites could be explained by mingling and hybridization of mantle-derived magma with a felsic melt derived from the partial melting of Pan-African juvenile island-arc crust or immature sediments. Textural evidence for hydration crystallization is common in some monzodiorite samples where original

Table 4
LA-ICPMS U–Pb isotopic data of zircons from the monzodiorite sample (TD10/6) in Chewo pluton. Sample location given in Fig. 3 and Table 2.

Measured isotopic ratios									Ages (Ma)						
Nr.	Th (ppm)	U (ppm)	$^{207}Pb/^{235}U$	2 σ (abs)	$^{206}Pb/^{238}U$	2 σ (abs)	$^{207}Pb/^{206}Pb$	2 σ (abs)	$^{207}Pb/^{235}U$	2 σ (abs)	$^{206}Pb/^{238}U$	2 σ (abs)	$^{207}Pb/^{206}Pb$	2 σ (abs)	Disc. [a] (%)
7	21	47	0.874	0.027	0.1015	0.0021	0.0635	0.0017	631	15	623	12	625	56	−1.3
8	20	46	0.873	0.025	0.101	0.002	0.0635	0.0015	632	14	620	12	643	50	−1.9
9	39	63	0.826	0.022	0.1001	0.0019	0.0603	0.0012	608	12	615	11	556	42	1.1
10	27	51	0.854	0.024	0.1004	0.0019	0.062	0.0014	621	13	617	11	602	47	−0.6
11	26	55	0.827	0.023	0.1005	0.0019	0.0604	0.0013	605	13	617	11	532	47	1.9
12	23	50	0.846	0.024	0.1002	0.0019	0.0618	0.0014	616	13	616	11	586	47	0.0
13	22	51	0.859	0.024	0.1023	0.002	0.062	0.0014	625	13	627	12	595	47	0.3
14	25	62	0.828	0.022	0.0999	0.0019	0.0608	0.0013	607	12	614	11	556	44	1.1
15	22	50	0.832	0.023	0.1004	0.0019	0.0605	0.0013	609	13	617	11	550	47	1.3
16	29	70	0.841	0.023	0.1005	0.0019	0.0609	0.0012	616	13	617	11	582	45	0.2
17	28	81	0.832	0.021	0.1016	0.0019	0.06	0.0011	611	12	623	11	544	40	1.9
18	22	55	0.847	0.024	0.1008	0.0019	0.0615	0.0014	618	13	619	11	579	47	0.2
19	34	58	0.836	0.023	0.1	0.0019	0.061	0.0013	611	13	614	11	570	47	0.5
20	26	70	0.827	0.022	0.0997	0.0019	0.0604	0.0012	607	12	612	11	559	43	0.8
27	24	69	0.832	0.022	0.0997	0.0019	0.061	0.0012	610	12	612	11	577	42	0.3
28	25	51	0.828	0.024	0.1007	0.0019	0.0602	0.0014	607	13	618	11	532	50	1.8
29	83	117	0.847	0.028	0.1012	0.0022	0.0611	0.0016	620	15	621	13	604	58	0.2
30	25	66	0.853	0.022	0.1018	0.0019	0.0615	0.0012	622	12	625	11	592	43	0.5
31	29	62	0.856	0.024	0.1023	0.002	0.0616	0.0013	624	13	627	12	594	46	0.5
32	28	57	0.837	0.023	0.0992	0.0019	0.0615	0.0013	614	13	609	11	596	45	−0.8
33	37	58	0.84	0.023	0.1005	0.0019	0.061	0.0013	615	13	617	11	571	45	0.3
34	29	52	0.827	0.024	0.1009	0.002	0.0601	0.0014	605	14	620	12	524	52	2.4
35	30	59	0.845	0.023	0.1003	0.0019	0.0618	0.0013	617	13	616	11	593	46	−0.2
36	37	70	0.811	0.022	0.0994	0.0019	0.0594	0.0012	599	12	611	11	524	43	2.0
37	28	62	0.831	0.025	0.1007	0.002	0.0608	0.0015	609	14	618	12	555	52	1.5
38	38	65	0.827	0.022	0.0998	0.0019	0.0605	0.0012	609	12	613	11	565	42	0.7
39	36	61	0.841	0.022	0.1021	0.0019	0.0601	0.0012	615	12	626	11	547	42	1.8
40	24	50	0.842	0.024	0.0989	0.0019	0.0624	0.0014	616	13	608	11	608	48	−1.3
48	42	67	0.839	0.022	0.1004	0.0019	0.0611	0.0012	615	12	616	11	585	42	0.2
49	27	49	0.836	0.025	0.1011	0.002	0.0603	0.0015	610	14	621	12	535	53	1.8
50	33	56	0.835	0.024	0.1	0.0019	0.0612	0.0014	611	13	614	11	555	50	0.5
51	41	65	0.838	0.022	0.1003	0.0019	0.061	0.0012	614	12	616	11	578	43	0.3
52	41	67	0.821	0.023	0.0998	0.0019	0.0599	0.0013	605	13	613	11	544	48	1.3
53	21	46	0.841	0.028	0.1014	0.0021	0.061	0.0017	612	15	622	12	543	59	1.6
54	39	68	0.821	0.021	0.0998	0.0019	0.0599	0.0012	604	12	613	11	544	42	1.5
55	76	105	0.841	0.021	0.1007	0.0019	0.061	0.0011	616	12	618	11	594	38	0.3
56	46	82	0.838	0.021	0.1027	0.0019	0.0596	0.0011	615	12	630	11	544	40	2.4
57	27	60	0.842	0.024	0.1026	0.002	0.0597	0.0013	615	13	629	11	532	46	2.2
59	26	62	0.82	0.022	0.1	0.0019	0.0599	0.0012	605	12	615	11	538	44	1.6
60	27	60	0.851	0.024	0.1022	0.0019	0.0609	0.0014	619	13	627	11	555	48	1.3

[a] Disc. $=(1-((^{206}Pb/^{238}U)/(^{207}Pb/^{235}U)))*100$; analyses that were more than 10% discordant were discarded.

clinopyroxene aggregates were partially replaced by amphibole (Fig. 8a), biotite and quartz (Beard et al., 2005). Sharp decrease in the La/Yb ratio (10–23) with increasing SiO_2 (Fig. 13d) indicates the role of amphibole fractionation (Davidson et al., 2007).

9.2. P/T conditions and emplacement of the Chewo Pluton

Estimated P-T conditions (Fig. 14) of monzodiorite crystallization (732 ± 45 °C and 0.36 ± 0.14 GPa) reveal slightly higher values compared to the prevalent quartz monzonite (703 ± 23 °C and 0.32 ± 0.08 GPa). The wider range of temperatures and pressures calculated for monzodiorite could be explained as a result of early crystallization due to interaction with cooler crustal melt during magma mixing (e.g. Bea, 2010; Buriánek et al., 2016). The magma mixing with crustal melts and crystallization of the monzodiorite occurred at pressure conditions (732 ± 45 °C and 0.36 ± 0.14 GPa) similar to those of the garnet-biotite-cordierite hornfels xenoliths (Fig. 14; 634 ± 78 °C and 0.41 ± 0.09 GPa). The mineral assemblage within the contact aureole indicates a variable grade of metamorphism from~ 200 °C in the external part (e.g. chlorite-muscovite schist) to 555–755 °C near the contact with pluton. The pressure 0.32 ± 0.08 GPa estimates from quartz monzonite are consistent with P–T conditions which have been calculated from the stable mineral assemblage of amphibolite hornfels in the contact aureole (711 ± 45 °C and 0.28 ± 0.06 GPa). These results are in good agreement with the field and petrological relationships indicating that the Chewo pluton was emplaced at a depth of~10–13 km. The estimated depth of the emplacement roughly corresponds to the Negash pluton with the P-T conditions of magma crystallization T: 682–788 °C and 795–856 °C, P: 0.22–0.46 GPa; Asrat et al., (2004) (see Fig. 14).

9.3. Pluton emplacement and implications for regional geodynamic evolution

The early magmatic fabrics in the Chewo Pluton (M1) inferred on the basis of mesoscopic mapping and AMS analysis are mostly parallel to the inward, steeply dipping intrusive contacts defining the overall sub concentric shape of the Chewo Pluton as well as the superimposed fabrics in the contact aureole. Towards the central part of the pluton these fabrics decrease in intensity and change their orientation to gently to moderately dipping to the NW or SE (Fig. 7d). The presence of localized transitional magmatic to high-temperature solid-state fabrics (M2), which have the regional orientation, probably resulted from a heterogeneous re-working of the original emplacement-related fabrics (M1) due to increments of regional stress-field at later stages of magma crystallization (Paterson et al., 1989, 1998; Bouchez et al., 1990; Benn,

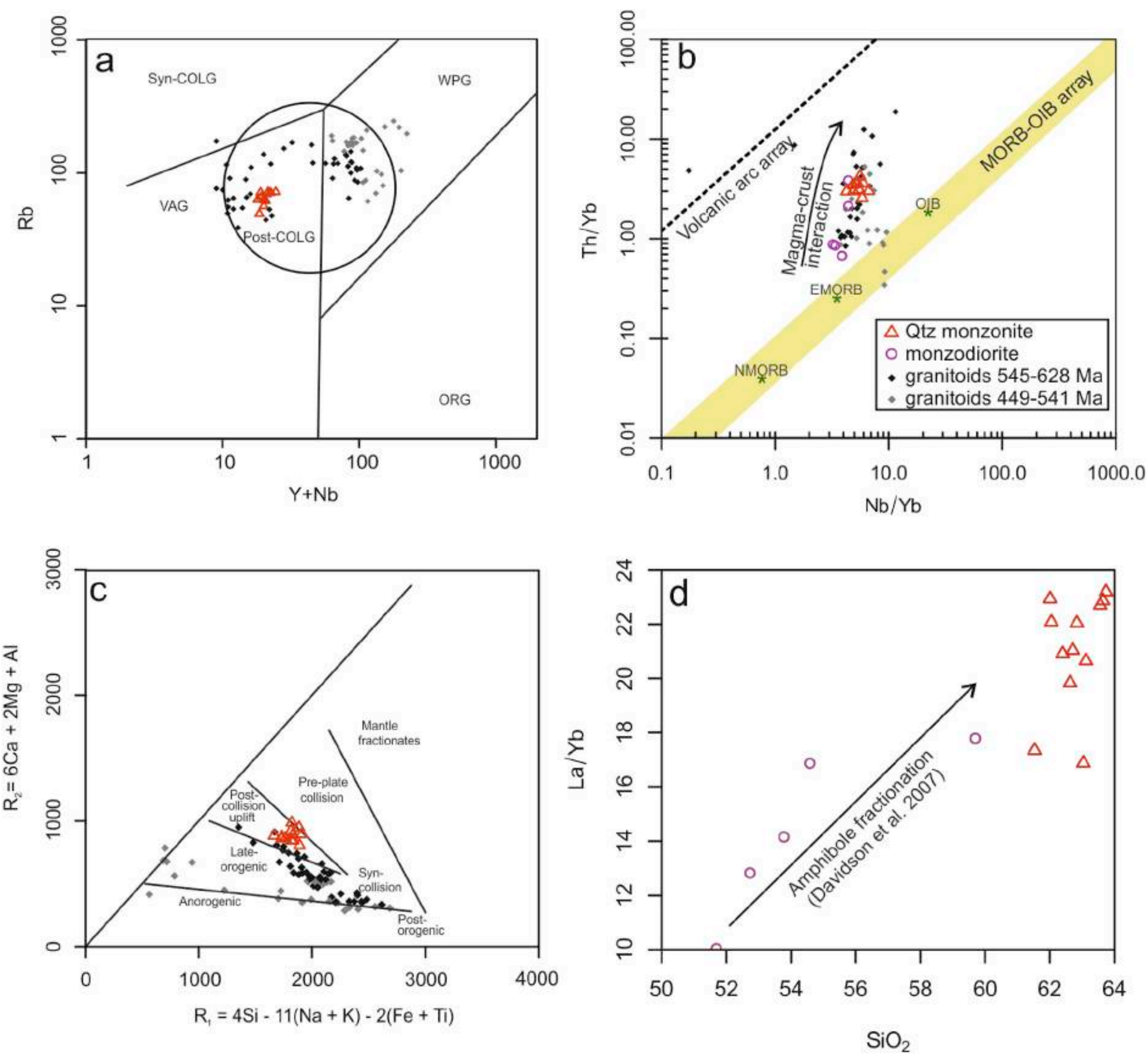

Fig. 13. Geotectonic discrimination diagrams of rocks from Chewo Pluton: (**a**) Discrimination diagram Rb vs (Y + Nb) of Pearce et al. (1984), with field of post-COLG (Pearce, 1996); Syn-COLG: syn-collision granites; VAG: volcanic arc granites; WPG: within-plate granites; ORG: ocean ridge granites; Post-COLG: post-collision granites. (**b**) Th/Yb vs. Nb/Yb diagram after Pearce (2008) with values typical for normal and enriched-mid ocean ridge basalt (N, E-MORB) and intraplate basalts to ocean island basalts (OIB). (**c**) R1-R2 [4Si - 11(Na + K) – 2(Fe + Ti) vs (6Ca + 2 Mg + Al)] diagram after Batchelor and Bowden (1985). (**d**) La/Yb vs. SiO_2 diagram. Geochemical data for Neoproterozoic and Lower Paleozoic granitoids (545–628 and 449–541 Ma) same as in Fig. 1.

2009). The complex geological pattern also reveals mechanisms that could have played a role in the pluton emplacement by providing space for the ascending magma (Fig. 15). These are mainly: (a) Local extension in the hinge part of the large-scale asymmetric Chewo syncline inferred on the basis of synchronous sub-solidus emplacement fabrics in the pluton at the later stages of regional WNW(NW)-ESE(SE) compression and related folding (e.g. Nyman and Karlstrom, 1997; Paterson and Miller, 1998; Kruger and Kisters, 2016) and (b) heterogeneous ductile shortening including the downward flow of thermally softened host rocks which can be inferred from the intensive tectonic overprint of steeply dipping stretching lineation in the pluton aureole (Paterson and Miller, 1998). This overall fabric pattern is typical for plutons emplaced diapirically, driven mainly by gravitational instability, but also supported by increments in the regional stress-field (e.g. He et al., 2009).

The zircon U/Pb crystallization age of the Chewo pluton of ca 618 Ma clearly indicates an affiliation to the group of post-collisional calc-alkaline intrusions from the southern ANS (Tadesse et al., 2000; Teklay et al., 2002; Eyal et al., 2010). In addition the age of the Chewo pluton also provides the upper limit for regional deformation related to the assembly of eastern and western Gondwana (for general overview see Fritz et al., 2013).

The data also provides certain implications for a better understanding of the geodynamic framework of the East African Orogen, which is associated with the closure of the Mozambique Ocean and Gondwana assembly between 650 and 620 Ma (Fritz et al., 2013). This paper presents a clarification of the succession, stress-field background and the timing of the main geodynamic events considered in the Tokar-Barka Terrain which are difficult to reconcile with our data from the same region - an early N–S oriented compression followed by regional folding (Alene and Sacchi, 2000; Sifta et al., 2005; Avigad et al., 2007; De Wall et al., 2011) and subsequently left-lateral oblique shearing (e.g. Tadesse, 1996; Tadesse, 1997).

The Tambien and Tsaliet groups which were formed ~850 to 735 Ma Ga; Sifeta et al., 2005; Avigad et al., 2007) are noted from our new data to have been tectonically affected by: (a) Folding of

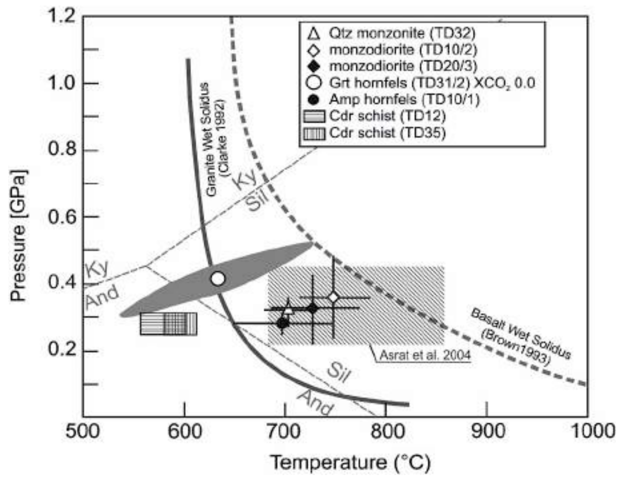

Fig. 14. Crystallization conditions for the selected igneous rocks from the Chewo Pluton estimated based on plagioclase-hornblende thermometry (Holland and Blundy, 1994) and amphibole–plagioclase barometry Molina et al. (2015). The P–T conditions for metamorphic rocks were estimated for garnet-bearing assemblages in the hornfels xenolith TD31/2 by THERMOCALC (Holland and Powell, 1998), amphibole-bearing assemblages in the hornfels xenolith (TD10/1; Table.2) and for the cordierite schist (vertically and horizontal hatched boxes) from the contact aureole (samples TD35/1, TD12/1; Table 2) by the Ti-in-biotite thermometer (Henry et al., 2005). The obliquely hatched area represents the PT conditions estimated for Negash Pluton (Asrat et al., 2004).

sedimentary bedding and subparallel low-grade schistosity with into asymmetric tight to open folds with well-developed axial cleavages dipping steeply to NW and fold axes that gently plunge to the NE or SW where no evidence for shearing deformation can be noted and (b) wide spread extensional joints and parallel calcite or quartz veins dipping steeply to NE or SW coeval with abundant “en échelon” structures in both mapped areas (Mai Kenetal and Chewo synclines). The deformations are hence consistent with WNW(NW)-ESE(SE), orogeny-perpendicular compression. Nevertheless, low-grade metamorphic overprint associated with burial of the volcano-sedimentary sequences might not be ruled out to pre-date the orogen-perpendicular compression as can be noted from the less conspicuous fabrics of the host rocks. On the other hand, the NW(N)-SE(S) trending left-lateral shearing has been dated from the synchronous emplacement of the Nakfa intrusive rocks (dated at~ 628 Ma; Teklay et al., 2001) and the polyphase in-situ emplacement of the Negash Pluton (dated at~ 608 Ma; Asrat et al., 2003). The formation of these~NNE-SSW trending shear zones/faults bearing both sinistral and dextral kinematics mapped across the Tokar-Barka Terrane (De Souza Filho and Drury, 1998; Drury and De Souza Filho, 1998; De Wall et al., 2011) could be explained as localized shearing in the general WNW(NW)-ESE(SE) regional compression deformation due to strain partitioning in rheologically heterogeneous environment.

The latest superimposed kink-band folds and low intensity axial cleavages dipping gently to NW are interpreted as being the result of subvertical shortening due to exhumation after crustal thickening. Predominant~NW-SE trending oblique-slip faults bearing both left- and right-lateral kinematics and younger kink-band folds with NW-SE trending axial cleavages are interpreted in accordance with De Wall et al. (2011) and Kusky and Matsah (2003) as belonging to the NW-SE trending Najd fault system due to oblique convergence in the northern ANS at around 540 Ma (Fritz et al., 2013).

10. Conclusions

The Chewo pluton built by pyroxene-amphibole to amphibole-biotite monzodiorite and quartz monzonite is a typical post-collisional intrusive body emplaced into a low-grade Neoproterozoic Tambien Group as part of the Tokar-Barka Terrain in the eastern Arabian–Nubian Shield. The pluton shows a high-K calc-alkaline and metaluminous composition with significant enrichment in both LREE and LILE originating due to hybridization and magma mixing between crustal and mantle-derived melts. The magma mixing and solidification of monzodiorite melt occurred at T: 732 ± 45 °C and P: 0.36 ± 0.14 GPa. The P-T conditions of final magma solidification is estimated at T: 703 ± 23 °C and P: 0.32 ± 0.08 GPa which, in combination with similar data from the pluton aureole revealing T: ~200–755 °C and P: 0.28 ± 0.06 GPa, indicates that the Chewo pluton was emplaced between~10 and 13 km of depth. The Chewo Pluton was emplaced diapirically, supported by local extension in the hinge part of a large-scale asymmetric syncline during the last increments of regional deformation – orogen-perpendicular WNW(NW)-ESE(SE) compression. This tectonic event was detected as the first phase of East African Orogeny in the Tokar-Barka Terrane. In concordance, the determined concordant U/Pb

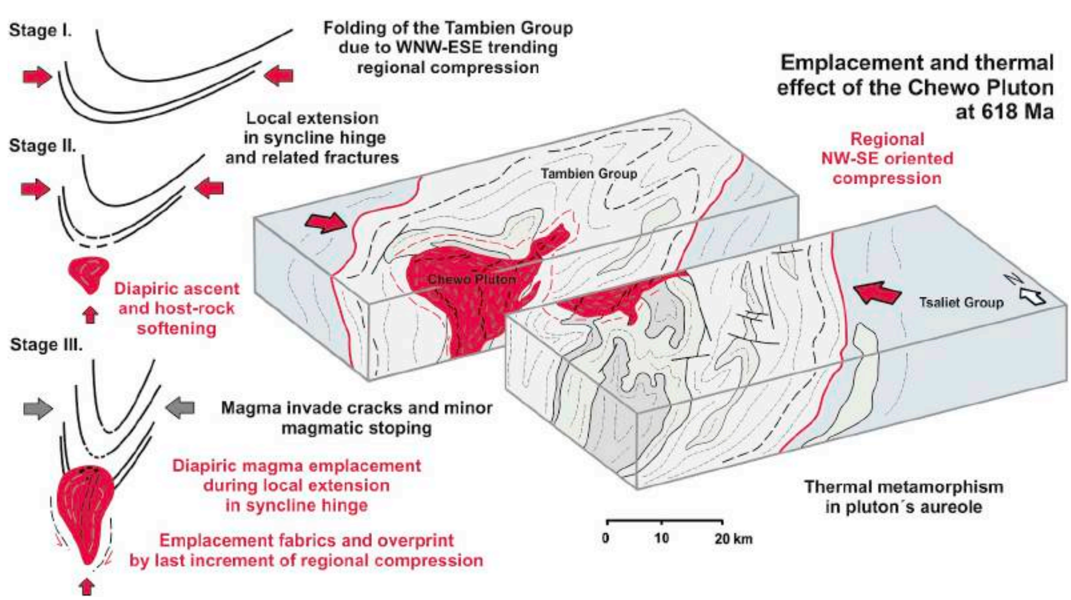

Fig. 15. Successive scenario of the Chewo Pluton magma ascent and emplacement in context of regional NW-SE oriented compression and simplified 3D block diagram.

zircon crystallization age of the Chewo pluton (618.1 ± 1.5 Ma) provides the upper limit for the activity of the regional stress-field related to the assembly of eastern and western Gondwana.

Declaration of competing interest

The authors declare that they have no known competing financial interests or personal relationships that could have appeared to influence the work reported in this paper.

Acknowledgements

The authors are grateful to the assistance of the Geological Survey of Ethiopia and Ethiopian Electric Power Corporation. Initial acquaintance to the study area through excursion to the Tekeze Hydroelectric Dam by Mohamed Abdel Salam. The contribution of Tarekegn Tadesse through several discussions on the geological settings and Filip Tomek for his help in AMS analyses is highly appreciated. We are grateful to the anonymous reviewer for construcutve comments.This paper was funded by the STARS Ph. D stipendium (to L. Megerssa), project Q45 Progres (Charles University, Faculty of Sciences), no. 15-34621L (GACR-FWF) and no. 310410 (Czech Geological Survey). Jiří Sláma was supported by institutional support for the Institute of Geology, ASCR, RVO 67985831.

Appendix A. Supplementary data

Supplementary data to this article can be found online at https://doi.org/10.1016/j.jafrearsci.2019.103695

References

Abdelsalam, M.G., Stern, R.J., 1996. Sutures and shear zones in the Arabian-Nubian Shield. J. Afr. Earth Sci. 23, 289–310.
Alemu, T., 1998. Geochemistry of Neoproterozoic granitoids from the Axum area, northern Ethiopia. J. Afr. Earth Sci. 27 (3–4), 437–460.
Alene, M., Jenkin, G.R., Leng, M.J., Darbyshire, D.F., 2006. The tambien group, Ethiopia: an early cryogenian (ca. 800–735 Ma) neoproterozoic sequence in the Arabian–Nubian Shield. Precambrian Res. 147 (1–2), 79–99.
Alene, M., Sacchi, D.R., 2000. The Neoproterozoic low-grade basement of Tigrai, northern Ethiopia. J. Afr. Earth Sci. 30 (4) 5-5.
Anderson, J.L., Smith, D.R., 1995. The effects of temperature and fO_2 on the Al-in-hornblende barometer. Am. Mineral. 80 (5–6), 549–559.
Archanjo, C.J., da Silva, E.R., Caby, R., 1999. Magnetic fabric and pluton emplacement in a transpressive shear zone system: the Itaporanga porphyritic granitic pluton (northeast Brazil). Tectonophysics 312 (2–4), 331–345.
Asrat, A., Barbey, P., 2003. Petrology, geochronology and Sr–Nd isotopic geochemistry of the Konso pluton, south-western Ethiopia: implications for transition from convergence to extension in the Mozambique Belt. Int. J. Earth Sci. 92 (6), 873–890.
Asrat, A., Barbey, P., Ludden, J.N., Reisberg, L., Gleizes, G., Ayalew, D., 2004. Petrology and isotope geochemistry of the pan-African Negash pluton, northern Ethiopia: mafic-felsic magma interactions during the construction of shallow-level calc-alkaline plutons. J. Petrol. 45, 1147–1179.
Asrat, A., Gleizes, G., Barbey, P., Ayalew, D., 2003. Magma emplacement and mafic–felsic magma hybridization: structural evidence from the Pan-African Negash pluton, Northern Ethiopia. J. Struct. Geol. 25 (9), 1451–1469.
Avigad, D., Gvirtzman, Z., 2009. Late Neoproterozoic rise and fall of the northern Arabian–Nubian Shield: the role of lithospheric mantle delamination and subsequent thermal subsidence. Tectonophysics 477 (3–4), 217–228.
Avigad, D., Stern, R.J., Beyth, M., Miller, N., McWilliams, M.O., 2007. Detrital zircon U–Pb geochronology of Cryogenian diamictites and Lower Paleozoic sandstone in Ethiopia (Tigrai): age constraints on Neoproterozoic glaciation and crustal evolution of the southern Arabian–Nubian Shield. Precambrian Res. 154 (1–2), 88–106.
Ayalew, T., Bell, K., Moore, M.J., Parish, R.R., 1990. U-Pb and Rb-Sr geochronology of western Ethiopian Shield. Geol. Soc. Am. Bull. 120, 1309–1316.
Azer, M.K., Obeid, M.A., Gahlan, H.A., 2016. Late Neoproterozoic layered mafic intrusion of arc-affinity in the Arabian-Nubian Shield: a case study from the Shahira layered mafic intrusion, southern Sinai, Egypt. Geol. Acta: Int. Earth Sci. J. 14 (3), 237–259.
Barbarin, B., 1999. A review of the relationships between granitoid types, their origins and their geodynamic environments. Lithos 46, 605–626.
Barbarin, B., 2005. Mafic magmatic enclaves and mafic rocks associated with some granitoids of the central Sierra Nevada batholith, California: nature, origin, and relations with the hosts. Lithos 80 (1–4), 155–177.
Batchelor, R.A., Bowden, P., 1985. Petrogenetic interpretation of granitoid rock series using multicationic parameters. Chem. Geol. 48 (1–4), 43–55.
Bea, F., 2010. Crystallization dynamics of granite magma chambers in the absence of regional stress: multiphysics modeling with natural examples. J. Petrol. 51, 1541–1569.
Beard, J.S., Ragland, P.C., Crawford, M.L., 2005. Reactive bulk assimilation: a model for crust-mantle mixing in silicic magmas. Geology 33 (8), 681–684.
Benn, K., 2009. Anisotropy of magnetic susceptibility fabrics in syntectonic plutons as tectonic strain markers: the example of the Canso pluton, Meguma Terrane, Nova Scotia. Earth Environ. Sci. Trans. R. Soc. Edinb. 100 (1–2), 147–158.
Beyth, M., 1972. The Geology of Central and Western Tigre, Ethiopia. Ph.D. dissertation. University of Bonn, Germany Unpublished.
Beyth, M., Avigad, D., Wetzel, H.U., Matthews, A., Berhe, S.M., 2003. Crustal exhumation and indications for snowball earth in the east African orogen: north Ethiopia and east Eritrea. Precambrian Res. 123 (2–4), 187–201.
Blundy, J.D., Sparks, R.S.J., 1992. Petrogenesis of mafic inclusions in granitoids of the Adamello Massif, Italy. J. Petrol. 33 (5), 1039–1104.
Bouchez, J.L., Gleizes, G., Djouadi, T., Rochette, P., 1990. Microstructure and magnetic susceptibility applied to emplacement kinematics of granites: the example of the Foix pluton (French Pyrenees). Tectonophysics 184 (2), 157–171.
Boynton, W.V., 1984. Cosmochemistry of the rare earth elements: meteorite studies. In: Developments in Geochemistry, vol. 2. pp. 63–114.
Buriánek, D., Janoušek, V., Hanzl, P., Jiang, Y., Schulmann, K., Lexa, O., Altanbaatar, B., 2016. Petrogenesis of the late carboniferous sagsai pluton in the SE Mongolian Altai. J. Geosci. 61 (1), 67–92.
Chen, R., Xing, G.F., Yang, Z.L., Shen, J.L., Zhou, Y.Z., 2005. Study on Beizhang and Lianglong granites and their dark enclaves. Geol. J. China Univ. 11 (2), 264–275.
Davidson, J., Turner, S., Handley, H., Macpherson, C., Dosseto, A., 2007. Amphibole "sponge" in arc crust? Geology 35 (9), 787–790.
Dawaï, D., Tchameni, R., Bascou, J., Wangmene, S.A., Tchunte, P.M.F., Bouchez, J.L., 2017. Microstructures and magnetic fabrics of the Ngaoundéré granite pluton (Cameroon): implications to the late-Pan-African evolution of Central Cameroon Shear Zone. J. Afr. Earth Sci. 129, 887–897.
De Souza Filho, C.R., Drury, S.A., 1998. A Neoproterozoic supra-subduction terrane in northern Eritrea, NE Africa. J. Geol. Soc. 155, 551–566 London.
De Wall, H., Dietl, C., Jungmann, O., Tegene, A.T., Pandit, M.K., 2011. Tectonic evolution of the Central Steep Zone, Axum area, northern Ethiopia: inferences from magnetic and geochemical data. In: In: Van Hinsbergen, D.J.J., Buiter, S.J.H., Torsvik, T.H., Gaina, C., Webb, S.J. (Eds.), The Formation and Evolution of Africa: A Synopsis of 3.8 Ga of Earth History, vol.357. Geological Society, London, Special Publications, pp. 85–106.
Debon, F., Le Fort, P., 1983. A chemical–mineralogical classification of common plutonic rocks and associations. Earth Environ. Sci. Trans. R. Soc. Edinb. 73 (3), 135–149.
Drury, S.A., de Souza Filho, C.R., 1998. Neoproterozoic terrane assemblages in Eritrea: review and prospects. J. Afr. Earth Sci. 27 (3–4), 331–348.
Dwivedi, S.B., Mohan, A., Lal, R.K., 1998. Recalibration of the Fe-Mg exchange reaction between garnet and cordierite as a thermometer. Eur. J. Mineral. Ohne Beihefte 10 (2), 281–290.
El-Bialy, M.Z., Streck, M.J., 2009. Late neoproterozoic alkaline magmatism in the Arabian–Nubian Shield: the postcollisional A-type granite of sahara–umm Adawi pluton, sinai, Egypt. Arabian J. Geosci. 2 (2), 151–174.
Eyal, M., Litvinovsky, B., Jahn, B.M., Zanvilevich, A., Katzir, Y., 2010. Origin and evolution of post-collisional magmatism: coeval Neoproterozoic calc-alkaline and alkaline suites of the Sinai Peninsula. Chem. Geol. 269, 153–179.
Farahat, E.S., Azer, M.K., 2011. Post-collisional magmatism in the northern Arabian–Nubian Shield: the geotectonic evolution of the alkaline suite at G. Tarbush area, south Sinai, Egypt. Chem. Erde 71, 247–266.
Fritz, H., Abdelsalam, M., Ali, K.A., Bingen, B., Collins, A.S., Fowler, A.R., Ghebreab, W., Hauzenberger, C.A., Johnson, P.R., Kusky, T.M., Macey, P., 2013. Orogen styles in the east African orogen: a review of the neoproterozoic to cambrian tectonic evolution. J. Afr. Earth Sci. 86, 65–106.
Gebreyohannes, G.W., 2014. Geology, Geochemistry and Geochronology of Neoproterozoic Rocks in Western Shire, Northern Ethiopia. Master's thesis. University of Oslo, Norway Unpublished.
Ghebreab, W., 1999. Tectono-metamorphic history of Neoproterozoic rocks in eastern Eritrea. Precambrian Res. 98 (1–2), 83–105.
Greiling, R.O., De Wall, H., Sadek, M.F., Dietl, C., 2014. Late Pan-African granite emplacement during regional deformation, evidence from magnetic fabric and structural studies in the Hammamat–Atalla area, Central Eastern Desert of Egypt. J. Afr. Earth Sci. 99, 109–121.
Hailu, T., 2000. Geological Map of Adi Arkay Sheet (1:250,000). Geological Survey of Ethiopia.
Hargrove, U.S., Stern, R.J., Kimura, J.I., Manton, W.I., Johnson, P.R., 2006. How juvenile is the Arabian-Nubian Shield? Evidence from Nd isotopes and pre-Neoproterozoic inherited zircon in the Bi'r Umq suture zone, Saudi Arabia. Earth Planet. Sci. Lett. 252, 308–326.
Harrison, T.M., Watson, E.B., 1984. The behavior of apatite during crustal anatexis: equilibrium and kinetic considerations. Geochem. Cosmochim. Acta 48 (7), 1467–1477.
He, B., Xu, Y.G., Paterson, S., 2009. Magmatic diapirism of the Fangshan pluton, southwest of Beijing, China. J. Struct. Geol. 31 (6), 615–626.
Henry, D.J., Guidotti, C.V., Thomson, J.A., 2005. The Ti-saturation surface for low-to-medium pressure metapelitic biotites: implications for geothermometry and Ti-substitution mechanisms. Am. Mineral. 90 (2–3), 316–328.
Holland, T., Blundy, J., 1994. Non-ideal interactions in calcic amphiboles and their bearing on amphibole-plagioclase thermometry. Contrib. Mineral. Petrol. 116 (4), 433–447.
Holland, T.J.B., Powell, R.T.J.B., 1998. An internally consistent thermodynamic data set for phases of petrological interest. J. Metamorph. Geol. 16 (3), 309–343.

Jacobs, J., Thomas, R.J., 2004. Himalayan-type indenter-escape tectonics model for the southern part of the late Neoproterozoic-early Paleozoic East African-Antarctic orogen. Geology 32, 721–724.
Janoušek, V., Braithwaite, C.J., Bowes, D.R., Gerdes, A., 2004. Magma-mixing in the genesis of Hercynian calc-alkaline granitoids: an integrated petrographic and geochemical study of the Sázava intrusion, Central Bohemian Pluton, Czech Republic. Lithos 78 (1–2), 67–99.
Johnson, P.R., 2014. An expanding Arabian-Nubian Shield geochronologic and isotopic dataset: defining limits and confirming the tectonic setting of a Neoproterozoic accretionary orogen. Open Geol. J. 8 (1), 3–33.
Johnson, P.R., Andresen, A., Collins, A.S., Fowler, A.R., Fritz, H., Ghebreab, W., Kusky, T., Stern, R.J., 2011. Late Cryogenian–Ediacaran history of the Arabian–Nubian Shield: a review of depositional, plutonic, structural, and tectonic events in the closing stages of the northern East African Orogen. J. Afr. Earth Sci. 61 (3), 167–232.
Khalil, A.E.S., Obeid, M.A., Azer, M.K., 2015. Late Neoproterozoic post-collisional mafic magmatism in the Arabian–Nubian Shield: a case study from Wadi El-Mahash gabbroic intrusion in southeast Sinai, Egypt. J. Afr. Earth Sci. 105, 29–46.
Kretz, R., 1983. Symbols of rock-forming minerals. Am. Mineral. 68, 277–279.
Kruger, T., Kisters, A., 2016. Magma accumulation and segregation during regional-scale folding: the Holland's dome granite injection complex, Damara belt, Namibia. J. Struct. Geol. 89, 1–18.
Kusky, T.M., Matsah, M.I., 2003. Neoproterozoic dextral faulting on the Najd fault system, Saudi Arabia, preceded sinistral faulting and escape tectonics related to closure of the Mozambique Ocean. Geol. Soc. Lond. Spec. Publ. 206 (1), 327–361.
Kusky, T.M., Abdel Salam, M.G., Stern, R.J., Tucker, R.D., 2003. Evolution of the east African and related orogens, and the assembly of Gondwana. Precambrian Res. 123 (2–4), 81–85.
Leake, B.E., Woolley, A.R., Arps, C.E., Birch, W.D., Gilbert, M.C., Grice, J.D., Hawthorne, F.C., Kato, A., Kisch, H.J., Krivovichev, V.G., Linthout, K., 1997. Nomenclature of amphiboles; report of the subcommittee on amphiboles of the international mineralogical association commission on new minerals and mineral names. Mineral. Mag. 61 (405), 295–310.
Le Bas, M.J., Le Maitre, R.W., Streckeisen, A., Zanettin, B., 1986. A chemical classification of volcanic rocks based on the total alkali-silica diagram. J. Petrol. 27 (3), 745–750.
Liégeois, J.P., Navez, J., Hertogen, J., Black, R., 1998. Contrasting origin of post-collisional high-K calc-alkaline and shoshonitic versus alkaline and peralkaline granitoids. The use of sliding normalization. Lithos 45 (1–4), 1–28.
Ludwig, K.R., 2003. User's Manual for Isoplot V. 3.00, a Geochronological Toolkit for Microsoft Excel. Berkeley Geochronological Center Special Publication no. 4.
Magee, C., Stevenson, C., O'driscoll, B., Schofield, N., McDermott, K., 2012. An alternative emplacement model for the classic Ardnamurchan cone sheet swarm, NW Scotland, involving lateral magma supply via regional dykes. J. Struct. Geol. 43, 73–91.
McDonough, W.F., Sun, S.S., 1995. The composition of the Earth. Chem. Geol. 120 (3–4), 223–253.
Middlemost, E.A., 1994. Naming materials in the magma/igneous rock system. Earth Sci. Rev. 37 (3–4), 215–224.
Miller, N.R., Alene, M., Sacchi, R., Stern, R.J., Conti, A., Kröner, A., Zuppi, G., 2003. Significance of the tambien group (tigrai, N. Ethiopia) for snowball earth events in the Arabian–Nubian Shield. Precambrian Res. 121 (3–4), 263–283.
Miller, N.R., Avigad, D., Stern, R.J., Beyth, M., 2011. The tambien group, northern Ethiopia (tigre). Geol. Soc. Lond. Mem. 36 (1), 263–276.
Molina, J.F., Moreno, J.A., Castro, A., Rodríguez, C., Fershtater, G.B., 2015. Calcic amphibole thermobarometry in metamorphic and igneous rocks: new calibrations based on plagioclase/amphibole Al-Si partitioning and amphibole/liquid Mg partitioning. Lithos 232, 286–305.
Nyman, M.W., Karlstrom, K.E., 1997. Pluton emplacement processes and tectonic setting of the 1.42 Ga Signal batholith, SW USA: important role of crustal anisotropy during regional shortening. Precambrian Res. 82 (3–4), 237–263.
Paterson, S.R., Miller, R.B., 1998. Magma emplacement during arc-perpendicular shortening: an example from the Cascades crystalline core, Washington. Tectonics 17 (4), 571–586.
Paterson, S.R., Fowler Jr., T.K., Schmidt, K.L., Yoshinobu, A.S., Yuan, E.S., Miller, R.B., 1998. Interpreting magmatic fabric patterns in plutons. Lithos 44 (1–2), 53–82.
Paterson, S.R., Vernon, R.H., Tobisch, O.T., 1989. A review of criteria for the identification of magmatic and tectonic foliations in granitoids. J. Struct. Geol. 11 (3), 349–363.
Pearce, J., 1996. Sources and settings of granitic rocks. Episodes 19, 120–125.
Pearce, J.A., 2008. Geochemical fingerprinting of oceanic basalts with applications to ophiolite classification and the search for Archean oceanic crust. Lithos 100 (1–4), 14–48.
Pearce, J.A., Harris, N.B.M., Toille, A.G., 1984. Trace element discrimination diagrams for the tectonic interpretation of granitic rocks. J. Petrol. 25, 956–983.
Peccerillo, A., Taylor, S.R., 1976. Geochemistry of Eocene calc-alkaline volcanic rocks from the Kastamonu area, northern Turkey. Contrib. Mineral. Petrol. 58 (1), 63–81.
Powell, R., Holland, T.J.B., 2008. On thermobarometry. J. Metamorph. Geol. 26 (2), 155–179.
Shand, S.J., 1943. Eruptive Rocks: Their Genesis, Composition, and Classification, with a Chapter on Meteorites. J. Wiley & sons, pp. 444 Incorporated.
Sifeta, K., Roser, B.P., Kimura, J.I., 2005. Geochemistry, provenance, and tectonic setting of Neoproterozoic metavolcanic and metasedimentary units, Werri area, Northern Ethiopia. J. Afr. Earth Sci. 41 (3), 212–234.
Słaby, E., Martin, H., 2008. Mafic and felsic magma interaction in granites: the hercynian karkonosze pluton (sudetes, bohemian massif). J. Petrol. 49 (2), 353–391.
Swanson-Hysell, N.L., Maloof, A.C., Condon, D.J., Jenkin, G.R., Alene, M., Tremblay, M.M., Tesema, T., Rooney, A.D., Haileab, B., 2015. Stratigraphy and geochronology of the Tambien Group, Ethiopia: evidence for globally synchronous carbon isotope change in the Neoproterozoic. Geology 43 (4), 323–326.
Sylvester, P.J., 1989. Post-collisional alkaline granites. J. Geol. 97, 261–280.
Sylvester, P.J., 1998. Post-collisional strongly peraluminous granites. Lithos 45 (1–4), 29–44.
Tadesse, T., 1996. Structure across a possible intra-oceanic suture zone in the low-grade Pan-African rocks of northern Ethiopia. J. Afr. Earth Sci. 23 (3), 375–381.
Tadesse, T., 1997. The Geology of Axum Area (ND 37-6). Ethiopian Institute of Geological Survey, Addis Ababa (Memoir No. 9).
Tadesse, T., Hoshino, M., Suzuki, K., Iizumi, S., 2000. Sm-Nd, Rb-Sr and Th-U-Pb zircon ages of syn-and post-tectonic granitoids from the Axum area of northern Ethiopia. J. Afr. Earth Sci. 30 (2), 313–327.
Tadesse, T., Suzuki, K., Hoshino, M., 1997. Chemical Th–U total Pb isochron age of zircon from the Mareb Granite in northern Ethiopia. J. Earth Planet. Sci. Nagoya Univ. 44, 21–27.
Teklay, M., Kröner, A., Mezger, K., 2002. Enrichment from plume interaction in the generation of Neoproterozoic arc rocks in northern Eritrea: implications for crustal accretion in the southern Arabian–Nubian Shield. Chem. Geol. 184 (1–2), 167–184.
Teklay, M., Kröner, A., Mezger, K., 2001. Geochemistry, geochronology and isotope geology of Nakfa intrusive rocks, northern Eritrea: products of a tectonically thickened Neoproterozoic arc crust. J. Afr. Earth Sci. 33 (2), 283–301.
Watson, E.B., Harrison, T.M., 1983. Zircon saturation revisited: temperature and composition effects in a variety of crustal magma types. Earth Planet. Sci. Lett. 64 (2), 295–304.
Whalen, J.B., Currie, K.L., Chappell, B.W., 1987. A-type granites: geochemical characteristics, discrimination and petrogenesis. Contrib. Mineral. Petrol. 95, 407–419.
White, A.J.R., Chappell, B.W., 1983. Granitoid types and their distribution in the lachlan fold belt, south western Australia. Geol. Soc. Am. Mem. 159, 21–34.

Supplementary Information 1
Major-element and trace-element composition of magmatic rocks based on whole-rock chemical analyses of samples from the Chewo Pluton

Emplacement and thermal effect of post-collisional Chewo Pluton (Arabian-Nubian Shield); implication for late East-African Orogeny.

Megerssa, L. *, Verner, K., Buriánek, D., Sláma, J. (2020).
Journal of African Earth Sciences, 162, 103695

* Coressponding author: megerssal@natur.cuni.cz; Institute of Petrology and Structural Geology, Faculty of Science, Charles University, Albertov 6, Prague, 12843, Czech Republic

Lithology	Monzodiorite					Quartz monzonite											
East		38.74613296			38.7529	38.7663	38.7461	38.7518	38.7507	38.75004999		38.7508	38.7646	38.7599	38.7591	38.7619	38.7632
North		13.42149102			13.4424	13.4612	13.4215	13.4378	13.4316	13.42349497		13.4207	13.4654	13.4628	13.4488	13.4562	13.4606
Sample	TD 10/2	TD 10/3	TD 10/4	TD 10/6	TD45	TD 32	TD 10/5	TD48	TD49	TD50/1	TD50/2	TD51	TD53	TD54	TD58	TD59	TD60
Major oxides (%)																	
SiO_2	52.73	54.58	51.69	53.78	59.7	62.71	62.05	63.04	61.53	63.56	62.01	63.65	63.74	62.84	62.63	62.4	63.12
Al_2O_3	17.31	17.43	18.24	17.8	14.47	16.19	16.07	15.32	15.31	15.84	15.69	16.16	16.08	15.74	15.42	15.41	15.73
Fe_2O_3	8.51	7.68	8.57	8.15	6.55	4.64	4.91	4.98	5.35	4.42	4.90	4.17	4.36	4.74	4.92	5.01	4.69
MgO	5.07	3.89	4.31	4.13	5.30	2.84	3.07	3.33	3.99	2.77	3.01	2.59	2.70	2.87	3.69	3.48	2.79
CaO	6.81	5.57	6.91	5.80	5.11	3.89	3.93	4.01	4.56	3.71	3.97	3.36	3.68	3.84	4.32	4.18	3.85
Na_2O	3.83	3.82	4.16	4.14	3.65	4.31	4.18	3.99	3.91	4.17	4.07	4.27	4.10	4.15	3.98	3.94	4.18
K_2O	2.08	2.06	1.13	2.20	2.74	3.32	2.89	3.10	3.13	3.44	3.74	3.04	3.54	3.45	3.12	3.40	3.63
TiO_2	1.59	1.51	1.66	1.55	1.06	0.83	0.85	0.85	0.90	0.79	0.93	0.73	0.75	0.87	0.82	0.88	0.87
P_2O_5	0.55	0.56	0.62	0.57	0.31	0.26	0.26	0.24	0.29	0.22	0.33	0.22	0.23	0.26	0.21	0.27	0.25
MnO	0.11	0.09	0.11	0.09	0.10	0.07	0.08	0.07	0.08	0.06	0.07	0.07	0.07	0.07	0.07	0.07	0.06
Cr_2O_3	0.006	0.007	0.009	0.008	0.030	0.011	0.012	0.014	0.019	0.010	0.010	0.009	0.009	0.010	0.021	0.017	0.011
Sc	19	14	17	16	14	9	10	10	12	8	10	8	8	9	10	11	9
LOI	0.9	2.4	2.2	1.3	0.6	0.6	1.3	0.7	0.6	0.7	0.9	1.4	0.4	0.8	0.5	0.6	0.5
Sum	*99.54*	*99.59*	*99.59*	*99.55*	*99.75*	*99.67*	*99.63*	*99.8*	*99.77*	*99.79*	*99.77*	*99.8*	*99.79*	*99.78*	*99.78*	*99.78*	*99.79*
Trace elements (ppm)																	
Ba	1118	1074	789	1350	929	1127	1287	1004	1042	1133	1256	1249	1174	1133	1009	1118	1079
Be	<1	2	3	<1	2	<1	1	2	3	4	2	2	2	2	<1	2	<1
Co	24.7	16.7	20.9	19.7	26.1	12.5	15.3	20.7	20.8	18.2	20.7	16.6	18.2	19.3	19.9	20.2	17.1
Cs	1.2	1.0	1.0	1.7	2.0	1.5	1.2	1.5	1.7	1.2	1.5	0.7	1.5	1.9	1.5	1.8	1.8
Ga	21.7	20.8	21.5	21	16.7	18.3	18.9	16.5	16.7	16.3	17.3	16.4	17.3	17.3	17.8	16.9	20.4
Hf	4.7	4.1	3.6	4.1	2.4	5.3	5.7	4.8	5.6	5.7	6.5	5.2	5.6	5.5	4.7	5.6	5.7
Nb	6.6	6.6	8.3	6.9	6.6	6.4	7.3	5.5	6.3	6.2	7.2	6.5	6.6	6.9	5.9	7.5	8.3
Rb	40.4	45.1	22.4	41.6	65	63	56.4	62.6	61.6	65.9	71.9	49.2	71.2	69.4	64.3	71	72

Lithology	Monzodiorite					Quartz monzonite											
East	38.74613296				38.7529	38.7663	38.7461	38.7518	38.7507	38.75004999		38.7508	38.7646	38.7599	38.7591	38.7619	38.7632
North	13.42149102				13.4424	13.4612	13.4215	13.4378	13.4316	13.42349497		13.4207	13.4654	13.4628	13.4488	13.4562	13.4606
Sample	TD 10/2	TD 10/3	TD 10/4	TD 10/6	TD45	TD 32	TD 10/5	TD48	TD49	TD50/1	TD50/2	TD51	TD53	TD54	TD58	TD59	TD60
Sn	2	1	1	1	1	1	1	<1	1	<1	1	1	1	1	1	1	1
Sr	1366.6	1264.7	1456.3	1312.9	860.5	828.6	971.6	759.4	831.7	832.6	832.7	807.6	811.1	898.2	837.7	802.5	842.4
Ta	0.4	0.5	0.5	0.4	0.5	0.4	0.3	0.5	0.5	0.4	0.5	0.4	0.5	0.5	0.4	0.5	0.5
Th	1.8	3.2	2.1	1.2	5.7	2.9	3.2	3.8	4.3	3.8	4.3	4.8	4.5	4.7	4.2	4.1	5.0
U	0.9	1.5	1.8	0.8	1.9	1.1	1.3	1.6	1.4	1.2	1.4	1.8	1.9	1.6	2.0	1.5	2.7
V	192	162	187	178	121	88	87	95	100	87	96	75	84	93	95	100	93
W		<0,5	<0,5	0.5	21.4	<0,5	<0,5	39.5	30.6	39.7	39.7	38.1	45.5	38.7	21.2	27.9	24.8
Zr	184.2	177	129.8	152.6	81.7	211.6	242.9	179.6	212.9	218.1	246.6	209.3	211.6	219.2	169	208.8	216.4
Y	23.6	17.6	26.7	21.7	15.3	11.7	12.7	14.5	14.4	13	17.3	12.1	12.4	14.2	14.3	15	13.3
La	26.3	25.3	24.6	25.2	26.5	20.2	27.6	21.6	24.8	27.7	32.8	26.3	28.3	29.1	24	27.6	28.5
Ce	62.6	48.3	60.7	55.1	59.8	43.7	53.1	45.8	54.9	57.8	69.7	55.3	61	60.4	50.8	60.3	60.7
Pr	8.38	6.26	8.24	7.73	7.12	5.22	6.44	5.39	6.34	6.63	8.21	6.26	6.89	6.96	5.84	6.95	6.8
Nd	38.7	26.5	38.9	34.8	27.3	20.9	25.4	21.6	24.3	25.4	32.8	23.5	26.4	27.7	22.8	27.3	25.5
Sm	6.98	5.29	8.03	6.19	5.04	3.89	4.61	3.86	4.45	4.25	5.53	3.96	4.28	4.7	4.06	4.73	4.22
Eu	2	1.5	2.19	1.9	1.33	0.98	1.21	1.14	1.27	1.14	1.3	1.12	1.15	1.28	1.12	1.26	1.2
Gd	6.06	4.47	6.48	5.5	4.38	3.17	3.65	3.34	3.73	3.54	4.56	3.2	3.37	3.81	3.24	3.8	3.59
Tb	0.85	0.63	0.94	0.75	0.58	0.41	0.48	0.47	0.54	0.46	0.59	0.42	0.45	0.49	0.46	0.5	0.51
Dy	4.18	3.53	5.2	4.24	3.18	2.16	2.72	2.76	3.1	2.71	3.36	2.33	2.69	2.81	2.53	2.95	2.81
Ho	0.95	0.65	1.02	0.78	0.61	0.41	0.48	0.45	0.52	0.5	0.6	0.43	0.48	0.51	0.46	0.54	0.49
Er	2.31	1.67	2.74	2.35	1.58	1.15	1.54	1.34	1.51	1.33	1.68	1.15	1.34	1.43	1.34	1.45	1.57
Tm	0.31	0.24	0.34	0.3	0.24	0.16	0.2	0.19	0.22	0.18	0.24	0.18	0.19	0.19	0.19	0.21	0.21
Yb	2.05	1.5	2.45	1.78	1.49	0.96	1.25	1.28	1.43	1.22	1.43	1.15	1.22	1.32	1.21	1.32	1.38
Lu	0.31	0.17	0.33	0.26	0.21	0.17	0.19	0.2	0.21	0.17	0.2	0.16	0.19	0.18	0.18	0.19	0.21
TOT/C	0.04	0.04	0.04	0.06	<0,02	0.04	0.02	0.02	<0,02	0.05	0.06	0.04	<0,02	0.05	0.02	<0,02	<0,02
TOT/S	0.05	0.03	0.07	0.06	<0,02	<0,02	<0,02	<0,02	<0,02	<0,02	<0,02	<0,02	<0,02	<0,02	0.02	<0,02	<0,02
Mo	0.3	0.2	0.3	0.3	0.5	0.4	0.3	0.4	0.6	0.4	0.4	0.2	0.4	0.2	0.5	0.5	0.5

Lithology	Monzodiorite					Quartz monzonite											
East	38.74613296				38.7529	38.7663	38.7461	38.7518	38.7507	38.75004999		38.7508	38.7646	38.7599	38.7591	38.7619	38.7632
North	13.42149102				13.4424	13.4612	13.4215	13.4378	13.4316	13.42349497		13.4207	13.4654	13.4628	13.4488	13.4562	13.4606
Sample	TD 10/2	TD 10/3	TD 10/4	TD 10/6	TD45	TD 32	TD 10/5	TD48	TD49	TD50/1	TD50/2	TD51	TD53	TD54	TD58	TD59	TD60
Cu	15.1	12	29	17.8	35	10.6	7.3	17.6	19.6	9	13	4.2	10.1	13.1	45.9	20.2	12.6
Pb	2.1	4.8	5.4	3.1	1.7	3.7	3.2	1.5	1.2	1.6	1.7	3	1.5	1.4	1.1	1.5	1.2
Zn	60	79	78	72	59	51	55	52	56	42	48	46	45	46	30	50	40
Ni	29.2	23.4	26	26	86.6	32.1	26.6	40	54.3	30.4	33.7	18.6	21.7	30.9	39.3	46.4	30
As	0.7	0.9	1	0.7	3.5	1.4	1.1	1.9	1.3	0.7	0.6	0.6	0.6	<0,5	1.4	1.9	2.1
Cd	<0,1	<0,1	<0,1	<0,1	<0,1	<0,1	<0,1	<0,1	<0,1	<0,1	<0,1	<0,1	<0,1	<0,1	<0,1	<0,1	<0,1
Sb	<0,1	<0,1	<0,1	<0,1	0.1	<0,1	<0,1	<0,1	0.1	<0,1	<0,1	<0,1	<0,1	<0,1	<0,1	<0,1	0.1
Bi	<0,1	<0,1	<0,1	<0,1	<0,1	<0,1	<0,1	<0,1	<0,1	<0,1	<0,1	<0,1	<0,1	<0,1	<0,1	<0,1	<0,1
Ag	<0,1	<0,1	<0,1	<0,1	0.3	<0,1	<0,1	<0,1	<0,1	<0,1	<0,1	<0,1	<0,1	<0,1	<0,1	<0,1	<0,1
Au	0.9	<0,5	0.9	0.7	<0,5	<0,5	<0,5	<0,5	<0,5	<0,5	2.2	<0,5	<0,5	<0,5	<0,5	<0,5	<0,5
Hg	<0,01	<0,01	<0,01	<0,01	<0,01	<0,01	<0,01	0.02	<0,01	<0,01	<0,01	<0,01	0.01	<0,01	<0,01	<0,01	<0,01
Tl	0.2	<0,1	<0,1	0.2	0.3	0.2	0.2	0.3	0.3	0.2	0.3	<0,1	0.3	0.3	0.2	0.4	0.3
Se	<0,5	<0,5	<0,5	<0,5	<0,5	<0,5	<0,5	<0,5	<0,5	<0,5	<0,5	<0,5	<0,5	<0,5	<0,5	<0,5	<0,5

Supplementary Information 2
Electron microprobe analysis data of major magmatic minerals from Chewo pluton

Emplacement and thermal effect of post-collisional Chewo Pluton (Arabian-Nubian Shield); implication for late East-African Orogeny.

Megerssa, L. *, Verner, K., Buriánek, D., Sláma, J. (2020).
Journal of African Earth Sciences, 162, 103695.
* Coressponding author: megerssal@natur.cuni.cz; Institute of Petrology and Structural Geology, Faculty of Science, Charles University, Albertov 6, Prague, 12843, Czech Republic

Representative electron-microprobe analyses of amphibole from the Chewo Pluton

North	38.74613296							38.892669			
East	13.42149102							13.40103499			
Sample	TD 10/2	TD 10/2	TD 10/2	TD 10/2	TD 10/2	TD 10/2	TD 10/2	TD 20/3	TD 20/3	TD 20/3	TD 20/3
Point	16	17	18	19	20	25	38	2	3	4	5
SiO_2	43.85	42.62	45.52	42.90	44.96	44.91	42.45	44.32	45.62	44.35	43.93
TiO_2	1.62	2.63	1.52	2.47	1.45	1.41	2.36	1.54	1.32	1.85	1.39
Al_2O_3	9.76	10.74	8.68	10.20	9.11	9.07	10.67	9.48	8.55	9.49	9.61
Cr_2O_3	0.04	0.02	0.03	0.03	0.04	0.01	0.00	0.02	0.05	0.03	0.04
FeO_{calc}	11.26	12.92	11.11	11.88	11.22	11.28	12.34	12.89	11.75	11.52	12.43
Fe_2O_{3calc}	5.67	4.19	4.97	5.12	5.01	5.09	5.62	4.65	5.84	6.13	5.96
MnO	0.23	0.30	0.38	0.32	0.30	0.37	0.30	0.34	0.34	0.32	0.35
MgO	11.35	10.50	11.84	10.99	11.84	11.79	10.38	10.78	11.40	11.08	10.67
CaO	11.75	11.62	11.55	11.69	11.92	11.91	11.57	11.73	11.67	11.36	11.70
Na_2O	1.54	1.79	1.48	1.70	1.43	1.42	1.67	1.55	1.45	1.78	1.53
K_2O	1.03	1.17	0.98	1.11	0.91	0.87	1.21	1.10	0.85	0.90	1.17
H_2O*	2.03	2.02	2.04	2.03	2.04	2.04	2.02	2.03	2.05	2.04	2.03
Cl	0.04	0.07	0.05	0.05	0.06	0.04	0.06	0.06	0.04	0.08	0.08
F	0.30	0.26	0.30	0.30	0.28	0.24	0.27	0.28	0.28	0.28	0.27
O=F,Cl	-0.13	-0.12	-0.14	-0.14	-0.13	-0.11	-0.13	-0.13	-0.13	-0.14	-0.13
Total	100.32	100.72	100.31	100.64	100.43	100.33	100.79	100.64	101.08	101.08	101.02
Si	6.523	6.359	6.732	6.393	6.651	6.649	6.337	6.599	6.721	6.554	6.533
^{IV}Al	1.477	1.641	1.268	1.607	1.349	1.351	1.663	1.401	1.279	1.446	1.467
^{VI}Al	0.233	0.247	0.244	0.184	0.240	0.232	0.214	0.262	0.206	0.206	0.217
Ti	0.181	0.295	0.169	0.276	0.161	0.157	0.265	0.173	0.147	0.205	0.156
Fe^{3+}	0.634	0.471	0.553	0.574	0.558	0.567	0.631	0.521	0.647	0.681	0.667
Cr	0.005	0.002	0.003	0.004	0.004	0.001	0.000	0.002	0.005	0.003	0.004

North	38.74613296							38.892669			
East	13.42149102							13.40103499			
Sample	TD 10/2	TD 10/2	TD 10/2	TD 10/2	TD 10/2	TD 10/2	TD 10/2	TD 20/3	TD 20/3	TD 20/3	TD 20/3
Point	16	17	18	19	20	25	38	2	3	4	5
Mg - C	2.517	2.335	2.609	2.441	2.611	2.601	2.311	2.393	2.504	2.441	2.366
Fe^{2+} - C	1.400	1.612	1.374	1.480	1.388	1.396	1.540	1.605	1.448	1.423	1.546
Mn - C	0.029	0.037	0.047	0.040	0.038	0.046	0.038	0.043	0.042	0.041	0.044
Mg - B	0.000	0.000	0.000	0.000	0.000	0.000	0.000	0.000	0.000	0.000	0.000
Fe^{2+} - B	0.000	0.000	0.000	0.000	0.000	0.000	0.000	0.000	0.000	0.000	0.000
Mn - B	0.000	0.000	0.000	0.000	0.000	0.000	0.000	0.000	0.000	0.000	0.000
Ca	1.872	1.857	1.830	1.866	1.889	1.890	1.850	1.872	1.842	1.799	1.865
Na - B	0.128	0.143	0.170	0.134	0.111	0.110	0.150	0.128	0.158	0.201	0.135
Na - A	0.315	0.374	0.255	0.357	0.297	0.297	0.334	0.318	0.257	0.309	0.306
K	0.195	0.222	0.185	0.210	0.172	0.164	0.230	0.210	0.160	0.170	0.222
Cl	0.010	0.017	0.012	0.012	0.015	0.011	0.015	0.015	0.010	0.019	0.020
F	0.139	0.123	0.141	0.141	0.133	0.113	0.127	0.130	0.131	0.133	0.125
Σ Cat.	15.649	15.720	15.581	15.708	15.602	15.574	15.691	15.657	15.548	15.611	15.653

Representative electron-microprobe analyses of feldspars from the Chewo Pluton

North	38.76439302					38.74613296					38.892669	
East	13.46518203					13.42149102					13.40103499	
Sample	TD 31/2					TD 10/2					TD 20/3	
Point	35	36	37	41	42	21	22	23	24	32	5	7
SiO_2	62.81	66.23	63.13	64.00	64.92	60.48	59.80	59.28	58.47	59.47	59.03	62.23
P_2O_5	0.28	0.39	0.33	0.25	0.46	0.01	0.00	0.03	0.00	0.00	0.04	0.00
Al_2O_3	23.05	21.15	23.19	22.68	22.07	24.71	25.11	25.58	26.08	25.35	25.83	23.87
FeO	0.02	0.03	0.03	0.07	0.05	0.14	0.20	0.08	0.15	0.18	0.19	0.09
CaO	3.70	1.32	3.90	3.25	2.74	5.90	6.81	6.81	7.92	7.22	7.70	4.59
Na_2O	9.37	10.88	9.49	9.56	10.02	8.22	7.68	7.37	6.83	7.67	7.09	8.39
K_2O	0.06	0.03	0.07	0.05	0.10	0.27	0.10	0.34	0.21	0.12	0.30	0.43
BaO	0.01	0.18	0.01	0.00	0.00	0.00	0.02	0.02	0.05	0.01	0.04	0.05
SrO	0.54	0.24	0.34	0.55	0.25	0.21	0.24	0.21	0.25	0.23	0.22	0.22
Total	99.28	100.02	100.15	99.87	100.35	99.72	99.70	99.49	99.66	100.02	100.18	99.59
Si	2.786	2.897	2.781	2.816	2.842	2.696	2.669	2.654	2.619	2.652	2.630	2.762
Al	1.205	1.090	1.204	1.176	1.139	1.298	1.321	1.350	1.376	1.332	1.356	1.249
Fe^{3+}	0.001	0.001	0.001	0.003	0.002	0.005	0.007	0.003	0.006	0.007	0.007	0.003
T-site	3.992	3.988	3.986	3.995	3.982	4.000	3.997	4.006	4.000	3.991	3.994	4.014
K	0.003	0.002	0.004	0.003	0.005	0.015	0.006	0.019	0.012	0.007	0.017	0.024

North	38.76439302					38.74613296					38.892669	
East	13.46518203					13.42149102					13.40103499	
Sample	TD 31/2					TD 10/2					TD 20/3	
Point	35	36	37	41	42	21	22	23	24	32	5	7
Na	0.806	0.923	0.811	0.816	0.850	0.710	0.665	0.640	0.593	0.663	0.612	0.722
Ca	0.173	0.061	0.182	0.151	0.127	0.278	0.322	0.323	0.375	0.341	0.363	0.215
Ba	0.000	0.003	0.000	0.000	0.000	0.000	0.000	0.000	0.001	0.000	0.001	0.001
Sr	0.014	0.006	0.009	0.014	0.006	0.005	0.006	0.005	0.006	0.006	0.006	0.006
Σ Cat.	4.989	4.983	4.992	4.978	4.971	5.009	4.996	4.994	4.988	5.007	4.993	4.982
An	18	6	18	16	13	28	32	33	38	34	37	22
Ab	82	94	81	84	87	71	67	65	60	66	62	75
Or	0	0	0	0	1	2	1	2	1	1	2	3

North	38.76625699				38.74623497			38.74613296		
East	13.46121202				13.41797599			13.42149102		
Sample	TD 32				TD 12/1			TD 10/1		
Point	23	24	25	32	24	27	28	39	40	41
SiO_2	65.19	65.05	63.73	63.33	58.56	58.90	59.19	58.67	58.32	58.30
P_2O_5	0.00	0.02	0.01	0.00	0.03	0.00	0.03	0.00	0.00	0.01
Al_2O_3	18.67	18.82	22.81	23.03	25.52	25.49	25.54	25.88	25.97	25.55
FeO	0.11	0.09	0.11	0.19	0.43	0.16	0.33	0.12	0.14	0.18
CaO	0.04	0.05	4.02	4.46	7.36	7.44	7.44	7.79	8.06	7.93
Na_2O	1.72	1.68	9.22	9.27	7.46	7.37	7.57	7.06	7.20	7.08
K_2O	13.97	14.20	0.35	0.29	0.04	0.01	0.03	0.17	0.10	0.11
BaO	0.70	0.45	0.01	0.00	0.00	0.00	0.01	0.01	0.03	0.02
SrO	0.15	0.08	0.06	0.09	0.00	0.03	0.07	0.23	0.20	0.17
Total	99.70	99.91	100.25	100.56	99.40	99.38	100.14	99.69	99.78	99.16
Si	2.987	2.981	2.809	2.789	2.629	2.644	2.637	2.627	2.613	2.627
Al	1.008	1.016	1.185	1.195	1.350	1.348	1.341	1.366	1.372	1.356
Fe^{3+}	0.004	0.003	0.004	0.007	0.016	0.006	0.012	0.004	0.005	0.007
T-site	4.000	4.001	3.998	3.991	3.995	3.998	3.991	3.997	3.990	3.990
K	0.817	0.830	0.020	0.016	0.002	0.001	0.002	0.010	0.006	0.006
Na	0.153	0.150	0.788	0.791	0.649	0.642	0.654	0.612	0.626	0.618
Ca	0.002	0.003	0.188	0.208	0.350	0.353	0.351	0.369	0.382	0.378
Ba	0.013	0.008	0.000	0.000	0.000	0.000	0.000	0.000	0.000	0.000
Sr	0.004	0.002	0.002	0.002	0.000	0.001	0.002	0.006	0.005	0.005
Σ Cat.	4.987	4.994	4.995	5.008	4.996	4.994	5.000	4.995	5.009	4.997
An	0	0	19	20	35	35	35	37	38	38
Ab	16	15	79	78	65	64	65	62	62	62
Or	84	85	2	2	0	0	0	1	1	1

Representative electron-microprobe analyses of biotite from the Chewo Pluton

North	38.74613296			38.892669		38.7662569	
East	13.42149102			13.40103499		13.4612120	
Sample	TD 10/2			TD 20/3		TD 32	
Point	28	29	30	11	12	33	34
SiO_2	36.04	37.55	37.20	36.43	36.38	37.23	37.58
TiO_2	3.96	3.05	2.47	3.93	4.11	4.30	3.84
Al_2O_3	14.80	14.84	15.42	14.86	14.81	13.58	13.40
FeO	18.16	17.93	17.36	20.09	20.06	18.45	18.46
MnO	0.25	0.14	0.16	0.21	0.17	0.29	0.22
MgO	11.08	11.78	12.06	10.01	10.10	11.57	12.12
CaO	0.05	0.02	0.01	0.00	0.03	0.02	0.01
Na_2O	0.25	0.18	0.20	0.22	0.13	0.05	0.07
K_2O	9.12	9.36	9.41	9.11	8.95	9.18	9.89
H_2O*	3.66	3.71	3.69	3.69	3.70	3.64	3.65
Cl	0.43	0.47	0.49	0.39	0.37	0.51	0.54
F	0.05	0.06	0.05	0.10	0.11	0.15	0.14
O=F,Cl	0.19	0.21	0.22	0.18	0.18	0.25	0.26
Total	97.66	98.86	98.30	98.83	98.73	98.73	99.66
Si	5.574	5.706	5.675	5.607	5.598	5.696	5.713
^{IV}Al	2.426	2.294	2.325	2.393	2.402	2.304	2.287
^{VI}Al	0.272	0.366	0.448	0.303	0.285	0.146	0.115
Ti	0.461	0.348	0.283	0.454	0.476	0.494	0.439
Fe	2.349	2.279	2.214	2.586	2.581	2.361	2.347
Mn	0.032	0.018	0.021	0.027	0.023	0.038	0.029
Mg	2.556	2.670	2.743	2.295	2.316	2.639	2.747
Ca	0.008	0.003	0.001	0.000	0.005	0.004	0.002
Na	0.075	0.052	0.060	0.064	0.039	0.015	0.019
K	1.800	1.815	1.830	1.788	1.757	1.792	1.918
OH	3.779	3.758	3.751	3.787	3.795	3.713	3.706
F	0.013	0.015	0.013	0.026	0.027	0.040	0.037
Σ Cat.	15.553	15.549	15.601	15.517	15.481	15.488	15.616

North	38.76439302										
East	13.46518203										
Sample	TD 31/2										
Point	26	28	30	32	34	36	38	40	42	44	46
SiO_2	35.37	35.72	34.80	34.82	34.69	34.60	34.78	35.10	35.14	34.79	34.73
TiO_2	1.66	1.74	1.71	1.80	2.27	1.69	2.72	2.24	2.24	2.36	1.73
Al_2O_3	19.74	19.66	19.48	19.81	18.89	19.60	18.95	19.52	19.47	19.18	19.57
FeO	21.59	21.58	22.24	22.23	22.07	20.74	20.91	20.73	20.25	22.68	22.48
MnO	0.03	0.00	0.02	0.02	0.02	0.01	0.00	0.00	0.03	0.02	0.05
MgO	8.25	7.67	7.40	7.45	7.56	8.16	7.87	7.74	8.16	7.01	7.07
CaO	0.03	0.01	0.03	0.00	0.04	0.01	0.04	0.02	0.04	0.00	0.00
Na_2O	0.39	0.53	0.40	0.46	0.36	0.46	0.43	0.59	0.43	0.36	0.33
K_2O	8.32	8.59	8.66	8.91	8.33	8.50	8.59	8.55	8.59	8.64	8.74
H_2O*	3.82	3.81	3.77	3.79	3.74	3.76	3.77	3.79	3.79	3.79	3.78
Cl	0.24	0.25	0.22	0.23	0.26	0.24	0.24	0.25	0.26	0.21	0.20
F	0.00	0.00	0.02	0.01	0.00	0.01	0.01	0.00	0.01	0.00	0.00
O=F,Cl	0.10	0.11	0.10	0.10	0.11	0.10	0.10	0.10	0.11	0.09	0.08
Total	99.33	99.46	98.66	99.42	98.11	97.66	98.22	98.42	98.29	98.95	98.60
Si	5.395	5.446	5.384	5.350	5.388	5.358	5.360	5.385	5.383	5.364	5.371
^{IV}Al	2.605	2.554	2.616	2.650	2.612	2.642	2.640	2.615	2.617	2.636	2.629
^{VI}Al	0.944	0.979	0.936	0.936	0.847	0.935	0.801	0.915	0.898	0.850	0.938
Ti	0.191	0.199	0.199	0.208	0.265	0.197	0.316	0.258	0.258	0.274	0.201
Fe	2.755	2.752	2.877	2.856	2.867	2.686	2.695	2.659	2.595	2.924	2.907
Mn	0.003	0.000	0.002	0.003	0.002	0.001	0.001	0.000	0.004	0.002	0.006
Mg	1.876	1.743	1.707	1.705	1.750	1.884	1.808	1.770	1.864	1.612	1.630
Ca	0.005	0.001	0.005	0.000	0.006	0.002	0.006	0.004	0.007	0.000	0.001
Na	0.115	0.156	0.121	0.137	0.108	0.137	0.128	0.175	0.128	0.107	0.100
K	1.619	1.671	1.709	1.745	1.651	1.678	1.689	1.673	1.679	1.699	1.724
OH	3.886	3.879	3.888	3.888	3.872	3.881	3.879	3.881	3.875	3.896	3.902
Cl	0.114	0.121	0.106	0.111	0.128	0.117	0.117	0.119	0.124	0.104	0.098
F	0.000	0.000	0.006	0.002	0.000	0.002	0.003	0.000	0.002	0.000	0.000
Σ Cat.	15.507	15.502	15.556	15.590	15.497	15.521	15.443	15.454	15.432	15.468	15.507

North	38.76961503			38.74623497			
East	13.47260596			13.41797599			
Sample	TD 35/1			TD 12/1			
Point	37	43	48	20	21	22	23
SiO_2	38.96	39.56	45.03	38.69	38.53	38.71	38.05
TiO_2	0.89	1.00	0.43	0.78	0.80	0.81	0.98
Al_2O_3	18.39	18.48	32.13	19.17	19.30	19.01	18.92
FeO	7.65	7.31	2.67	8.01	7.75	7.82	8.16
MnO	0.22	0.28	0.03	0.24	0.21	0.26	0.25
MgO	18.35	18.30	1.55	18.77	18.58	18.29	18.47
CaO	0.01	0.02	0.04	0.07	0.07	0.04	0.05
Na_2O	0.54	0.58	1.75	0.38	0.42	0.41	0.30
K_2O	8.46	8.52	8.08	8.51	8.64	8.73	8.79
H_2O*	3.84	3.90	4.27	3.92	3.94	3.91	3.88
Cl	0.61	0.55	0.12	0.54	0.47	0.50	0.53
F	0.00	0.02	0.00	0.00	0.01	0.01	0.00
O=F,Cl	0.26	0.24	0.05	0.23	0.20	0.21	0.22
Total	97.66	98.28	96.03	98.84	98.54	98.27	98.15
Si	5.653	5.691	6.232	5.555	5.548	5.592	5.523
^{IV}Al	2.347	2.309	1.768	2.445	2.452	2.408	2.477
^{VI}Al	0.798	0.824	3.474	0.799	0.825	0.829	0.759
Ti	0.097	0.108	0.044	0.084	0.087	0.088	0.107
Fe	0.928	0.879	0.309	0.961	0.934	0.944	0.990
Mn	0.027	0.035	0.003	0.029	0.026	0.031	0.031
Mg	3.968	3.925	0.319	4.018	3.989	3.939	3.996
Ca	0.001	0.002	0.005	0.011	0.011	0.006	0.008
Na	0.151	0.161	0.469	0.104	0.118	0.114	0.085
K	1.566	1.563	1.426	1.559	1.587	1.610	1.628
OH	3.719	3.744	3.945	3.754	3.781	3.767	3.759
Cl	0.280	0.252	0.054	0.246	0.216	0.230	0.241
F	0.001	0.004	0.001	0.000	0.003	0.003	0.000
Σ Cat.	15.536	15.497	14.050	15.565	15.578	15.562	15.603

North	38.76625699				38.74613296				
East	13.46121202				13.42149102				
Sample	TD 32	TD 32	TD 32	TD 32	TD 10/1	TD 10/1	TD 10/1	TD 10/1	TD 10/1
Point	7	8	9	10	35	36	37	38	39
SiO_2	45.30	45.54	46.42	44.90	47.55	47.13	45.84	45.97	45.78
TiO_2	1.38	1.49	1.11	1.51	0.62	1.59	2.00	1.93	2.01
Al_2O_3	8.20	8.18	7.69	8.31	7.16	7.27	8.18	8.11	8.74
Cr_2O_3	0.03	0.03	0.05	0.02	0.09	0.04	0.08	0.10	0.07
FeO_{calc}	11.14	12.23	11.75	12.29	10.48	9.92	8.65	9.27	8.87
Fe_2O_{3calc}	6.10	4.89	4.66	4.77	3.09	3.62	4.63	3.78	4.70
MnO	0.47	0.35	0.34	0.41	0.29	0.30	0.27	0.28	0.21
MgO	11.78	11.59	12.27	11.52	13.53	13.47	13.64	13.68	13.37
CaO	11.46	11.39	11.82	11.44	12.27	11.53	11.38	11.69	11.42
Na_2O	1.78	1.90	1.62	2.04	1.11	1.35	1.55	1.48	1.56
K_2O	1.06	1.02	0.98	1.07	0.44	0.72	0.85	0.84	0.90
H_2O*	2.04	2.04	2.05	2.03	2.05	2.05	2.05	2.05	2.06
Cl	0.15	0.15	0.11	0.17	0.03	0.03	0.03	0.03	0.03
F	0.34	0.31	0.32	0.35	0.14	0.13	0.14	0.15	0.20
O=F,Cl	-0.18	-0.16	-0.16	-0.19	-0.06	-0.06	-0.07	-0.07	-0.09
Total	101.06	100.95	101.03	100.62	98.79	99.07	99.22	99.28	99.83
Si	6.699	6.742	6.836	6.692	7.021	6.942	6.747	6.770	6.709
^{IV}Al	1.301	1.258	1.164	1.308	0.979	1.058	1.253	1.230	1.291
^{VI}Al	0.129	0.170	0.170	0.152	0.267	0.203	0.165	0.177	0.218
Ti	0.154	0.166	0.123	0.169	0.069	0.176	0.222	0.214	0.221
Fe^{3+}	0.679	0.545	0.516	0.535	0.344	0.401	0.513	0.419	0.519
Cr	0.004	0.004	0.006	0.002	0.011	0.005	0.009	0.011	0.008
Mg - C	2.598	2.557	2.695	2.559	2.979	2.957	2.993	3.003	2.921
Fe^{2+} - C	1.378	1.514	1.447	1.531	1.294	1.221	1.065	1.141	1.087
Mn - C	0.059	0.044	0.043	0.051	0.037	0.037	0.033	0.035	0.026
Mg - B	0.000	0.000	0.000	0.000	0.000	0.000	0.000	0.000	0.000
Fe^{2+} - B	0.000	0.000	0.000	0.000	0.000	0.000	0.000	0.000	0.000
Mn - B	0.000	0.000	0.000	0.000	0.000	0.000	0.000	0.000	0.000
Ca	1.815	1.807	1.865	1.827	1.941	1.820	1.794	1.844	1.792
Na - B	0.185	0.193	0.135	0.173	0.059	0.180	0.206	0.156	0.208
Na - A	0.325	0.352	0.327	0.415	0.259	0.205	0.236	0.265	0.236
K	0.200	0.193	0.184	0.204	0.083	0.135	0.159	0.157	0.168
Cl	0.038	0.037	0.027	0.043	0.009	0.008	0.008	0.007	0.007
F	0.159	0.145	0.150	0.165	0.063	0.061	0.067	0.071	0.092
Σ Cat.	15.684	15.689	15.661	15.784	15.405	15.401	15.461	15.494	15.496

Supplementary Information 3
Compiled age of published ages of plutons in the southern Arabian Nubian Shield

Emplacement and thermal effect of post-collisional Chewo Pluton (Arabian-Nubian Shield); implication for late East-African Orogeny.

Megerssa, L. *, Verner, K., Buriánek, D., Sláma, J. (2020). Journal of African Earth Sciences, 162, 103695.

* Coressponding author: megerssal@natur.cuni.cz; Institute of Petrology and Structural Geology, Faculty of Science, Charles University, Albertov 6, Prague, 12843, Czech Republic

No	Pluton	Age (Ma)	Dating method	Reference
Syn-tectonic				
1	Granite clast within the Gulgula Group, Eritrea	862 ±6	Single Zircon, Pb/Pb evaporation method	Teklay et al. 2003
2	Deformed volcanic rocks in Eritrea	854 ±3	Single Zircon, Pb/Pb evaporation method	Teklay et al. 2002
3	Granite from Eritrea	811 ±11	SHRIMP U-Pb analyses on zircons	
4	Granites in Tsaliet group, Northern ethiopia	806 ±21 to 756 ±33	Sm-Nd and chaemical Th-U-Pb Zr isochron method	Tadesse et al. 2000
5	Azeho, Northern Ethiopia	756 ±33	Sm-Nd (WR)	
6	Desset, Northern Ethiopia	757 ±30	Th-U-Pb (Zrn)	
7	Chila, Northern Ethiopia	806 ±21	Th-U-Pb (Zrn)	
8	Rama, Northern Ethiopia	740 ±42	Sm-Nd (WR)	
9	Granitoid, Northern Ethiopia	784 ±14	SHRIMP U–Pb–Th analytical data for zircons	Avigad et al. 2007
10	Felsic rock, Northern Ethiopia	774.7 ±4.8	SHRIMP U–Pb–Th analytical data for zircons	Avigad et al. 2007
11	Leucogneiss	782.8 ±12.8	Ar-Ar (Kfs)	Mock et al. 1999
12	Metagranodiorite	736.6 ±12.8	Ar-Ar (Bt)	
Post-tectonic				
13	Maikenetal Granite, Northern Ethiopia	612.3 ±5.7	U–Pb zircon	Avigad et al. 2007
14	Hauzien Granite, Northern ethiopia	613.4 ±0.9	single-zircon Pb/Pb evaporation	Miller et al. 2003
15	Negash Pluton, Northern ethiopia	606 ±0.9	single-zircon Pb/Pb evaporation	

No	Pluton	Age (Ma)	Dating method	Reference
16	Negash Pluton, Northern ethiopia	608 ±7	Zicon, U-Pb	Asrat et al. 2004
17	Post-orogenic intrusives	628 ±4	U-Pb multi grain titanite and Zircon	Teklay et al. 2001
18	Post-orogenic intrusives	622 ±1	single Zircon, Pb/Pb evaporation method	
19	Post-orogenic intrusives , Jabal Um Achabe granite, South east of Tokar, Sudan	652 ±14	Pb-Pb, singke zircon	Kröner et al. 1991
20	Maikenetal, Pre D2 folding	~650	K-Ar age	Beyth 1972
21	Late to post tectonic granites in Northern Ethiopia	660 – 540	K-Ar age and Ar-Ar ages	Miller et al. 1967; Garland 1980; Mock et al. 1999
22	Mica schist, Zula, Eritrea	~986	K-Ar (Ms)	Frazier 1970
23	Granite, Zula, Eritrea	~685	K-Ar (Bt)	
24	Granite, Hauzien, North Ethiopia	583 ±16	K-Ar (Bt)	Garland 1980
25	Granite, Hauzien, North Ethiopia	621 ±27	K-Ar (Bt)	
26	Granodiorite, Adi Aro River, Adigrat, North Ethiopia	582 ±22	K-Ar (Bt)	
27	Granodiorite, Adi Aro River, Adigrat, North Ethiopia	570 ±31	K-Ar (Bt)	
28	Granodiorite, Mereb River, North Ethiopia	690 ±4	K-Ar (Bt)	Miller et al. 1967
29	Granodiorite, Saganeitti, Eritrea	670 ±5	K-Ar (Bt)	
30	Red Granite, Negash, Northern Ethiopia	663.7 ±14	Ar-Ar (Ms)	Mock et al. 1999
31	Red Granite, Negash, Northern Ethiopia	622.7 ±13.7	Ar-Ar (Bt)	
32	Red Granite, Negash, Northern Ethiopia	597.8 ±9.6	Ar-Ar (Kfs)	
33	Tonalite, Negash, Northern Ethiopia	665.8 ±13	Ar-Ar (Bt)	
34	Tonalite, Negash, Northern Ethiopia	647.2 ±13	Ar-Ar (Bt)	
35	Leucogneiss, Axum, Northern ethiopia	510 ±8.9	Ar-Ar (Kfs)	
36	Red Granite, Axum (Adigrat road), Northern ethiopia	600.3 ±10.7	Ar-Ar (Bt)	
37	Red Granite, Axum (Adigrat road), Northern ethiopia	565.2 ±10	Ar-Ar (Kfs)	
38	Negash pluton	676–589	Ar–Ar (Ms)	
39	Mareb Granite, Northern ethiopia	545 ±24	CHIME zircon	Tadesse 1997
40	Mereb, Northern Ethiopia	633 ±62	Rb-Sr (WR)	Alemu 1998
41	Sibta, Northern Ethiopia	550 ±35	Rb-Sr (WR)	Tadesse et al. 2000
42	Shire, Northern Ethiopia	559 ±22	Rb-Sr (WR)	

References

Alemu, T., 1998. Geochemistry of Neoproterozoic granitoids from the Axum area, northern Ethiopia. Journal of African Earth Sciences 27(3-4), 437-460.

Asrat, A., Barbey, P., Ludden, J.N., Reisberg, L., Gleizes, G., Ayalew, D., 2004. Petrology and isotope geochemistry of the Pan-African Negash Pluton, Northern Ethiopia: Mafic-Felsic Magma Interactions during the Construction of Shallow-level Calc-alkaline Plutons. Journal of Petrology 45, 1147–1179.

Avigad, D., Stern, R.J., Beyth, M., Miller, N., McWilliams, M.O., 2007. Detrital zircon U–Pb geochronology of Cryogenian diamictites and Lower Paleozoic sandstone in Ethiopia (Tigrai): age constraints on Neoproterozoic glaciation and crustal evolution of the southern Arabian–Nubian Shield. Precambrian Research 154(1-2), 88-106.

Beyth, M., 1972. The geology of central and western Tigre, Ethiopia. Unpublished Ph.D. dissertation, University of Bonn, Germany.

Frazier, S.B., 1970. Adjacent structures of Ethiopia: that portion of the Red Sea coast including Dahlak Kebir Island and the Gulf of Zula. Philosophical Transactions for the Royal Society of London. Series A, Mathematical and Physical Sciences, 131-141.

Garland, C.R., 1980. Geology of the Adigrat area, Memoir No. 1. Ministry of mines. Addis Ababa, Ethiopia.

Kröner, A., Linnebacher, P., Stern, R.J., Reischmann, T., Manton, W. and Hussein, I.M., 1991. Evolution of Pan-African island arc assemblages in the southern Red Sea Hills, Sudan, and in southwestern Arabia as exemplified by geochemistry and geochronology. Precambrian Research, 53(1-2), 99-118.

Miller, J.A., Mohr, P.A., Rogers, A.S., 1967. Some new K-Ar age determinations of basement rocks from Eritrea. Bulletin of Geophysical Observatory, AAU, Ethiopia, 10, 53-57.

Miller, N.R., Alene, M., Sacchi, R., Stern, R.J., Conti, A., Kröner, A., Zuppi, G., 2003. Significance of the Tambien Group (Tigrai, N. Ethiopia) for Snowball Earth events in the Arabian–Nubian Shield. Precambrian Research 121(3-4), 263-283.

Mock, C., Arnaud, N.O., Cantagrel, J.M., Yirgu, G., 1999. 40Ar/39Ar thermochronology of the Ethiopian and Yemeni basements: reheating related to the Afar plume?. Tectonophysics, 314(4), 351-372.

Tadesse, T., Hoshino, M., Suzuki, K., Iizumi, S., 2000. Sm-Nd, Rb-Sr and Th-U-Pb zircon ages of syn- and post-tectonic granitoids from the Axum area of northern Ethiopia. Journal of African Earth Sciences 30(2), 313-327.

Tadesse, T., Suzuki, K., Hoshino, M., 1997. Chemical Th–U total Pb isochron age of zircon from the Mareb Granite in northern Ethiopia. Journal of Earth and Planetary Sciences, Negoya Univérsity 44, 21–27.

Teklay, M., Berhe, K., Reimold, W.U., Armstrong, R., Asmerom, Y., Watson, J., 2002. Geochemistry and geochronology of a Neoproterozoic low-K tholeiite-boninite association in central Eritrea. Gondwana Research, 5(3), 597-611.

Teklay, M., Haile, T., Kröner, A., Asmerom, Y., Watson, J., 2003. A back-arc palaeotectonic setting for the Augaro Neoproterozoic magmatic rocks of western Eritrea. Gondwana Research, 6(4), 629-640.

Teklay, M., Kröner, A., Mezger, K., 2001. Geochemistry, geochronology and isotope geology of Nakfa intrusive rocks, northern Eritrea: products of a tectonically thickened Neoproterozoic arc crust. Journal of African Earth Sciences 33(2), 283-301.

Appendix 2

Precambrian Research 361 (2021) 106270

Contents lists available at ScienceDirect

Precambrian Research

journal homepage: www.elsevier.com/locate/precamres

Tectonometamorphic evolution and U–Pb dating of the high-grade Hammar Domain (Southern Ethiopian Shield); implications for the East-African Orogeny

Kryštof Verner [a,b,*], David Buriánek [b], Martin Svojtka [c], Vít Peřestý [a], Leta Megerssa [a,b], Tarekegn Tadesse [d], Aspiron Kussita [e], Diriba Alemayehu [d], Tomáš Hroch [b]

[a] Institute of Petrology and Structural Geology, Faculty of Science, Charles University, Albertov 6, Prague 2, 128 43, Czech Republic
[b] Czech Geological Survey, Klárov 131/3, Prague 1, 118 21, Czech Republic
[c] Institute of Geology of the Czech Academy of Sciences, Rozvojová 269, Prague 6, 165 00, Czech Republic
[d] Addis Ababa Science and Technology University, Applied Science College, Addis Ababa, Ethiopia
[e] Addis Ababa University, College of Natural and Computational Sciences, Addis Ababa, Ethiopia

ARTICLE INFO

Keywords:
Eastern African Orogeny
Arabian-Nubian Shield
P-T modelling
Fabric pattern
U–Pb Zircon dating

ABSTRACT

Based on new U–Pb zircon data, field structural analysis and a detailed petrological study of the plutonic and high-grade metamorphic rocks of the Hammar Domain (Southern Ethiopian Shield) overall geodynamic scenario was inferred, bringing broad implications for the East-African Orogeny. The structural evolution of the Hammar Domain can be summarized into four phases, D_1 to D_4, resulting in (a) relict compositional banding (S_1), (b) flat-lying migmatite foliation (S_2) defining the primary contacts of granulites and migmatites, (c) superimposed steeply dipping N–S trending compressional foliation (S_3) due to regional ~E–W oriented compression and (d) later ~NW–SE trending left-lateral transpressive fabric (S_4). New geochronological data point to long-lasting orogenic convergence forming the East-African Orogeny which resulted in two main geodynamic events: (a) Late Tonian to late Cryogenian episode (ca. 770 to 650 Ma) where large volcanic arc construction as the source of rock photoliths (dated at ca. 770 Ma) was followed by crustal accretion and flat-lying fabrics origin (D_2 stage), intense migmatization and HT-MP metamorphism (T: 700–850 °C and P: 0.7–0.9 GPa) at depths of ~25–35 km (dated at ca. 720 and 715 Ma). (b) Late Cryogenian to early Ediacaran episode (ca. 650 to 620 Ma) as the key era of continental collision leading to the Greater Gondwana assembly. An early ~E–W oriented compression (D_3 stage) resulted in ~N–S trending fabrics that have been continuously changed to the left-lateral transpression (D_4 stage) forming ~NW–SE oriented foliations. The time-scale of D_3 and D_4 events is inferred by *syn*-tectonic granitoid intrusions yielded at ca. 648 Ma and ca. 630 Ma respectively. Furthermore, the syn- to post-tectonic leucogranite dike, dated at ca. 630 Ma, marks the upper limit for the ductile or brittle-ductile deformation and regional metamorphic events.

1. Introduction

The East African Orogen (EAO; Fig. 1a) is one of the major orogenic belts extending from southern Israel in the north to Mozambique and Madagascar in the south (e.g. Stern, 1994; Fritz et al., 2013; Johnson, 2014). The EAO includes several orogenic episodes (for review see Fritz et al., 2013), e.g. the Mozambique Ocean closure, island-arcs construction and microcontinents accretion (ca. 850 to 650 Ma) continued by continental collision and Greater Gondwana assembly termed as the "East African Orogeny" (ca. 650 to 620 Ma). Although a general consensus on the geodynamic evolution of EAO has been framed in light of plate tectonic model similar to the modern day destructive plate margin (for review see Fritz et al., 2013), a number of contrasting hypotheses have been suggested regarding the time-scale and tectonometamorphic evolution of individual segments of EAO, especially for the Neo-Proterozoic metamorphic rocks of Ethiopian shields (e.g. de Wit and Chewaka, 1981, Ayalew, 1997; Yibas et al., 2002; Bowden et al., 2020). The Neo-Proterozoic metamorphic rocks of southern Ethiopia (Fig. 1b,c) form a key segment of the EAO characterized by medium to high-grade metamorphic rocks of the southern EAO (the Mozambique

* Corresponding author at: Institute of Petrology and Structural Geology, Faculty of Science, Charles University, Albertov 6, Prague 2, 128 43, Czech Republic.
E-mail address: krystof.verner@geology.cz (K. Verner).

https://doi.org/10.1016/j.precamres.2021.106270
Received 17 October 2020; Received in revised form 8 March 2021; Accepted 10 May 2021
Available online 31 May 2021

Belt) which are tectonically interleaved with the predominantly lower grade, accreted arc terranes of the northern EAO (the Arabian Nubian Shield). Despite several studies from southern Ethiopia (e.g. Worku and Schandelmeier, 1996; Yibas et al., 2002; Teklay et al., 1998, Asrat and Barbey, 2003), the Neoproterozoic crust in the region remains poorly understood mainly in terms of the style and timing of tectonometamorphic evolution and magmatism.

This paper describes the overall structural pattern, metamorphic evolution and five new U–Pb laser ablation ICP-MS zircon ages of syn- to post-tectonic granitoids and the high-grade rocks from the Hammar Domain (Davidson, 1983), which belongs to the Southern Ethiopian Shield (SES, Fig. 1b,c). The area of our interest straddles along the WNW–ESE oriented profile between the towns of Jinka and Konso in southwestern Ethiopia (Fig. 1c). A comprehensive interpretation of the new U–Pb geochronological data, particularly with respect to tectonic and metamorphic patterns of the Hammar Domain, opens the opportunity to shed some light on the geodynamic evolution and magmatism of the southern Arabian-Nubian Shield (ANS) within the EAO.

2. Geological setting

The East-African Orogen (EAO) evolved as a Neoproterozoic to early Cambrian (ca. 890 to 550 Ma), collision-accretion-type orogeny which greatly contributed to the consolidation of the Gondwana

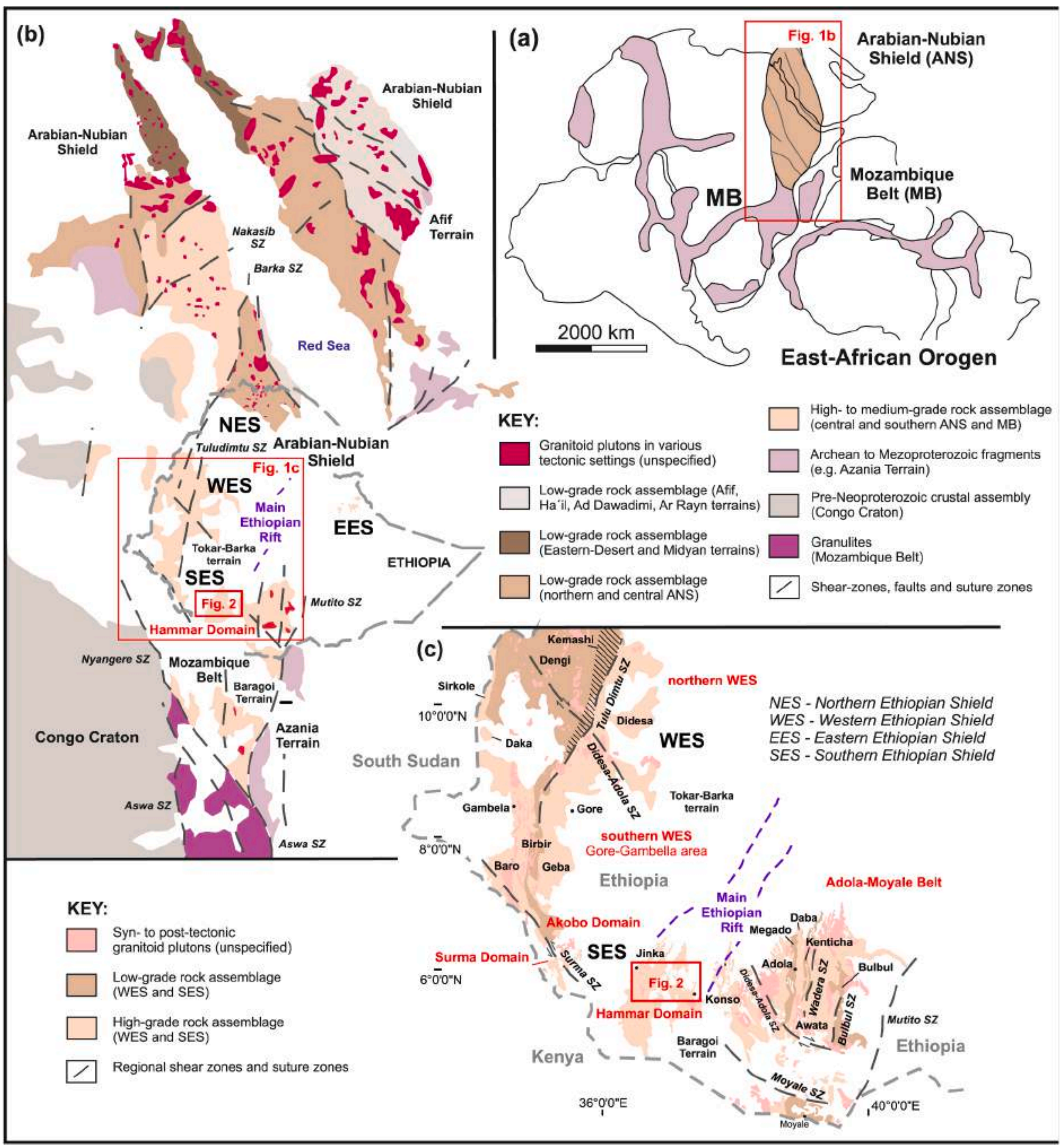

Fig. 1. (a) Sketch of Gondwana supercontinent assembly and position of ANS (after Fritz et al., 2013; Johnson, 2014); (b) Sketch of ANS terranes and related plutons (modified after Fritz et al., 2013); (c) Simplified geological map of the WES and SES including the Hammar Domain (modified after Davidson, 1983; Allen and Tadesse, 2003; and Stern et al., 2012).

supercontinent (Fritz et al., 2013 and references therein). The EAO involved terrane accretion forming the Arabian-Nubian Shield (ANS) and continued by continental collision with the Sahara and Congo–Tanzania cratons to the west and Azania and the Afif terranes to the east. Coevally in the southern part, the EAO evolved through the closure of the intervening Ocean and collision between the Azania microcontinent and Congo-Tanzania Craton at around 640 to 630 Ma (Collins, 2006), followed by the post-orogenic extension (e.g. Stern et al., 2012; Fritz et al., 2013). The northern segment of the EAO (Fig. 1b) is comprised of mostly juvenile low- to medium-grade rock assemblages of the Arabian Nubian Shield (ANS), while its southern part is constituted of high-grade metamorphic rocks of the older Paleoproterozoic crust traditionally referred to as the Mozambique Belt (MB) (Holmes, 1951; Sommer et al., 2003; Kusky et al., 2003; Hauzenberger et al., 2004; Hargrove et al., 2006; Fritz et al., 2013).

However, it has recently become widely accepted that orogenic events in both segments of the EAO were coeval and differed mainly by the intensity and depth of crustal thickening (Fritz et al., 2013). In this perspective, the Mozambique Belt mainly represents the orogenic root domain showing a higher degree of metamorphic overprint (e.g. Asrat et al., 2001; Allen and Tadesse, 2003; Fritz et al., 2013). Several geodynamic episodes were defined in the EAO (e.g. Fritz et al., 2013 and references therein): (a) Sea-floor spreading (up to 830 Ma) followed by subduction and volcanic arcs and back arcs formation (ca. 890 to 750 Ma); (b) widespread crustal accretion followed by continent–continent collision (ca. 750 to 620 Ma) associated with polyphase deformation and a high- to low-grade metamorphic overprint and (c) late-orogenic extension corresponding to post-collisional granite magmatism continuing up to ca. 550 Ma.

The area under study (Fig. 1b,c) is located in southwestern Ethiopia belonging to the Tokar-Barka and Baragoi terranes of the western part of the EAO (e.g. Fritz et al., 2013) surrounded by the Nakasib suture zone in the north, and the Nyangere and Mutitio shear zones in the south (Fig. 1b). These terranes are partly overlaid by Phanerozoic volcano-sedimentary sequences and exposed in separated basement shields as the Northern (NES), Western (WES), Southern (SES) and Eastern (EES) Ethiopian shields (Fig. 1b). The Southern Ethiopian Shield (SES) encompassing the study area has been mostly considered to be the northern continuation of the Mozambique Belt (MB) owing to the prevalence of medium to high-grade metamorphic rocks that are similar to the MB rocks further south in Kenya and Tanzania (e.g. Tolessa et al., 1991; Alene and Barker, 1993; Hauzenberger et al., 2005). However, the low to medium grade volcano-sedimentary rocks of the Arabian Nubian Shield (ANS) in the SES occur as tectonically interleaved belts together with prevailing high grade rocks (e.g. Kusky and Matsah, 2003) as the result of the collision between East and West Gondwana (Bonavia and Chorowicz, 1992; Yibas et al., 2002).

2.1. The western Ethiopian Shield (WES)

The Western Ethiopian Shield (WES; Fig. 1c) is built by high-grade paragneisses, orthogneisses and migmatites with intervening low-grade volcano-sedimentary sequences and intrusive bodies of mafic, ultramafic and felsic or granitic composition (Blades et al., 2015 and references therein). The gneisses and migmatites have been described as juvenile crust by earlier works in the ANS (e.g. Hargrove et al., 2006). The central part of the WES is covered by Phanerozoic volcanic rocks which separates it into the northern part including the Didessa, Kemashi, Dengi, Sirkole and Daka domains (Alemu and Abebe, 2007; Allen and Tadesse, 2003) and the southern part formed by Geba, Baro and Birbir domains (Tefera and Berhe, 1987; Ayalew et al., 1990; Ayalew, 1997; Allen and Tadesse, 2003). In addition, there is a linear arrangement of strongly altered and deformed mafic to ultramafic rocks, described variably as the Tulu Dimtu Belt (e.g. Alemu and Abebe, 2007; Allen and Tadesse, 2003). These rocks mostly portray metamorphic conditions reaching T: 600–800 °C and P: 0.5–0.8 GPa and a later low-temperature retrograde overprint (Ayalew and Johnson, 2002). A slightly lower degree of regional metamorphism was estimated in the Baro Domain, at T: 520° C and P: 0.4 GPa (Ayalew, 1997). Multiple deformation events have been recognized in the entire WES (e.g. Ayalew, 1997; Ayalew and Johnson, 2002; Allen and Tadesse, 2003; Alemu and Abebe, 2007). In the region, prominent NNE–SSW trending, moderately to steeply dipping foliation and latter conjugate ductile NW–SE and NE–SW trending shear zones with both left- and right-lateral kinematics were interpreted as resulting from E–W and WNW–ESE progressively rotational compressional stress (e.g. Allen and Tadesse, 2003). The tectonic evolution started by early westward thrusting and the associated D_1 recumbent folding, followed by continued E–W shortening which produced the N–S trending folds and associated prevailing N–S regional foliation and culminated with conjugate ductile shear zones (Alemu and Abebe, 2007). In the WES, several geodynamic episodes were also defined in the context of the ANS evolution: (a) Early rifting of the Rodinia supercontinent associated with plume-type magmatism (ca. 900–860 Ma) continued by continental passive margin formation in the range between ca. 860 and 830 Ma (Woldemichael et al., 2010), (b) subduction and volcanic arc formation (ca. 830–750 Ma; Ayalew and Johnson, 2002; Woldemichael et al., 2010) gently overlapped with (c) high-grade metamorphism, migmatization in the collisional stage (dated at ~775 Ma; Bowden et al., 2020) and anhydrous magmatism (dated at 774.6 Ma; Bowden et al., 2020). These events followed by (d) terrain accretion and *syn*-tectonic intrusions in the range of ca. 750–650 Ma (Woldemichael et al., 2010). The late-stage crustal thickening was constrained between ca. 650 and 635 Ma followed by later gravitational collapse associated with shearing and post-tectonic intrusions up to 550 Ma (Tsige and Abdelsalam, 2005; Ayalew and Johnson, 2002; Woldemichael et al., 2010; Bowden et al., 2020).

2.2. The southern Ethiopian Shield (SES)

Several lithotectonic units are exposed in the SES (Fig. 1c) including the low- to high-grade Adola-Moyale Belt (Worku and Schandelmeier, 1996; Yibas et al., 2002), the high-grade Akobo, Surma and Hammar domains (Davidson, 1983). The Akobo Domain dominated by medium-grade schists and gneisses intruded by gabbroic to granitic rocks. Its southern boundary is the ~NW–SE trending left-lateral Surma Shear Zone separating the Surma Domain composed of medium-grade biotite and hornblende quartz-feldspathic gneisses with abundant layers of amphibolite and calc-silicate gneisses (Davidson, 1983; Bonavia and Chorowicz, 1992). The Adola-Moyale Belt is constituted by N–S striking tectonically interleaved, high and low grade metamorphic units. The high-grade rocks were partially subjected to peak metamorphic conditions reaching temperatures of 800–850 °C and pressures of 0.9 GPa (Gichile, 1992). Gneisses and migmatites intercalated with amphibolite and kyanite-bearing schists recorded regional metamorphic conditions at pressures 0.6–0.7 GPa and temperatures 590–640 °C (Tsige, 2006; Yihunie et al., 2004). These rocks are tectonically interleaved with the lower-grade ophiolitic–volcano–sedimentary units of the Kenticha, Megado and Bulbul units (Ghebreab, 1992; Worku and Schandelmeier, 1996; Yibas et al., 2002; Allen and Tadesse, 2003; Yihunie et al., 2004; Stern et al., 2012). The ophiolitic rocks of the Kenticha Belt underwent relatively lower metamorphic conditions (T: 580–520 °C and P: 0.4–0.5 GPa; Yihunie et al., 2004). Similarly, the mafic and ultramafic rocks of the Bulbul Unit were affected by low-grade metamorphic conditions with temperatures of ca. 450 °C and pressures of ca. 0.3 GPa (Yihunie et al., 2004). The overall tectonic pattern in the Adola-Moyale Belt can be summarized as (Berhe, 1988; Alene and Barker, 1993): (a) the formation of ~E-W trending folds, (b) partial overprinting by a ~N–S trending folds and (c) ~NW–SE shearing showing both right- and left-lateral kinematics.

In the Adola-Moyale Belt, rare pre-Neoproterozoic ages were obtained from xenocrysts in the metasedimentary rocks (1030 ± 4 Ma; Rb-Sr; Yibas et al., 2002) and ca. 1660 and 1125 Ma ages from inherited zircon cores in the Neoproterozoic *meta*-rhyolite representing a remnant sliver of older crust (Teklay et al., 1998). On the other hand, the SES is dominated by four major tectonothermal events and the accompanying magmatic episodes (Teklay et al., 1998; Yibas et al., 2002; Stern et al., 2012): (a) The late-Tonian to early-Cryogenian episode overlapping the Bulbul-Awata tectonothermal event (ca. 840–890 Ma) and (b) later the Megado tectonothermal event (ca. 770–700 Ma) both of which are associated with volcanic arc formation followed by (c) the Moyale tectonothermal event (ca. 660 Ma) and (d) the Ediacaran-Cambrian Pan-African episode (ca. 630–500 Ma) mainly related to the continental collision between East Gondwana and the consolidated Congo-Tanzanian-Saharan craton (West Gondwana). Crustal thickening,

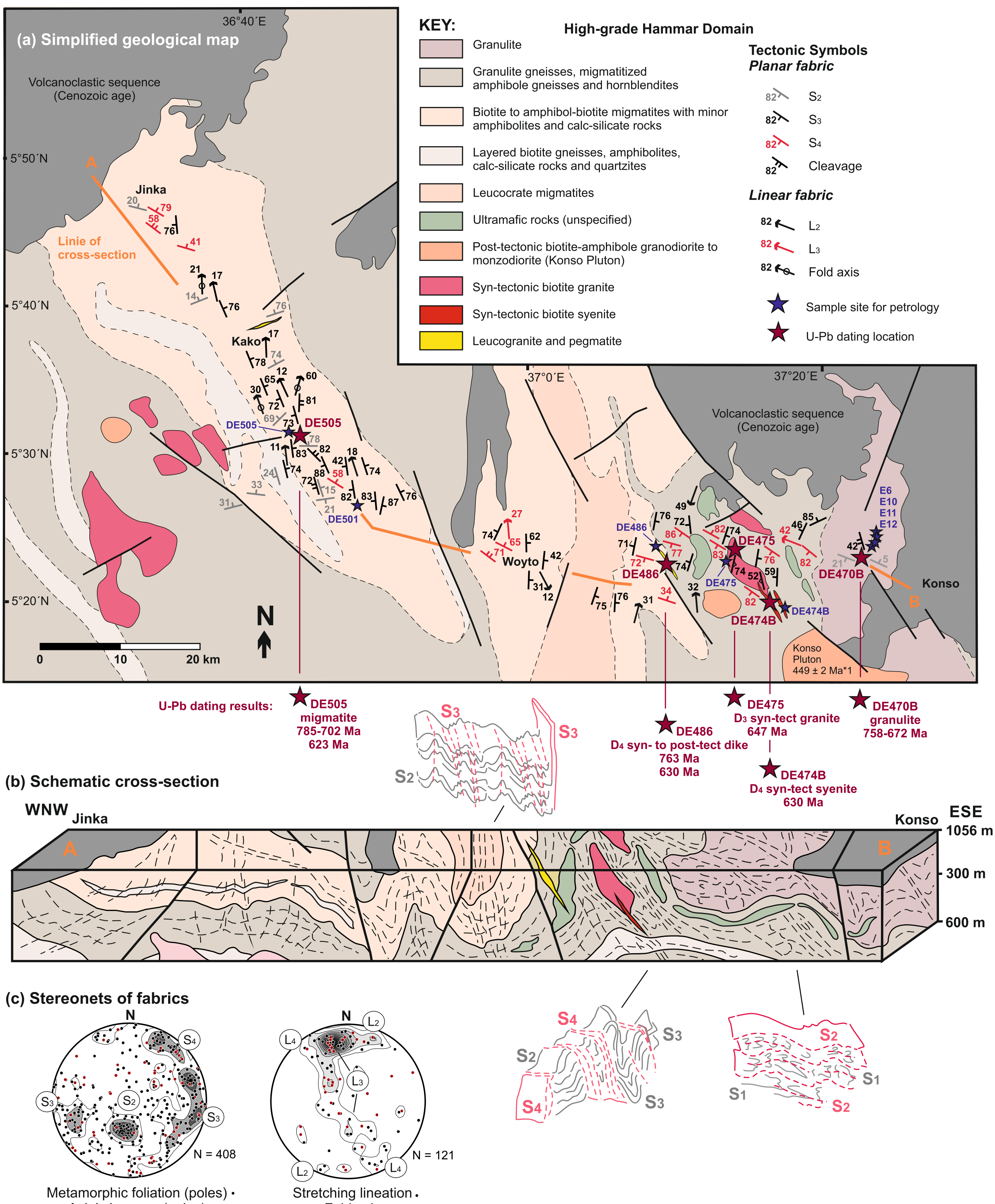

Fig. 2. (a) Simplified geological and structural map of the Central Hammar Domain including the location of U–Pb sites and samples for petrology; (b) Schematic structural WNW–ESE oriented cross-section between towns Jinka and Konso; (c) Stereonets of field structural data (equal area lower hemisphere projection).

driven by the continued ~E–W compression, triggered significant melting and the subsequent uplift over a wider region, involving shearing in the later stage as manifested by the Wadera shear zone dated at 580 Ma (Yibas et al., 2002).

2.3. The Hammar Domain

The studied Hammar Domain (Fig. 1b,c) is comprised of predominantly ~NNW–SSE trending high-grade biotite to amphibole-biotite migmatites interlayered with amphibolites, calc-silicate rocks, amphibole-pyroxene gneiss and felsic granulites that underwent amphibolite- to granulite-facies metamorphism and polyphase deformation (Kazmin et al., 1978; Davidson, 1983; Teklay et al., 1998; Asrat and Barbey, 2003). According to Davidson, (1983) and Bonavia and Chorowicz (1992) the Hammar Domain forms an anticlinorium with an axial plane dipping steeply to the east. The zircon data of granulites

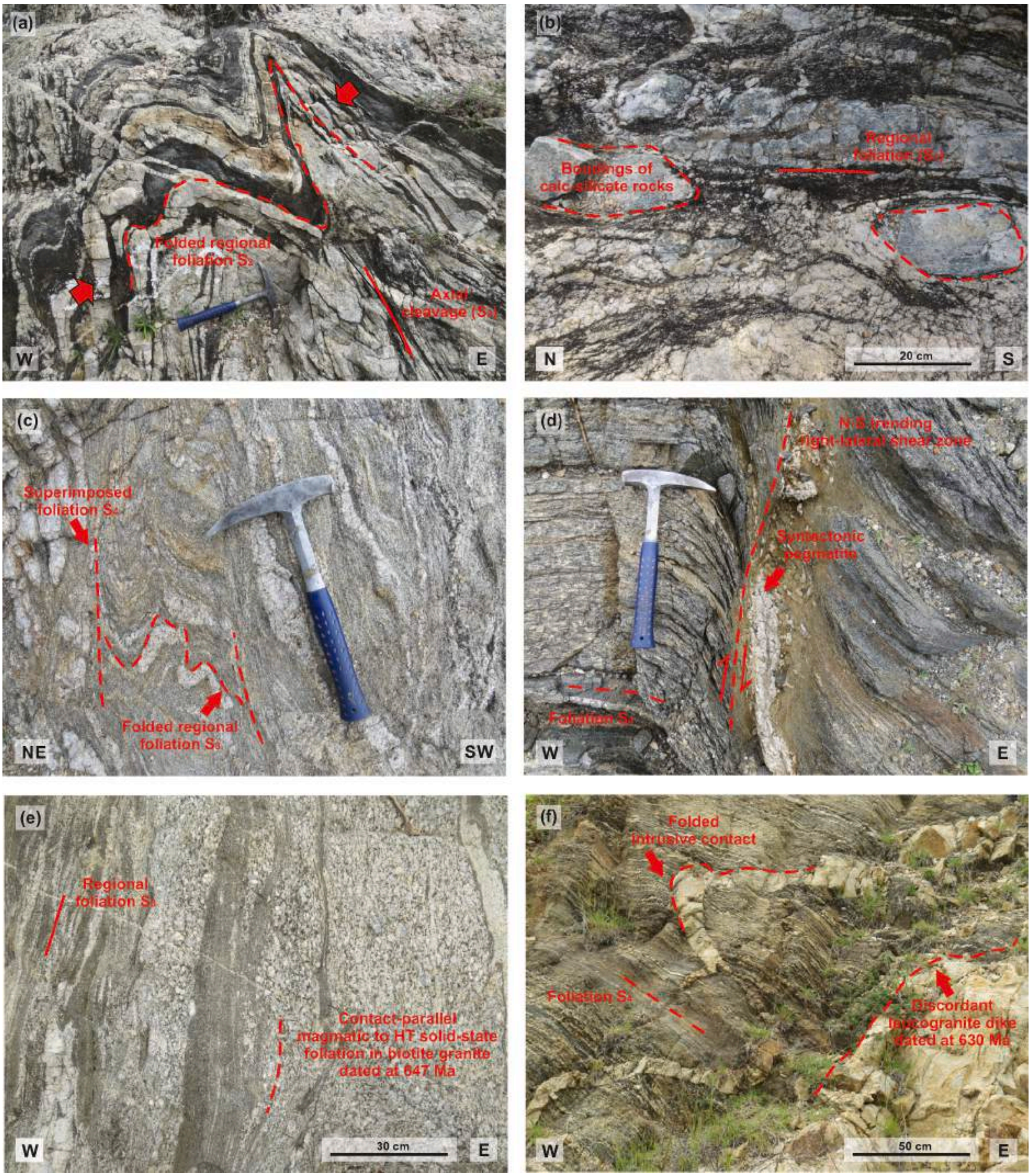

Fig. 3. Field photographs from the central part of the Hammar Domain: (a) Asymmetric folds of regional foliation S_2 heterogeneously transposed to NNE(N)–SSW(S) directions of S_3 and the associated axial cleavage; (b) Symmetric boudins of more competent calc-silicate rocks within the regional S_2 foliation; (c) Superimposed transpressive WNW(NW)–ESE(SE) trending foliation (S_4) with relics of folded foliation S_3; (d) Right-lateral N–S trending shear zones with *syn*-tectonic leucogranite dike affecting the entire set of S_1-S_4 foliations; (e) Contact-parallel intrusion of *syn*-tectonic granite showing transitional magmatic to high-temperature solid-state fabrics parallel to the regional foliation S_3. (f) Discordant leucogranite dike with gently folded intrusive contact discordant to later S_4 foliation.

(721 ± 12 Ma; SHRIMP U–Pb method and 728.6 ± 0.6 Ma; Pb–Pb evaporation method) determined by Teklay et al. (1998) were interpreted as the age of the protolith. Although the description of their data weighs on more of metamorphic overprint, a magmatic source is supposed by Teklay et al. (1998). In fact, from the age and isotopic signature point of view, these granulites have been suggested to be comparable to the Jebel Moya granulite in Sudan (Stern and Dawoud, 1991; Teklay et al., 1998). It has been suggested that the Hammar Domain reflects similar geodynamic episodes as the Adola-Moyale Belt involving early rifting and passive margin development (ca. 1100–1000 Ma; de Wit and Chewaka, 1981; Davidson, 1983; Gichile, 1992), west-dipping subduction associated with volcanic arc formation at ca. 900–750 Ma, followed by crustal extension (ca. 750–650 Ma) and a collisional stage and uplift between 650 and 450 Ma. The post-collisional magmatism was inferred from the emplacement of the A-type Konso pluton dated at 449 ± 2 Ma; Asrat and Barbey, 2003).

3. Structural pattern

3.1. High-grade rocks of the Hammar Domain

In the eastern Hammar Domain (Figs. 1c, 2a) two high-grade metamorphic fabrics, S_1 and S_2 were distinguished as a result of progressive D_1 and D_2 deformational events, which were heterogeneously overprinted by retrograde S_3 and S_4 fabrics associated with D_3 and D_4 deformation events. Representative geological cross-section and structural data of all the fabrics described below are shown on Fig. 2a-c. The oldest systematically observed planar fabrics is a compositional banding of flat-lying orientation (S_2) with relics of intensively folded early S_1 fabrics. These isoclinal to rootless folds are well preserved in the low-strain domains, mainly in the western and eastern parts of the Jinka-Konso profile (Fig. 2a,b). Furthermore, the S_2 foliation defines the original contacts of the major lithologies such as granulites, granulite gneisses and high-grade migmatites. Widespread boudinage of the more competent lithologies such as calc-silicate rocks and amphibolites and common isoclinal folds (relics of S_1 fabrics) are found within the S_2 foliation. The boudinages are also associated with the well-developed ~N(NNE)–S(SSW) trending lineation L_2 defined by stretching the mineral aggregates perpendicular to the boudins. Across the studied area the earlier planar fabric S_2 is heterogeneously transposed (re-folded) into a regional ~NNE(N)–SSW(S) trending steeply to moderately dipping metamorphic foliation S_3 (Fig. 3a). Strain partitioning is apparent in the D_3 deformation owing to the contrasting rheology of the different lithologies. As a consequence, different types of fold structures, such as open to tight, rootless or isoclinal folds within the S_3 foliation, are present. The axial planes and associated axial cleavage of S_3 dip steeply to WSW(W) or ENE(E) (Fig. 3a). In addition, the boudinage of more competent calc-silicate rocks is developed in the domains intensively overprinted by S_3 foliation (Fig. 3b). These boudins are mostly symmetrical with axes plunging steeply to ~N(NNW). The associated well-developed stretching or mineral lineation L_3 (linear elongation of quartz, feldspar and biotite aggregates) and widespread fold axes reveal a similarity in the orientation, plunging gently to steeply to ~N(NNW). It is obvious that the initial stages of structural overprint (from S_2 to S_3) were accompanied by the formation of a gently plunging lineation, while the later stages of deformation tend to produce steep fold axes and the associated steep stretching lineation.

The last phase of regional deformation (D_4) resulted in heterogeneous gentle to open folding and the formation of the S_4 cleavage and/or penetrative deformation banding in the high-strain domains with an identical steep to moderate dip to ~NNE(NE). The intensity of this later D_4 overprint decreases westward, whereby the eastern part of the Jinka-Konso profile was affected mostly by the D_4 event (Fig. 2a; 3c). The S_4 planar fabric is often associated with a well-developed stretching lineation (L_4) plunging gently to moderately to ~NNW(NW) or SSE(SE). A prevailing left-lateral shearing asymmetry was observed in the L-par section of the S_4 foliation. This D_4 fabric pattern is consistent with the ~NW–SE trending Surma and Moyale shear zones (Fig. 1c) which can be traced south-eastwards (Bonavia and Chorowicz, 1992). Several narrow low-grade shear zones (D_4 stage) with prevailing right-lateral kinematics (Fig. 3d) affecting the overall fabric pattern were identified across the Hammar Domain. These shear zones, up to 1 m in width, dip steeply to ~ENE to ~ESE bearing stretching lineation plunging to the ~NE and are also commonly associated with narrow pegmatite dikes. In addition, there are abundant, mostly vertical thin quartz veins and leucogranite dykes (with thickness up to 0.1 m) predominantly trending ~N–S or E–W. The brittle structures are mainly manifested as a series of major ~NE–SW trending faults and almost orthogonal ~NW(NNW)–SE(ESE) trending faults that partly offset all the lithologies.

3.2. Granite plutons and other intrusives

Several granite plutons and other intrusives, associated with and marking various tectonic episodes, were identified across the Hammar Domain (Fig. 2a). The early, well foliated syn-tectonic (with respect to D_3 stage) biotite granite and syenite form slightly ~NW–SE elongated intrusions or sheets of up to 10 km in the longer dimension contacts mostly parallel to the regional S_3 or S_4 foliations (for location see Fig. 2a, b). These granite intrusions reveal a transitional magmatic to submagmatic foliation characterized by planar crystal-shape preferred orientation of quartz, K-feldspar and biotite aggregates partly affected by recrystallization and deformation (criteria according to Vernon, 2000). The magmatic to submagmatic foliation is parallel to the intrusive contacts and the host metamorphic foliation S_3, both dipping steeply to ~E(ENE) (Fig. 3e). A ~NW–SE trending syenite sheet, with a thickness of up to 7 m, was mapped in the southern tip of the granite intrusion (Fig. 2a). This syenite sheet has intrusive contacts and contains magmatic fabrics that are partly discordant to the S_3 foliation and granite pluton boundaries, but parallel to the later superimposed S_4 fabrics. Several other leucogranite, pegmatite and microdiorite dikes, syn- to post-tectonic to the later S_4 fabrics were found across the Hammar Domain. One of these intrusions, which can be a representative for the majority, is the subvertical ~NNW–SSE trending leucogranite dike swarm (up to 5 m in thickness). These dikes crosscut the entire set of ductile structures (S_1 to S_4) discordantly, however at most places the dikes are gently folded with an axial plane parallel to the S_4 foliation (Fig. 3f), reflecting the last strain increments of the last regional D_4 event. The most conspicuous post-tectonic granite plutons (e.g. Konso Pluton, dated at ~ 449 Ma; Asrat and Barbey, 2003) is characterised by purely magmatic fabrics and discordant contacts and is the youngest magmatic episode in the Hammar Domain.

4. Petrology and mineral chemistry

A detailed description of the main lithologies of the Hammar Domain based on 11 samples representing different lithological types, mineralogical and textural characteristics (Tab. 1) is given. The abbreviations of the mineral names used in the text correspond to Whitney and Evans (2010).

4.1. High-grade rocks of the Hammar Domain

Biotite and amphibole-biotite migmatites occur across the Hammar Domain, together with layers and lenses of partially molten amphibolites. The textures of the migmatites vary from metatexite to diatexite according to Brown (1973). Metatexites are characterized by alternated fine to medium-grained leucocratic and melanocratic bands on a centimetre scale, diatexites are characterized by a high content of a medium-grained melanocratic assemblage. The schlieren layering along the contacts between various lithologies is mostly gradational. Their mineral assemblage comprises of anhedral quartz, anhedral to subhedral, partly altered plagioclase and biotite and minor perthitic K-feldspar crystals (Fig. 4a). Secondary minerals are muscovite, which occurs mainly along the microcracks in the K-feldspar and chlorite replacing biotite. Accessory minerals are zircon, apatite, monazite and opaque minerals. The representative sample DE505 was used for U–Pb dating (Tab. 1).

Garnet-bearing calc-silicate rocks appear as up to 2 m-thick layers and lenticular bodies within leucocratic migmatites. It is a medium-grained granoblastic rock consisting of quartz, plagioclase, garnet, clinopyroxene, magnetite, ilmenite and titanite. Plagioclase (Fig. 5a; $An_{73–75}$ $Ab_{24–26}$ $Or_{0–1}$) forms a granoblastic aggregate or forms a symplectite with diopside (Fig. 5b; X_{Fe} = 0.63–0.72, Al 0.12–0.20 apfu) and garnet (Fig. 5c, d; $Alm_{8–9}$ Prp_1 $Grs_{27–30}$ $Sps_{0–1}$ $Andr_{61–63}$). K-feldspar (Fig. 5a; $Or_{92–94}$ Ab_6 $An_{0–2}$) forms small inclusions or antiperthite within the plagioclase. Garnet forms euhedral porphyroblasts without significant chemical zoning ($Alm_{5–8}$ $Prp_{0–1}$ $Grs_{26–31}$ $Sps_{0–1}$ $Andr_{64–66}$) and with scarce inclusions of quartz, pyroxene and plagioclase ($An_{49–50}$ $Ab_{48–50}$

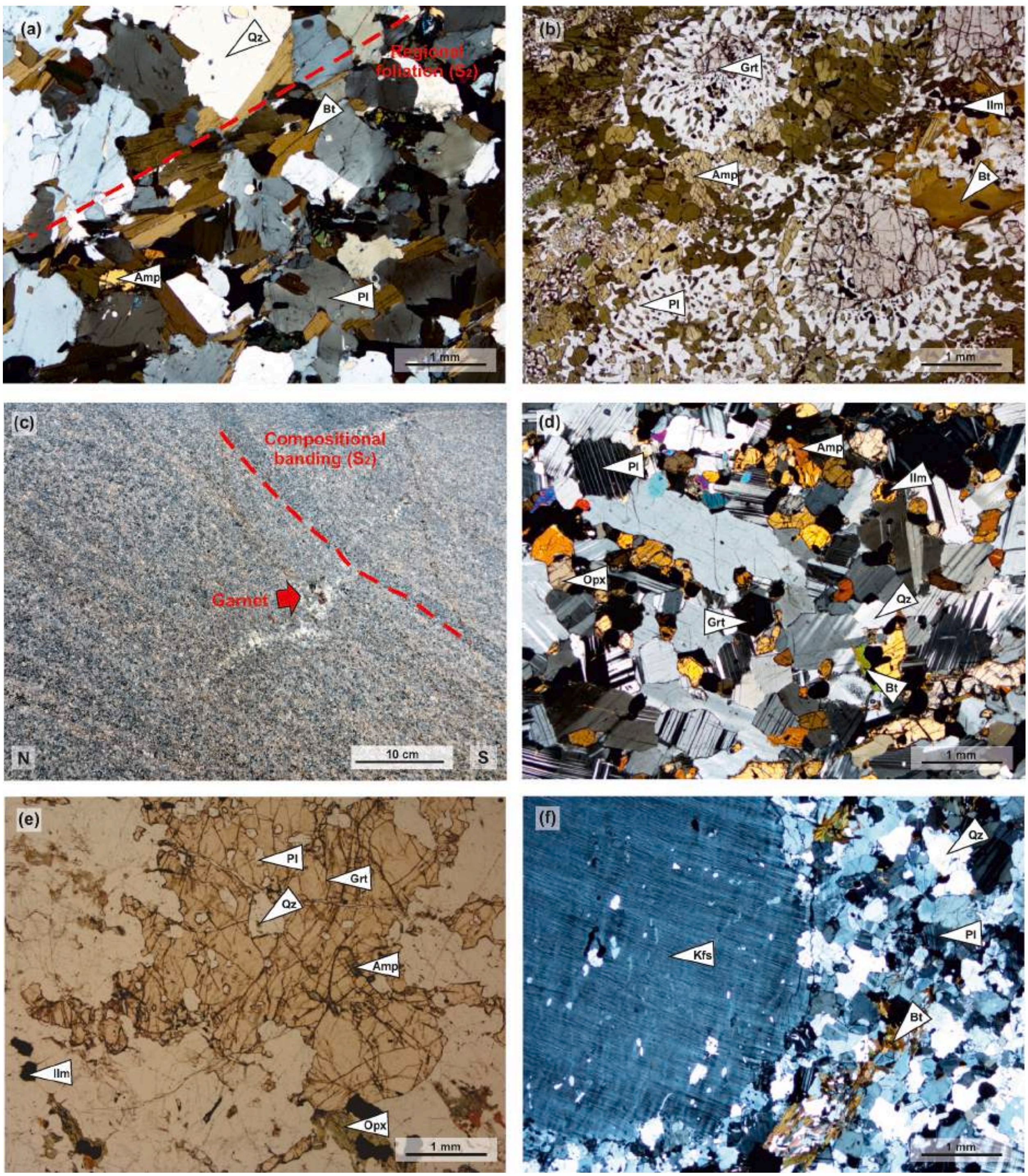

Fig. 4. Field photograph and photomicrographs showing the main studied rock types: (a) amphibole-biotite metatexite with S_2 regional foliation (XPL; sample DE505). (b) Amphibolite with relics of the garnet porphyroblasts surrounded by plagioclase + amphibole + clinopyroxene symplectites (PPL; sample DE501). (c) Photograph of two-pyroxene granulite with foliation S_2 and younger garnet porphyroblasts surrounded by leucosome cross-cutting strong layering, including layers rich in garnet. (d) Garnet-orthopyroxene granulite (XPL; sample E12). (e) Small garnet porphyroblast surrounded by narrow leucosome, containing inclusions of amphibole, plagioclase, quartz and orthopyroxene (PPL; granulite sample E6D). (f) Syn-tectonic granite (XPL; sample DE475).

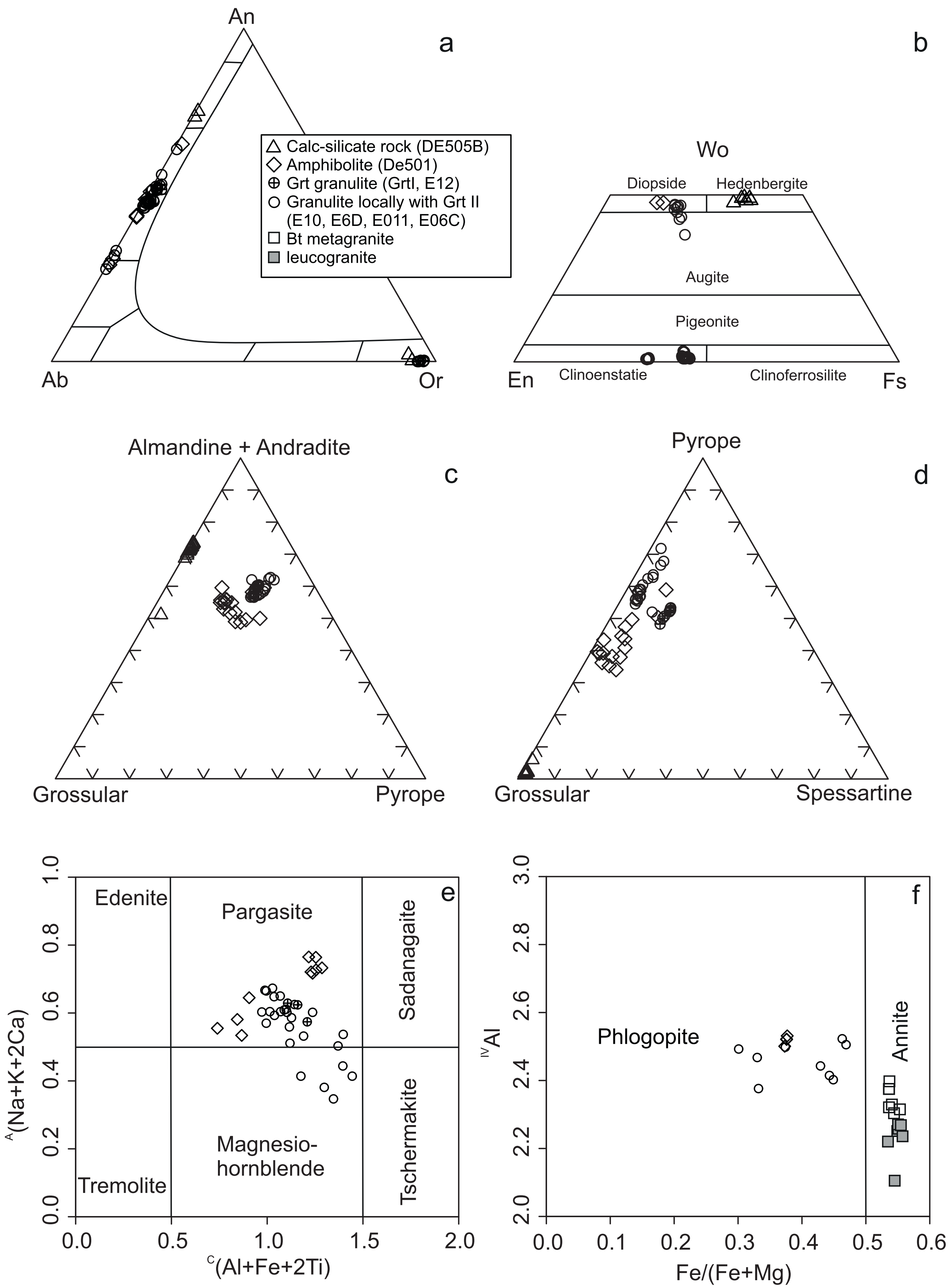

Fig. 5. Compositions of selected rock forming minerals: (a) ternary diagram Ab–An–Or for feldspar classification. (b) Ternary classification diagram of pyroxene $Mg_2Si_20_6$ (En) – $Ca_2Si_20_6$ (Wo) – $Fe_2Si_20_6$ (Fs) after Morimoto (1988). (c and d) Grossular – Almandine + Andradite – Pyrope and Grossular – Pyrope – Spessartine ternary diagrams of garnets. (e) ^{C}(Al + Fe + 2Ti) vs. ^{A}(Na + K + 2Ca) classification diagram for calcic amphiboles after Hawthorne et al. (2012).

Or_{0-1}). The accessory minerals are apatite, magnetite, ilmenite, pyrrhotite. Titanite forms small inclusions in the garnet. A representative sample, DE505B, was used for conventional thermobarometry.

Amphibolite is a medium to coarse-grained rock composed of subhedral to euhedral amphibole (65–49%) classified as pargasite; (Fig. 5e; ^{T}Al 1.27–1.93, $^{A}Na+^{A}K$ 0.53–0.77 apfu) and normally zoned, partly recrystallized plagioclase (43–20%) with the composition (Fig. 5a; An_{43-65} Ab_{33-56} Or_{0-1}). Minor biotite (6%) (Fig. 5f; X_{Fe} 0.37–0.38, ^{IV}Al 2.50–2.53 apfu) mainly occurs intergrown in the amphibole aggregates. Rare garnet (Fig. 5c, d; Alm_{46-56} Prp_{15-30} Grs_{13-28} Sps_{1-6} $Andr_{0-6}$) is equant (Fig. 4b), poikiloblastic and partially resorbed by symplectite composed of diopside ($X_{Fe} = 0.25$–0.28, Al 0.00–0.03 apfu; Fig. 5b) and plagioclase (An_{29-30} Ab_{69-70} Or_{0-1}). Minor amounts of secondary epidote (Fe^{3+} 0.73–0.77 apfu), calcite, chlorite, quartz (2%) and accessory magnetite, ilmenite and apatite are present. Locally present foliation is defined by compositional variations and/or the preferred orientation of amphibole. Sample DE501 was used for thermobarometry.

Medium-grained, two-pyroxene granulite is locally interlayered by thin beds and lenses of amphibole-rich granulite and amphibolite (Fig. 4c). Two-pyroxene, medium-grained granulite (Fig. 4d) consists of relatively homogeneous euhedral to subhedral orthopyroxene (28–54%) (Fig. 5b; $X_{Fe} = 0.34$–0.45, Al 0.03–0.09 apfu), subhedral normally zoned plagioclase (20–35%) (An_{28-64} Ab_{36-72} Or_{0-3}), clinopyroxene (5–10%) of a diopside–augite composition (Fig. 5b; $X_{Fe} = 0.33$–0.40, Al 0.10–0.13 apfu) often overgrown by younger amphibole (0–10%), quartz (4–14%) ± scapolite (0–17%) ± subhedral, perthitic or mesoperthitic K-feldspar (0–12%) (Or_{95-97} Ab_{3-5}) ± biotite (0–7%) ± garnet (0–3%, all in vol. %) and accessory magnetite, ilmenite and apatite. The foliation is defined by the alternation of layers with a variable content of mafic minerals (Fig. 4c). Subhedral to anhedral amphibole is subordinate (Fig. 5e; magnesio-hornblende, potassic-pargasite and pargasite; ^{T}Al 1.50–1.86, $^{A}Na+^{A}K$ 0.41–0.67 apfu), subhedral biotite (Fig. 5f; X_{Fe} 0.30–0.47, ^{IV}Al 2.38–2.52 apfu) and anhedral quartz. Small subhedral to euhedral, equant garnet I (Fig. 4d) is a rare constituent of some granulites (Fig. 5c, d; Alm_{50-52} Prp_{21-24} Grs_{14-18} Sps_{6-7} $Andr_{2-5}$). Lenses of plagioclase-rich leucosomes with euhedral peritectic garnet II (Fig. 5c, d; Alm_{53-58} Prp_{21-28} Grs_{10-18} Sps_{1-4} $Andr_{2-6}$), plagioclase and quartz, which are up to several cm thick, are locally present. Garnet porphyroblasts (Fig. 4e) are up to 1 cm in size and contain inclusions of quartz, plagioclase (An_{32-33} Ab_{67-68}), K-feldspar, apatite, magnesio-hornblende (^{T}Al 1.58–1.59, $^{A}Na+^{A}K$ 0.35–0.38 apfu) and rare orthopyroxene. Scapolite (Me_{66-76}, Cl 0.00–0.10 apfu, S 0.17–0.50 apfu) is often present as subhedral grains associated with anhedral calcite up to 1 mm. Pyroxenes are sometimes rimmed by amphibole and/or biotite-plagioclase symplectites. Biotite is partially replaced by calcite and chlorite. The accessory minerals are apatite, zircon, magnetite, ilmenite, rutile titanite, pyrrhotite, chalcopyrite and fluorite. The representative sample E12 was used for geochronology (Tab. 1) and pseudosection modelling. Samples E6C, E6D, E10, E11, E12 were used for thermobarometry.

4.2. *Granite plutons and other intrusives*

The plutonic rocks occur as discrete bodies of ultramafic rocks, gabbros, diorites, syn-, late- tectonic granites accompanied with leucogranite, aplite and pegmatite dikes. The high-grade metamorphic complex is intruded by *syn*-D_3 foliated biotite granites. The medium- to coarse-grained often porphyroclastic metagranites (Fig. 4f) consist of anhedral quartz (41–46%), subhedral plagioclase (29–32%), anhedral to subhedral 1–2 cm long K-feldspar (20–25%) and biotite (7–12%), with subordinate quantities of zircon, apatite, monazite and ilmenite. Biotite flakes (Fig. 5f; X_{Fe} 0.53–0.55, ^{IV}Al 2.31–2.40 apfu) are slightly warped around some porphyroclasts or form symplectite with quartz. Plagioclase (An_{25-26} Ab_{73-74} Or_1) and K-feldspar (Ab_{7-9} Or_{93-91}) are altered to fine-grained white mica by hydrothermal alteration. Ilmenite is partially replaced by titanite. Medium-grained, foliated biotite syenite is composed of perthitic alkali feldspar (49%), plagioclase (27%), and quartz (19%), with minor biotite (5%). The medium-grained, muscovite-biotite and muscovite-garnet leucogranites consist of anhedral quartz (42–45%), K-feldspar (39–41%), plagioclase (25–30%), biotite (1–5%), muscovite (0–4%) and/or garnet (0–3%). Their accessory minerals include zircon, apatite, monazite and ilmenite. Perthitic K-feldspar (Ab_{4-6} Or_{94-96}) occurs as subhedral to anhedral grains or phenocrysts ranging from 0.01 mm to 15 mm. Plagioclase (An_{7-9} Ab_{81-91} Or_1) occurs commonly as subhedral crystals. Biotite (Fig. 5f; X_{Fe} 0.53–0.56, ^{IV}Al 2.11–2.27 apfu) and muscovite form small flakes. The representative samples DE475, DE474B and DE486, showing different relations to the deformation structures of rocks were used for U–Pb dating (Tab. 1). The representative chemical composition of minerals analysed are shown in ESM Table 1.

5. Estimation of P-T conditions

The equilibration P-T conditions were estimated using pseudosection modelling and conventional thermobarometry. The detailed methodological approach, including the sensitivity of water content and oxygen fugacity on the pseudosection modelling results and representative mineral analyses, is given in the Electronic Supplementary Material (ESM; Table 1). The granulite sample E12 (for location see Fig. 2a) was used for pseudosection modelling and conventional thermobarometry. The samples used for conventional thermobarometry only are DE505B, E6C, E6D, E10, E11, E12; Table 1; Fig. 2a).

5.1. *Results of pseudosection modelling*

The granulite sample E12 contains plagioclase (Table 2), quartz, orthopyroxene (X_{Mg} = 0.57–0.59), clinopyroxene (X_{Mg} = 0.70–0.71), garnet (X_{Ca} = 0.19–0.20, X_{Mn} = 0.06–0.07, X_{Mg} = 0.30–0.31 and Fe^{3+}=0.04–0.05), K-feldspar (Table 2), ilmenite and retrograde biotite (Table 2) and amphibole (Table 2). K-feldspar probably occurs as a product of granulite melting. In a pseudosection, such an assemblage corresponds to a large field Liq-Grt-Opx-Ilm-Qz-Pl-Cpx above 800 °C and 0.6–1.0 GPa, above the stability of biotite and amphibole (dotted field in Fig. 6a).

Garnet compositional isopleths of Ca, Mn, X_{Mg} and Fe^{3+} intersect at the high-temperature part of the Opx + Grt field, around 950 °C and 0.8–0.9 GPa (Fig. 6b-e). At different oxygen fugacities, garnet isopleths do not intersect (for a discussion on the sensitivity of modelling results see the ESM; Table 1). The measured composition of clinopyroxene (X_{Mg} = 0.70–0.71) is not reproduced by the pseudosection modelling (X_{Mg} < 0.67 in the Grt + Opx stability fields) and similarly the orthopyroxene composition (X_{Mg} = 0.57–0.59) is also not reproduced (X_{Mg} < 0.67 in the g + opx stability fields). Because of this bias and the sensitivity to the Fe^{3+} content and partly also to the water content (which in this case generally increases the peak temperature estimate for the given composition of phases - for details see ESM; Table 1), further consideration was given to P-T conditions based on mineral assemblage rather than the composition of phases. Thus, the most probable P-T estimate can be considered by the principal assemblage Liq + Cpx + Opx + Grt above the stability fields of biotite and amphibole at a pressure of 0.6–1.0 GPa and a temperature of > 800 °C. Since amphibole and biotite represent disequilibrium retrograde phases in this sample, their composition cannot be compared with the equilibrium P-T modelling.

5.2. *Results of conventional thermobarometry*

Three different types of geothermometers and two geobarometers were applied for the mineral assemblage of the metamorphic rocks under study (Table 2): (1) The temperature (T) and pressure (P) of formation of the garnet porphyroblast and garnet-rich symplectite (coronas surrounding garnet porphyroblast) were estimated using a garnet–clinopyroxene geothermometer (Ravna, 2000a) and a

Table 1
Location and brief petrological description of geochemical and petrological samples (secondary minerals in parentheses and accessory minerals in italics). The abbreviations of mineral names are after Whitney and Evans (2010).

Name	Lon	Lat	Rock name	Pet.	Min.	Dat.	Mineral composition
DE501	E36.77592°	N5.94079°	amphibolite	x	x		Pl, Amp, Bt, Grt, Cpx, Qz, *Ilm, Ap, Zrn*
DE505	E36.72850°	N5.54416°	migmatite	x		x	Kfs, Qz, Pl, Bt, Cpx, Amp, *Ap, Ttn*
DE505B	E36.72850°	N5.54416°	calc-silicate rock	x	x		Grt, Pl, Qtz, Cpx, *Ap, Ilm, Ttn, Mag*
E6C	E37.36452°	N5.38853°	Opx granulite	x	x		Cpx, Opx, Pl, Qz, Amp, (Scp, Chl), *Ilm, Ap, Mag, Py, Ccp*
E6D	E37.36452°	N5.38853°	granulite	x	x		Cpx, Opx, Pl, Grt, Qz, Amp, Bt, (Scp), *Ilm, Ap, Mag, Ccp*
E10	E37.36533°	N5.38993°	granulite	x	x		Cpx, Opx, Pl, Grt, Qz, Amp, Scp, Bt, Ms, (Cal, Mgz), *Ilm, Ap, Mgs*
E11	E37.37398°	N5.39647°	Opx granulite	x	x		Opx, Amp, Pl, Scp, Qz, (Chl), *Py, Ilm, Ap, Mag*
E12	E37.36711°	N5.39147°	granulite	x	x	x	Cpx, Opx, Pl, Amp, Grt, Qz, (Scp, Kfs), *Ilm, Ap, Mgs*
DE474B	E37.24861°	N5.37724°	syenite	x		x	Qz, Pl, Kfs, Bt, *Zr, Ap*
DE475	E37.24580°	N5.38937°	granite	x	x	x	Qz, Pl, Kfs, Bt, (Czo), *Zr, Ap, Ttn, Ilm*
DE486	E37.14979°	N5.39948°	granite	x	x	x	Qz, Pl, Kfs, Bt, Ms, (Chl), *Zr, Ap*

pyroxene–plagioclase–quartz geobarometer (Eckert et al., 1991). (2) Temperatures for the formation of the peritectic garnet samples were calculated using the garnet-hornblende geothermometer (Ravna, 2000b). The P-T conditions of the retrograde metamorphic stage were estimated using calcic amphibole-plagioclase (Holland and Blundy, 1994) and an amphibole-plagioclase geobarometer (Molina et al., 2015).

The P-T conditions for the formation of garnets in the granulite (garnets I and II) and calc-silicate rocks (Table 2) were also determined using the average PT method of the computer program THERMOCALC 3.3 (Powell et al., 1998). The mineral activities of end member phases from selected electron microprobe analyses were calculated with the computer program AX2 (Powell and Holland, 1994). The P–T conditions estimated from the plagioclase and pyroxene inclusions in the garnet porphyroblast from calc-silicate rock (sample DE505B) yielded ~0.80 GPa and ~863 °C. Conventional thermobarometry for symplectites surrounding the garnet porphyroblast in the calc-silicate rock (sample DE505B) provided P-T estimates at upper amphibolite facies conditions (0.50–0.69 GPa and 719–771 °C).

The average P-T method by THERMOCALC from the garnet granulite (sample E12) yielded ca. 0.89 GPa and ~865 °C (Fig. 4c, Table 2). These agree with the P-T estimates from calc-silicate and broadly overlap with P-T conditions for the peak metamorphic assemblage calculated with pseudosection modelling. In the granulite, the younger peritectic garnet poikiloblasts in the melt crosscutting S_2 foliation (Fig. 4c) grew in the presence of amphibole, plagioclase, biotite and orthopyroxene probably as products of the simplified garnet forming reaction: Liq/H_2O + Cpx + Opx + Pl = Grt + Amp + Qtz (similar textures have been described by Barink, 1984; Pattison, 2003). The results of conventional garnet-hornblende thermometry (Ravna, 2000b) are comparable with the average P-T method of the computer program THERMOCALC (Table 2; Powell and Holland, 1994). For the granulite samples, E10 and E6D, garnet, amphibole, orthopyroxene, biotite, plagioclase, quartz, ilmenite and magnetite are considered as the mineral assemblage of the formation of peritectic garnet at the P-T conditions ca. 0.87–0.95 GPa and ~708–847 °C (Table 2). The thermobarometric calculation with the amphibole-plagioclase pair from granulite samples and amphibolite (Table 2), using the calibrations of Holland and Powell (1998) and Molina et al., (2015) produces consistently higher pressures (0.73–1.01 GPa) and similar temperatures (713–801 °C) as symplectites from calc-silicate rocks. The P-T conditions of crystallization (P = 0.15–0.19 GPa and T = ~706–713 °C) for the leucogranite sample (DE498B) were calculated using the Ti-in-biotite geothermometer (Henry et al., 2005) and alumina in biotite barometry (Uchida et al., 2007). The summary of average P-T calculations and the result of conventional thermobarometry from the metamorphic rocks and leucogranite is shown on Fig. 7.

6. U–Pb dating

In order to assess the timing of the geodynamic evolution and granite emplacement in the Hammar Domain with its broad implications for the wider region of the southern ANS and northern MB, the high-grade granulites, migmatites and three syn- to post-tectonic granitoids were dated using the U–Pb laser ablation ICP-MS technique method on zircons (for sample location see Fig. 2a). Representative cathodoluminescence images of analysed zircons are shown on Fig. 8. Dating methods and a full set of analytical results with corresponding ages are provided in the Electronic Supplementary Material (ESM; Table 2). During the data reduction, each signal was individually monitored and carefully evaluated, using only the flat signal parts and avoiding inclusions. Analyses that showed signs of mixing were discarded. In addition, to better refine individual events, a relatively strict criterion of discordance was chosen that is > 1%. But all discordant data that were not used for age calculation are presented in the ESM; Table 2 and Fig. 9. All the uncertainties of the individual analyses discussed below are reported at the 2σ level. Concordia age plots are displayed with the mean squared weighted deviation (MSWD) and the probability of concordance.

6.1. Granulite (sample DE470B)

The zircon population of the granulite (sample DE470B; Fig. 2a) contains clear or, rarely, pale brown, mostly euhedral, both short- and long-prismatic or oval grains, 120–300 μm long. The internal zircon structures studied in the cathodoluminescence images (CL) exhibit a prevailing polygonal sector and curvilinear zoning with homogenously zoned bands that are preserved in nearly all the imaged grains together with infrequent small relic corroded and zoned cores (Fig. 8a). These zircon textures are typical for granulites being indicative of slow growth under water-saturated subsolidus conditions (Hanchar and Miller, 1993) or during intense melting above solidus during high-grade metamorphic conditions (Rubatto, 2002; Corfu et al., 2003). Besides, CL-brighter featureless rims up to 30 μm wide are present in all metamorphic zircons, which can be attributed to Pb loss due to metamorphic overprint. The Th/U ratios are in a relatively wide range of from ca. 0.05 to 1.8 with an average of 0.8 (see ESM; Table 2). While the lower Th/U limit (< 0.1) could be an indication of metamorphic origin, metamorphic zircons with higher Th/U can also be expected in high-grade rocks, especially in the absence or scarcity of Th-rich mineral phases (Rubatto, 2002) as is the case in the studied granulites. Dating yielded ages of zircons (12% of analyses were filtered above the 1% threshold) scattered between ca. 672 Ma and 758 Ma (ESM Table 2; Fig. 9a). The oldest detected ages are exclusively connected to core analyses located in polygonal zoned grains typical for a magmatic origin (Corfu et al., 2003) giving a weighted mean age of ca. 752 Ma (6 analyses, ESM; Table 2; Fig. 9a). The rest of zircon analyses (40 analyses; ESM Table 2; Fig. 9a) provide a weighted mean of ca. 715 Ma.

6.2. Migmatite (sample DE505)

The zircon populations from the migmatite (sample DE505) mainly

Table 2
Mineralogy and PT crystallization and metamorphic conditions for selected rocks in the Hammar Domain (minerals used for P-T calculations in THERMOCALC are in italics): GPP = garnet-pyroxene-plagioclase-quartz geobarometer (Eckert et al., 1991), GCPX = garnet-clinopyroxene geothermometer (Ravna, 2000a), GH = garnet-hornblende geothermometer (Ravna, 2000b), PHP = hornblende-plagioclase geobarometer (Molina et al., 2015), THP = hornblende-plagioclase geothermometer (Holland and Powell, 1998), TBT = biotite geothermometry (Henry et al., 2005), PBT = biotite geobarometer Uchida et al. (2007).

Sample no.	Lithology	Minerals in P-T calculation	Opx (X_{Fe})	Cpx (X_{Fe})	Biotite (X_{Fe})	Amphibile (Si)	Plagioclase (An)	K-feldspar (Or)	Garnet (Alm)	T(°C)	P (GPa)	Method
DE505B	Calc-silicate rock	*Pl* + *Cpx* + *Grt* + *Qz* + Ilm + Mag	–	0.63–0.72	–	–	49–75	92–94	5–8	727**, sd = 197 719–771** (863*)	0.60**, sd = 0.24 0.50–0.69** (0.81*)	THERMOCALC, corr = 0.879, sigfit = 1.31 GPP + GCPX
E12	Granulite	*Opx* + Pl + Amp + *Grt* + Bt + Qz + Ilm + *Mag*	0.42–0.44	0.33–0.34	0.33–0.47	6.27–6.30	51–53	87–91	51–52	865, sd = 183 761–777	0.89, sd = 0.13 0.90–1.01	THERMOCALC, corr = 0.569, sigfit = 1.09 THP + PHP
E10	Granulite	*Opx* + *Pl* + *Amp* + *Bt* + *Grt* + *Qz* + *Ilm* + *Mag*	0.45	–	0.43–0.45	6.33–6.48	46–47	–	53–58	847, sd = 66 861–874 713–778	0.95, sd = 0.13 0.83–0.90	THERMOCALC, corr = 0.529, sigfit = 1.33 GH THP + PHP
E6D	Granulite	*Opx* + *Pl* + *Amp* + *Bt* + *Grt* + *Qz* + *Mag*	0.43–0.44	0.38	0.30–0.33	6.12–6.29	42–64	–	54–58	708, sd = 60 712–808 654–779	0.87, sd = 0.14 0.83–0.97	THERMOCALC, corr = 0.648, sigfit = 1.16 GH THP + PHP
E6C	Granulite	Pl + Amp + Qz	0.43–0.44	–	–	6.34–6.39	47–49	–	–	765–798	0.79–0.90	THP + PHP
E11	Granulite	Pl + Amp + Qz	0.33–0.34	–	–	6.37–6.50	28–48	–	–	770–801	0.73–0.89	THP + PHP
DE501	Amphibolite	Pl + Amp + Qz	–	0.25–0.28	0.37–0.38	6.06–6.72	43–65	–	46–56	727–868**	0.84–1.11**	THP + PHP
DE498B	Leucogranite	Bt + Kfs + Qtz + Mag	–	–	0.53–0.56	–	7–9	94–96	–	706–713	0.15–0.19	TBT + PBT

*garnet core
**symplectite surrounding garnet porphyroblasts

consist of clear prismatic or stubby grains or their fragments with a length of 120–350 μm. In CL, most of the grains are euhedral to subhedral and represent complex growth zoning with frequent resorption, weakly zoned or unzoned cores, and polygonal oscillatory zoning (Fig. 8b). The Th/U ratios of zircon grains (ESM; Table 2) vary between 0.1 and 3.1, regardless of the parts of the grain analysed. The Th/U ratio is commonly influenced by the amount of monazite in the system which also depends on LREE concentration and degree of migmatization. When monazite become consumed during anatexis, the zircon in equilibrium with the melt would have relatively higher Th/U ratio unless there is an additional sink for Th (Yakymchuk et al., 2018).

U–Pb dating of the zircons (25% of analyses were filtered above the 1% threshold) yielded a relatively wide spread of variously metamorphosed zircon ages between ca. 785 to 620 Ma with two age-scatters presumably reflecting different geodynamic episodes. The older U–Pb zircon ages vary from ca. 785 to 702 Ma have been detected in the homogeneous, euhedral, mostly weakly oscillatory zoned or unzoned cores as well as in polygonal oscillatory zoned rims bearing evidence of resorption (Fig. 8b). From the statistical point of view in the older age scatter is possible to distinguish two age peaks having a weighted mean of ca. 720 Ma and 770 Ma (Fig. 8b; ESM; table 2). The younger age-scatter between ca. 632 Ma to 618 Ma (ESM Table 2; Fig. 9b) is found exclusively in the homogeneous rims of the zircon grains (Fig. 8b) commonly separated from the cores by irregular interfaces yielding a single concordant age of ca. 623 ± 6 Ma (MSWD = 2.1; probability 0.14; Fig. 9b).

6.3. *Syn-tectonic (D_3) granite (sample DE475)*

The zircons from the *syn*-tectonic granite (sample DE475) are predominantly clear and generally reveal prismatic or stubby shapes or fragments with a length of 200–500 μm. Internal structures in CL display symmetrical, but also irregular concentric zoning locally overprinted by zones of new growth. In most grains, there is a well-preserved, thin bright rim up to 30 μm that reflects similar ages as both oscillatory zoned rims and cores (Fig. 8c). The studied grains have Th/U ratios of 0.5–1.6 (average 0.5, ESM; Table 2). The U–Pb zircon dating of sample DE475 (25% of samples were filtered above the 1% threshold) yielded wider scatter ages between ca. 630 Ma and 690 Ma (ESM; Table 2) that constitute a weighted mean of 647 ± 6 Ma (MSWD = 3.8; 48 analyses; Fig. 9c), interpreted as the age of magma crystallization.

6.4. *Syn-tectonic (D_4) syenite (sample DE474B)*

The zircons from the syenite DE474B are mainly clear or pale brown, euhedral to subhedral grains. Most of them are 400 to 900 μm long. In CL images (Fig. 8e), most zircons have oscillatory zoning with darker homogeneous or faintly zoned cores. This corresponds to a relatively uniform Th/U ratio (range 0.2–0.7 with average 0.5, ESM; Table 2) typical of magmatic zircons (Hoskin and Schaltegger, 2003 and references therein). Both cores and rims yielded a single concordant age of 630 ± 4 Ma (MSWD = 1.0, probability = 0.29, 59 analyses; Fig. 9d) where none of samples were filtered above the 1% threshold. The age of 630 ± 4 Ma is interpreted as the age of magma crystallization.

6.5. *Syn- to post-tectonic (D_4) leucogranite dike (sample DE486)*

The majority of zircons from granite dike DE486 are pale brown or clear, euhedral, both short- and long-prismatic, mostly 150 to 350 μm long. These zircons show patchy or weakly zoned cores bearing evidence of mostly local resorption, which were systematically overgrown by narrow rims having fine oscillatory zoning (Fig. 8d). The zircons have Th/U ratios of 0.1–1.9 (ESM; Table 2). Analyses of 26 grains yielded two distinct age clusters. The dating of zircon cores (16 analyses) yielded a single concordant age of 763 ± 7 Ma (MSWD = 2.2; probability 0.13; Fig. 9e) likely suggesting that the zircon xenocrysts in the migmatites

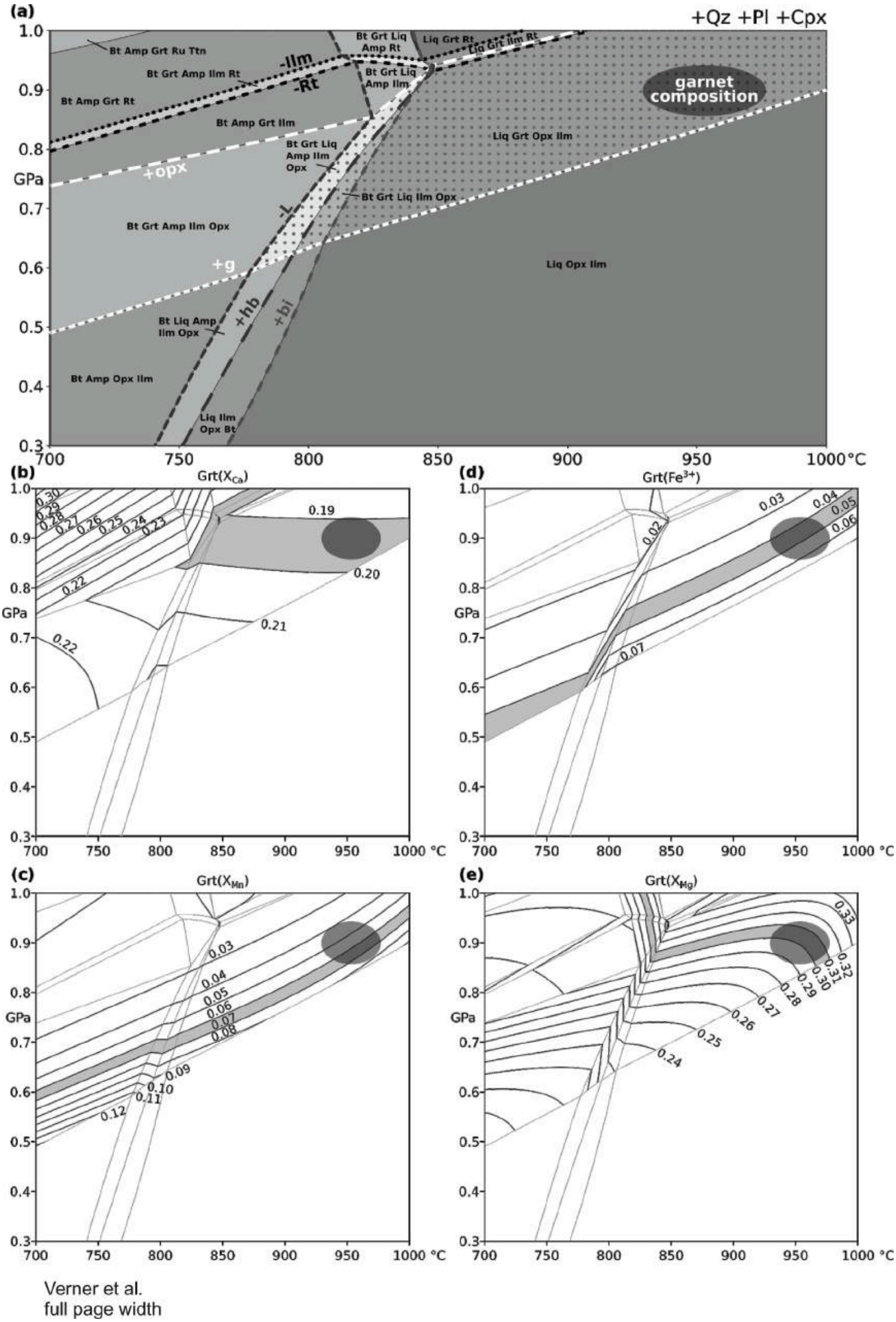

Fig. 6. (a) The P-T pseudosection calculated in THERMOCALC 3.45 in a complete MnNCKFMASHTO system with the bulk rock composition $SiO_2 = 63.77$, $Al_2O_3 = 11.52$, $CaO = 9.36$, $MgO = 4.70$, $FeO = 6.65$, $K_2O = 0.31$, $Na_2O = 2.91$, $TiO_2 = 0.59$, $MnO = 0.20$, $H_2O = 0.72$, $O = 0.1$. Dotted field corresponds to the mineral assemblage observed in the sample. (b)-(e) The garnet compositional isopleths, shaded fields correspond to the measured garnet composition.

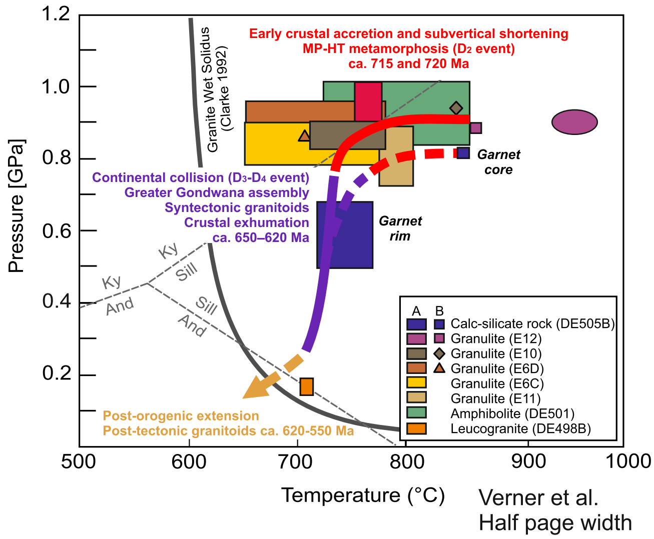

Fig. 7. The summary of average P-T calculations by THERMOCALC v 3.3 (Powell et al.. 1998) and the result of conventional thermobarometry from the metamorphic rocks and leucogranite. Alumino-silicate stability fields after Powell and Holland (1990). P-T trajectory from early granulite (full arrow) and calc-silicate rocks (dashed arrow) parageneses to the P-T conditions for the crystallization of leucogranite: (a) P-T results of conventional thermobarometry of the conditions from peak and/or retrograde mineral assemblages selected metamorphic rocks as well as the P-T conditions for the crystallization of leucogranite. The purple ellipse indicates peak metamorphic conditions for the granulite sample E12 estimated from the P-T pseudosection (Fig. 6); (b) Coloured symbols represent the results of P-T conditions from garnet rims obtained with THERMOCALC v 3.3. Detailed results as well as the mineral assemblage used for average P-T calculations are in Table 2.

correspond to an igneous or volcano-sedimentary rock assemblage protolith (compared with the oldest age cluster found in migmatites; DE505; Fig. 8b). A gentle peak in the age spectra has been exclusively detected in the oscillatory zoned rims (6 analyses) yielding a single concordant age of 630 ± 6 Ma (MSWD = 4.6; probability 0.03; Fig. 9d) which is interpreted as the crystallization age. In the case of sample DE486 44% of zircons were filtered above the 1% threshold.

7. Discussion

Considerations of field structural analysis, P-T modelling and U–Pb zircon laser ablation ICP-MS dating results from high-grade rocks and syn- to post-tectonic granite and syenite intrusions from the Hammar Domain as a representative part of the Southern Ethiopian Shield (SES) are given below. These data bring a broad implication for the time-scale and overall geodynamic scenario of the deeper parts of the EAO (e.g. Ayalew et al., 1990; Yibas et al., 2002; Woldemichael et al., 2010; Johnson et al., 2011; Stern et al., 2012; Fritz et al., 2013; Bowden et al., 2020 and references therein).

The structural evolution of the Hammar Domain can be summarized by several successive deformation phases (D_1 to D_4): (a) Regional flat-lying compositional banding (S_2) identified in migmatites and granulites including abundant isoclinal to rootless folds as the relics of early S_1 foliation. The original flat-lying S_2 migmatite banding is interpreted as being the result of subvertical shortening presumably due to orogenic collapse (e.g. Vanderhaeghe and Teyssier, 2001) or gravity-driven horizontal flow at the early stages of collisional processes (e.g. Cagnard et al., 2006). (b) Superimposed steeply dipping ~N–S and ~NW–SE trending foliations (S_3 and S_4, respectively) and a similar fabric pattern in the *syn*-tectonic intrusives. These structures have a compressional (transpressional) pattern as the result of regional ~E–W shortening typical for the entire EAO, especially at the latter stages of the East African Orogeny (e.g. Stern et al., 2012; Fritz et al., 2013).

The peak P-T conditions of regional HT-MP metamorphism in granulite (T: ~700–850 °C and P: ~0.7–1.0 GPa; Fig. 7) have been constrained using the stable mineral assemblage Liq + Amp + Opx + Grt clearly defining flat-lying S_2 foliation in granulites. Similar P-T conditions were also obtained from host amphibolites and migmatites. These P-T data well correspond to the mid-crustal re-equilibration (at a depth of ~25–35 km) on the geotherm ~30 °C/km. During this peak metamorphic event, the high-grade rocks underwent intensive melting (migmatization) as typical for incubated large collisional orogens (e.g. Cagnard et al., 2006; Beaumont et al., 2010) or continental-like crust in lower segments of island arcs (e.g. Garrido et al., 2006). Superimposed metamorphic conditions (T: ~700–800 °C and a P: ~0.5–0.7 GPa; Fig. 7) recording a near isothermal decompression P-T path estimated from the symplectites around the garnet in calc-silicate rocks and the cross-cutting melt in the granulites have no direct link to the regional fabric

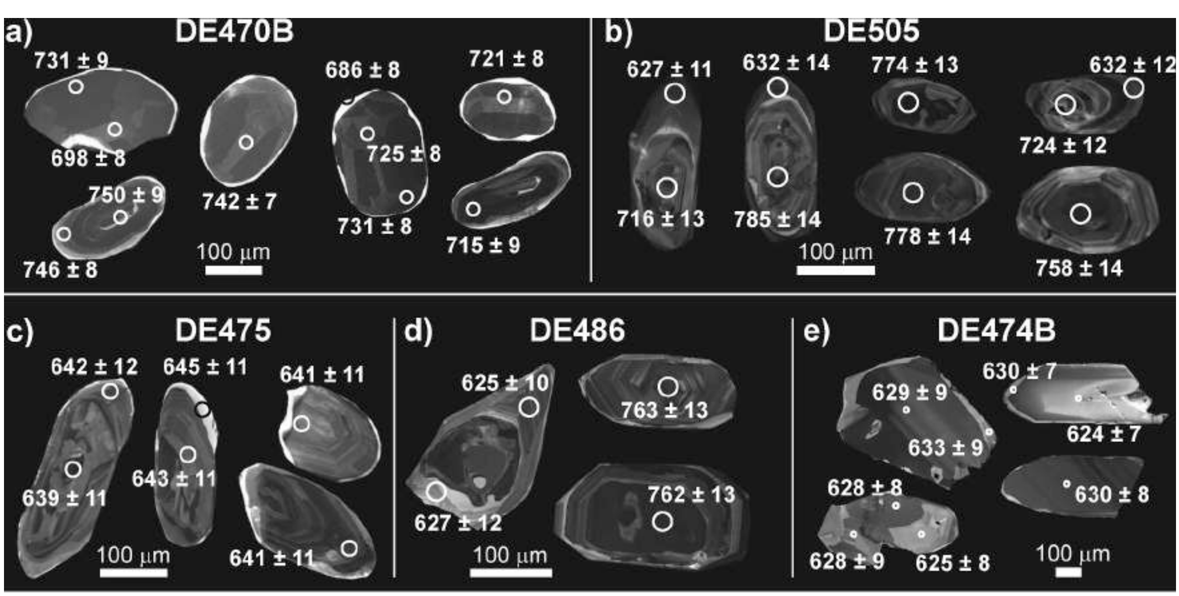

Fig. 8. Representative cathodoluminescence images of the typical detrital zircons from the Hammar Domain: (a) granulite (DE470B), (b) migmatite (DE505), (c) D_3 *syn*-tectonic granite (DE475), (d) D_4 *syn- to post*-tectonic leucogranite dike (DE486) and (e) D_4 *syn*-tectonic syenite (DE474B). Laser-ablation ICP-MS analysis spots (25 µm) marked with concordant $^{206}Pb/^{238}U$ ages ± 2σ uncertainties.

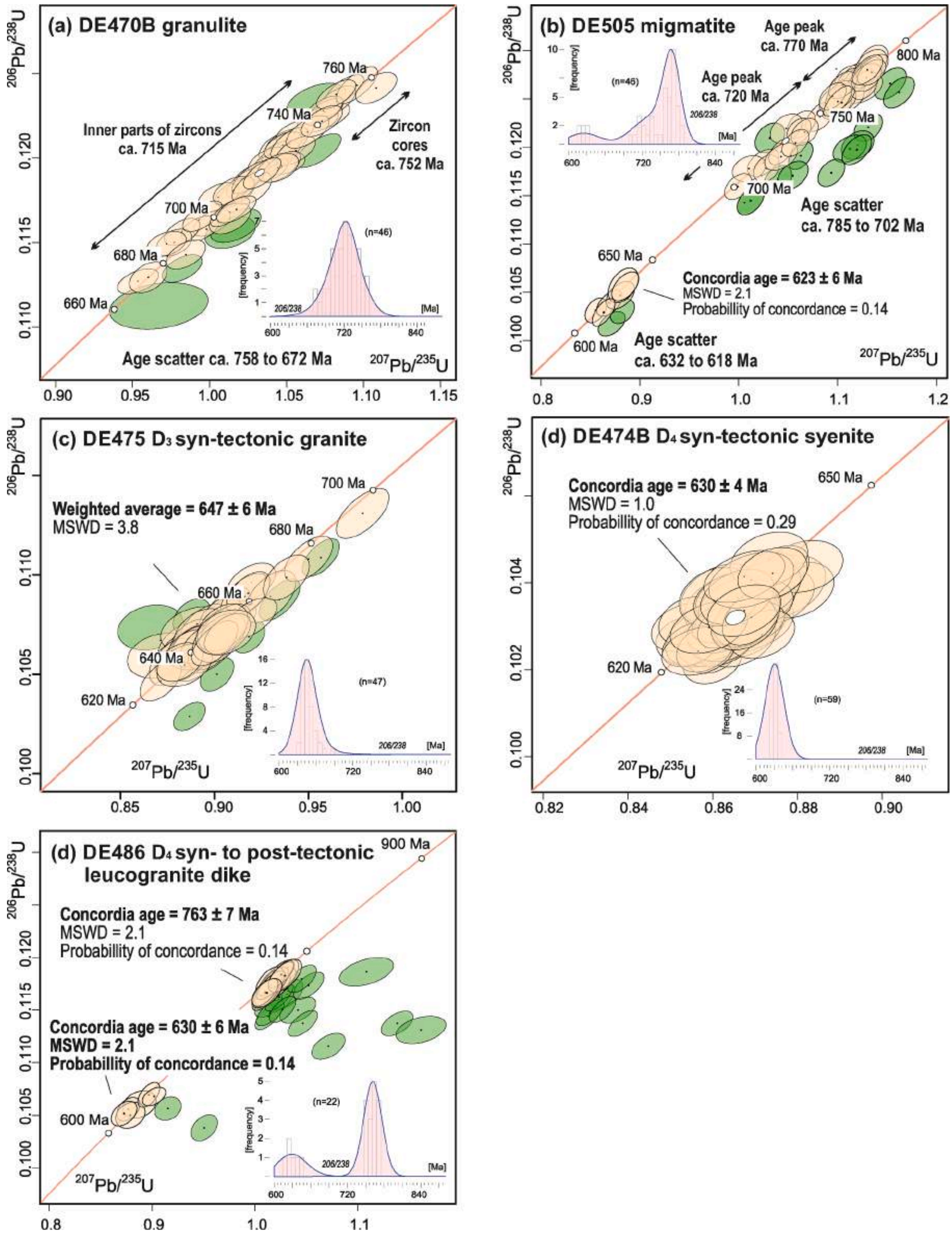

Fig. 9. Concordia $^{206}Pb/^{238}U$ vs $^{207}Pb/^{235}U$ age plot or the weighted mean age $^{206}Pb/^{238}U$ of laser ablation ICP-MS U–Pb analyses of studied zircons. Individual samples represent: (a) granulite (DE470B), (b) migmatite (DE505), (c) D_3 *syn*-tectonic granite (DE475), (d) D_4 *syn*-tectonic syenite (DE474B) and (e) D_4 *syn- to post*-tectonic leucogranite dike (DE486). Green ellipses represent discordant data that were not used for age calculations.

pattern. These P-T conditions correspond to depths of ~27 to 16 km similar to the prevailing rocks of the entire WES and SES (e.g. Tsige, 2006; Yihunie et al., 2004; Ayalew and Johnson, 2002). The lower pressure limit of the decompression P-T path is given by the crystallization conditions of the post-tectonic leucogranite dike, estimated at P ~0.2 GPa (Fig. 7). Such an isothermal decompression path is also notable in the central part of the Mozambique Belt in Tanzania (Sommer et al., 2008) further south, which has been attributed to fast exhumation after crustal thickening (for review see Fritz et al., 2013).

The overall time-scale of the tectonometamorphic events recorded in the Hammar Domain has been constrained using U–Pb zircon dating of representative high-grade rocks (migmatites and granulites) and syn- to post-tectonic intrusives. The granulites (sample DE470B) provide the larger age-scatter, between ca. 672 Ma and 758 Ma (ESM Table 2; Fig. 9a), including a small cluster of ca. 752 Ma exclusively connected to core analyses located in polygonal zoned grains typical for a magmatic origin (Corfu et al., 2003) which can be interpreted as the age of the inherited component derived from an igneous protolith (Fig. 8a). The rest of the zircon analyses of grains bearing a polygonal sector and curvilinear zoning with homogenously zoned bands (40 analyses; ESM Table 2) provide a weighted mean of ca. 715 Ma. The textural features of the zircon grains giving a metamorphic origin, larger scatter of U–Pb data (ca. 672 to 758 Ma) and HT-MP metamorphic conditions of granulites (T: ~700–850 °C and P: ~0.7–1.0 GPa; Fig. 7) suggest a long-lasting or multiphase high-grade metamorphic event (e.g. an episode of slow zircon dissolution, resorption and recrystallization) also typical for other granulites (Kohn et al., 2015; Tedeschi et al., 2017).

In migmatites, two age scatters were detected (represented by sample DE505; Fig. 9b). The older U–Pb zircon age-scatter varies from ca. 785 to 702 Ma where it is possible to distinguish two age groups having a weighted mean age of ca. 720 Ma and 770 Ma (Fig. 8b; ESM; table 2). Due to the heterogenity in zircon textures showing magmatic origin as well as complex and sector growth zoning with evidence of resorption (e.g. Corfu et al., 2003) regardless of the age and also higher variability of Th/U ratios (from 0.1 to 3.1), the older age-scatter (ca. 785 to 702 Ma) reflects mixed age of the inherited component derived from an igneous or volcano-sedimentary protolith which has been partly modified during the HT-MP metamorphosis and extensive melting. By considering U–Pb data from granulites giving the age of HT-MP metamorphism at ca. 715 Ma, similarity in structural pattern and P-T conditions with host migmatites it can be supposed that an age peak ca. 720 Ma found in migmatites could correspond to similar geodynamic event. The relatively older age peak in migmatites (ca. 770 Ma) probably reflects the age of inherited component from a volcano-sedimentary source. The younger age-scatter, 623 ± 6 Ma, detected exclusively in the homogeneous rims of zircons from migmatite points to the subsequent metamorphic event (T: ~700–800 °C and a P: ~0.5–0.7 GPa; Fig. 7), linked with synchronous ~E–W shortening and crustal exhumation (D_3 and D_4 stage) supported by heat contribution from granite intrusions and hydrothermal fluid migration.

In addition, the cluster-like ages in migmatites and larger age spectra in granulites may reflect a different character for zircon growth and recrystallization in the wet and dry system respectively, as both migmatites and granulites show a similar P-T history and structural pattern. It is noteworthy, that the oldest U–Pb data from the high-grade rocks, which are interpreted as an inherited component derived from igneous or volcano-sedimentary protolith, do not exceed 780 Ma. It suggests that the Southern Ethiopian Shield has a juvenile origin far away from cratonic sources and might have been derived from a volcano-sedimentary intra-oceanic magmatic arc in the early stage of EAO (e.g. Fritz et al., 2013).

The single concordant age of 648 ± 6 Ma, of strongly foliated *syn*-D_3 granite (sample DE475, Fig. 9c) is interpreted as the age of magma emplacement and crystallization synchronously with the regional D_3 deformation. Similarly, the age of 630 ± 6 Ma obtained from a *syn*-D_4 syenite (sample DE474B, Fig. 9d) reveals an episode of D_4 deformation. The oldest single concordant ages of the *syn- to post*-tectonic D_4 leucogranite dike 763 ± 7 Ma (sample DE486; Fig. 9e) reflect the inherited age from an igneous or volcano-sedimentary protolith showing similarity with the oldest age cluster in the host migmatites. The younger age cluster (630 ± 6 Ma), interpreted as the age of dike emplacement and crystallization, means the upper limit for regional deformation and metamorphism in the SES.

The data set listed above allows a specification of the two prominent geodynamic events during the East African Orogeny (Fig. 10) that affected the Hammar Domain:

7.1. Late Tonian to late Cryogenian episode (ca. 770 to 650 Ma): From arc construction to early crustal accretion

The oldest U–Pb ages at ca. 770 obtained from granulites, migmatites and post-tectonic granites reflect an inherited component from a volcano-sedimentary or igneous protolith, which is also common in the wider region of the ANS (e.g. Hauzenberger et al., 2004, 2005; Hargrove et al., 2006; Avigad et al., 2007; Stern et al., 2012 and references therein). Because of the lack of older ages, the source material for these rocks was probably derived from juvenile arc-related magmatic (volcanic) activity, referred as the "Megado tectonothermal event" at ca. 770 to 700 Ma (Ayalew and Johnson, 2002; Yibas et al., 2002; Woldemichael et al., 2010). In the southern ANS, these processes continued contemporaneously with early crustal accretion at ca. 750–650 Ma (Accretion Stage I.; Fritz et al., 2013). In this context, based on the zircon textures showing growth or recrystallization during extensive melting (migmatization), regional flat-lying migmatite banding (S_2) preceding steep compressional fabrics (S_3) with a stable HT-MP granulite facies mineral assemblage giving T: ~700–850 °C and P: ~0.7–0.9 GPa it can be supposed that the older age cluster in granulites (ca. 715 Ma) and similar age scatter from migmatites (ca. 720 Ma) point to the main accretion event associated with large-scale anatexis, granulite facies metamorphism and subvertical shortening (D_2 event). It must also be admitted that the partial resetting of the U–Pb isotopic system, due to the very high temperature of regional metamorphism, could justify the relatively wide spectra of the ages documented in the granulites. Similar metamorphic conditions reaching T: ~800–850 °C and P: ~0.9 GPa were also identified in the Eastern Granulite Belt (northern Mozambique Belt) located to the south (e.g. Fritz et al., 2009; Sommer and Kröner, 2013), in the Adola-Moyale Domain (Berhe, 1988; Alene and Barker, 1993) and also from the Sagan half graben (the southernmost offshoot of the Main Ethiopian Rift). These are supposed to be formed as a result of regional thermal perturbations in the Himalayan-type collision supposed for the entire EAO (Gichile, 1992). Further to the northwest in Sudan similar granulite age of ca. 720 Ma (from Rb-Sr data of Zircon; Kröner et al., 1987) is known from high grade gneisses of Sabaloka (north of Khartoum), which were interpreted as representing an elevated thermal event. They also showed that isotopic homogenization of granulites took place by about 700 Ma (Kröner et al., 1987).

7.2. Late Cryogenian to early Ediacaran episode (ca. 650 to 620 Ma): Main continental collision and Greater Gondwana assembly

The regional ~NNW–SSE trending melt-induced to solid-state foliation (S_3) with no kinematic symmetry apparent in the L-par section are interpreted as being the result of an intense sub-horizontal ~E–W (orogen-perpendicular) shortening and synchronous elongation in the L-par direction. The superimposed D_4 event resulted in ~NW–SE trending foliation (S_4) bearing well-developed stretching lineation and left-lateral kinematic indicators that could be associated with ongoing oblique shortening (left-lateral transpression) under a minor clockwise change in the orientation of the regional stress-field. This lattermost pattern is consistent with the activity of the regional ~NW–SE trending Nyangere and Athi shear zones (Fig. 1b,c) separating the southernmost part of the ANS from the Eastern Granulite Belt (northern Mozambique Belt) (e.g. Katumwehe et al., 2016).

Given the metamorphic overprint of early S_2 fabrics, the D_3 phase may roughly correspond to the estimated decompression P-T path in the range T: ~700–800° C, P: ~0.5–0.7 GPa. The lower limit for the subsequent D_4 event is the emplacement of the syn- to post-tectonic leucogranite dike, estimated at P: ~0.2 GPa. These latter tectonometamorphic events are interpreted as the key phase in the continental collision of the EAO leading to the overall Greater

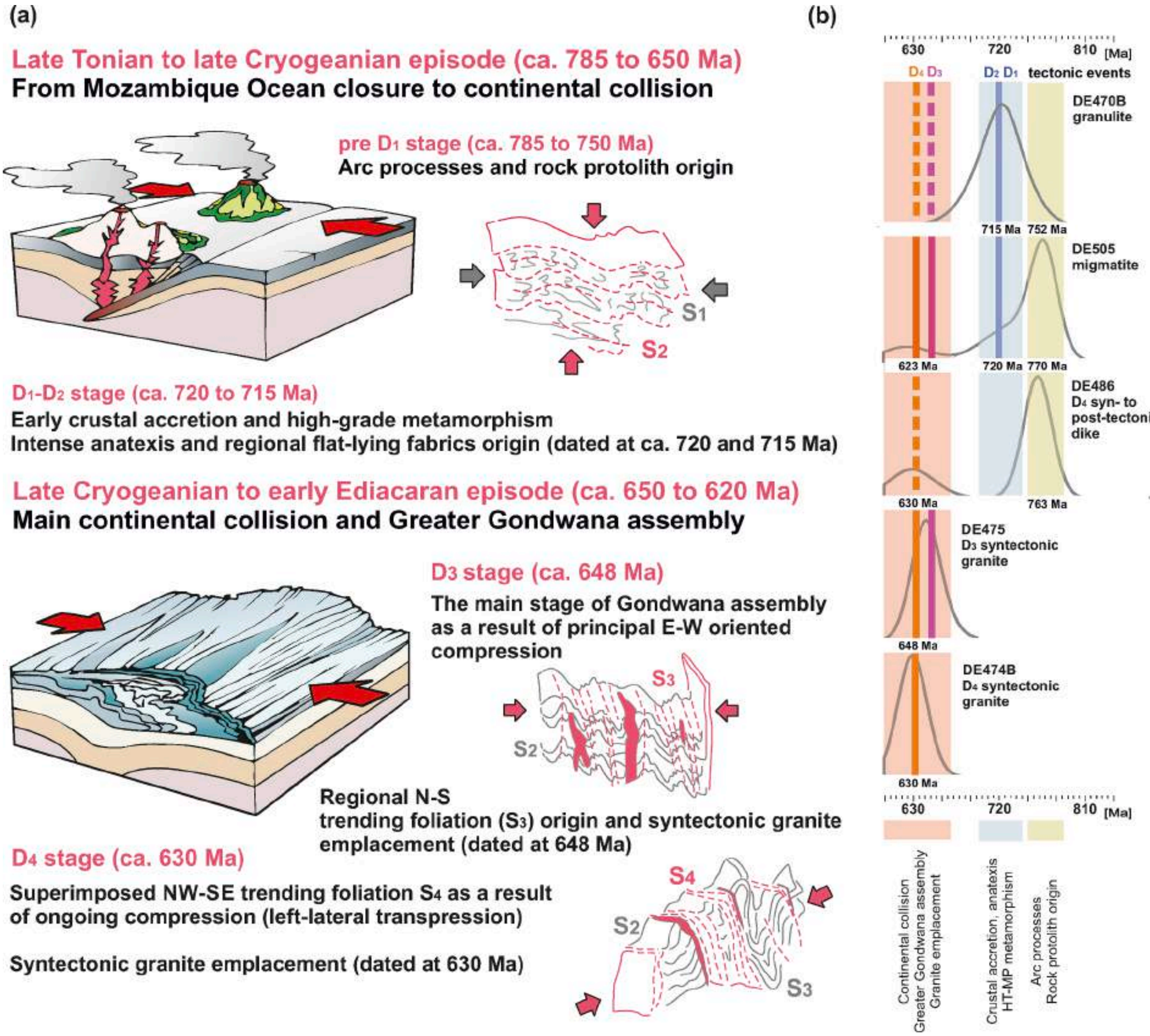

Fig. 10. Overall geodynamic scenario resulted in two main geodynamic episodes forming the Hammar Domain: (a) Interpretative blockdiagram; (b) U–Pb age histogram with main tectonic events.

Gondwana assembly on a global scale (Johnson et al., 2011; Fritz et al., 2013 and references therein).

The S_3 *syn*-tectonic granite (sample DE475, Fig. 9c) constitutes a single concordant peak of ca. 648 ± 6 Ma pointing to the main stage of the collisional processes (D_3 event). The next, slightly younger single concordant peak of ca. 630 ± 6 Ma obtained from the S_4 *syn*-tectonic syenite sheet (sample DE474B, Fig. 9d) indicates the age of the subsequent left-lateral transpression. The last increments of the regional D_4 event were disclosed by the second concordant age of ca. 630 ± 6 Ma found in the discordant, gently folded leucogranite dike (sample DE486; Fig. 9e). In this context, a similar age cluster of ca. 623 ± 6 Ma, known from the narrow zircon rims of the migmatites (sample DE505; Fig. 9b), probably reflects the main decompression event of the already juxtaposed metamorphic complex.

In the SES and WES, the main collisional events between the Eastern and Western Gondwana continents are assumed in a wider range, from ca. 750 to 550 Ma (e.g. Johnson et al., 2011; Stern et al., 2012; Fritz et al., 2013; Bowden et al., 2020). However, our new data give credence to the idea that the main Greater Gondwana assembly occurred in this part of the EAO in a relatively small time-span, between ca. 650 and 620 Ma. These processes took place in isothermal decompression mode associated with rapid exhumation, driven by intense ~E–W oriented compression (D_3 event), extravasated into left-lateral transpression (D_4 event). Inferred main collisional age closely matches the metamorphic overprint ca. 622 Ma from the Rb-Sr data of whole rock in Kenya ("Baragoian" stage in East African Orogeny; Key et al., 1989). Similarly, the peak of granulite facies metamorphism was constrained to ca. 630 to 645 Ma in the Mozambique Belt in SE Kenya (SHRIMP data metamorphic zircon rims; Hauzenberger et al., 2007). These were similar to metamorphic ages commonly found in the Mozambique Belt of central and north-eastern Tanzania (e.g. Muhongo et al., 2001; Sommer et al., 2003).

In continuity, several post-collisional granitoid plutons, dated in the range ca. 600 to 550 Ma (e.g. Yibas et al., 2002; Stern et al., 2012 and references therein), intruded the metamorphic complex in various stages of crustal uplift and post-orogenic extension.

8. Conclusions

The structural evolution of the Hammar Domain can be summarized into four phases, D_1 to D_4, resulting in (a) relict compositional banding (S_1), (b) flat-lying migmatite foliation (S_2) defining the primary contacts of granulites and migmatites, (c) superimposed steeply dipping N–S compressional foliation (S_3) due to regional ~E–W oriented compression and (d) later ~NW–SE trending left-lateral transpressive fabric (S_4). The Southern Ethiopian Shield has a juvenile origin far away from cratonic sources derived from a volcano-sedimentary intra-oceanic magmatic arc of early EAO (ca. 770 Ma).

Two principal geodynamic events forming the East-African Orogeny in the southern ANS can be defined: (a) **Late Tonian to late Cryogenian episode (~770 to 650 Ma)** where large volcanic arc construction (dated at ca. 770 Ma) was followed by crustal accretion and flat-lying fabrics origin (D_2 stage), intense migmatization and HT-MP metamorphism (T: ~700–850 °C and P: ~0.7–0.9 GPa) at depths of ~25–35 km (dated at ca. 720 and 715 Ma). (b) **Late Cryogenian to early Ediacaran episode (**ca. **650 to 620 Ma)** as the key era of continental collision leading to the Greater Gondwana assembly. An early ~E–W oriented compression (D_3 stage) resulted in ~N–S trending fabrics that have been continuously changed to the left-lateral transpression (D_4 stage) forming ~NW–SE oriented foliations. The time-scale of D_3 and D_4 events is inferred by *syn*-tectonic granitoid intrusions yielded at ca. 648 Ma and ca. 630 Ma respectively. Furthermore, the syn- to post-tectonic leucogranite dike, dated at ca. 630 Ma, marks the upper limit for the ductile or brittle-ductile deformation and regional metamorphic events.

CRediT authorship contribution statement

Kryštof Verner: Conceptualization, Data curation, Formal analysis, Funding acquisition, Investigation, Methodology, Project administration, Resources, Software, Supervision, Validation, Visualization, Writing - original draft, Writing - review & editing. **David Buriánek:** Data curation, Investigation, Methodology, Software, Validation, Visualization, Writing - original draft. **Martin Svojtka:** Data curation, Investigation, Methodology, Validation, Software, Visualization, Writing - original draft. **Vít Peřestý:** Data curation, Formal analysis, Investigation, Methodology, Software, Validation, Visualization, Writing - original draft. **Leta Megerssa:** Data curation, Formal analysis, Investigation, Methodology, Validation, Writing - original draft. **Tarekegn Tadesse:** Conceptualization, Data curation, Investigation, Methodology, Validation. **Aspiron Kussita:** Data curation, Investigation, Methodology, Validation. **Diriba Alemayehu:** Data curation, Investigation, Methodology, Validation. **Tomáš Hroch:** Data curation, Investigation, Methodology, Validation.

Declaration of Competing Interest

The authors declare that they have no known competing financial interests or personal relationships that could have appeared to influence the work reported in this paper.

Acknowledgements

The research was funded by the Czech Development Agency in the framework of development project No. 281226/2018-ČRA "Implementation of a Methodical Approach in Geological Sciences to Enhance the Quality of Doctoral Studies at the Addis Ababa University (Ethiopia)" (to K. Verner) and project No. 280614/2019-ČRA "Ensuring Sustainable Land Management in Selected Areas of Ethiopia on the Basis of Geoscientific Mapping" (to K. Verner). This study was financially supported by the Centre for Geosphere Dynamics (UNCE/SCI/006) and institutional support RVO67985831 (to M. Svojtka). The authors are also thankful for the great administrative support of the research by the Addis Ababa University and the Addis Ababa Science and Technological University as well as the Embassy of the Czech Republic in Addis Ababa.

Appendix A. Supplementary data

Supplementary data to this article can be found online at https://doi.org/10.1016/j.precamres.2021.106270.

References

Alemu, T., Abebe, T., 2007. Geology and tectonic evolution of the Pan-African Tulu Dimtu Belt, Western Ethiopia. Online Journal of Earth Sciences 1 (1), 24–42.

Alene, M., Barker, A.J., 1993. Tectonometamorphic evolution of the Moyale region, southern Ethiopia. Precambr. Res. 62 (3), 271–283.

Allen, A., Tadesse, G., 2003. Geological setting and tectonic subdivision of the Neoproterozoic orogenic belt of Tuludimtu, western Ethiopia. J. Afr. Earth Sc. 36 (4), 329–343.

Asrat, A., Barbey, P., 2003. Petrology, geochronology and Sr–Nd isotopic geochemistry of the Konso pluton, south-western Ethiopia: implications for transition from convergence to extension in the Mozambique Belt. Int. J. Earth Sci. 92 (6), 873–890.

Asrat, A., Barbey, P., Gleizes, G., 2001. The Precambrian geology of Ethiopia: a review. Africa Geoscience Review 8 (3/4), 271–288.

Avigad, D., Stern, R.J., Beyth, M., Miller, N., McWilliams, M.O., 2007. Detrital zircon U-Pb geochronology of Cryogenian diamictites and Lower Paleozoic sandstone in Ethiopia (Tigrai): age constraints on Neoproterozoic glaciation and crustal evolution of the southern Arabian-Nubian Shield. Precambr. Res. 154 (1–2), 88–106.

Ayalew, T., 1997. Metamorphic and structural evolution of the Gore-Gambella area, Western Ethiopia. SINET: Ethiopian Journal of. Science 20 (2), 235–259.

Ayalew, T., Bell, K., Moore, J.M., Parrish, R.R., 1990. U-Pb and Rb–Sr geochronology of the western Ethiopian shield. Geol. Soc. Am. Bull. 102 (9), 1309–1316.

Ayalew, T., Johnson, T.E., 2002. The geotectonic evolution of the Western Ethiopian shield. SINET: Ethiopian Journal of. Science 25 (2), 227–252.

Barink, H.W., 1984. Replacement of pyroxene by hornblende, isochemically balanced with replacement of plagioclase by garnet, in a metagabbro of upper-amphibolite grade. Lithos 17, 247–258.

Beaumont, C., Jamieson, R., Nguyen, M., 2010. Models of large, hot orogens containing a collage of reworked and accreted terranes. Can. J. Earth Sci. 47 (4), 485–515.

Berhe, S.M., 1988. The geologic and tectonic evolution of the Pan-African/Mozambique Belt in East Africa (Doctoral dissertation. The Open University).

Blades, M.L., Collins, A.S., Foden, J., Payne, J.L., Xu, X., Alemu, T., Woldetinsae, G., Clark, C., Taylor, R.J., 2015. Age and hafnium isotopic evolution of the Didesa and Kemashi Domains, western Ethiopia. Precambr. Res. 270, 267–284.

Bonavia, F.F., Chorowicz, J., 1992. Northward expulsion of the Pan-African of northeast Africa guided by a reentrant zone of the Tanzania craton. Geology 20 (11), 1023–1026.

Bowden, S., Gani, N.D., Alemu, T., O'Sullivan, P., Abebe, B., Tadesse, K., 2020. Evolution of the Western Ethiopian Shield revealed through U-Pb geochronology, petrogenesis, and geochemistry of syn-and post-tectonic intrusive rocks. Precambr. Res. 338, 105588.

Brown, M., 1973. The definition of metatexis, diatexis and migmatite. Proc. Geol. Assoc. 84, 371–382.

Cagnard, F., Durrieu, N., Gapais, D., Brun, J.P., Ehlers, C., 2006. Crustal thickening and lateral flow during compression of hot lithospheres, with particular reference to Precambrian times. Terra Nova 18, 72–78.

Collins, A.S., 2006. Madagascar and the amalgamation of Central Gondwana. Gondwana Res. 9 (1–2), 3–16.

Corfu, F., Hanchar, J.M., Hoskin, P.W., Kinny, P., 2003. Atlas of zircon textures. Rev. Mineral. Geochem. 53, 469–500.

Davidson, A., 1983. The Omo River project: reconnaissance geology and geochemistry of parts of Illubabor, Kefa, Gemu and Sidamo. Ethiopia, Bulletin Ethiopian Institute of Geological Surveys, Ministry of Mines and Energy, p. 2.

de Wit, M.J., Chewaka, S., 1981. Plate tectonic evolution of Ethiopia and the origin of its mineral deposits: an overview. In: Chewaka S, de Wit MJ (eds) Plate tectonics and metallogenesis: some guidelines to Ethiopian mineral deposits. Ethiopian Inst Geol Surv Bull 2:115–129.

Eckert, J.O., Newton, R.C., Kleppa, O.J., 1991. The ΔH of reaction and recalibration of garnet-pyroxene-plagioclase-quartz geobarometers in the CMAS system by solution calorimetry. Am. Mineral. 76 (1–2), 148–160.

Fritz, H., Abdelsalam, M., Ali, K.A., Bingen, B., Collins, A.S., Fowler, A.R., Ghebreab, W., Hauzenberger, C.A., Johnson, P.R., Kusky, T.M., Macey, P., 2013. Orogen styles in the East African Orogen: a review of the Neoproterozoic to Cambrian tectonic evolution. J. Afr. Earth Sc. 86, 65–106.

Fritz, H., Tenczer, V., Hauzenberger, C., Wallbrecher, E., Muhongo, S., 2009. Hot granulite nappes—tectonic styles and thermal evolution of the Proterozoic granulite belts in East Africa. Tectonophysics 477 (3–4), 160–173.

Garrido, C.J., Bodinier, J.L., Burg, J.P., Zeilinger, G., Hussain, S.S., Dawood, H., Chaudhry, M.N., Gervilla, F., 2006. Petrogenesis of mafic garnet granulite in the lower crust of the Kohistan paleo-arc complex (Northern Pakistan): implications for intra-crustal differentiation of island arcs and generation of continental crust. J. Petrol. 47 (10), 1873–1914.

Ghebreab, W., 1992. The geological evolution of the Adola Precambrian greenstone belt, southern Ethiopia. Journal of African Earth Sciences (and the Middle East) 14 (4), 457–469.

Gichile, S., 1992. Granulites in the Precambrian basement of southern Ethiopia: geochemistry, P-T conditions of metamorphism and tectonic setting. J. Afr. Earth Sci. 16, 251–263.

Hanchar, J.M., Miller, C.F., 1993. Zircon zonation patterns as revealed by cathodoluminescence and backscattered electron images: implications for interpretation of complex crustal histories. Chem. Geol. 110 (1–3), 1–13.

Hargrove, U.S., Stern, R.J., Kimura, J.I., Manton, W.I., Johnson, P.R., 2006. How juvenile is the Arabian-Nubian Shield? Evidence from Nd isotopes and pre-Neoproterozoic inherited zircon in the Bi'r Umq suture zone, Saudi Arabia. Earth Planet. Sci. Lett. 252, 308–326.

Hauzenberger, C.A., Bauernhofer, A., Hoinkes, G., Wallbrecher, E., Mathu, E., 2004. Pan-African high pressure granulites from SE-Kenya: petrological and geothermobarometric evidence for polyphase evolution in the Mozambique Belt. J. Afr. Earth Sc. 40, 245–268.

Hauzenberger, C.A., Robl, J., Stüwe, K., 2005. Garnet zoning in high pressure granulite-facies metapelites, Mozambique belt, SE-Kenya: constraints on the cooling history. Eur. J. Mineral. 17 (1), 43–55.

Hauzenberger, C.A., Sommer, H., Fritz, H., Bauernhofer, A., Kröner, A., Hoinkes, G., Wallbrecher, E., Thöni, M., 2007. SHRIMP U-Pb zircon and Sm–Nd garnet ages from the granulite-facies basement of SE Kenya: evidence for Neoproterozoic polycyclic assembly of the Mozambique Belt. Journal of the Geological Society 164 (1), 189–201.

Henry, D.J., Guidotti, C.V., Thomson, J.A., 2005. The Ti-saturation surface for low-to-medium pressure metapelitic biotites: Implications for geothermometry and Ti-substitution mechanisms. Am. Mineral. 90 (2–3), 316–328.

Holland, T., Blundy, J., 1994. Non-ideal interactions in calcic amphiboles and their bearing on amphibole-plagioclase thermometry. Contrib. Miner. Petrol. 116 (4), 433–447.

Holland, T.J.B., Powell, R.T.J.B., 1998. An internally consistent thermodynamic data set for phases of petrological interest. J. Metamorph. Geol. 16 (3), 309–343.

Holmes, A., 1951. The sequence of pre-Cambrian orogenic belts in south and central Africa. Proceeding of the International Geological Congress, London 18, 254–269.

Hoskin, P.W., Schaltegger, U., 2003. The composition of zircon and igneous and metamorphic petrogenesis. Rev. Mineral. Geochem. 53 (1), 27–62.

Johnson, P.R., 2014. An expanding Arabian-Nubian Shield geochronologic and isotopic dataset: defining limits and confirming the tectonic setting of a Neoproterozoic accretionary orogen. The Open Geology Journal 8 (1), 3–33.

Johnson, P.R., Andresen, A., Collins, A.S., Fowler, A.R., Fritz, H., Ghebreab, W., Kusky, T., Stern, R.J., 2011. Late Cryogenian-Ediacaran history of the Arabian-Nubian Shield: a review of depositional, plutonic, structural, and tectonic events in the closing stages of the northern East African Orogen. J. Afr. Earth Sc. 61 (3), 167–232.

Katumwehe, A.B., Abdelsalam, M.G., Atekwana, E.A., Laó-Dávila, D.A., 2016. Extent, kinematics and tectonic origin of the Precambrian Aswa Shear Zone in eastern Africa. Gondwana Res. 34, 241–253.

Kazmin, V., Shiferaw, A., Balcha, T., 1978. The Ethiopian Basement and possible manner of evolution. Geol Rundsch 67, 531–546.

Key, R.M., Charsley, T.J., Hackman, B.D., Wilkinson, A.F., Rundle, C.C., 1989. Superimposed upper Proterozoic collision-controlled orogenies in the Mozambique orogenic belt of Kenya. Precambr. Res. 44, 197–225.

Kohn, M.J., Corrie, S.L., Markley, C., 2015. The fall and rise of metamorphic zircon. Am. Mineral. 100, 897–908.

Kröner, A., Stern, R.J., Dawoud, A.S., Compston, W., Reischmann, T., 1987. The Pan-African continental margin in northeastern Africa: evidence from a geochronological study of granulites at Sabaloka. Sudan. Earth and Planetary Science Letters 85 (1–3), 91–104.

Kusky, T.M., Abdel Salam, M.G., Stern, R.J., Tucker, R.D., 2003. Evolution of the East African and related orogens, and the assembly of Gondwana. Precambr. Res. 123 (2–4), 81–85.

Kusky, T.M., Matsah, M.I., 2003. Neoproterozoic dextral faulting on the Najd fault system, Saudi Arabia, preceded sinistral faulting and escape tectonics related to closure of the Mozambique Ocean. Geological Society, London, Special Publications 206 (1), 327–361.

Molina, J.F., Moreno, J.A., Castro, A., Rodríguez, C., Fershtater, G.B., 2015. Calcic amphibole thermobarometry in metamorphic and igneous rocks: New calibrations based on plagioclase/amphibole Al -Si partitioning and amphibole/liquid Mg partitioning. Lithos 232, 286–305.

Morimoto, N., 1988. Nomenclature of pyroxenes. Mineral. Petrol. 39 (1), 55–76.

Muhongo, S., Kröner, A., Nemchin, A.A., 2001. Zircon ages from granulite facies rocks in the Mozambique Belt of Tanzania and implications for Gondwana assembly. J. Geol. 109, 171–189.

Pattison, D.R.M., 2003. Petrogenetic significance of orthopyroxene-free garnet + clinopyroxene + plagioclase ± quartz-bearing metabasites with respect to the amphibolite and granulite facies. J. Metamorph. Geol. 21, 21–34.

Powell, R., Holland, T., 1990. Calculated mineral equilibria in the pelite system, KFMASH (K 2 O-FeO-MgO-Al 2 O 3-SiO 2-H 2 O). Am. Mineral. 75 (3–4), 367–380.

Powell, R., Holland, T., 1994. Optimal geothermometry and geobarometry. Am. Mineral. 79 (1–2), 120–133.

Powell, R., Holland, T.J.B.H., Worley, B., 1998. Calculating phase diagrams involving solid solutions via non-linear equations, with examples using THERMOCALC. J. Metamorph. Geol. 16 (4), 577–588.

Ravna, E.K., 2000a. The garnet–clinopyroxene Fe2+–Mg geothermometer: an updated calibration. J. Metamorph. Geol. 18 (2), 211–219.

Ravna, E.K., 2000b. Distribution of Fe2+ and Mg between coexisting garnet and hornblende in synthetic and natural systems: an empirical calibration of the garnet–hornblende Fe–Mg geothermometer. Lithos 53 (3–4), 265–277.

Rubatto, D., 2002. Zircon trace element geochemistry: partitioning with garnet and the link between U-Pb ages and metamorphism. Chem. Geol. 184, 123–138.

Sommer, H., Hauzenberger, C., Kröner, A., Muhongo, S., 2008. Isothermal decompression history in the "Western Granulite" terrain, central Tanzania: Evidence from reaction textures and trapped fluids in metapelites. J. Afr. Earth Sc. 51 (3), 123–144.

Sommer, H., Kröner, A., 2013. Ultra-high temperature granulite-facies metamorphic rocks from the Mozambique belt of SW Tanzania. Lithos 170, 117–143.

Sommer, H., Kröner, A., Hauzenberger, C., Muhongo, S., Wingate, M.T.D., 2003. Metamorphic petrology and zircon geochronology of high-grade rocks from the central Mozambique Belt of Tanzania: crustal recycling of Archean and Palaeoproterozoic material during the Pan-African orogeny. J. Metamorph. Geol. 21 (9), 915–934.

Stern, R.J., 1994. Arc assembly and continental collision in the Neoproterozoic East African Orogen: implications for the consolidation of Gondwanaland. Annual Review of Earth and Planetary Science 22, 319–351.

Stern, R.J., Ali, K.A., Abdelsalam, M.G., Wilde, S.A., Zhou, Q., 2012. U-Pb zircon geochronology of the eastern part of the Southern Ethiopian Shield. Precambr. Res. 206, 159–167.

Stern, R.J., Dawoud, A.S., 1991. Late Precambrian (740 Ma) charnockite, enderbite, and granite from Jebel Moya, Sudan: a link between the Mozambique Belt and the Arabian-Nubian Shield? J. Geol. 99 (5), 649–659.

Tedeschi, M., Lanari, P., Rubatto, D., Pedrosa-Soares, A., Hermann, J., Dussin, I., Pinheiro, M.A.P., Bouvier, A.-S., Baumgartner, L., 2017. Reconstruction of multiple PT-t stages from retrogressed mafic rocks: Subduction versus collision in the Southern Brasília orogen (SE Brazil). Lithos 294–295, 283–303.

Tadesse, T., Hoshino, M., Suzuki, K., Iizumi, S., 2000. Sm-Nd, Rb–Sr and Th–U–Pb zircon ages of syn-and post-tectonic granitoids from the Axum area of northern Ethiopia. J. Afr. Earth Sc. 30 (2), 313–327.

Tefera, M., Berhe, S.M., 1987. Geological map of Gore area (1: 250, 000). Ethiopian Institute of Geological Survey, Addis Ababa, Ethiopia.

Teklay, M., Kröner, A., Mezger, K., Oberhänsli, R., 1998. Geochemistry, Pb-Pb single zircon ages and Nd-Sr isotope composition of Precambrian rocks from southern and eastern Ethiopia: implications for crustal evolution in East Africa. J. Afr. Earth Sc. 26 (2), 207–227.

Tolessa, S., Bonavia, F.F., Solomon, M., Awoke, H., Eshete, T., 1991. Structural pattern of Pan-African rocks around Moyale, southern Ethiopia. Precambrian Res. 52, 179–186.

Tsige, L., 2006. Metamorphism and gold mineralization of the Kenticha-Katawicha area: Adola belt, southern Ethiopia. J. Afr. Earth Sc. 45 (1), 16–32.

Tsige, L., Abdelsalam, M.G., 2005. Neoproterozoic-Early Paleozoic gravitational tectonic collapse in the southern part of the Arabian-Nubian Shield: the Bulbul Belt of southern Ethiopia. Precambr. Res. 138 (3–4), 297–318.

Uchida, E., Endo, S., Makino, M., 2007. Relationship between solidification depth of granitic rocks and formation of hydrothermal ore deposits. Resour. Geol. 57 (1), 47–56.

Vanderhaeghe, O., Teyssier, C., 2001. Crustal-scale rheological transitions during late-orogenic collapse. Tectonophysics 335 (1–2), 211–228.

Vernon, R.H., 2000. Review of microstructural evidence of magmatic and solid-state flow. Vis. Geosci. 5 (2), 1–23.

Whitney, D.L., Evans, B.W., 2010. Abbreviations for names of rock-forming minerals. Am. Mineral. 95 (1), 185–187.

Woldemichael, B.W., Kimura, J.I., Dunkley, D.J., Tani, K., Ohira, H., 2010. SHRIMP U-Pb zircon geochronology and Sr–Nd isotopic systematic of the Neoproterozoic Ghimbi-Nedjo mafic to intermediate intrusions of Western Ethiopia: a record of passive margin magmatism at 855 Ma? Int. J. Earth Sci. 99 (8), 1773–1790.

Worku, H., Schandelmeier, H., 1996. Tectonic evolution of the Neoproterozoic Adola Belt of southern Ethiopia: evidence for a Wilson Cycle process and implications for oblique plate collision. Precambr. Res. 77 (3–4), 179–210.

Yakymchuk, C., Kirkland, C.L., Clark, C., 2018. Th/U ratios in metamorphic zircon. J. Metamorph. Geol. 36 (6), 715–737.

Yibas, B., Reimold, W.U., Armstrong, R., Koeberl, C., Anhaeusser, C.R., Phillips, D., 2002. The tectonostratigraphy, granitoid geochronology and geological evolution of the Precambrian of southern Ethiopia. J. Afr. Earth Sc. 34 (1–2), 57–84.

Yihunie, T., Adachi, M., Takeuchi, M., 2004. P-T conditions of metamorphism in the Neoproterozoic rocks of the Negele area, southern Ethiopia. Gondwana Res. 7 (2), 489–500.

Supplementary Information 1
Representative chemical composition of major minerals in the metamorphic rocks from the Hammar domain.

Tectonometamorphic evolution and U–Pb dating of the high-grade Hammar Domain (Southern Ethiopian Shield); implications for the East-African Orogeny

Verner, K*., Buriánek, D., Svojtka, M., Peřestý, V., **Megerssa, L.**, Tadesse, T., Kussita A., Alemayehu, D., Hroch, T. (2021).

Precambrian Research, 361, 106270.

* Coressponding author: krystof.verner@geology.cz; Institute of Petrology and Structural Geology, Faculty of Science, Charles University, Albertov 6, Prague, 12843, Czech Republic

Representative chemical analyses of amphibole (values in wt%) Chemical composition of clinopyroxene and orthopyroxene from metamorphic rocks of the Hammar domain.

Rock	Amfibolite			Granulite										
Sample	DE501	DE501	DE501	E011	E011	E011	E006D	E006D	E012	E012	E006C	E006C	E010	E010
No.	1	5	6	83	84	85	10	11	50	52	15	17	5	6
Group	OH,F,Cl	OH,F,Cl	OH,F,Cl	OH,F,Cl	OH,F,Cl	OH,F,Cl	OH,F,Cl	OH,F,Cl	OH,F,Cl	OH,F,Cl	OH,F,Cl	OH,F,Cl	OH,F,Cl	OH,F,Cl
Subgroup of (OH,]	Ca	Ca	Ca	Ca	Ca	Ca	Ca	Ca	Ca	Ca	Ca	Ca	Ca	Ca
Species	pargasite	pargasite	pargasite	pargasite	pargasite	pargasite	‹-pargasite	g-hornblende	K-pargasite	K-pargasite	pargasite	pargasite	Mg-hornblende	K-pargasite
SiO_2	44.29	40.61	41.26	43.13	43.21	43.75	41.14	43.45	41.42	41.54	42.37	42.13	44.07	42.07
TiO_2	1.94	1.83	1.37	1.73	1.69	1.43	1.10	0.95	1.65	1.77	1.89	2.07	1.42	1.90
Al_2O_3	9.69	14.89	14.98	12.16	12.18	12.15	14.51	12.40	12.77	12.86	11.93	12.07	12.46	12.79
V_2O_3	0.11	0.09	0.02	0.00	0.00	0.00	0.00	0.00	0.00	0.00	0.00	0.00	0.00	0.00
Cr_2O_3	0.05	0.05	0.05	0.03	0.05	0.07	0.03	0.02	0.00	0.00	0.00	0.01	0.04	0.01
MnO	0.23	0.12	0.14	0.17	0.20	0.18	0.23	0.08	0.25	0.26	0.14	0.19	0.02	0.21
FeO	14.39	13.80	12.11	10.68	10.75	10.40	11.96	9.27	13.81	14.72	14.66	14.41	10.37	14.83
Fe_2O_3	0.72	0.82	1.55	0.98	1.33	1.39	4.04	4.61	2.11	0.95	1.19	1.19	2.00	1.47
MgO	11.50	10.19	11.24	13.20	13.11	13.31	10.20	12.43	10.16	9.98	10.47	10.62	12.60	9.92
CaO	11.80	11.61	11.40	11.93	11.54	11.72	11.55	11.50	11.74	11.70	11.53	11.64	11.83	11.53
Na_2O	1.78	2.42	2.26	1.62	1.72	1.48	1.00	1.18	1.03	0.97	1.48	1.34	1.00	0.92
K_2O	0.68	0.77	0.83	1.32	1.43	1.32	1.73	0.75	1.93	1.97	1.22	1.37	1.08	1.64
F	0.13	0.13	0.16	0.65	0.65	0.61	0.17	0.14	0.21	0.19	0.26	0.27	0.22	0.16
Cl	0.10	0.08	0.15	0.02	0.05	0.02	0.13	0.15	0.07	0.10	0.09	0.08	0.03	0.09
H_2O^+	1.93	1.93	1.92	1.73	1.72	1.75	1.90	1.95	1.88	1.89	1.87	1.86	1.95	1.91
O = F, Cl	-0.08	-0.07	-0.10	-0.28	-0.28	-0.26	-0.10	-0.09	-0.10	-0.10	-0.13	-0.13	-0.10	-0.09
Total	99.36	99.30	99.35	99.06	99.33	99.32	99.59	98.78	98.92	98.79	98.97	99.11	98.98	99.37
Si	6.620	6.085	6.128	6.382	6.383	6.438	6.143	6.416	6.268	6.298	6.387	6.344	6.481	6.326
Al	1.380	1.915	1.872	1.618	1.617	1.562	1.857	1.584	1.732	1.702	1.613	1.656	1.519	1.674
T subtotal	8.000	8.000	8.000	8.000	8.000	8.000	8.000	8.000	8.000	8.000	8.000	8.000	8.000	8.000
Ti	0.218	0.206	0.153	0.192	0.188	0.158	0.124	0.106	0.187	0.201	0.214	0.234	0.157	0.215
Al	0.326	0.713	0.751	0.502	0.504	0.545	0.696	0.574	0.545	0.596	0.507	0.486	0.641	0.594
V	0.013	0.011	0.003	0.000	0.000	0.000	0.000	0.000	0.000	0.000	0.000	0.000	0.000	0.000
Cr	0.006	0.006	0.006	0.004	0.006	0.008	0.003	0.002	0.000	0.000	0.000	0.001	0.005	0.002
Fe^{3+}	0.082	0.092	0.172	0.109	0.148	0.153	0.453	0.512	0.240	0.109	0.135	0.135	0.221	0.166
Fe^{2+}	1.781	1.693	1.423	1.280	1.268	1.215	1.452	1.070	1.735	1.837	1.790	1.760	1.215	1.800
Mg	2.562	2.276	2.489	2.912	2.887	2.920	2.271	2.737	2.292	2.256	2.353	2.383	2.762	2.224
C subtotal	4.999	5.001	5.000	4.999	5.001	4.999	4.999	5.001	4.999	4.999	4.999	4.999	5.001	5.001
Mn^{2+}	0.029	0.015	0.018	0.022	0.025	0.023	0.030	0.010	0.032	0.034	0.018	0.024	0.003	0.026
Fe^{2+}	0.017	0.038	0.081	0.041	0.059	0.065	0.042	0.075	0.013	0.029	0.058	0.053	0.060	0.066
Ca	1.890	1.864	1.815	1.891	1.826	1.848	1.847	1.819	1.904	1.901	1.862	1.877	1.863	1.857
Na	0.064	0.084	0.087	0.047	0.090	0.064	0.081	0.096	0.051	0.036	0.062	0.046	0.074	0.051
B subtotal	2.000	2.001	2.001	2.001	2.000	2.000	2.000	2.000	2.000	2.000	2.000	2.000	2.000	2.000
Na	0.451	0.618	0.563	0.416	0.403	0.357	0.208	0.240	0.251	0.249	0.370	0.346	0.212	0.218
K	0.130	0.147	0.158	0.249	0.270	0.247	0.329	0.141	0.373	0.380	0.234	0.263	0.202	0.314
A subtotal	0.581	0.765	0.721	0.665	0.673	0.604	0.537	0.381	0.624	0.629	0.604	0.609	0.414	0.532
O (non-W)	22.000	22.000	22.000	22.000	22.000	22.000	22.000	22.000	22.000	22.000	22.000	22.000	22.000	22.000
OH	1.914	1.917	1.890	1.691	1.685	1.710	1.888	1.897	1.881	1.885	1.856	1.852	1.890	1.899
F	0.060	0.063	0.073	0.303	0.304	0.285	0.078	0.066	0.100	0.089	0.122	0.128	0.104	0.078
Cl	0.026	0.021	0.037	0.006	0.011	0.005	0.034	0.037	0.019	0.025	0.022	0.020	0.006	0.023
W subtotal	2.000	2.001	2.000	2.000	2.000	2.000	2.000	2.000	2.000	1.999	2.000	2.000	2.000	2.000
Sum T, C, B, A	15.580	15.767	15.722	15.665	15.674	15.603	15.536	15.382	15.623	15.628	15.603	15.608	15.415	15.533
Structural formulas (per 24 (O, OH, F, Cl)) were calculated according to the recommendations of Hawthorne et al. (2012)														

Representative chemical composition of clinopyroxene and orthopyroxene (values in wt%) from metamorphic rocks of the Hammar domain.

Rock	Calc-silicate rocks		Amfibolite		Granulite									
Sample	DE505b	DE505b	DE501	DE501	E012	E012	E012	E006C	E006C	E006C	E006C	E011	E006D	E006D
No.	56	60	80	81	42	66	43	12	39	9	10	87	5	15
SiO_2	46.52	45.58	52.81	53.49	50.62	50.70	50.33	50.71	50.73	50.07	49.67	52.38	50.92	49.61
TiO_2	0.37	0.33	0.10	0.09	0.06	0.08	0.31	0.06	0.07	0.35	0.30	0.06	0.09	0.33
Al_2O_3	4.71	4.71	0.95	1.12	2.43	2.60	3.75	2.25	2.31	3.87	3.67	2.02	2.53	3.87
Cr_2O_3	0.01	0.02	0.01	0.00	0.00	0.01	0.00	0.02	0.00	0.01	0.00	0.01	0.00	0.01
Fe_2O_3	5.58	6.65	1.34	0.00	1.15	0.89	2.30	1.10	1.27	2.79	3.24	1.21	0.53	2.91
FeO	14.71	15.38	6.72	8.85	24.36	25.46	8.69	25.23	25.32	8.69	11.80	20.27	24.84	9.89
MnO	0.05	0.05	0.33	0.33	1.23	1.10	0.50	0.74	0.74	0.33	0.50	0.65	0.84	0.43
MgO	5.28	4.61	13.67	12.87	19.17	18.66	11.93	19.06	18.92	11.38	12.33	23.00	19.10	11.63
CaO	21.92	21.66	23.31	22.82	0.49	0.59	21.38	0.51	0.62	21.70	17.87	0.43	0.84	20.16
Na_2O	0.78	0.74	0.42	0.40	0.04	0.02	0.56	0.01	0.02	0.66	0.54	0.05	0.04	0.58
K_2O	0.03	0.00	0.00	0.01	0.00	0.01	0.00	0.00	0.02	0.01	0.00	0.00	0.00	0.02
TOTAL	99.96	99.71	99.66	100.00	99.55	100.11	99.75	99.69	100.00	99.86	99.91	100.07	99.72	99.43
Si	1.828	1.809	1.973	2.000	1.929	1.927	1.896	1.932	1.929	1.888	1.883	1.939	1.935	1.884
Al	0.172	0.191	0.027	0.000	0.071	0.073	0.104	0.068	0.071	0.112	0.117	0.061	0.065	0.116
Fe^{3+}	0.165	0.199	0.038	0.000	0.033	0.025	0.065	0.032	0.036	0.079	0.092	0.034	0.015	0.083
Cr	0.000	0.001	0.000	0.000	0.000	0.000	0.000	0.001	0.000	0.000	0.000	0.000	0.000	0.000
Ti	0.011	0.010	0.003	0.003	0.002	0.002	0.009	0.002	0.002	0.010	0.009	0.002	0.003	0.009
Fe^{2+}	0.483	0.510	0.210	0.277	0.776	0.809	0.274	0.804	0.805	0.274	0.374	0.627	0.789	0.314
Mn	0.002	0.002	0.010	0.011	0.040	0.035	0.016	0.024	0.024	0.010	0.016	0.020	0.027	0.014
Mg	0.309	0.273	0.761	0.717	1.089	1.057	0.670	1.083	1.073	0.640	0.697	1.269	1.082	0.658
Ca	0.922	0.921	0.933	0.914	0.020	0.024	0.863	0.021	0.025	0.877	0.726	0.017	0.034	0.820
Na	0.060	0.057	0.030	0.029	0.003	0.001	0.041	0.001	0.001	0.048	0.039	0.003	0.003	0.043
K	0.001	0.000	0.000	0.000	0.000	0.000	0.000	0.000	0.001	0.001	0.000	0.000	0.000	0.001
Sum Cat.	4.000	4.000	4.000	4.000	4.000	4.000	4.000	4.000	4.000	4.000	4.000	4.000	4.000	4.000
Fe/(Fe+Mg)	0.677	0.722	0.245	0.278	0.426	0.441	0.336	0.435	0.440	0.356	0.401	0.342	0.427	0.376

Structural formulas were calculated on the basis of 4 cations (per formula unit, apfu) and method for estimating ferric iron given by Droop (1987).

Representative chemical composition of feldspars (values in wt%) from metamorphic rocks of the Hammar domain.

Rock	Calc-silicate rocks			Amfibolite		Granulite								
Sample	D505B	D505B	D505B	DE501	DE501	E012	E006C	E006C	E011	E011	E006D	E006D	E006D	E006D
No.	46	55	62	83	108	71	14	15	74	91	7	23	29	34
SiO_2	56.39	50.27	64.42	61.24	57.09	55.29	55.94	56.21	61.41	56.40	55.03	59.93	54.86	55.17
P_2O_5	0.04	0.01	0.00	0.00	0.01	0.03	0.00	0.03	0.02	0.03	0.05	0.01	0.01	0.02
Al_2O_3	27.14	30.94	18.13	24.06	26.26	27.66	27.01	27.02	24.19	27.61	27.98	24.82	27.55	27.68
FeO	0.27	0.12	0.06	0.11	0.21	0.11	0.12	0.11	0.27	0.10	0.06	0.23	0.05	0.04
CaO	9.87	14.77	0.05	6.06	9.18	10.63	9.87	9.91	5.80	9.74	11.03	7.03	10.52	10.68
Na_2O	5.59	2.86	0.64	8.02	6.48	5.21	5.80	5.78	8.22	6.03	5.33	7.67	5.43	5.44
K_2O	0.18	0.09	15.04	0.10	0.07	0.26	0.33	0.29	0.05	0.08	0.16	0.03	0.05	0.08
BaO	0.00	0.00	0.09	0.00	0.00	0.03	0.06	0.04	0.00	0.08	0.03	0.01	0.01	0.02
SrO	0.25	0.47	0.67	0.00	0.04	0.06	0.01	0.05	0.03	0.31	0.02	0.00	0.04	0.02
Total	99.47	99.07	98.34	99.59	99.30	99.19	99.06	99.33	99.97	99.99	99.63	99.71	98.47	99.12
Si	2.542	2.308	3.001	2.730	2.579	2.509	2.540	2.544	2.724	2.531	2.491	2.677	2.508	2.507
Al	1.441	1.674	0.996	1.264	1.398	1.479	1.446	1.441	1.265	1.460	1.493	1.306	1.484	1.483
Fe^{3+}	0.010	0.005	0.002	0.004	0.008	0.004	0.004	0.004	0.010	0.004	0.002	0.008	0.002	0.002
T-site	3.993	3.987	3.999	3.998	3.985	3.993	3.990	3.989	3.999	3.994	3.986	3.992	3.994	3.991
K	0.010	0.005	0.894	0.006	0.004	0.015	0.019	0.017	0.003	0.005	0.009	0.002	0.003	0.005
Na	0.488	0.255	0.058	0.693	0.567	0.458	0.511	0.507	0.707	0.525	0.468	0.664	0.481	0.479
Ca	0.471	0.717	0.002	0.286	0.439	0.511	0.474	0.474	0.272	0.462	0.528	0.332	0.509	0.513
Ba	0.000	0.000	0.002	0.000	0.000	0.000	0.001	0.001	0.000	0.001	0.000	0.000	0.000	0.000
Sr	0.007	0.013	0.018	0.000	0.001	0.002	0.000	0.001	0.001	0.008	0.001	0.000	0.001	0.001
O-site	0.975	0.990	0.974	0.985	1.011	0.986	1.005	1.000	0.983	1.001	1.006	0.998	0.994	0.998
An	49	73	0	29	43	52	47	48	28	47	53	33	51	51
Ab	50	26	6	70	56	47	51	51	72	53	47	67	48	48
Or	1	1	94	1	0	2	2	2	0	0	1	0	0	0

Structural formulas were calculated on the basis of 8 oxygen atoms per formula unit (apfu).

Representative chemical composition of biotite (values in wt%) from metamorphic rocks of the Hammar domain.

Rock	Amfibolite				Granulite				
Sample	DE501	DE501	DE501	E012	E012	E010	E010	E010	E006D
No.	65	66	67	81	82	26	27	28	13
SiO2	36.50	36.46	36.33	35.32	35.38	36.72	36.71	36.69	36.80
TiO2	3.64	3.67	3.85	4.46	4.32	3.59	3.35	3.37	2.90
Al2O3	15.99	15.95	15.85	15.63	15.40	16.59	16.47	16.34	16.23
FeO	15.26	15.01	14.91	16.52	16.95	15.78	16.27	16.43	13.23
MnO	0.01	0.06	0.04	0.13	0.20	0.03	0.00	0.00	0.07
MgO	14.13	14.01	13.86	10.74	10.76	11.78	11.48	11.30	15.07
CaO	0.00	0.02	0.01	0.01	0.01	0.00	0.00	0.01	0.11
Na2O	0.49	0.40	0.38	0.02	0.00	0.04	0.04	0.05	0.03
K2O	8.98	8.91	8.97	9.19	9.25	9.74	9.54	9.48	9.13
BaO	0.14	0.22	0.22	2.39	2.13	0.23	0.24	0.24	0.35
ZnO	0.00	0.06	0.00	0.07	0.06	0.10	0.07	0.05	
F	0.16	0.15	0.19	0.23	0.24	0.29	0.31	0.28	0.23
Cl	0.06	0.06	0.06	0.09	0.08	0.07	0.12	0.10	0.01
Cr2O3	0.00	0.03	0.05	0.00	0.01	0.00	0.02	0.03	
H2O*	3.91	3.90	3.87	3.74	3.73	3.81	3.76	3.77	3.88
O = F, Cl	0.08	0.08	0.09	0.12	0.12	0.14	0.16	0.14	0.10
Total	99.19	98.83	98.50	98.51	98.39	98.62	98.23	98.00	97.93
Si	5.469	5.479	5.478	5.477	5.495	5.557	5.585	5.598	5.532
^{IV}Al	2.531	2.521	2.522	2.523	2.505	2.443	2.415	2.402	2.468
^{VI}Al	0.293	0.305	0.295	0.334	0.313	0.517	0.539	0.536	0.408
Ti	0.410	0.415	0.437	0.521	0.504	0.408	0.384	0.386	0.328
Cr	0.000	0.003	0.006	0.000	0.001	0.000	0.003	0.004	0.000
Fe	1.911	1.887	1.880	2.143	2.201	1.997	2.070	2.096	1.663
Mn	0.001	0.008	0.005	0.017	0.026	0.004	0.000	0.000	0.009
Mg	3.156	3.138	3.115	2.483	2.491	2.659	2.605	2.570	3.377
Zn	0.000	0.007	0.000	0.008	0.006	0.011	0.008	0.006	0.000
Ca	0.000	0.004	0.001	0.001	0.002	0.000	0.000	0.001	0.017
Na	0.142	0.116	0.111	0.005	0.000	0.011	0.011	0.015	0.008
K	1.716	1.709	1.726	1.818	1.832	1.880	1.852	1.845	1.751
Ba	0.008	0.013	0.013	0.145	0.130	0.014	0.014	0.014	0.021
OH*	3.909	3.913	3.894	3.864	3.860	3.842	3.821	3.836	3.887
F	0.077	0.073	0.091	0.111	0.120	0.140	0.147	0.137	0.110
Cl	0.014	0.014	0.016	0.024	0.020	0.018	0.032	0.027	0.003
Sum Cat.	19.638	19.604	19.592	19.485	19.507	19.500	19.484	19.475	19.582
Al total	2.82	2.83	2.82	2.86	2.82	2.96	2.95	2.94	2.88
Fe/Fe+Mg	0.38	0.38	0.38	0.46	0.47	0.43	0.44	0.45	0.33
Structural formulas were calculated on the basis of 22 oxygen atoms per formula unit (apfu).									
All Fe was treated as Fe2+, and OH was calculated by stoichiometry									

Representative chemical composition of garnet (values in wt%) from metamorphic rocks of the Hammar domain.

Rock	Calc-silicate rocks			Amfibolite				Granulite						
Sample	DE505B	DE505B	DE505B	DE501	DE501	DE501	DE501	E012	E012	E010	E010	E010	E006D	E006D
No.	38	40	52	68	69	92	97	64	65	5	7	11	26	32
SiO_2	36.24	36.26	36.20	39.00	38.51	38.35	38.15	38.05	38.42	38.16	38.57	38.53	38.21	37.65
TiO_2	0.63	0.65	0.65	0.03	0.03	0.08	0.07	0.04	0.03	0.19	0.12	0.10	0.09	0.20
Y_2O_3	0.00	0.00	0.00	0.00	0.00	0.00	0.00	0.07	0.04	0.00	0.00	0.01	0.02	0.00
Al_2O_3	7.02	7.13	7.36	21.60	21.53	21.22	21.29	20.52	20.47	20.91	20.83	20.64	20.80	20.43
Cr_2O_3	0.01	0.02	0.02	0.00	0.02	0.00	0.02	0.00	0.00	0.03	0.02	0.00	0.03	0.00
V_2O_3	0.09	0.06	0.10	0.00	0.01	0.01	0.03	0.04	0.00	0.01	0.03	0.02	0.03	0.05
Fe_2O_3	20.40	19.86	19.78	1.06	0.13	0.85	0.99	1.54	0.74	1.48	0.78	0.99	0.94	1.66
FeO	4.86	5.05	5.15	21.45	26.13	23.29	23.76	23.52	23.96	24.37	25.28	25.25	26.88	24.64
MnO	0.15	0.20	0.13	0.82	2.06	1.82	0.71	2.93	2.96	0.70	0.76	0.89	0.48	1.86
MgO	0.14	0.14	0.14	7.78	6.52	4.52	4.49	5.80	5.66	6.38	6.21	6.10	7.05	5.33
Na_2O	0.03	0.00	0.02	0.01	0.00	0.06	0.03	0.02	0.02	0.03	0.00	0.00	0.02	0.02
CaO	30.05	30.01	29.85	8.18	4.86	9.74	10.20	6.73	6.89	7.19	7.10	7.16	4.49	7.12
F	-	-	-	-	-	-	-	0.01	0.02	0.04	0.01	0.04	0.02	0.04
Total	99.62	99.38	99.40	99.92	99.80	99.93	99.73	99.31	99.23	99.50	99.72	99.73	99.06	99.00
Si	2.987	2.993	2.986	2.992	3.000	2.997	2.985	2.997	3.000	2.981	3.000	3.000	3.000	2.982
Al	0.013	0.007	0.014	0.008	0.000	0.003	0.015	0.002	0.000	0.016	0.000	0.000	0.000	0.015
T - site	3.000	3.000	3.000	3.000	3.000	3.000	3.000	2.999	3.000	2.997	3.000	3.000	3.000	2.998
Si	0.000	0.000	0.000	0.000	0.004	0.000	0.000	0.000	0.025	0.000	0.010	0.011	0.002	0.000
Al	0.669	0.687	0.701	1.944	1.979	1.951	1.949	1.903	1.900	1.909	1.915	1.901	1.926	1.892
Cr	0.000	0.001	0.001	0.000	0.001	0.000	0.001	0.000	0.000	0.002	0.001	0.000	0.002	0.000
Fe^{3+}	1.265	1.234	1.228	0.061	0.008	0.050	0.058	0.091	0.044	0.087	0.046	0.058	0.056	0.099
Fe^{2+}	0.021	0.034	0.023	0.000	0.001	0.000	0.000	0.000	0.002	0.000	0.008	0.011	0.005	0.000
Ti	0.039	0.040	0.040	0.002	0.001	0.005	0.004	0.003	0.002	0.011	0.007	0.006	0.005	0.012
Mg	0.000	0.000	0.000	0.000	0.004	0.000	0.000	0.000	0.025	0.000	0.010	0.011	0.002	0.000
V	0.006	0.004	0.007	0.000	0.001	0.000	0.002	0.002	0.000	0.001	0.002	0.001	0.002	0.003
B - site	1.994	1.996	1.993	2.007	1.995	2.006	2.013	1.998	1.975	2.009	1.988	1.987	1.996	2.003
Fe^{2+}	0.314	0.315	0.333	1.376	1.703	1.522	1.555	1.549	1.576	1.593	1.642	1.640	1.762	1.632
Mn^{2+}	0.010	0.014	0.009	0.054	0.136	0.121	0.047	0.196	0.197	0.047	0.050	0.059	0.032	0.125
Mg	0.017	0.017	0.017	0.889	0.754	0.527	0.524	0.681	0.639	0.744	0.713	0.699	0.823	0.629
Ca	2.653	2.654	2.638	0.673	0.406	0.815	0.855	0.568	0.581	0.602	0.593	0.600	0.378	0.604
Na	0.005	0.000	0.003	0.001	0.000	0.008	0.004	0.003	0.004	0.005	0.000	0.000	0.004	0.003
Y	0.000	0.000	0.000	0.000	0.000	0.000	0.000	0.003	0.002	0.000	0.000	0.001	0.001	0.000
B - site	3.000	3.000	3.000	2.992	3.000	2.993	2.986	3.000	2.999	2.990	2.999	2.998	2.999	2.994
O anions	12.000	12.000	12.000	12.000	12.000	12.000	12.000	11.997	11.996	11.990	11.997	11.991	11.996	11.991
F anions	-	-	-	-	-	-	-	0.003	0.004	0.010	0.003	0.009	0.004	0.009
Almandine	8	7	9	46	56	51	52	52	51	53	54	53	58	54
Andradite	65	64	63	3	0	3	3	5	2	4	2	3	3	5
Grossular	26	28	27	19	13	25	26	14	18	16	18	17	10	15
Pyrope	1	1	1	30	25	18	18	23	23	25	25	24	28	21
Spessartine	0	0	0	2	5	4	2	7	7	2	2	2	1	4
Uvarovite	0	0	0	0	0	0	0	0	0	0	0	0	0	0

Structural formulae were calculated on the basis of 12 oxygen atoms per formula unit (apfu) and with Fe2+/Fe3+ calculated assuming full site occupancy

Supplementary Information 2
U-Pb-Th isotopic data of dated samples from the Hammar domain

Tectonometamorphic evolution and U–Pb dating of the high-grade Hammar Domain (Southern Ethiopian Shield); implications for the East-African Orogeny

Verner, K*., Buriánek, D., Svojtka, M., Peřestý, V., **Megerssa, L**., Tadesse, T., Kussita A., Alemayehu, D., Hroch, T. (2021).

Precambrian Research, 361, 106270.

* Coressponding author: krystof.verner@geology.cz; Institute of Petrology and Structural Geology, Faculty of Science, Charles University, Albertov 6, Prague, 12843, Czech Republic

Data from a granulite rock sample, DE470B

No.	Corrected isotope ratios					Apparent ages (Ma)						U, Th and Pb content (ppm)							*disc.	CL internal textures and growth description	
	$^{207}Pb/^{235}U$	±2σ	$^{206}Pb/^{238}U$	±2σ	error corr.	$^{207}Pb/^{235}U$	±2σ	$^{206}Pb/^{238}U$	±2σ	$^{207}Pb/^{206}U$	±2σ	Approx U	±2σ	Approx Th	±2σ	Approx Pb	±2σ	Th/U	%	shape	textures
analyses in zircon core (~ 752 Ma)																					
1	1.0780	0.0200	0.1226	0.0014	0.6661	742	10	746	8	711	30	686	9.9	104	9.7	126	11	0.2	-0.6	BRRC	PZ, SC
2	1.0870	0.0210	0.1234	0.0016	0.6471	747	10	750	9	721	32	604	7.1	312	9.6	354	9.7	0.5	-0.4	BRRC	PZ, SC
3	1.0870	0.0210	0.1239	0.0015	0.6318	747	10	753	9	730	33	533	5.8	470	9.3	537	10	0.9	-0.9	BRRC	PZ, SC
4	1.0940	0.0200	0.1243	0.0015	0.6752	751	10	755	9	695	32	390	5.9	76	1.1	81	1.8	0.2	-0.6	BRRC	PZ, SC
5	1.1180	0.0220	0.1244	0.0016	0.5349	761	11	756	9	742	35	529	9.7	272	5.7	330	6	0.5	0.7	BRRC	PZ, SC
6	1.1030	0.0220	0.1246	0.0019	0.7080	754	11	758	11	748	33	492	7.9	222	11	250	13	0.5	-0.6	BRRC	PZ, SC
analyses in inner parts of grains (ca. 715 Ma)																					
7	0.9340	0.0220	0.1099	0.0013	0.5122	670	11	672	8	647	41	131	1.8	85	1.4	89	1.8	0.7	-0.3	BRNCV	CZHZB
8	0.9420	0.0200	0.1102	0.0016	0.4092	675	11	675	9	662	40	373	6.2	354	5.9	385	6	0.9	0.0	BRRC	PZ, SOC
9	0.9710	0.0210	0.1119	0.0015	0.5041	688	11	683	9	683	38	359	19	276	16	303	16	0.8	0.7	BRNCV	CZHZB
10	0.9560	0.0210	0.1127	0.0013	0.3787	682	11	689	8	678	41	202	3.5	201	3.6	211	3.3	1.0	-1.0	BRNCV	sector and CZHZB
11	0.9620	0.0190	0.1128	0.0014	0.3897	685	10	689	8	646	37	230	6.3	268	7.8	290	8.4	1.2	-0.6	BRNCV	CZHZB
12	0.9680	0.0190	0.1136	0.0014	0.5108	688	10	693	8	642	36	338	6.6	159	5.7	171	5.5	0.5	-0.8	BRNCV	CZHZB
13	0.9870	0.0210	0.1138	0.0016	0.6255	697	10	695	9	670	36	435	9.1	294	7.9	328	7.9	0.7	0.3	BRRC	PZ, SOC
14	0.9910	0.0200	0.1143	0.0014	0.5587	699	10	698	8	651	34	296	5.5	347	6	357	5.6	1.2	0.2	BRNCV	sector and CZHZB
15	0.9810	0.0200	0.1145	0.0013	0.4521	693	10	698	8	660	36	256	3.9	148	3	169	3.5	0.6	-0.7	BRRC	sector and CZHZB
16	1.0050	0.0220	0.1146	0.0016	0.4704	707	11	700	9	703	40	391	6	305	4	356	7	0.8	0.9	BRRC	PZ, SOC
17	1.0050	0.0210	0.1151	0.0015	0.7087	705	11	702	9	696	34	443	9.3	286	8.6	321	10	0.6	0.4	BRRC	PZ, SOC
18	1.0100	0.0210	0.1153	0.0014	0.6344	708	11	703	8	725	33	494	11	469	21	502	23	0.9	0.7	BRRC	PZ, SOC
19	0.9960	0.0220	0.1162	0.0015	0.4644	701	11	708	9	701	39	252	3.2	188	4.2	199	3.9	0.7	-1.0	BRNCV	sector and CZHZB
20	1.0100	0.0200	0.1165	0.0015	0.6112	708	10	710	9	686	33	502	5.8	24	0.33	27	0.76	0.0	-0.3	BRNCV	CZHZB
21	1.0070	0.0190	0.1166	0.0014	0.6474	707	10	711	8	687	32	387	7.3	439	8.3	485	7.1	1.1	-0.5	BRNCV	CZHZB
22	1.0080	0.0220	0.1167	0.0015	0.4834	709	11	712	9	687	39	291	8.8	281	8	314	8.1	1.0	-0.4	WBRNCV	CZHZB
23	1.0220	0.0210	0.1169	0.0017	0.5085	714	10	713	10	689	36	478	10	672	13	807	16	1.4	0.2	BRNCV	sector and CZHZB
24	1.0160	0.0190	0.1173	0.0015	0.7026	712	10	715	9	688	29	940	12	44	0.57	48	1	0.0	-0.5	BRRC	PZ, SOC
25	1.0180	0.0190	0.1175	0.0016	0.6612	713	9	716	9	687	31	752	9.5	36	0.7	40	1	0.05	-0.4	BRNCV	CZHZB
26	1.0210	0.0200	0.1177	0.0017	0.7427	714	10	717	10	729	31	769	17	252	4.5	259	5.9	0.3	-0.4	BRNCV	sector and CZHZB
27	1.0300	0.0200	0.1180	0.0016	0.6829	719	10	719	9	693	32	666	15	600	13	689	14	0.9	0.1	BRRC	PZ, SOC
28	1.0350	0.0200	0.1184	0.0014	0.3804	721	10	721	8	700	37	196	3.5	219	4.2	245	4.2	1.1	0.0	BRNCV	CZHZB
29	1.0450	0.0200	0.1185	0.0016	0.6246	726	10	722	9	732	31	937	17	267	4.3	299	5.9	0.3	0.7	BRNCV	sector and CZHZB
30	1.0420	0.0220	0.1184	0.0015	0.4211	724	11	722	9	731	38	405	7.2	259	7.2	312	8.1	0.6	0.3	BRRC	PZ, SOC
31	1.0470	0.0220	0.1188	0.0012	0.2728	725	10	724	7	700	35	227	4.4	94	1.5	96	1.9	0.4	0.2	BRNCV	CZHZB
32	1.0330	0.0190	0.1190	0.0013	0.6113	720	10	725	8	702	33	402	5.1	720	8.5	714	8.7	1.8	-0.6	BRNCV	CZHZB
33	1.0380	0.0200	0.1190	0.0014	0.6099	722	10	725	8	700	32	398	5.3	491	7.4	537	7.5	1.2	-0.5	BRNCV	CZHZB
34	1.0440	0.0200	0.1192	0.0015	0.6428	726	10	726	9	682	31	498	8.8	123	2.1	129	2.4	0.2	0.0	WBRNCV	CZHZB
35	1.0440	0.0200	0.1195	0.0013	0.4845	726	10	727	8	688	33	271	2.7	359	3.3	402	4.6	1.3	-0.2	BRNCV	SCZ
36	1.0560	0.0210	0.1197	0.0015	0.5854	733	10	729	9	705	33	506	9.5	317	5.6	362	6.1	0.6	0.5	BRNCV	CZHZB
37	1.0460	0.0200	0.1201	0.0014	0.5565	727	10	731	8	701	32	390	5.1	708	9.5	723	8.5	1.8	-0.6	BRNCV	CZHZB
38	1.0420	0.0200	0.1200	0.0015	0.5669	725	10	731	9	684	33	518	9.7	832	18	847	18	1.6	-0.9	BRNCV	sector and CZHZB
39	1.0510	0.0200	0.1202	0.0017	0.6279	729	10	731	10	725	33	929	16	42	0.68	47	1.3	0.0	-0.4	BRRC	PZ, SOC
40	1.0480	0.0210	0.1203	0.0014	0.5350	728	10	733	8	694	35	337	6.8	475	12	541	12	1.4	-0.7	BRNCV	sector and CZHZB
41	1.0550	0.0200	0.1210	0.0013	0.4850	731	10	736	8	703	35	233	3.4	229	3.2	262	3.9	1.0	-0.7	BRRC	SCZ
42	1.0650	0.0230	0.1211	0.0017	0.6247	737	11	736	10	722	36	569	7	242	6.2	298	8.1	0.4	0.0	BRRC	PZ, SR
43	1.0760	0.0220	0.1219	0.0016	0.6037	741	11	741	9	715	36	490	10	655	15	806	17	1.3	0.0	BRNCV	CZHZB
44	1.0730	0.0220	0.1220	0.0013	0.4238	740	11	742	7	711	39	173	2.4	169	1.8	185	2.6	1.0	-0.3	BRNCV	CZHZB
45	1.0830	0.0200	0.1223	0.0013	0.5427	745	10	744	8	714	32	237	3	102	3.5	114	3.3	0.4	0.1	WBRNCV	sector and CZHZB
46	1.0770	0.0210	0.1227	0.0015	0.6137	742	10	746	9	735	33	376	4.7	253	2.9	289	5.1	0.7	-0.5	WBRNCV	CZHZB
*47	0.9920	0.0240	0.1129	0.0015	0.3493	698	12	690	9	679	44	91	1.2	92	1.2	92	2	1.0	1.2	BRNCV	CZHZB, SR
*48	1.0560	0.0280	0.1221	0.0017	0.4654	732	14	742	10	676	47	136	2.2	141	2.6	166	2.9	1.0	-1.4	WBRNCV	CZHZB, SR
*49	0.9400	0.0470	0.1076	0.0022	0.2423	668	25	658	13	680	110	28	0.5	99	1.7	106	2.4	3.6	1.5	BG	patchy zoning
*50	0.9960	0.0240	0.1134	0.0016	0.4993	704	12	693	9	702	45	280	4.3	56	0.72	61	1.7	0.2	1.6	WBRNCV	CZHZB
*51	1.0560	0.0220	0.1188	0.0016	0.6865	732	11	723	9	738	32	745	16	1163	34	1381	34	1.6	1.2	BRNCV	sector and CZHZB
*52	0.9570	0.0190	0.1103	0.0013	0.5347	682	10	674	7	670	34	540	6.8	220	2.5	237	4.1	0.4	1.1	BRRC	PZ, SOC

*disc D=[1-((206Pb/238U) ⁄ (207Pb/235U))] × 100; * discordant data that were not used for age calculations

BRRC – narow CL-bright rim, small relic core
BRNCV – narow CL-bright rim, no core visible
WBRNCV – wider CL-bright rim, no core visible
BG – CL-bright grain
PZ – polygonal zoning

CZHZB – curvilinear zoning with homogenously zoned bands
SCZ – sector and curvilinear zoning
SR – spot in rim
SC – spot in core
SOC – spot outside core

Data from a migmatite rock sample, DE505

No.	Corrected isotope ratios					Apparent ages (Ma)						U, Th and Pb content (ppm)							*disc.	CL internal textures and growth description	
	$^{207}Pb/^{235}U$	±2σ	$^{206}Pb/^{238}U$	±2σ	error corr.	$^{207}Pb/^{235}U$	±2σ	$^{206}Pb/^{238}U$	±2σ	$^{207}Pb/^{206}U$	±2σ	Approx U	±2σ	Approx Th	±2σ	Approx Pb	±2σ	Th/U	%	shape	texture
oscillatory zoned rims (623 ± 6 Ma)																					
1	0.8320	0.0150	0.1006	0.0017	0.4153	616	8	618	10	620	34	249	3.3	114	3.6	115	3.4	0.5	-0.3	XCR	CGZR, POZ, SR
2	0.8400	0.0160	0.1004	0.0019	0.6281	619	9	618	11	627	33	350	8.2	21	0.75	31	1	0.1	0.2	XCR	CGZR, POZ, SR
3	0.8460	0.0180	0.1013	0.0018	0.5470	622	10	622	10	614	38	296	5.4	209	6.1	131	4	0.7	0.05	XCBCR	CGZR, POZ, SR
4	0.8570	0.0200	0.1021	0.0019	0.4567	627	11	627	11	624	43	139	2.2	3	0.12	4	0.35	0.0	0.1	XCR	CGZ , POZ, SR
5	0.8600	0.0210	0.1031	0.0024	0.4321	630	12	632	14	631	49	90	2.8	58	2.1	70	2.6	0.6	-0.3	XCR	CGZR, POZ, SR
6	0.8620	0.0190	0.1030	0.0020	0.5379	631	10	632	12	620	39	307	5	19	0.41	24	0.76	0.1	-0.1	XCR	CGZR, POZ, SR
weakly and UCs, combination of rim/spot analyses; age scatter ca 785 to 702 Ma with two age peaks (ca. 770 Ma and ca. 720 Ma)																					
7	0.9970	0.0220	0.1147	0.0021	0.4723	702	11	700	12	697	39	211	3.6	366	24	217	16	1.7	0.3	XCR	CGZR,WZC and POZ in rim, SC
8	1.0250	0.0280	0.1160	0.0022	0.2244	714	14	707	13	738	57	71	1	125	1.3	70	1.4	1.8	0.9	XCR	CGZR, UC and POZ, SC
9	1.0310	0.0210	0.1168	0.0022	0.3211	719	11	712	13	712	43	179	3.1	260	8.1	162	5.2	1.5	1.0	XCR	CGZR,WZC and POZ in rim, SC
10	1.0100	0.0270	0.1168	0.0021	0.2700	706	14	712	12	681	54	66	1.6	15	0.4	35	1.2	0.2	-0.8	XCR	CGZR, UC and POZ in rim, SC
11	1.0270	0.0260	0.1175	0.0022	0.4665	717	13	716	13	702	46	153	3.9	130	2.8	190	4.3	0.8	0.1	XCR	CGZR, UC and POZ in rim, SC
12	1.0480	0.0200	0.1188	0.0021	0.5140	729	10	724	12	756	34	218	3.3	480	16	665	16	2.2	0.6	XCR	CGZR in core, POZ in rim, SC
13	1.0650	0.0220	0.1198	0.0022	0.4833	736	11	729	13	761	40	141	2	144	2.9	223	4.8	1.0	0.9	XCR	CGZR, UC and POZ in rim, SC
14	1.0760	0.0220	0.1211	0.0022	0.3951	741	11	737	13	749	39	133	1.5	68	1	121	2.7	0.5	0.6	XCR	CGZR in core, POZ in rim, SC
15	1.0480	0.0270	0.1182	0.0022	0.4457	726	13	721	13	758	47	101	1.2	110	1.2	152	2.3	1.1	0.7	XCR	CGZR, UC and POZ in rim, SR
16	1.0690	0.0200	0.1212	0.0021	0.3756	739	10	738	12	749	36	110	1.1	78	1.2	131	2.8	0.7	0.2	XCR	CGZR, UC and POZ in rim, SR
17	1.0540	0.0260	0.1215	0.0024	0.3943	732	13	739	14	716	46	97	1.6	110	1.8	134	2.5	1.1	-1.0	XCBR	CGZR, UC and POZ in rim, SR/SC
18	1.0720	0.0230	0.1220	0.0022	0.4092	740	11	742	13	755	39	135	2.1	53	0.52	125	1.9	0.4	-0.3	XCR	CGZR, WZC and POZ in rim, SR
19	1.0940	0.0230	0.1229	0.0024	0.5186	752	11	748	14	754	36	172	2.4	136	1.9	296	5.4	0.8	0.5	XCR	CGZR, POZ, SR
20	1.1110	0.0210	0.1242	0.0022	0.4716	759	10	754	13	778	33	278	3.8	722	8.7	431	5.8	2.6	0.6	XCR	CGZR, POZ, SC
21	1.1160	0.0220	0.1244	0.0021	0.3777	760	11	756	12	752	37	206	2.1	212	2.1	216	2.7	1.0	0.5	XCR	CGZR, UC and POZ in rim, SR
22	1.1150	0.0230	0.1247	0.0025	0.7026	761	11	758	14	770	33	245	4.4	436	14	391	11	1.8	0.3	XCR	CGZR,WZC and POZ in rim, SC
23	1.1150	0.0300	0.1248	0.0025	0.3447	761	14	759	14	783	48	107	1.4	83	2.4	219	7.6	0.8	0.3	XCR	CGZR,WZC and POZ in rim, SC
24	1.1280	0.0250	0.1251	0.0023	0.4065	766	12	760	13	772	41	167	3.3	315	7.9	282	8.5	1.9	0.8	XCR	CGZR, UC and POZ in rim, SC
25	1.1190	0.0260	0.1251	0.0024	0.4483	762	12	760	14	784	43	85	1.3	37	0.43	90	1.7	0.4	0.3	XCR	CGZR, UC and POZ, SR
26	1.1090	0.0220	0.1253	0.0022	0.4621	758	10	761	13	752	35	136	2.7	126	1.7	183	2.7	0.9	-0.4	XCR	CGZR,WZC and POZ in rim, SR
27	1.1180	0.0240	0.1254	0.0024	0.4570	761	11	762	13	746	40	124	1.6	74	0.88	174	2.7	0.6	-0.2	XCR	CGZR,WZC and POZ in rim, SR
28	1.1200	0.0200	0.1258	0.0021	0.4201	763	9	764	12	768	31	174	2.1	83	1.4	196	3.4	0.5	-0.1	XCR	CGZR in core, POZ, SC
29	1.1390	0.0240	0.1262	0.0024	0.3892	771	11	767	13	787	40	222	3.5	500	5.5	247	5	2.3	0.5	XCR	CGZR in core, POZ, SR
30	1.1440	0.0330	0.1263	0.0025	0.3922	775	15	767	15	754	53	88	2.2	65	1.6	51	1.6	0.7	1.0	XCR	CGZR, UC and POZ in rim, SR
31	1.1240	0.0260	0.1265	0.0022	0.3673	762	13	768	13	755	45	93	1.3	60	0.62	51	1	0.7	-0.7	XCR	CGZR, UC and POZ, SR
32	1.1210	0.0230	0.1266	0.0022	0.4685	762	11	768	13	762	36	138	1.4	98	1	222	3.5	0.7	-0.8	XCR	CGZR,WZC and POZ in rim, SC
33	1.1420	0.0200	0.1268	0.0021	0.4133	773	10	769	12	768	32	250	4.6	234	12	505	24	0.9	0.5	XCR	CGZR, UC and POZ in rim, SR
34	1.1460	0.0220	0.1266	0.0023	0.3425	775	10	769	13	785	40	103	1.4	55	0.84	146	2.5	0.5	0.7	XCR	CGZR,WZC and POZ in rim, SR
35	1.1280	0.0200	0.1270	0.0022	0.4804	766	10	771	12	748	31	551	5.2	158	110	889	15	0.3	-0.5	XCR	CGZR,WZC and POZ in rim, SC
36	1.1390	0.0250	0.1273	0.0024	0.5221	771	12	772	14	775	38	233	4	646	26	195	3	2.8	-0.1	XCR	CGZR, POZ, SR
37	1.1320	0.0280	0.1273	0.0023	0.2593	768	13	773	13	745	50	127	2.5	394	7	103	2.4	3.1	-0.6	XCR	CGZR, POZ, SR
38	1.1490	0.0240	0.1275	0.0023	0.4070	777	11	774	13	779	38	95	1.7	48	0.71	85	1.5	0.5	0.4	XCR	CGZR, UC and POZ in rim, SC
39	1.1360	0.0230	0.1276	0.0023	0.4588	772	11	774	13	773	38	170	3.9	191	5.2	171	4.4	1.1	-0.2	XCR	CGZR, POZ, SR
40	1.1440	0.0210	0.1276	0.0023	0.5377	774	10	774	13	770	31	404	8.7	134	32	587	16	0.3	-0.1	XCR	CGZR,WZC and POZ in rim, SC
41	1.1550	0.0230	0.1281	0.0021	0.4597	780	11	777	12	786	35	110	1.2	66	0.8	124	2.4	0.6	0.5	XCR	CGZR, UC and POZ in rim, SR
42	1.1490	0.0230	0.1281	0.0025	0.5631	776	11	777	14	784	37	199	3.9	142	4.4	271	7.6	0.7	-0.1	XCR	CGZR,WZC and POZ in rim, SC
43	1.1550	0.0270	0.1284	0.0025	0.6194	778	13	778	14	775	36	121	2	62	0.88	167	2.6	0.5	0.0	XCR	CGZR,WZC and POZ in rim, SR
44	1.1500	0.0250	0.1284	0.0024	0.5732	778	12	778	14	785	37	86	1.1	50	0.7	93	1.8	0.6	-0.1	XCR	CGZR,WZC and POZ in rim, SC
45	1.1540	0.0260	0.1290	0.0025	0.4381	780	12	782	14	769	41	205	3.4	225	2.7	157	2.8	1.1	-0.3	XCR	CGZR,WZC and POZ in rim, SC
46	1.1570	0.0240	0.1295	0.0025	0.3494	782	12	785	14	784	43	109	1.4	95	0.92	145	2.5	0.9	-0.4	XCR	CGZR, UC and POZ in rim, SC
*47	1.0260	0.0220	0.1198	0.0022	0.3328	717	11	729	13	699	41	148.3	3.6	116.9	1.9	77.4	1.5	0.8	1.7	XCR	CGZR, UC and POZ, SR
*48	1.1380	0.0210	0.1210	0.0021	0.3839	771	10	736	12	846	35	226.7	3.9	283.6	7.5	257.6	6.4	1.3	4.5	RCR	CGZR, RCPZ, SR
*49	1.0610	0.0180	0.1178	0.0020	0.4714	736	9	718	12	776	30	248.8	3.4	333.3	6.1	769.5	9.9	1.3	2.4	XCR	CGZR, UC and POZ, SC
*50	1.1630	0.0240	0.1259	0.0023	0.4819	784	11	764	13	847	38	125.6	1.5	73.02	0.78	143.9	2.3	0.6	2.5	XCR	CGZR,WZC and POZ in rim, SR
*51	1.0350	0.0210	0.1151	0.0021	0.3587	721	11	702	12	778	41	190.1	5.3	205.2	6.9	161.2	5.8	1.1	2.7	XCR	CGZR in core and POZ, SC
*52	0.8460	0.0200	0.0990	0.0018	0.4822	622	11	609	10	658	43	101.8	1.3	50.8	1	79.9	1.8	0.5	2.1	XCR	CGZR in core and POZ, SR
*53	1.0040	0.0200	0.1128	0.0021	0.4627	706	10	689	12	752	35	176.1	1.9	144.8	4.6	149.2	6	0.8	2.5	XCR	CGZR, UC and POZ in rim, SC
*54	1.0520	0.0230	0.1156	0.0021	0.4210	731	11	705	12	814	40	132.2	2.1	83	2	202.1	5	0.6	3.6	XCR	CGZR,WZC and POZ in rim, SC
*55	1.1730	0.0230	0.1249	0.0023	0.5212	788	11	759	13	878	33	109.9	1.2	66.35	0.79	142.2	2.6	0.6	3.7	XCR	CGZR,WZC and POZ in rim, SR
*56	1.1260	0.0240	0.1190	0.0021	0.3275	765	11	725	12	884	41	111.9	1.9	89.85	0.88	182.3	2.6	0.8	5.3	XCR	CGZR, POZ, SC
*57	1.1170	0.0250	0.1186	0.0020	0.3839	761	12	723	12	871	39	227.5	4.6	258.6	5.6	218.5	4.6	1.1	5.1	XCR	CGZR, UC and POZ in rim, SC
*58	1.1250	0.0220	0.1185	0.0022	0.5226	764	11	721	13	874	34	153.3	1.8	79.63	0.9	200.6	3.1	0.5	5.6	XCR	CGZR, UC and POZ in rim, SC
*59	1.0960	0.0200	0.1159	0.0020	0.4246	751	10	707	11	885	34	239	3.9	639.2	9.4	225.1	3.7	2.7	5.9	XCR	CGZR in core and POZ, SC
*60	0.8580	0.0180	0.1004	0.0018	0.3549	628	10	617	10	655	40	131.3	1.7	2.02	0.1	2.96	0.29	0.0	1.7	XCR	CGZR, UC and POZ in rim, SR

*disc D=[1-((206Pb/238U) ⁄ (207Pb/235U))] × 100; * discordant data that were not used for age calculations

CGZR – complex growth zoning with resorption
POZ – polygonal oscillatory zoning
CGZ – complex growth zoning
XCR – xenocrystic core and rim
WZC – weakly zoned core
UC – unzoned core
RCR – relic core and rim
XCBR – xenocrystic core and CL-bright rim
XCBCR – xenocrystic core and CL-bright core and rim
RCR – RCRrelic core and rim
SC – spot in core
SR – spot in rim
RCPZ – relic core and patchy zoning

Data from a syenite rock sample, DE474B

No.	Corrected isotope ratios					Apparent ages (Ma)						U, Th and Pb content (ppm)							*disc.
	$^{207}Pb/^{235}U$	±2s	$^{206}Pb/^{238}U$	±2s	error corr.	$^{207}Pb/^{235}U$	±2s	$^{206}Pb/^{238}U$	±2s	$^{207}Pb/^{206}U$	±2s	Approx U	±2s	Approx Th	±2s	Approx Pb	±2s	Th/U	%
Sample DE474B																			
1	0.8560	0.0150	0.1013	0.0012	0.2803	628	8	623	7	661	44	186.5	2.8	103.6	1.5	99.9	2.1	0.6	0.9
2	0.8690	0.0170	0.1028	0.0014	0.2616	635	9	631	8	652	48	150.7	2.1	91.4	1.2	84.5	1.8	0.6	0.7
3	0.8560	0.0140	0.1016	0.0012	0.2866	627	8	624	7	676	40	214.2	2.1	115.6	1.2	107.7	1.7	0.5	0.6
4	0.8660	0.0200	0.1025	0.0014	0.2156	634	11	629	8	693	54	86	1.3	39.41	0.52	36.42	0.85	0.5	0.8
5	0.8580	0.0150	0.1022	0.0012	0.3288	631	8	627	7	694	42	148.9	2.5	88.5	1.4	84.5	1.7	0.6	0.6
6	0.8680	0.0150	0.1023	0.0013	0.4047	634	8	628	8	593	42	172.8	2.6	91.4	1.5	86.3	1.6	0.5	1.0
7	0.8510	0.0200	0.1019	0.0014	0.0860	625	11	625	8	576	60	79	1.2	38.06	0.61	35.74	0.98	0.5	0.0
8	0.8480	0.0170	0.1023	0.0013	0.2883	623	9	628	8	593	46	137.5	2.4	93.7	1.7	89.6	1.8	0.7	-0.7
9	0.8590	0.0180	0.1024	0.0015	0.2968	630	10	628	9	625	48	107.2	1.4	55.38	0.61	53.8	1	0.5	0.2
10	0.8610	0.0190	0.1025	0.0014	0.1430	631	10	629	8	635	55	74.1	1.3	21.23	0.33	20.52	0.71	0.3	0.2
11	0.8590	0.0170	0.1019	0.0013	0.3540	629	9	626	8	613	47	113.7	1.7	31.66	0.36	29.23	0.88	0.3	0.5
12	0.8610	0.0170	0.1025	0.0014	0.2167	630	9	629	8	608	50	97.7	1.4	36.6	0.5	36.11	0.95	0.4	0.2
13	0.8680	0.0200	0.1025	0.0015	0.2463	632	11	629	9	659	56	94.7	1.1	45.69	0.54	45.9	1.1	0.5	0.5
14	0.8520	0.0170	0.1020	0.0015	0.3382	626	9	626	9	640	48	115.6	1.3	42.98	0.42	43	1	0.4	0.0
15	0.8670	0.0200	0.1029	0.0017	0.3871	635	11	631	10	622	56	94.6	1.4	44.82	0.61	44.5	1.2	0.5	0.6
16	0.8620	0.0210	0.1026	0.0017	0.4296	629	11	629	10	635	54	88.6	1.8	39.13	0.46	39.14	0.98	0.4	-0.1
17	0.8670	0.0160	0.1022	0.0014	0.4348	634	9	627	8	660	44	159.5	2.6	84	1.2	83.2	1.7	0.5	1.1
18	0.8760	0.0220	0.1035	0.0017	0.3355	637	12	635	10	687	57	58.5	1.2	21.05	0.43	21.53	0.82	0.4	0.3
19	0.8700	0.0190	0.1036	0.0017	0.3972	636	10	636	10	659	54	104.2	1.3	57.43	0.98	56.2	1.3	0.6	0.1
20	0.8760	0.0160	0.1032	0.0014	0.3618	638	9	633	8	689	44	138.8	1.9	101.7	1	99.3	1.6	0.7	0.8
21	0.8590	0.0200	0.1029	0.0016	0.2473	630	11	631	9	679	53	75.85	0.9	21.8	0.28	21.48	0.74	0.3	-0.2
22	0.8690	0.0180	0.1034	0.0015	0.3562	634	10	634	9	684	50	138.4	2.5	76.6	1.3	75.5	1.9	0.6	0.0
23	0.8640	0.0180	0.1019	0.0014	0.3795	631	10	626	8	711	50	96.5	1.1	41.22	0.44	40.3	0.99	0.4	0.9
24	0.8800	0.0190	0.1034	0.0015	0.2979	639	10	635	9	709	51	81.3	1.5	30.24	0.65	29.77	0.9	0.4	0.7
25	0.8600	0.0180	0.1021	0.0014	0.4629	629	10	627	8	626	43	141.3	2	81.5	1.1	79.4	1.6	0.6	0.4
26	0.8580	0.0200	0.1033	0.0016	0.3701	629	11	633	9	558	54	83.08	0.91	33.68	0.34	32.24	0.75	0.4	-0.7
27	0.8570	0.0200	0.1019	0.0014	0.2487	627	11	626	9	562	56	84.91	0.96	27.52	0.35	26.38	0.72	0.3	0.2
28	0.8580	0.0160	0.1021	0.0014	0.3632	629	9	627	8	586	42	137	2.1	80.06	0.98	77.3	1.6	0.6	0.4
29	0.8590	0.0170	0.1020	0.0013	0.2192	628	9	626	8	552	47	136.1	1.5	86.73	0.84	82.5	1.4	0.6	0.3
30	0.8490	0.0150	0.1025	0.0013	0.2809	623	9	629	8	526	43	153.8	2.7	88	1.3	83.6	1.8	0.6	-0.9
31	0.8500	0.0150	0.1018	0.0012	0.3537	625	8	625	7	549	42	182.5	3.1	130.4	2.5	123.8	2.7	0.7	0.0
32	0.8690	0.0190	0.1032	0.0014	0.1664	635	11	633	8	690	53	124.2	1.6	54.93	0.66	53	1.2	0.4	0.3
33	0.8820	0.0200	0.1041	0.0014	0.2327	642	11	639	8	711	55	84.7	1.1	36.59	0.37	34.98	0.94	0.4	0.5
34	0.8700	0.0200	0.1034	0.0016	0.3768	635	11	634	9	629	50	82.3	1.5	40.75	0.6	39.43	0.94	0.5	0.1
35	0.8740	0.0170	0.1039	0.0015	0.4232	637	9	637	9	612	48	140.3	1.8	75.63	0.81	71.7	1.3	0.5	-0.1
36	0.8630	0.0220	0.1025	0.0016	0.3196	632	12	629	9	597	56	50.11	0.76	14.26	0.21	12.97	0.49	0.3	0.5
37	0.8570	0.0190	0.1032	0.0016	0.2510	630	10	633	9	561	52	77.9	1.3	35.64	0.53	34.71	0.94	0.5	-0.5
38	0.8600	0.0160	0.1032	0.0013	0.3685	630	9	633	8	566	46	133.2	2.2	79.2	1.3	77.2	1.7	0.6	-0.5
39	0.8630	0.0200	0.1030	0.0014	0.3420	633	11	633	8	586	53	124.2	1.8	75.5	1	72.5	1.6	0.6	0.1
40	0.8690	0.0180	0.1030	0.0013	0.2362	633	10	632	8	577	51	106.5	2.3	60.1	1.5	58.1	1.6	0.6	0.2
41	0.8580	0.0170	0.1022	0.0012	0.2672	629	9	627	7	586	48	88	1.3	22.69	0.3	22.45	0.77	0.3	0.2
42	0.8640	0.0160	0.1024	0.0013	0.3504	631	9	629	8	592	42	137.4	2.3	82.9	1.3	77.8	1.8	0.6	0.4
43	0.8540	0.0150	0.1017	0.0013	0.3201	626	8	624	7	583	44	135.2	1.8	76.4	1.4	71.9	1.8	0.6	0.3
44	0.8600	0.0180	0.1025	0.0012	0.4234	631	10	630	7	595	47	122.9	1.8	75.7	1	72.9	1.5	0.6	0.2
45	0.8520	0.0190	0.1016	0.0013	0.2680	625	10	624	8	629	52	75.3	1.1	35.48	0.49	34.25	0.84	0.5	0.1
46	0.8600	0.0150	0.1024	0.0013	0.4286	629	8	628	7	666	42	145.6	2.5	80.6	1.3	76.8	1.6	0.6	0.1
47	0.8660	0.0190	0.1024	0.0012	0.3638	633	11	628	7	650	49	67	0.85	16.73	0.24	15.69	0.55	0.2	0.7
48	0.8650	0.0160	0.1025	0.0014	0.2632	632	9	630	8	633	47	142.5	2.5	80.2	1.4	76.4	1.6	0.6	0.3
49	0.8700	0.0170	0.1021	0.0013	0.2829	635	9	627	8	638	46	127.8	1.8	73.05	0.93	68.6	1.5	0.6	1.3
50	0.8650	0.0170	0.1024	0.0014	0.3017	632	10	629	8	634	46	104.5	1.1	56.76	0.51	54.7	1	0.5	0.5
51	0.8550	0.0200	0.1023	0.0014	0.3407	631	11	628	8	598	49	83.3	1.2	32.99	0.51	31.29	0.75	0.4	0.5
52	0.8600	0.0170	0.1031	0.0014	0.2547	628	10	633	8	602	48	117.6	2.5	67.6	1.3	65.3	1.5	0.6	-0.7
53	0.8720	0.0200	0.1043	0.0015	0.2837	636	10	639	9	628	53	74.4	1	36.52	0.51	35.12	0.91	0.5	-0.4
54	0.8630	0.0190	0.1032	0.0015	0.3506	631	10	633	9	655	51	96	4	49.3	1.9	46.8	1.9	0.5	-0.2
55	0.8670	0.0150	0.1026	0.0015	0.4104	633	8	629	9	686	42	195.3	3.6	126.8	3	120.2	3.1	0.6	0.6
56	0.8670	0.0220	0.1037	0.0015	0.3636	632	12	636	9	705	56	69.2	0.99	33.39	0.43	32.27	0.84	0.5	-0.6
57	0.8650	0.0210	0.1038	0.0014	0.4230	634	12	636	8	722	50	89.8	1	44.44	0.48	41.4	1.1	0.5	-0.4
58	0.8730	0.0180	0.1039	0.0014	0.2830	636	10	637	8	767	49	96.8	1.2	52.38	0.66	50	1.2	0.5	-0.1
59	0.8650	0.0190	0.1028	0.0014	0.3400	633	10	630	8	747	52	121.9	2.9	67.9	1.9	65.1	1.9	0.6	0.3

*disc D=[1-((206Pb/238U)∕(207Pb/235U))] × 100; * discordant data that were not used for age calculations

Data from a leucogranite dyke sample DE486

No.	Corrected isotope ratios					Apparent ages (Ma)						U, Th and Pb content (ppm)							*disc.
	$^{207}Pb/^{235}U$	±2s	$^{206}Pb/^{238}U$	±2s	error corr.	$^{207}Pb/^{235}U$	±2s	$^{206}Pb/^{238}U$	±2s	$^{207}Pb/^{206}U$	±2s	Approx U	±2s	Approx Th	±2s	Approx Pb	±2s	Th/U	%
Sample DE486																			
1	1.1360	0.0210	0.1261	0.0021	0.5601	771	10	765	12	785	23	927	13	651	11	581.8	6.4	0.7	0.7
2	1.1250	0.0210	0.1250	0.0022	0.6258	765	10	759	12	758	23	737	16	710	15	491.5	9.5	1.0	0.7
3	1.1060	0.0220	0.1233	0.0023	0.7222	756	11	749	13	753	24	728	11	614.7	9.3	592.9	8.7	0.8	1.0
4	1.1220	0.0240	0.1248	0.0022	0.6441	764	12	759	13	760	27	390	7	244.3	5.2	267.1	4.9	0.6	0.6
5	1.1400	0.0220	0.1271	0.0024	0.5884	773	10	771	14	783	27	511	10	327.5	6.8	384.5	7.3	0.6	0.2
6	1.1170	0.0220	0.1254	0.0023	0.5305	762	11	761	13	766	30	473.1	6.7	793	12	406.3	6.5	1.7	0.1
7	1.1110	0.0220	0.1241	0.0023	0.6196	757	11	755	13	772	27	407.7	5.9	383.3	5.5	192.2	3.3	0.9	0.4
8	0.8650	0.0260	0.1029	0.0021	0.2634	632	14	631	12	626	56	55.5	1.1	10.03	0.22	11.35	0.63	0.2	0.2
9	0.8440	0.0180	0.1020	0.0018	0.4261	622	10	626	11	614	37	245.7	4.2	63.42	0.94	76.9	1.8	0.3	-0.7
10	1.1300	0.0220	0.1272	0.0022	0.7056	768	11	772	13	783	23	599	16	312.1	9	465	12	0.5	-0.5
11	0.8480	0.0230	0.1009	0.0020	0.2409	624	12	619	12	643	48	68	1.1	11.0	0.17	11.4	0.56	0.2	0.8
12	0.8360	0.0200	0.1012	0.0019	0.4218	616	11	621	11	603	41	224.6	4.4	12.7	0.031	0.85	0.28	0.1	-0.8
13	1.1040	0.0210	0.1236	0.0022	0.5986	756	11	751	13	771	27	481	11	648	22	895	21	1.3	0.6
14	0.8830	0.0170	0.1047	0.0019	0.5529	643	9	642	11	646	28	559.7	9.8	46.6	1.9	66.8	3.2	0.1	0.2
15	1.1200	0.0230	0.1258	0.0023	0.6458	764	11	765	13	764	26	498	7.7	285	3.2	386.3	4.8	0.6	-0.1
16	0.8930	0.0180	0.1044	0.0014	0.4611	648	10	641	8	661	38	240.9	3.1	25.2	0.42	29	1.3	0.1	1.0
17	1.1120	0.0210	0.1260	0.0022	0.5993	759	10	765	13	755	24	788	12	472.3	5.6	579.4	6.5	0.6	-0.9
18	1.1140	0.0220	0.1252	0.0022	0.7469	759	11	761	13	756	22	575	13	326.8	7.2	486.6	9.4	0.6	-0.3
19	1.1340	0.0200	0.1272	0.0020	0.7282	770	10	772	12	765	19	1049	19	997	23	733	14	1.0	-0.3
20	1.1410	0.0260	0.1270	0.0025	0.5916	772	12	770	14	787	31	466.2	6.7	228.9	3.6	129.3	2.4	0.5	0.2
21	1.1040	0.0200	0.1239	0.0021	0.6450	756	10	753	12	779	23	1813	28	3379	61	814	13	1.9	0.4
22	1.1070	0.0230	0.1238	0.0022	0.5183	755	11	753	13	766	31	793.9	9.9	1045	14	179.8	2.7	1.3	0.3
*23	1.3110	0.0230	0.1175	0.0019	0.5358	851	10	717	11	1212	23	1002	17	958	43	639.9	8	1.0	-10.0
*24	1.0840	0.0190	0.1188	0.0020	0.6713	745	9	723	11	815	20	1296	31	780	18	883	20	0.6	-20.9
*25	1.1080	0.0190	0.1222	0.0021	0.6493	757	9	743	12	808	21	1015	14	595.6	9.5	832	13	0.6	-29.0
*26	1.3530	0.0360	0.1163	0.0021	0.3658	863	15	710	12	1273	38	283.3	5	158.3	3.6	238.5	4.2	0.6	20.0
*27	1.1170	0.0230	0.1230	0.0023	0.5294	762	11	747	13	815	31	301.4	3.7	189.2	2.2	261.9	4.1	0.6	-18.2
*28	1.0840	0.0200	0.1210	0.0019	0.5294	745	10	736	11	765	25	648.4	9.1	196.9	2.8	281.9	4.5	0.3	-12.2
*29	1.1360	0.0260	0.1200	0.0020	0.5231	768	11	730	12	859	27	1484	16	1029	15	1055	18	0.7	-9.1
*30	1.1900	0.0240	0.1132	0.0020	0.4933	795	11	691	12	1102	28	349	14	350.3	9.3	353.4	8.8	1.0	-9.1
*31	1.0870	0.0200	0.1195	0.0020	0.6426	747	10	728	11	808	22	775	13	448.5	9.8	497.8	9.9	0.6	-11.1
*32	1.1550	0.0220	0.1246	0.0021	0.6050	779	10	757	12	840	26	943	20	589	18	720	18	0.6	-20.0
*33	1.1030	0.0200	0.1224	0.0021	0.7410	755	10	744	12	772	19	857	12	366.5	5.1	494.1	6.4	0.4	-22.4
*34	1.2570	0.0390	0.1272	0.0022	0.4550	822	17	772	13	958	45	336.6	6.9	151.1	3.2	272	8.8	0.4	23.5
*35	1.1090	0.0190	0.1201	0.0020	0.6228	757	9	731	12	851	21	2715	31	11590	320	1092	17	4.3	-27.7
*36	1.1430	0.0210	0.1259	0.0021	0.6043	774	10	764	12	813	23	3634	87	23600	1300	1151	27	6.5	-21.2
*37	0.9710	0.0190	0.0979	0.0020	0.3927	690	10	602	12	972	33	525	12	192.9	6.1	275	10	0.4	-25.0
*38	1.1450	0.0210	0.1175	0.0020	0.6424	775	10	716	11	960	21	517.4	6.8	506.1	6.1	480.7	5.3	1.0	-10.0
*39	0.9070	0.0190	0.1015	0.0018	0.2301	655	10	623	11	750	38	218.8	3.4	80.4	3.1	28.2	1.8	0.4	-10.0

*D=[1-((206Pb/238U)∕(207Pb/235U))] × 100; 24% of samples were filtered above 1 percent threshold

Data from syn-tectonic granite sample, DE475

No.	Corrected isotope ratios					Apparent ages (Ma)						U, Th and Pb content (ppm)							*disc.
	$^{207}Pb/^{235}U$	±2σ	$^{206}Pb/^{238}U$	±2σ	error corr.	$^{207}Pb/^{235}U$	±2σ	$^{206}Pb/^{238}U$	±2σ	$^{207}Pb/^{206}U$	±2σ	Approx U	±2σ	Approx Th	±2σ	Approx Pb	±2σ	Th/U	%
Sample DE475																			
1	0.8590	0.0290	0.1041	0.0020	0.2267	632	16	638	12	623	76	42.69	0.8	15.78	0.26	15.23	0.58	0.4	-0.9
2	0.9010	0.0190	0.1069	0.0017	0.5929	652	10	655	10	647	46	403.5	5.2	276.5	3.4	277.4	3.6	0.7	-0.4
3	0.8720	0.0200	0.1049	0.0018	0.4806	637	11	643	10	622	50	228.2	3.4	122.9	1.8	126	2.5	0.5	-1.0
4	0.8920	0.0200	0.1052	0.0018	0.5573	648	11	644	10	655	48	325.9	5.2	182.6	2.6	191.4	3.1	0.6	0.5
5	0.8800	0.0290	0.1058	0.0020	0.3271	641	15	648	12	593	71	51.24	0.9	14.51	0.28	15.62	0.6	0.3	-1.0
6	0.9160	0.0220	0.1065	0.0018	0.5493	660	12	653	11	686	49	179.7	5.7	145.3	5.1	157.5	4.7	0.8	1.0
7	0.9060	0.0180	0.1064	0.0017	0.4913	655	10	651	10	663	45	422.8	5.7	341.6	4.7	391.5	5.9	0.8	0.5
8	0.9160	0.0210	0.1088	0.0017	0.4583	661	11	666	10	640	51	183.6	5	91.3	5.1	110.3	5.4	0.5	-0.8
9	0.8810	0.0190	0.1037	0.0017	0.5344	641	10	636	10	662	47	354.7	7.8	207.5	4.4	223	5.7	0.6	0.8
10	0.8930	0.0190	0.1049	0.0017	0.2347	648	10	643	10	651	51	204.8	3	112.6	2	127	2.4	0.5	0.7
11	0.9010	0.0200	0.1071	0.0019	0.5694	652	11	656	11	644	48	371.4	6.8	183.8	4.7	201	5.1	0.5	-0.7
12	0.8860	0.0200	0.1061	0.0018	0.5646	643	10	650	10	630	49	335	4.6	233.6	3.1	245.6	4.2	0.7	-1.0
13	0.8960	0.0180	0.1067	0.0017	0.5652	649	10	653	10	643	46	385.3	6.6	42.04	0.7	46.9	1.4	0.1	-0.7
14	0.9120	0.0210	0.1079	0.0020	0.5651	658	11	660	11	654	49	274.2	7	125.9	4	142.4	3.8	0.5	-0.3
15	0.8840	0.0200	0.1045	0.0018	0.5854	643	11	641	10	654	45	408.8	5.9	208.5	2.7	205.5	3.6	0.5	0.4
16	0.8910	0.0190	0.1054	0.0018	0.5483	646	10	646	10	642	47	464.7	9.3	232	4.6	226.1	4.8	0.5	0.0
17	0.8980	0.0200	0.1055	0.0018	0.3984	649	11	646	11	650	50	284.6	4.9	189.2	3.1	181.4	3.3	0.7	0.4
18	0.8890	0.0210	0.1044	0.0019	0.4811	645	11	640	11	661	52	222	5.5	126.7	3.1	120.7	2.8	0.6	0.8
19	0.8840	0.0200	0.1046	0.0021	0.6613	642	11	641	12	648	48	440.2	8	294.6	4.4	280.8	5.7	0.7	0.1
20	0.8790	0.0210	0.1047	0.0020	0.4894	641	11	642	12	626	54	167.8	3.4	54.1	1.5	52.8	1.5	0.3	-0.2
21	0.8710	0.0200	0.1043	0.0019	0.5200	636	11	639	11	631	50	329.5	8	189.5	8.3	163	7	0.6	-0.6
22	0.8720	0.0230	0.1039	0.0020	0.3401	637	13	637	11	637	60	122.8	1.8	77.6	2	72.5	2.5	0.6	0.0
23	0.9280	0.0220	0.1079	0.0023	0.5503	665	12	661	13	694	54	254.2	7.7	254.3	9.1	234.7	7.5	1.0	0.6
24	0.8900	0.0220	0.1049	0.0020	0.4528	647	12	645	11	659	54	176.3	3.1	108.9	1.7	99.5	2.2	0.6	0.3
25	0.8790	0.0200	0.1050	0.0020	0.4266	640	11	643	11	632	55	215.3	4.5	129.8	2.6	123.3	2.6	0.6	-0.4
26	0.8840	0.0230	0.1056	0.0021	0.3997	645	12	648	13	645	58	115.3	3.2	54.8	2.1	52.8	2.1	0.5	-0.4
27	0.8920	0.0190	0.1057	0.0020	0.6762	647	10	649	11	661	45	745	21	73	1.9	69.5	2	0.1	-0.3
28	0.8880	0.0180	0.1051	0.0018	0.6121	646	10	645	10	644	46	990	21	64	1.2	61.6	1.5	0.1	0.1
29	0.8670	0.0210	0.1037	0.0021	0.4694	635	11	636	12	623	54	159.3	6	75	1.8	72.8	2.1	0.5	-0.2
30	0.8980	0.0220	0.1059	0.0021	0.3774	650	12	650	12	665	60	136.3	3.1	62	1.2	60	1.7	0.5	0.0
31	0.8790	0.0210	0.1047	0.0019	0.5032	639	11	641	11	634	51	217.7	4.4	299.1	5.1	276.6	4.4	1.4	-0.4
32	0.8800	0.0200	0.1047	0.0018	0.4045	642	11	642	10	633	52	263.9	7.5	163.4	4.8	156.8	4.6	0.6	0.0
33	0.8800	0.0230	0.1045	0.0018	0.2683	639	13	641	11	640	62	121.2	2.4	61.6	1	57.7	1.4	0.5	-0.3
34	0.9860	0.0230	0.1132	0.0022	0.6452	696	12	691	13	737	50	387.9	7.2	49.9	1.1	47.8	1.5	0.1	0.7
35	0.8590	0.0180	0.1025	0.0018	0.5503	628	10	629	10	630	49	351.7	4.8	223.1	2.6	203.3	3.3	0.6	-0.1
36	0.8900	0.0190	0.1046	0.0018	0.5810	645	10	641	11	660	47	498.2	6.9	275.4	4.1	249.8	4.6	0.6	0.7
37	0.9140	0.0190	0.1081	0.0019	0.5382	662	10	662	11	650	49	335.2	5.4	238.6	3.4	233.4	3.7	0.7	0.1
38	0.8860	0.0200	0.1049	0.0018	0.5778	644	11	644	11	636	48	266.9	3.3	161.4	2.1	157.1	2.7	0.6	0.0
39	0.8930	0.0200	0.1049	0.0020	0.6055	647	11	643	11	671	48	339.1	5.9	225.8	3.8	209.6	4	0.7	0.6
40	0.9010	0.0200	0.1055	0.0018	0.4744	653	10	646	11	668	51	248.9	3.3	124.9	1.6	121.1	2.6	0.5	1.0
41	0.9520	0.0210	0.1103	0.0020	0.5873	679	11	674	12	690	46	479	8.3	87.4	1.5	95.8	2.3	0.2	0.7
42	0.9000	0.0260	0.1056	0.0020	0.3085	651	14	647	12	681	62	47.73	0.7	15.27	0.36	17.06	0.71	0.3	0.6
43	0.8900	0.0190	0.1045	0.0018	0.4752	646	10	641	11	659	49	319.8	6.1	175	3.6	183.2	4	0.5	0.9
44	0.9380	0.0200	0.1091	0.0020	0.5238	673	11	667	12	677	50	222.6	3.7	35.65	0.7	38.8	1.2	0.2	0.8
45	0.8740	0.0240	0.1035	0.0019	0.3772	637	13	634	11	640	61	60.56	0.8	13.6	0.16	13.89	0.56	0.2	0.4
46	0.8710	0.0200	0.1037	0.0017	0.3583	635	11	636	10	639	51	206.3	2.3	329.5	3.8	329	5.5	1.6	-0.1
47	0.9000	0.0210	0.1061	0.0018	0.5206	651	11	650	10	662	49	158.5	3.7	95.6	2.6	97.1	2.5	0.6	0.2
*48	0.8690	0.0180	0.1002	0.0015	0.4861	635	10	616	9	701	46	332.9	5.8	289.5	7.2	267	6.8	0.9	3.1
*49	0.9550	0.0210	0.1100	0.0020	0.6028	682	11	672	12	680	46	460.7	7.2	82.1	1.2	90	1.8	0.2	1.4
*50	0.9280	0.0230	0.1074	0.0022	0.6252	667	12	657	13	699	51	392	22	291	21	278	18	0.7	1.5
*51	0.8500	0.0370	0.1049	0.0024	0.1909	624	20	645	14	554	95	20.89	0.3	8.12	0.13	8.12	0.44	0.4	3.4
*52	0.9080	0.0180	0.1051	0.0017	0.4110	657	10	644	10	696	47	260.7	3.2	132	1.5	133.8	1.9	0.5	1.9
*53	0.8740	0.0210	0.1059	0.0019	0.3901	638	11	649	11	619	55	224	6.6	167.7	4.1	152.7	4.3	0.7	1.7
*54	0.8870	0.0190	0.1028	0.0018	0.4535	644	10	630	11	693	48	236.6	3.4	190.2	3.2	184.7	3.1	0.8	2.1

*disc D=[1-((206Pb/238U)∕(207Pb/235U))] × 100; * discordant data that were not used for age calculations

Appendix 3

Geoheritage (2019) 11:1643–1653
https://doi.org/10.1007/s12371-019-00393-y

ORIGINAL ARTICLE

Inventory of Key Geosites in the Butajira Volcanic Field: Perspective for the First Geopark in Ethiopia

Leta Megerssa[1,2,3] · Vladislav Rapprich[3] · Roman Novotný[3] · Kryštof Verner[1,3] · Vojtěch Erban[3] · Firdawok Legesse[2] · Mihret Manaye[4]

Received: 9 July 2019 / Accepted: 26 July 2019 / Published online: 12 August 2019

Abstract
Notable attractions of a geological environment in Ethiopia are described as potential for geosites. Apart from the UNESCO-recognised sites of cultural and historical values, we appraise the potential of a volcanic landscape endowed with multitude of natural attractions in central Main Ethiopian Rift near the town of Butajira. A volcano that stands still with the crystalized lava flow from its top to several kilometres forming a lava canyon, a spectacular crater lake, a mystic cave in a basaltic rock, a series of majestic waterfalls, and geysers and still the rich local cultural and cuisine experiences all converge at the locality. Each of the attractions is described and put to context as call out to the concerned entities for the attention to develop a scheme for appraising, developing, and protecting such sites elsewhere in the country and utilise them as additional attractions.

Keywords Volcanic geoheritage · Continental rift · Volcanic field · Scoria cone · Maar · Butajira volcanic field

Introduction

The interest in geoheritage- and geology-focused geotourism has increased rapidly in the last two decades, and tourism located around geological features is becoming an important source of income in many rural areas (e.g. Brocx and Semeniuk 2007; Dowling 2011). This trend is reflected and also accelerated by initiatives establishing national, European, and global geopark networks, which seek to promote and conserve the planet's geological heritage, as well as encourage sustainable research and development by the communities concerned (e.g. Zouros and McKeever 2004; Horváth and Csüllög 2013; Woo et al. 2013; Fung and Jim 2015; Žáček et al. 2017). The Global Geopark Network includes 120 areas in 33 countries but only two areas have the status of a Global Geopark in the entire continent of Africa: M'Goun Global Geopark in Morocco and Ngorongoro Lengai Geopark in Tanzania (Global Geoparks Network, 2019.) Besides this, the whole continent of Africa possesses 37 natural and five mixed natural-cultural UNESCO properties (World Heritage Convention, 2019) and numerous areas with various degrees of protection, many of them with a great potential for geotourism (for a definition of the term 'geotourism' see Dowling 2011).

Tourism represents an important sector of the growing economy in Ethiopia (NPC 2016). The country is endowed with numerous tourist attractions in addition to wild life which is among the most threatened faunal diversity in the current state (e.g. Gottelli et al. 2004; Gebremedhin et al. 2009). Some of the attractions include those recognised as UNESCO (mostly cultural) heritages (World Heritage Convention, 2019), namely Rock-Hewn Churches of Lalibela (Renzulli et al. 2011), Simien

This article is part of the Topical Collection on Geoheritage: the foundation for sustainable geotourism

✉ Leta Megerssa
Megerssal@natur.cuni.cz

Vladislav Rapprich
vladislav.rapprich@geology.cz

Firdawok Legesse
firdelegese@gmail.com

Mihret Manaye
mihret.manaye@gmail.com

1 Faculty of Science, Institute of Petrology and Structural Geology, Charles University in Prague, Albertov 6, 128 43 Prague, Czech Republic

2 Geological Survey of Ethiopia, P.O. Box 2302, Addis Ababa, Ethiopia

3 Czech Geological Survey, Klárov 3, 118 21 Prague, Czech Republic

4 Construction Design and Supervision Enterprise of Ethiopia, Addis Ababa, Ethiopia

Mountains National Park (Asrat et al. 2012), Fasiledes Ghebbi ruins of a medieval castle in Gondar Region (Zerihun 2017), and Obelisks in the ruins of the ancient city of Aksum (Hagos et al. 2017) that lasted from first to eighth century AD (Fig. 1). Among others, palaeontological finds such as the oldest ever almost complete hominid skeleton nicknamed Lucy and the lately added find of an older skeleton nicknamed Ardi with ages of 3.2 and 4.4 million years old respectively (Kimbel and Delezene 2009; Potts 2012) are notable.2009; Potts 2012). Similar rich archaeological sites of the Lower Valley of the Omo River also add up to more intriguing offers of the region. About 46 twelfth and fourteenth centuries (Joussaume 1985; Christopher 2006) steles are found near Soddo town at the locality called Tiya with yet another wonder for the archaeological and prehistoric enthusiasts and explorers decorated with rich symbols and marks not yet fully deciphered. Similar extensive steles estimated around 10,000 pieces (Christopher 2006) are also listed from a number of sites throughout Ethiopia such as the Tuto Fela and Tututi near the town of Dilla and further south. The defensive walls locally called Jegol running 3342 m long around the Fortified Historic Town of Harar built in the sixteenth century are on the other hand still lively with open arms for tourists (Hailu 2007). In terms of landscape, Konso Cultural Landscape with its stone-walled terraces and fortified settlements in the highlands is nothing but an exemplary for resilience towards its arid environment making the settlement lush green and fertile whilst also fostering existence of generation of inhabitants with unique local administration (Watson 2009).

Establishing the geoparks and/or geosites in rural or developing regions has a potential for sustainable development producing numbers of jobs (e.g. Žáček et al. 2016). In Ethiopia, such initiative might help in economic development of areas with great potential, but also vulnerable environment. The first area proposed for potential geopark is located within the Simien Mountains National Park (Asrat et al. 2012) in Northern Ethiopia. Probably, the actual presence of the National Park in Simien Mountains reduces the urgency for establishing the geopark in this area.

Geological projects conducted within the framework of the Czech Development Cooperation in Ethiopia were focused on water resources and geohazards (e.g. Rapprich et al. 2016; Kycl et al. 2017). Similarly to geohazard projects of the Czech Development Cooperation in Nicaragua (Žáček et al. 2017), the systematic geological investigation led to discovery of area with significant geo-touristic potential. In this contribution, we highlight the potential of the Butajira volcanic field area (Fig. 1) that can be considered worthy of being considered as the first geopark in Ethiopia. The Butajira volcanic field (BVF) represents an area of picturesque landscape of sub-recent monogenetic volcanic field aligned along the margin of the continental rift with well-developed and exposed links between tectonics and volcanism on the continental rift margin (see, e.g. van Wyk de Vries et al. 2018). Similar studies have been applied in other similar geologic setting for example in Argentina (Risso et al. 2006). These links can be well demonstrated and explained in the BVF landscape, and correlated to Chaine des Puys landscape in France, exposed under distinct climatic and vegetation conditions. The area of BVF is inhabited by the Guraghe and Silte tribes with specific culture. In addition, the traditional housing

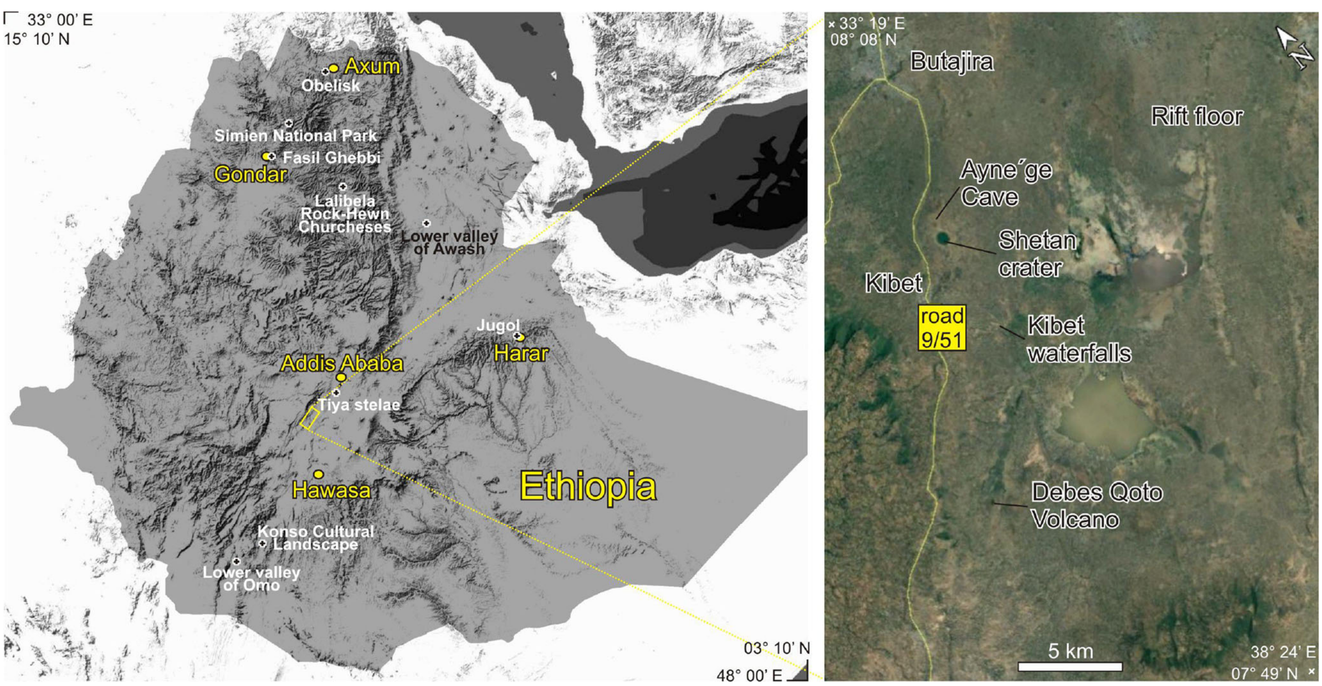

Fig. 1 Location of Butajira volcanic field (BVF) and notable UNESCO heritage sites (left). Described Geosites in BVF (right).

architecture is well inspired by shape of the volcanic cones, being in harmony with each other (Fig. 2). Last but not least, the BVF is well accessible and provides good accommodation and alimentation facilities at various levels of comfort in Butajira Town. Together with its location on the main road towards the southern attractions make the listed advantages BVF good candidate for additional tourist target on the long way to Southern Ethiopia.

The BVF has not yet earned the worldwide fame it deserves, and as a first step for promoting a new geopark area, the principal geosites and their geoheritage, education, and hazard-communication values are summarised in this contribution. We also provide an example, how other areas in Eastern Africa can be promoted as geoheritage valuable areas, complementing the worldwide known faunal values.

Geological and Cultural Setting

Geology

This monogenetic volcanic field is located on the edge of an active continental rift and provides insight into the relationship between extensional tectonics and basaltic volcanism in a continental rift setting. Rows of scoria cones can be viewed from rift scarps whilst the rift floor is observed from peaks of these numerous aligned scoria cones respectively.

The Butajira volcanic field is located in the Silti-Butajira-Debre Zeyit Fault Zone (SBDFZ) on the western margin of the Main Ethiopian Rift (MER). SBDFZ is basically followed by linear chains of numerous scoria cones and associated lava flows (e.g. Rooney et al. 2011). The extent of the SBDFZ has been proposed to include the foot of the western rift escarpment from 6.5° N to 9° N (Rooney et al. 2011). The BVF is hence a part among the three geographically distinct but adjacent quaternary and active volcanic systems (from south to north: Bilate volcanic field, Butajira volcanic field, Bishoftu volcanic field), making up this belt (e.g. Mazzarini et al. 2013).

Fig. 2 Landscape of volcanic cones with Saar-bet (Tukul or grass-roofed house)

Distinct in terms of rift trend, fault timing, and patterns and lithospheric characteristics (Hayward and Ebinger 1996; Bonini et al. 2005; Corti 2009), the MER is segmented into three parts of which the central segment hosts the SBDFZ. The region is bound by Late Miocene-Pliocene boundary faults (post-6–7 Ma) which are well developed and accommodated most of the deformation in the quaternary (Corti et al. 2013a). The boundary faults further underwent major deformation in the Late Pleistocene-Holocene (post-30 ka: Agostini et al. 2011; Corti et al. 2013a). The entire MER has since been characterised by recent deformation concentrated in the axial parts in northern MER segment and on the border foots of marginal faults elsewhere including the central MER segment which form belts of volcano-tectonic segments with nearly north-south trend. Two of these are an *en echelon* arranged volcano-tectonic segments of Wonji Fault Belt (WFB) and the less known Silti-Butajira-Debre Zeyit (SBDFZ) belt. In particular, in the central segment, the SBDFZ are localised to the foot of the western rift margin whilst WFB is clustered in the eastern margin. The two belts are distinct in terms of lacking discernible faulting in SBDFZ contrary to the WFB which on the other hand has less explosion craters (Rooney et al. 2007, 2011; Rooney 2010).

In the area, the older volcanism constitutes silicic volcanic centres of Zuqualla and Bede Gebabe (Rooney et al. 2005), not far from the Butajira volcanic field located to the northeast, and are dated 0.36 Ma (Mazzarini et al. 1999). The numerous basaltic monogenetic volcanoes in the form of cinder cones, maars, and associated lava flows represent the youngest volcanism (e.g. Rooney et al. 2005). The BVF is one of the most recent manifestations of volcanism, dated at 0.13 Ma and rooted on extension fractures (Korme et al. 1997; Rooney et al. 2005). Major element compositions of the SBDFZ basalts in general show very shallow source for melts compared with other magmas erupted in the East African Rift System (Rooney et al. 2005).

Climate

In the BVF region with the elevations ranging between 1800 and 2200 m a.s.l., the annual rainfall varies from 310 to 1740 mm, based on a 30-year data at Indibir Town Meteorological Station (Yirga et al. 2017). In the minor rainy season, locally called the 'belg' which runs from February to April, the area receives 100 to 480 mm of rain, and during the main rainy season of 'Kiremt' from May to October, it received 160 to 1200 mm of rainfall. On average, the area receives rain for 140 days of the year in total from both seasons separated with a dry season (Yirga et al. 2017). The annual mean maximum temperature reaches 29 °C whilst the annual mean minimum temperature is 23 °C.

Culture

The location also has a little more to offer than the fascinating geological setting with the added benefit it offers for visitors, through the experience of very traditional endemic cuisine and culture of the Gurage and Silte nationalities. The Gurage and Silte people are famous for their age-old and rare hide handicraft, made with stone tools (Brandt et al. 1996). Here are people with distinct tendency of industriousness and enterprise, most renowned for their peculiar social rituals, cuisine, and social hierarchy as well as work ethics allowing them to live on a well off subsistence level for the most part. They have trading skills as well as elaborated farming practice, namely with *Ensete* also called false banana (*Ensete ventricosum*), an endogenous plant which serves as a staple food in most of southern Ethiopia (Brandt et al. 1996), used for production of specific local bread. Many more untold celebrations, myths, and games from the Gurage are quite captivating for ethno-archaeologists and the curious visitor.

The Gurage people are also unique in southern Ethiopia as they speak distinct language (Semitic family), contrary to the Cushitic family languages spoken in the vast neighbourhood. Similarly, the Silte people also have distinct roots of Semitic origin along with very few others found further south estranged with the wider regional Cushitic-speaking region in harmony for centuries. Such Semitic origins, although not yet understood well, are speculated to have migrated to their current homeland in the last era of Axumite Kingdom (e.g. Henze 2000). During military expeditions to the south, some military colonies were probably left behind, eventually became isolated and assimilated with the local people at that time (Brandt et al. 1996). In the Gurage, there are about six clans: Soddo, Inor, Mesqan, Mesmes, Zay, and Sebat Bet which differ slightly in dialect as well as crafts. The housing is also of peculiar beauty with most attention given to orderliness, organisation, and cleanness. The houses have the form of round Tukul (Saar-bet or grass-roofed house; Fig. 2) made of mud, grass, and wooden poles with roofs made of thatched grass having conical round geometry supported in the centre on a wooden vertical pole. The shape of these grass houses strongly resembles the shape of volcanic cones around, pointing on the strong links between the local inhabitants and the landscape.

The Gurage have also one of the most peculiar dancing styles which are physically quite demanding. It features sporty moves which are also faster with the rhythm and utilise the entire body making it liked by many. Also known is the specially spiced Ethiopian tartare beef steak, locally called ‘Kitfo’ which is served raw. The red part of the meet is carefully selected and sliced or minced finely which then is marinated with spice, hot chilli, and clarified butter, called ‘Nitir Kibe’, a form of butter similar to Ghee but simmered with special aromatic spices.

List of Principal Geosites

The regions of geoheritage values consist of individual geosites, as the basic geoheritage features. Geosites are generally those sites that are best and the most representative for a specific geomorphological (geomorphosites) or geological (geosites) process (time-independent) or a stage of Earth history (time-dependent). Such sites can be intrinsically or culturally significant, or ideally combined elements of both (e.g. Panizza 2001, 2009; Risso et al. 2006; Henriques et al. 2011; Reynard et al. 2009, 2011; Kazancı 2012; Fuertes-Gutierrez and Fernandez-Martinez 2012; Moufti et al. 2013a, 2015; Gravis et al. 2017; Rapprich et al. 2019). For that reason, to express the geoheritage and educational values of the BVF, we provide the list of key geosites with their characteristics.

Lake Shetan (8° 02.7′ N, 38° 21.1′ E)

First in the list of potential attractive sites in the prospective geosites is the Shetan Lake (7 km south of Butajira Town)—a perfectly round maar crater (750 m in diameter) hosting a lake 500 m across that changes its colour throughout the year. This is the only lake-filled maar in the BVF (Fig. 3) and is rimmed by a tuff ring, reaching up to 16 m of thickness that consists of phreatomagmatic pyroclastic deposits. Below the tuff ring deposits, underlying solid volcanic rocks are exposed in the crater walls. The basement volcanic rocks comprise basaltic lava overlying older (Pleistocene) rhyolitic ignimbrites. The tuff-ring deposits are well exposed at several sites around the crater providing the opportunity to observe the short eruptive history of this volcano. Two layers of ill-sorted deposits with angular fragments of underlying rocks are separated with a 35-cm-thick layer of black basaltic scoriae with bread-crusted bombs up to 50 cm in length. The phreatomagmatic deposits contain large (up to 1 m in diameter) fragments of the underlying ignimbrites (Fig. 3d). Whereas the phreatomagmatic deposits are dominated by country-rock lithics, namely the welded rhyolitic ignimbrites, the composition of erupted magma can be identified from the layer of black basaltic scoria. The larger bombs consist of olivine-rich alkali basalt. The ignimbrite blocks ejected from the crater cover the surface of the tuff-ring outer slopes, and can be found as far as 300 m from the edge of the tuff-ring (Fig. 3e). The thickness of the phreatomagmatic pyroclastic deposits of the Shetan maar rapidly decreases with increasing distance from the crater, but can be traced and identified as far as 5 km from the crater. The presence of scoria layer within the phreatomagmatic deposits suggests that during the initial phreatomagmatic eruption, all water was consumed in the root zone (e.g. Lorenz et al. 2003; Lorenz and Kurszlaukis 2007). The subsequently ascending magma batch was not affected by phreatomagmatic reaction and erupted in dry conditions leading to Strombolian style (Walker 1973; Cas and Wright 1987) eruption producing

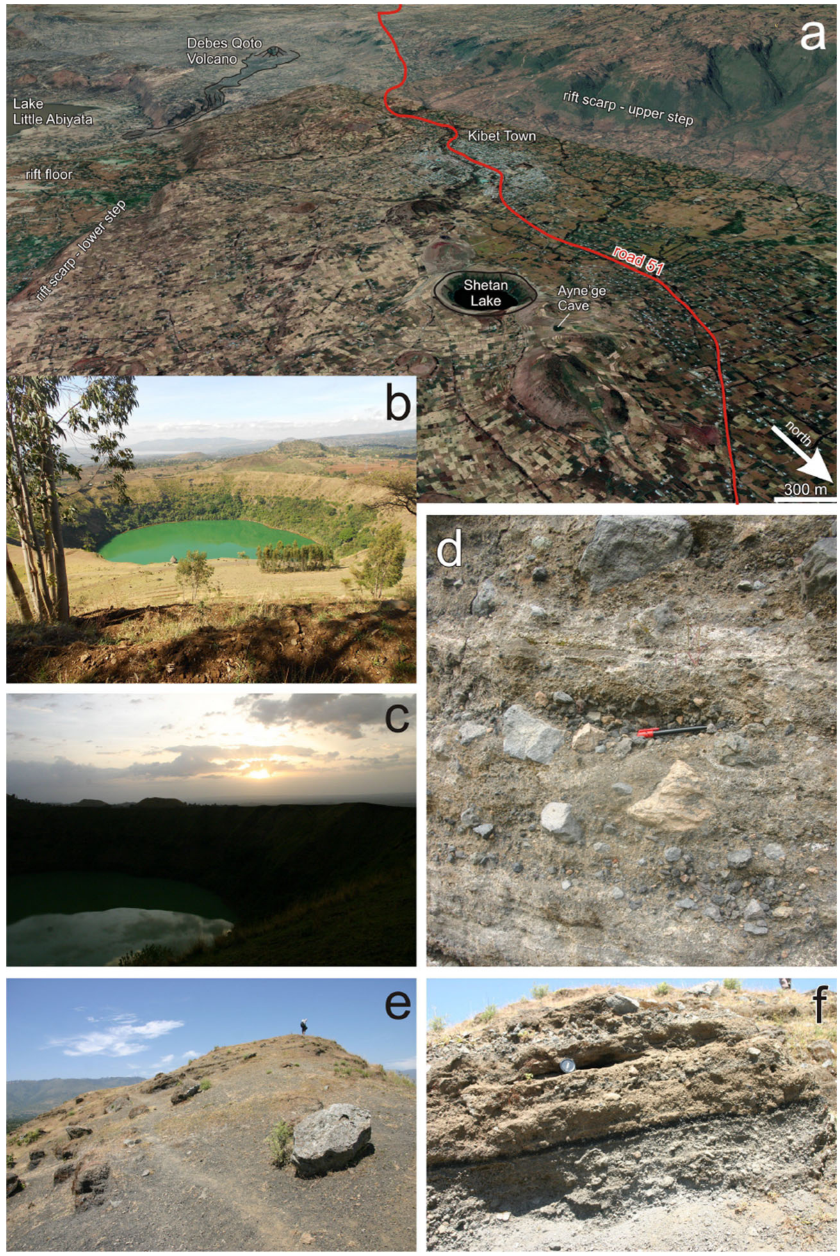

Fig. 3 Shetan Lake. **a** Wider landscape with location of Shetan Lake and other key geosites. **b** Shetan Lake seen from north. **c** Sunrise above Shetan Lake. **d** Blocks of underlying basalts and ignimbrites in ill-sorted phreatomagmatic deposits of Shetan maar. **e** Large block ejected on the tuff ring. **f** Thin scoria layer, separating the phreatomagmatic deposits into two units

scoria layer. Replenishment of the water saturation in the maar-diatreme volcano root zone resulted in returning of the eruption style back to phreatomagmatic (Fig. 3f).

Ay'nege Cave (*syn.* Butajira Cave, Shetan Cave; 8° 03.1′ N, 38° 21.38′ E)

About 530 m to the NNE from the edge of the Shetan crater, the entrance to the Ay'nege Cave is located in the saddle between two scoria cones (Fig. 4; Brigani 2008). The cave is unique in that it did not form through the usual chemical dissolution of carbonates or evaporites but it formed in a crystalline volcanic rock. This particular cave is developed in basalt (Fig. 4). Lava tubes and tunnels are known from many volcanic regions around the world (Peterson et al. 1994; Calvari and Pinkerton 1999), in many areas representing geoheritage sites (e.g. Joyce 2010; Dóniz-Páez et al. 2011; Garofano and Govoni 2012; Gao et al. 2013; Moufti et al. 2013b; Newsome and Johnson 2013), but such lava caves have characteristic geometry and morphology.

The Ay'nege Cave is not oriented in the axis of the lava flow, and its walls are not decorated with lava stalactites. The cave is oriented NNE-SSW (Fig. 4a), parallel to the axis of the Main Ethiopian Rift of roughly N 30° E to N 35° E trending. The onset of the first faulting in the central segment of the Main Ethiopian Rift, which encompasses the vicinity of the geosite, is estimated to be around 8.3–9.7 Ma (Bonini et al. 2005, Corti 2009). The Ay'nege Cave is hosted in basaltic

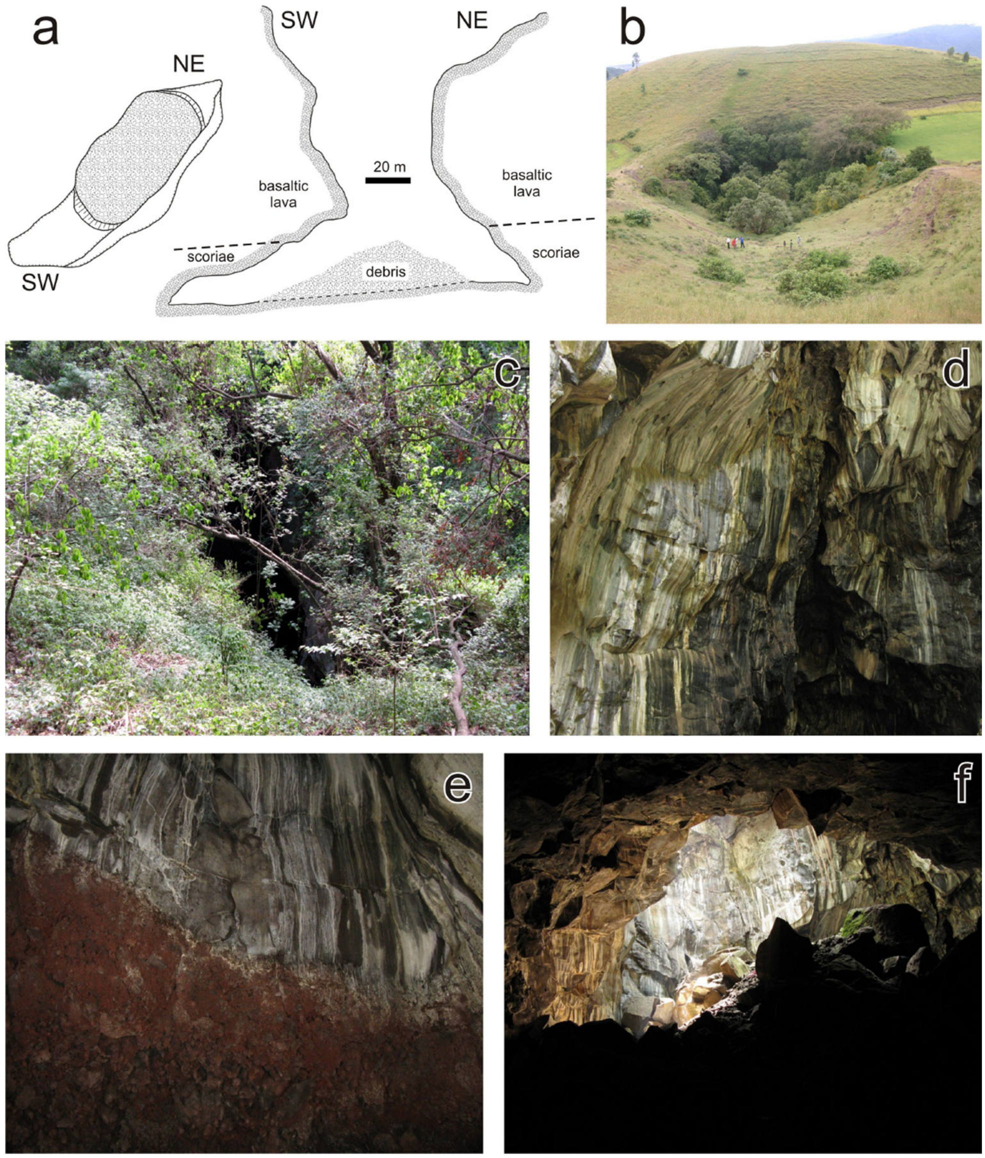

Fig. 4 Ay'nege Cave. **a** Profile of the cave (after Brigani 2008). **b** Entrance to the cave in a small tectonic graben forming a saddle between two scoria cones. **c** Narrow entrance to the cave hidden in the bush. **d** Fracture in the basaltic lava, along which the cave was formed. **e** Scoriae deposits underlying the basaltic lava. **f** Entrance to the cave and accumulation of debris from collapsed roof of the cave

lavas overlying scoriae deposits. The central part is partly filled with accumulation of talus from the collapsing roof of the cave (Fig. 4f). Geometry of sedimentary bodies in fine deposits at the bottom of the cave indicates the presence of water during rainy seasons flowing through the cave towards SSW (Shetan Crater). The cave opens in the basalts due to extensional tectonics, but the widening of the cave's bottom seems to reflect the sub-surface erosion of loose scoriae by flowing water, their transport along discrete cracks and re-deposition in the Shetan Crater (Fig. 4e). Together with weathered and eroded scoria, the water flowing in the cave during rainy seasons probably also re-deposited thick accumulations of guano from the large bat population in the cave. Supply of the Shetan Lake with phosphates from the guano during rainy seasons might be the reason for higher activity of algae and changes of water colour after the rainy season, although adequate biochemical study supporting this hypothesis is missing yet.

Within our field investigations, we have measured the orientation of the fault planes and their groove casts, and we have characterised the surface of the faults and determined the movement direction upon these faults. The movement directions upon the fault planes have been deduced from Riedel shears, pressure shadows, carbonate precipitations in the pressure shadows, and, in some cases, from smeared clasts. The locality around the Butajira Cave is featured by two major frameworks of faults. The NE-SW and the E-W systems are reflected in the overall tectonic image of the area, characterised by high relief energy and by an extension regime.

The main fault of the NE-SW framework penetrating the Ay'nege Cave is closely related to the respective segment of the Main Ethiopian Rift. The faults of the NE-SW direction exhibit mostly dextral kinematics and disrupt the E-W faults. The NE-SW framework of faults is still active. The planes of the E-W system are subsiding under a steep angle in the Ay'nege Cave. We assume that the extension has not only led to a formation of additional faults but, more importantly, it has reactivated the earlier structures. This structure extends further in the southwest direction beyond the studied area. It is accompanied by manifestation of morphological features and connected to important landslide areas.

The occurrence of series of dip-slip faults in the area attests to the affinity of extensional regime in the area, although less pronounced compared with other sectors of the rift (e.g. Woldegabriel et al. 1990; Corti et al. 2013b). The series of escarps, leading to the Main Ethiopian Rift axis that gave the outstanding terraced morphology to the area, are probably driven by two factors. On the one hand, interlayered lithological units of contrasting competence posed different rates of erosion and, on the other hand, morphological adjustment through surficial reworking in response to geodynamic changes brought by multiple episodes of dip-slip faulting also contribute to the terrace formation.

Debes Qoto Volcano (7° 56.5′ N, 38° 17.8′ E)

Debes Qoto scoria cone, located 20 km SSW from Butajira, is an interesting site which is most likely the youngest volcano in the BVF. This scoria cone differs from other cones in the BVF by significantly better preserved morphology with sharp crater rim unaffected by erosion (Fig. 5). The young age deduced from fresh morphology is further supported by distinct

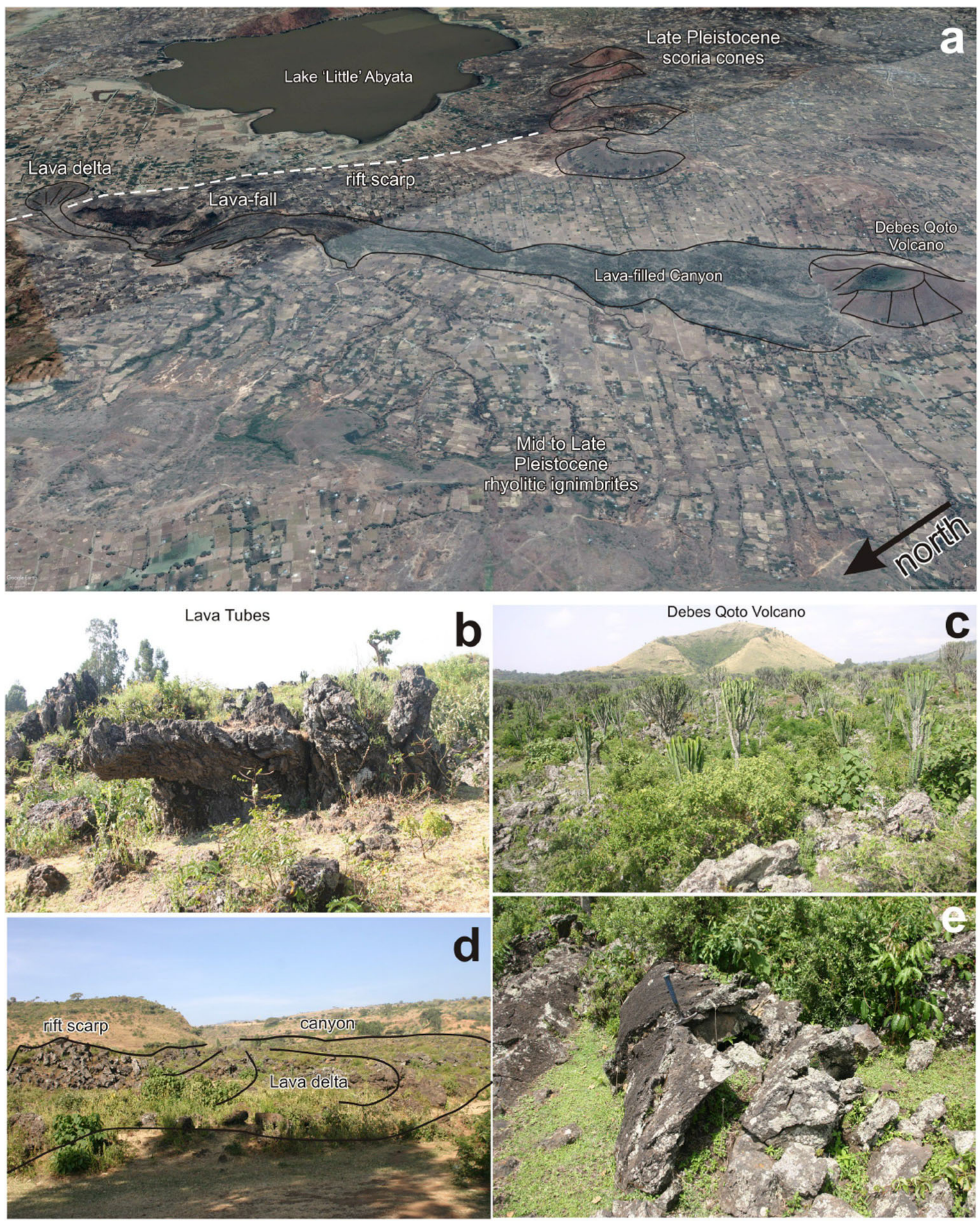

Fig. 5 Debes Qoto Volcano. a Synoptic view of the volcano and the surrounding. b Preserved lava flow tube. c View to asymmetric crater lava covered with spurge forest. d Lava delta spread in a conyon near the rim of Lake little Abaya e Lava flow.

Fig. 6 Temporary geyser in the area that erupted during water-well drilling

reflection of visible light, possibly reflecting lower degree of scoriae oxidation (Debebe et al. 2014). The cone is horseshoe-shaped with crater open towards NNE and only poorly vegetated. This volcano produced a 6-km-long lava flow which filled one small canyon on its way down from the rift flank to the rift floor. The lava has spectacular irregular surface and is partly covered with spurge forest.

Debes Qoto Lava Delta

The lava poured out of the Debes Qoto Volcano stretches for about 5.5 km in a narrow canyon and splays out on plains of the 'little' Abiyata Lake shore. Along the volcanic lava flow, various spectacular lava tubes can be seen which are formed as the surface of a lava flow cools, but lava continues to flow below the surface (Fig. 5b,d).

Temporary Geyser

Hydrothermal activity is present on the western side of the MER, in the Butajira-Silte zone (Imba Koto springs) west of Lake Ziway as a consequence of the recent volcano-tectonic activity in the area (Le Turdu et al. 1999). In May 2014, a temporary geyser occurred in a site of irrigation drilling (Fig. 6). The geyser remained active for about a month before deceasing. This event provides an evidence of high-level hydrothermal activity within the BVF area, providing a perspective of thermal water exploitation and use in the future (e.g. balneotherapeutical beneficiation, geothermal energy).

Waterfalls

The steep scarps on the rift margin, in the area of Ajora, host enormous waterfalls with exposures of Late Miocene to Pleistocene rhyolitic ignimbrites. Other notable series of waterfalls occur inside the proposed geosite periphery on the streams running southeast across the strike of the tectonic structures and contacts of the various lithologies. The alternating layered occurrence of the soft, non-welded pyroclastic deposits (including non-welded facies of ignimbrites) and hard, basaltic lavas and welded facies of rhyolitic ignimbrites

Fig. 7 The scheme of waterfalls occurrence in the area (not drawn to scale). 1 Senea waterfall. 2 Lebo waterfall. 3 Lamore waterfall

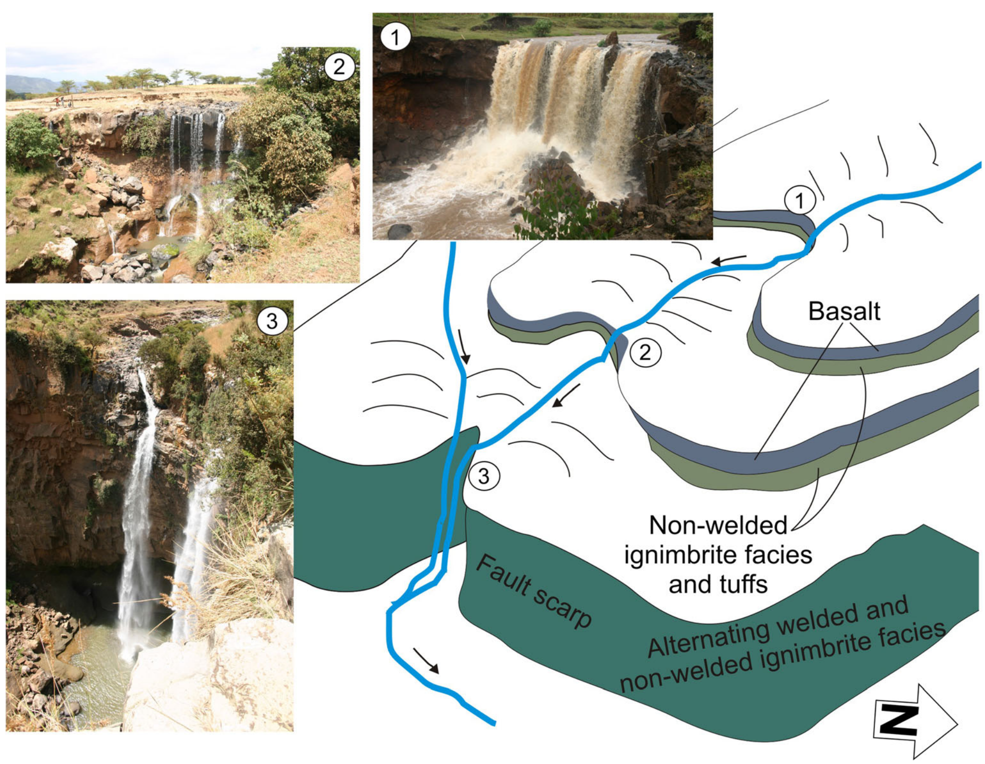

in the area particularly gave rise to the formation of series of waterfalls in response to different rates of down cutting in each formation (Fig. 7). The waterfalls appear to have propagated upstream in response to regional geodynamics involving major tectonic slip of normal kinematic sense which is apparent in the high steeps where the longest waterfall, 'Lamore', occurs. The Lamore waterfall is spectacular where two streams, namely 'Garore' and 'Lebo', join as both streams emerge on the escarp of about 50 m high. The entire exposed tectonic escarp is comprised of ignimbrite with columnar joint.

Three series of waterfalls occur moving upstream to the north from the last major escarp described above. These waterfalls all share common characteristics in occurrence except difference in heights of the waterfall escarps. The waterfalls at the edge of the hard basaltic lava layers where they had eroded away, headward, all the intervening layer of soft tuffaceous material, exposed along the waterfall escarps. The current normal flow of the streams is hence all along the hard basaltic lava rocks that were exposed after removal of the overlying soft tuffaceous deposits. The volume of water changes from clear and scanty during the dry season to muddy and enormous in the monsoon (rainy) seasons.

Discussion and Conclusions

Apart from the listed major sites, numerous other sites that have educational value on important geomorphological and geological features and processes associated with continental rifting, volcanoes, and geomorphological diversities are present in the BVF.

The advantage of the geosites is also its close proximity to other unique geoheritage sites including the Melka Kunture archaeological site which has been among the tentative list of UNESCO's world heritage and the Tiya stelae site which has been declared a UNESCO World Heritage (World Heritage Convention 2019). Both sites are found close to the main road in the distance of about 70 km to the north east. Further south of the proposed geosites on the other hand is a magnificent twin waterfalls called the Ajora waterfalls (Ajacho and Soke) on more than 200 m high cliff (Culture and Tourism Bureau, 2016).

The range of young volcanogenic and tectonic interferences and influence on geomorphology is profoundly expressed in the described potential geosite. Young aligned numerous monogenetic volcanoes together with large silicic volcanoes and tectonically developed basins filled with lakes amass the region in and around the geosite locality. From the major older fault escarps of the rift margin to the more evolved and younger but sharp fault escarps in the centre of the rift valley result in formation of numerous waterfalls as they intercept natural streams. The nearby riches of archaeological artefacts and historical monuments added with the unique authentic culture of the highly observed cuisine and celebratory art and practice the designation of the area as a protected heritage site is well deserved.

These collective natural geo-archaeological attractions should be new destinations for development and preservation through ecotourism. The establishment of the geosite can help change the image of the country as source of a still untapped geosite wonder and a laboratory of deciphering the prehistoric hominid activity. The potential of creating opportunity for employment and income generation among local inhabitants is also quite substantial.

Such endeavours should be the direction to be adopted by the local and regional administration to also spread the tourism culture within the country's realm in parallel to the foreign tourist turn out. We hope that there will be a will to establish the first Ethiopian geosite in the BVF, and that this will take place sooner.

In addition, close links between tectonics and volcanism on relatively small area, which can be easily overseen by a visitor, provide an excellent example of continental rift, where geological processes can be well demonstrated to wider public. Besides demonstration of common geological processes, the hazardous phenomena can be also better explained on smaller examples fitting the scope of visitors view. Among the hazards, namely volcanic hazards and active tectonics responsible for opening of ground cavities, are well displayed within the BVF area.

Acknowledgments The geoheritage potential has been evaluated concurrently with research on geological hazards in the Southern Nations, Nationalities and Peoples Region within the framework of the Czech-Ethiopian Development Cooperation supported by the Czech Ministry of Foreign Affairs through the Czech Development Agency. We are grateful to the Geological Survey of Ethiopia and its staff as well as to local people for assistance during field work, namely at the entrance to Shetan Cave. The manuscript was completed with support from the Czech Geological Survey (project 310410).

References

Agostini A, Bonini M, Corti G, Sani F, Mazzarini F (2011) Fault architecture in the Main Ethiopian Rift and comparison with experimental models: implications for rift evolution and Nubia–Somalia kinematics. Earth Planet Sci Lett 301:479–492

Asrat A, Demissie M, Mogessie A (2012) Geoheritage conservation in Ethiopia: the case of the Simien Mountains. QuaGeo 31:7–23

Bonini M, Corti G, Innocenti F, Manetti P, Mazzarini F, Abebe T, Pécskay Z (2005) Evolution of the Main Ethiopian Rift in the frame of Afar and Kenya rifts propagation. Tectonics 24(1)

Brandt AS, Weedman JK, Hundie G (1996) Gurage hide working, stone tool use and social identity; an Ethiopian ethnoarcheological perspective. In: Hudson G (ed) Essays on Gurage language and culture. Harrassowitz Verlag, p 241

Brigani R (2008) Speleology in Ethiopia. Bulletin of the Grotte Milano CAI-SEM Group https://issuu.com/ilgrottesco/docs/grottesco55

Brocx M, Semeniuk V (2007) Geoheritage and conservation: history, definition, scope and scale. J R Soc West Aust 90:53–87

Calvari S, Pinkerton H (1999) Lava tube morphology on Etna and evidence for lava flow emplacement mechanisms. J Volcanol Geotherm Res 90:263–280

Cas RAF, Wright JV (1987) Volcanic successions, modern and ancient: a geological approach to processes, products and successions. Allen and Unwin, Winchester, p 528

Christopher G (2006) "Stones, slabs, and stelae: the origins and symbolism of contemporary Oromo burial practice and grave art". Independent Study Project (ISP) Collection. Paper 263, unpublished Report

Corti G (2009) Continental rift evolution: from rift initiation to incipient break-up in the Main Ethiopian Rift, East Africa. Earth-Sci. Rev. 96: 1–53.

Corti G, Philippon M, Sani F, Keir D, Kidane T (2013a) Re-orientation of the extension direction and pure extensional faulting at oblique rift margins: comparison between the Main Ethiopian Rift and laboratory experiments. Terra Nova 25:396–404

Culture and Tourism Bureau, 2016, Federal Democratic Republic of Ethiopia, Southern Nations, Nationalities and Peoples' Region Bureau, 2016. http://www.southtourism.gov.et/ajora-waterfalls Accessed 24 March 2019

Corti G, Sani F, Philippon M, Sokoutis D, Willingshofer E, Molin P (2013b) Quaternary volcano-tectonic activity in the Soddo region, western margin of the Southern Main Ethiopian Rift. Tectonics 32(4):861–879

Debebe N, Yekoye B, Rapprich V (eds) (2014) Geological hazards and engineering geology maps of Hosaina NB 37-2. explanatory notes. Czech Geological Survey, Prague, Aquatest a.s., Prague, Geological Survey of Ethiopia, Addis Ababa, pp 1–148

Dóniz-Páez J, Becerra-Ramírez R, González-Cárdenas E, Guillén-Martín C, Escobar-Lahoz E (2011) Geomorphosites and geotourism in volcanic landscape: the example of La Corona del Lajial cinder cone (El Hierro, Canary Islands, Spain). Geojournal Tour Geosites 2:185–197

Dowling RK (2011) Geotourism's global growth. Geoheritage 3:1–13

Fuertes-Gutierrez I, Fernandez-Martinez E (2012) Mapping geosites for geoheritage management: a methodological proposal for the regional park of Picos de Europa (Leon, Spain). Environ Manag 50:789–806

Fung CKW, Jim CY (2015) Unraveling Hong Kong Geopark experience with visitor-employed photography method. Appl Geogr 62:301–313

Gao W, Li J, Mao X, Li H (2013) Geological and geomorphological value of the monogenetic volcanoes in Wudalianchi National Park, NE China. Geoheritage 5:73–85

Garofano M, Govoni D (2012) Underground geotourism: a historic and economic overview of show caves and show mines in Italy. Geoheritage 4:79–92

Gebremedhin B, Ficetola GF, Naderi S, Rezaei HR, Maudet C, Rioux D, Luikart G, Flagstad Ø, Thuiller W, Taberlet P (2009) Combining genetic and ecological data to assess the conservation status of the endangered Ethiopian walia ibex. Anim Conserv 12:89–100

Global Geoparks Network, 2019, Accessed 29 June 2019. http://www.globalgeopark.org/aboutGGN/list

Gottelli D, Marino J, Sillero-Zubiri C, Funk SM (2004) The effect of the last glacial age on speciation and population genetic structure of the endangered Ethiopian wolf (Canis simensis). Mol Ecol 13:2275–2286

Gravis I, Németh K, Procter JN (2017) The role of cultural and indigenous values in geosite evaluations on a quaternary monogenetic volcanic landscape at Ihumātao, Auckland volcanic field New Zealand. Geoheritage 9:373–393

Hagos M, Koeberl C, Jourdan F (2017) Geochemistry and geochronology of phonolitic and trachytic source rocks of the Axum Obelisks and other stone artifacts, Axum, Ethiopia. Geoheritage 9:479–494

Hailu Z (2007) Some notes on the Great Walls of Wolayta and Dawro. AnnEth 23:399–412

Hayward NJ, Ebinger CJ (1996) Variations in the along-axis segmentation of the Afar Rift system. Tectonics 15:244–257

Henriques MH, dos Reis RP, Brilha J, Mota T (2011) Geoconservation as an emerging geoscience. Geoheritage 3:1–12

Henze PB (2000) Layers of time: a history of Ethiopia. Springer, p 372

Horváth G, Csüllög G (2013) A new Slovakian-Hungarian cross-border geopark in Central Europe -possibility for promoting better connections between the two countries. Europ Countrys 5:146–162

http://whc.unesco.org/en/. Accessed on 26 March 2019

http://www.globalgeopark.org/aboutGGN/list. Accessed on 29 June 2019

http://www.southtourism.gov.et/ajora-waterfalls. Accessed 24 March 2019

Joussaume R (1985) Tiya. Une Campagne de Fouilles. AnnÉth 13:69–84

Joyce EB (2010) Australia's geoheritage: history of study, a new inventory of geosites and applications to geotourism and geoparks. Geoheritage 2:39–56

Kazancı N (2012) Geological background and three vulnerable geosites of the Kızılcahamam–Çamlıdere geopark project in Ankara, Turkey. Geoheritage 4:249–261

Kimbel WH, Delezene LK (2009) "Lucy" redux: a review of research on Australopithecus afarensis. Am J Phys Anthropol 140:2–48

Korme T, Chorowicz J, Collet B, Bonavia F F (1997) Volcanic vents rooted on extension fractures and their geodynamic implications in the Ethiopian Rift. J Volcanol Geotherm Res, 79(3-4): 205-222.

Kycl P, Rapprich V, Verner K, Novotný J, Hroch T, Mišurec J, Eshetu H, Tadesse Haile E, Alemayehu L, Goslar T (2017) Tectonic control of complex slope failures in the Ameka River Valley (Lower Gibe Area, central Ethiopia): implications for landslide formation. Geomorphology 288:175–187

Le Turdu C, Tiercelin J J, Gibert E, Travi Y, Lezzar K E, Richert J P, Massault M, Gasse F, Bonnefille R, Decobert M, Gensous B (1999) The Ziway–Shala lake basin system, Main Ethiopian Rift: influence of volcanism, tectonics, and climatic forcing on basin formation and sedimentation. Palaeogeogr Palaeoclimatol Palaeoecol, 150(3-4): 135-177.

Lorenz V, Kurszlaukis S (2007) Root zone processes in the phreatomagmatic pipe emplacement model and consequences for the evolution of maar–diatreme volcanoes. J Volcanol Geotherm Res 159:4–32

Lorenz V, Suhr P, Goth K (2003) Maar–Diatrem-Vulkanismus – Ursachen und Folgen. Die Guttauer Vulkangruppe in Ostsachsen als Beispiel für die komplexen Zusammenhänge. Z Geol Wiss 31: 267–312

Mazzarini F, Abebe T, Innocenti F, Manetti P, Pareschi MT (1999) Geology of the Debre Zeyt area (Ethiopia)(with a geological map at scale 1: 100,000). Acta Vulcanol 11:131–142

Mazzarini F, Keir D, Isola I (2013) Spatial relationship between earthquakes and volcanic vents in the central-northern Main Ethiopian Rift. J Volcanol Geotherm Res 262:123–133

Moufti MR, Németh K, Murcia H, Lindsay JM, El-Masry N (2013a) Geosite of a steep lava spatter cone of the 1256 AD, Al Madinah eruption, Kingdom of Saudi Arabia. Cent Eur J Geosci 5:189–195

Moufti M, Németh K, El-Masry N, Qaddah A (2013b) Geoheritage values of one of the largest maar craters in the Arabian Peninsula: the Al Wahbah Crater and other volcanoes (Harrat Kishb, Saudi Arabia). Open Geosci 5(2):254–271

Moufti MR, Németh K, El-Masry N, Qaddah A (2015) Volcanic geotopes and their geosites preserved in an arid climate related to landscape and climate changes since the neogene in Northern Saudi Arabia: Harrat Hutaymah (Hai'il Region). Geoheritage 7:103–118

Newsome D, Johnson CP (2013) Potential geotourism and the prospect of raising awareness about geoheritage and environment on Mauritius. Geoheritage 5:1–9

NPC (National Planning Commission) (2016) Growth and transformation plan II, 2015/16-2019/20. Federal Democratic Republic of Ethiopia. Addis Ababa

Panizza M (2001) Geomorphosites: concepts, methods and examples of geomorphological survey. Chin Sci Bull 46:4–6
Panizza M (2009) The geomorphodiversity of the dolomites (Italy): a key of geoheritage assessment. Geoheritage 1:33–42
Peterson DW, Holcomb RT, Tilling RI, Christiansen RL (1994) Development of lava tubes in the light of observations at Mauna Ulu, Kilauea Volcano, Hawaii. Bull Volcanol 56:343–360
Potts R (2012) Evolution and environmental change in early human prehistory. Annu Rev Anthropol 41:151–167
Rapprich V, Žáček V, Verner K, Erban V, Goslar T, Bekele Y, Legesa F, Hroch T, Hejtmánková P (2016) Wendo Koshe Pumice: the latest Holocene silicic explosive eruption product of the Corbetti volcanic system (southern Ethiopia). J Volcanol Geotherm Res 310:159–171
Rapprich V, Valenta J, Brož M, Kadlecová E, van Wyk de Vries B, Petronis MS, Rojík P (2019) A crucial site in the argument between Neptunists and Plutonists: reopening of the Historical Adit in the Komorní hůrka (Kammerbühl) Volcano after 180 years. Geoheritage 11:347–358
Renzulli A, Antonelli F, Margottini C, Santi P, Fratini F (2011) What kind of volcanite the rock-hewn churches of the Lalibela UNESCO's world heritage site are made of? J Cult Herit 12:227–235
Reynard E, Coratz P, Regolini-Bissing G (2009) Geomorphosites. Verlag Dr. Friedrich Pfeil, München, Germany
Reynard E, Coratza P, Giusti C (2011) Geomorphosites and geotourism. Geoheritage 3:129–130
Risso C, Németh K, Martin U (2006) Proposed geosites on Pliocene to recent pyroclastic cone fields in Mendoza, Argentina [Geotopvorschläge für pliozäne bis rezente Vulkanfelder in Mendoza, Argentinien]. Z Dtsch Ges Geowiss 157:477–490
Rooney TO (2010) Geochemical evidence of lithospheric thinning in the southern Main Ethiopian Rift. Lithos 117:33–48
Rooney TO, Furman T, Yirgu G, Ayalew D (2005) Structure of the Ethiopian lithosphere: xenolith evidence in the Main Ethiopian Rift. Geochim Cosmochim Acta 69:3889–3910
Rooney TO, Furman T, Bastow I, Ayalew D, Yirgu G (2007) Lithospheric modification during crustal extension in the Main Ethiopian Rift. J Geophys Res Solid Earth 112(B10)
Rooney TO, Bastow ID, Keir D (2011) Insights into extensional processes during magma assisted rifting: evidence from aligned scoria cones. J Volcanol Geotherm Res 201:83–96
Van Wyk de Vries B, Byrne P, Delcamp A, Einarson P, Göğüş O, Guilbaud MN, Hagos M, Harangi S, Jerram D, Matenco L, Mossoux S, Németh K, Maghsoudi M, Petronis MS, Rapprich V, Rose WI, Vye E (2018) A global framework for the earth: putting geological sciences in context. Glob Planet Chang 171:293–321
Walker GPL (1973) Explosive volcanic eruptions—a new classification scheme. Geol Rundsch 62:431–446
Watson E (2009) Living Terraces in Ethiopia: Konso Landscape, Culture and Development. Boydell & Brewer, Woodbridge United Kingdom 247 pp.
Woldegabriel G, Aronson JL, Walter RC (1990) Geology, geochronology, and rift basin development in the central sector of the Main Ethiopia Rift. Geol Soc Am Bull 102(4):439–458
World Heritage Convention 2019, UNESCO, Accessed 26 March 2019 http://whc.unesco.org/en
Woo KS, Sohn YK, Yoon SH, San Ahn U, Spate A (2013) Jeju Island geopark—a volcanic wonder of Korea. Springer, Berlin Heidelberg, p 88
Yirga S, Mamo G, Mengesha M (2017) Rainfall and temperature trend analysis at Indibir Station, Gurage Zone. J Environ Earth Sci 7(9):1–11
Žáček V, Hradecký P, Kycl P, Ševčík J, Novotný R, Baroň I (2017). The Somoto grand canyon (Nicaragua)—a volcanic geoheritage one decade after discovery:from field geological mapping to the creation of a Geopark. Geoheritage 9:299–309
Zerihun ME (2017) Web based GIS for tourism development using effective free and open source software case study: Gondor town and its surrounding area, Ethiopia. J Geogr Inf Syst 9:47–58
Zouros N, McKeever P (2004) The European geoparks network. Episodes 27:165–171

Publisher's Note Springer Nature remains neutral with regard to jurisdictional claims in published maps and institutional affiliations.

Appendix 4

Received: 7 January 2021 | Revised: 15 July 2021 | Accepted: 18 July 2021

DOI: 10.1002/esp.5227

RESEARCH ARTICLE

ESPL WILEY

Ground fissures within the Main Ethiopian Rift: Tectonic, lithological and piping controls

Jan Valenta[1] | Kryštof Verner[2,4] | Karel Martínek[3,4] | Tomáš Hroch[4] | David Buriánek[4] | Leta Alemayehu Megerssa[2,4] | Jan Boháč[1] | Muluken Kassa[5] | Ferdawok Legesse[6] | Meheret Yakob[6] | Bisrat Kebede[5] | Jiří Málek[7]

[1]Institute of Hydrogeology, Engineering Geology and Applied Geophysics, Charles University, Prague, Czech Republic

[2]Institute of Petrology and Structural Geology, Charles University, Prague, Czech Republic

[3]Institute of Geology and Palaeontology, Charles University, Prague, Czech Republic

[4]Czech Geological Survey, Prague, Czech Republic

[5]School of Earth Sciences, Addis Ababa University, Addis Ababa, Ethiopia

[6]Geological Survey of Ethiopia, Addis Ababa, Ethiopia

[7]Institute of Rock Structure and Mechanics, Czech Academy of Sciences, Prague, Czech Republic

Correspondence
Jan Valenta, Institute of Hydrogeology, Engineering Geology and Applied Geophysics, Charles University, Albertov 6, Prague, 128 43, Czech Republic.
Email: valentah@natur.cuni.cz

Funding information
Charles University, Faculty of Science, Grant/Award Number: Q45 Progress; Czech Development Agency, Grant/Award Numbers: 280614/2019-ČRA, 281226/2018-ČRA

Abstract

Ground fissures, especially if they open due to a sudden collapse of the surface, is a serious risk for populated areas. Their common occurrence in unconsolidated sediments of the Main Ethiopian Rift was found to be mostly a result of piping.

The fissures start by piping in linear sub-horizontal underground voids, which often propagate upwards resulting in ceiling collapse and formation of deep and long ground fissures with vertical walls. In the southern and central Main Ethiopian Rift the fissures pose a serious risk to infrastructure and settlements. The ground fissures are often linear (up to several kilometres long and often tens of metres deep) and accompanied by sinkholes (along the length). A detailed field mapping of the geological (rock composition, orientation and character of lithological boundaries, primary fabrics and brittle structures) and geomorphological features (especially a length, width and depth of fissures, sinkholes and gullies) followed by *in situ* seismic anisotropy measurements and a laboratory determination of the geomechanical properties of volcanoclastic deposits was carried out to investigate the ground fissures' origin. The conditions and factors leading to the formation of the ground fissures have been linked to: (a) the presence of regional normal faults and the associated extensional joints and (b) the alternation of lithological units with contrasting hydraulic permeability. The latter corresponds to a sequence of less permeable hard rocks (e.g., rhyolitic ignimbrites) overlain by heterogeneous, soft and permeable, unconsolidated volcaniclastic deposits with a low amount of clay (less than 10%). The ground fissures' occurrence has shown affiliation to areas which have a significantly high seismic anisotropy (more than 20% at the study sites), which can be used as a proxy to map out high risk areas prone to piping and ground fissure formation.

KEYWORDS
geomechanical properties, pipe collapses, pyroclastics, seismic anisotropy, soil, subsurface erosion, surface waves, unconsolidated sediments

1 | INTRODUCTION

The characteristic geomorphological features in active continental rifts such as ground fissures and, in particular, their sudden opening are one of the most important geological hazards bearing a significant threat to the life of residents. These phenomena have been described from many localities all over the world with various geological settings (e.g., Asfaw, 1982, 1998; Ayalew et al., 2004; Bell, 1981; Bell et al., 1992; Carpenter, 1993; Holzer, 1984; Ngecu & Nyambok, 2000; Pacheco-Martínez et al., 2013; Peng et al., 2018; Williams et al., 2004).

There are several processes reported worldwide which can lead to the formation of ground fissures in soils and unconsolidated sediments. Ground-fissures are commonly attributed to: (a) shallow sub-surface erosion such as 'piping' also called 'tunnel erosion or tunnelling erosion' (e.g., Richards & Reddy, 2012; Bernatek-Jakiel & Poesen, 2018, and references cited therein), (b) hydrocompaction and related changes in the volume of material (e.g., Carpenter, 1993; Schumann & Poland, 1970) or (c) deeper processes like aquifer-system compaction and horizontal seepage stresses commonly connected to a decline in the groundwater table (e.g., Ayalew et al., 2004; Carpenter, 1993; Nikbakhti et al., 2017) which could also be coupled with stretching in a basal fault system (Type D fissures described by Zang et al. [2019]). Furthermore, the ground fissures could open (d) due to earthquakes (Asfaw, 1982) and displacement along the faults (Sheng & Helm, 1998; Asfaw, 1998; Peng et al., 2018).

Ground-fissures often occur in the tectonically active continental rift structures such as the Main Ethiopian Rift (MER; Figure 1) belonging to the East African Rift System that separates the Nubia and Somalia plates (e.g., Agostini et al., 2011). In addition to tectonic activity connected with rifting (a rift-related tectonic and lithological pattern, including various volcaniclastic rocks exposed to intense weathering) the area provides a seasonal precipitation with periods of heavy rain and significant changes in groundwater level (e.g., Rapprich et al., 2014; Yismaw et al., 2015; Hroch et al., 2018a, 2018b; Verner et al., 2018; Buriánek et al., 2018).

The ground fissures at the MER, opening in soils and unconsolidated sediments, have been reported since the 1950s (e.g., Asfaw, 1998). However, the first comprehensive study was carried out 30 years later (Asfaw, 1982) in relation to the expansion of settlements and infrastructure. The fissures open in unconsolidated sediments and their triggering mechanism is still unclear (e.g., Ayalew et al., 2004). Their genesis was first considered to be related to earthquakes and the shape of the gullies to be influenced by vegetation and its rooting system (Asfaw, 1982) or were attributed to active tectonics (Asfaw, 1998). Nevertheless, based on field observations, the newly published studies relate them to piping (e.g., Ayalew et al., 2004; Le Turdu et al., 1999; Moges & Holden, 2008), although the authors do not provide any explanation or description of the processes involved in their formation. This hypothesis is supported by evidence of pipes and fissures as old as the Pliocene (Laury & Albriton, 1975; Benvenuti et al., 2005).

The fissures in the MER open rapidly – several hundreds of metres in length in a few months (according to the historical Google Earth aerial photographs [e.g., Site 1 described hereafter] and reports from local farmers). Such rapid formation endangers constructions and the overall infrastructure. Moreover, loss of livestock and even of human lives have been reported in connection with ground fissure openings/collapses (Asfaw, 1998; personal communication with local inhabitants). Also, Moges and Holden (2008) report casualties in connection with gullies, some of which are the result of piping.

This study aims to explain the mechanism of ground fissure formation in the MER, proving or rejecting the earlier-mentioned hypothesis of piping and establishing a way of evaluating the risk of fissuring on specific sites. For these reasons, the central and southern part of the MER between the lakes Ziway and Abaya (Figure 1) was chosen as a model area.

2 | STUDY AREA (GEOLOGICAL, GEOMORPHOLOGICAL AND CLIMATIC SETTINGS)

The MER is a spectacular, active approximately north-northeast–south-southwest (~NNE–SSW) oriented, intra-continental rift system between the African and Somalian plates (e.g., Hayward & Ebinger, 1996; Kazmin et al., 1980; Wolfenden et al., 2004) with well-developed geological and geomorphological attributes. The current rate of plate east–west (E–W) oriented extension varies from 5.2 + 0.9 mm/yr (Saria et al., 2014) to 7 mm/yr (Stamps et al., 2008).

2.1 | Lithology and stratigraphy

The studied area is situated on the boundary between the central and southern MER (Figures 1 and 2a). The geological evolution can be divided into three main stages (e.g., Bonini et al., 2005; Buriánek et al., 2018; Ebinger et al., 1993, 2000; Mohr et al., 1980; Rapprich et al., 2016; Verner et al., 2018):

a. the Eocene to Oligocene 'pre-rift' volcanic activity (~45 to 27 Ma) including mainly tholeiitic to alkaline basalt lava flows and the associated volcaniclastic deposits (e.g., Amaro-Gamo Basalts) with the presence of rhyolitic ignimbrites (e.g., Shole Ignimbrites) and minor trachytes;
b. the Miocene 'syn-rift' volcanic products (~22 to 8 Ma) which are mainly represented by basalts, felsic volcanites and volcaniclastic rocks (rhyolite lava, minor ignimbrites, trachyte lava flows and related pyroclastic deposits) depicted as the Getra and Kele sequences followed by
c. a later period (~7 Ma) of drastically lower volcanism with small eruptions of peralkaline pantelleritic ignimbrites intercalated with minor basaltic lava flows (Bonini et al., 2005).
d. The Pleistocene to Holocene 'post-rift' volcanic activity (~3 to 0.5 Ma) are bi-modal volcanites and volcaniclastic rocks such as olivine basalts, rhyolites, strongly welded rhyolitic ignimbrites and other pyroclastic deposits (e.g., Ebinger et al., 1993). A typical example of post-rift volcanic activity (unconsolidated pyroclastic deposits) has been associated with the formation of the Corbetti Volcanic System (182 ± 28 ka; Hutchison et al., 2016) and the Awassa Caldera (Fontijn et al., 2018; Rapprich et al., 2016). The Awassa syn- to post-caldera pyroclastic deposits (dated at 240 ± 30 ka) are locally interbedded with late-Quaternary lacustrine sediments (Mohr et al., 1980). In addition, tectonic depressions and grabens have been filled by unconsolidated pyroclastic, resedimented volcaniclastic (epiclastic), alluvial and lacustrine deposits from the Pleistocene and Holocene ages.

2.2 | Tectonics

In pre- to syn-rift sequences (Figure 2a,b) the predominant faults dip steeply to approximately east-southeast (~ESE) in the western part of the rift and to approximately west-northwest (~WNW) along its eastern margin and are mostly aligned parallel to the main axis of the MER

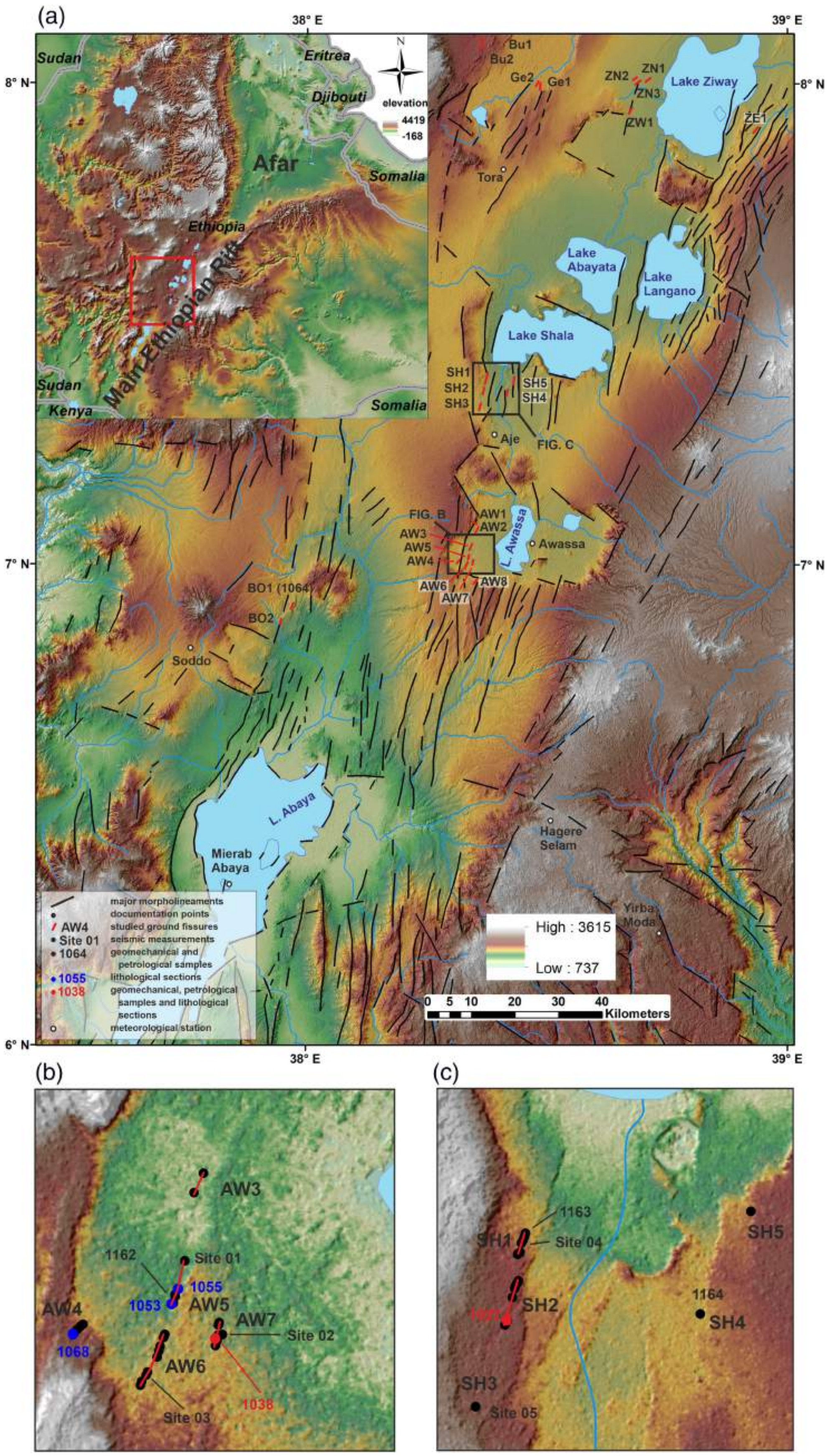

FIGURE 1 (a) Digital elevation model the Main Ethiopian Rift (MER) and the study area at the boundary between the central and southern MER. Location of field geological and geophysical study southwest of Lake Awassa (b) and southwest of Lake Shala (c) including the meteorological stations discussed in the text. (Coordinates of meteorological stations, documentation points and other study sites can be found in Supporting Information Datasets S1 and S2 together with available field data.) [Color figure can be viewed at wileyonlinelibrary.com]

forming prominent escarpments. These faults are associated with fault lineation (slickensides) plunging steeply to moderately to ~ESE (in the western escarpment) to approximately northwest (~NW) (in the eastern escarpment) bearing exclusively normal kinematic indicators. In addition, three subordinate sets of normal or oblique-slip faults were identified: (a) subvertical ~NNW(N) to SSE(S) trending faults including steeply plunging lineations which are oblique by ~20° to 30° to the main fault system; (b) mostly perpendicular, steeply ~NNE(N) dipping faults with approximately north-northwest (~NNW) plunging slickensides and (c) steeply ~NNW dipping normal faults.

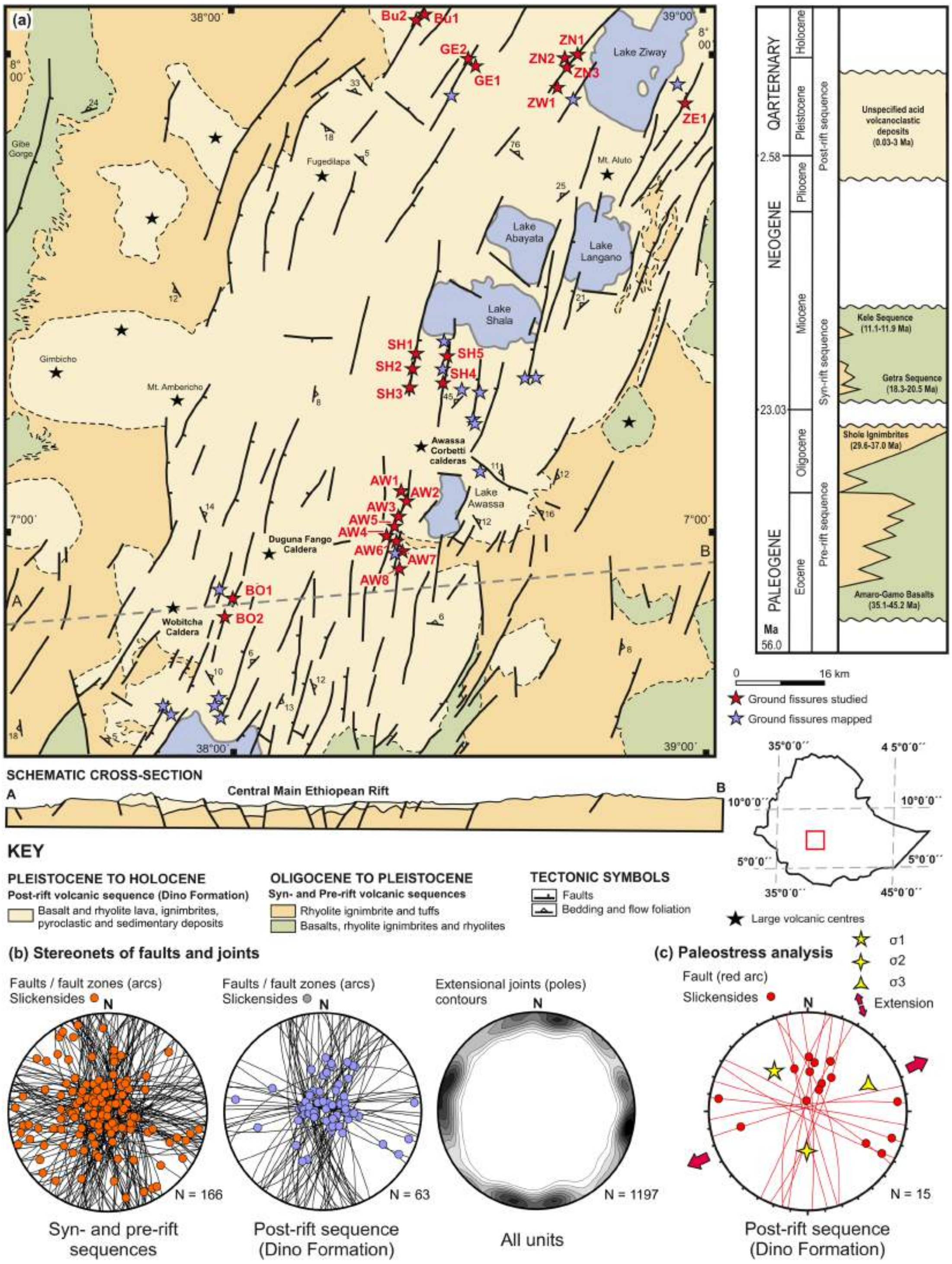

FIGURE 2 (a) Simplified geological map and a stratigraphic chart of the studied area (compiled after Zenebe et al., 2012; Yismaw et al., 2015; Verner et al., 2018; Hroch et al., 2018a, 2018b; Buriánek et al., 2018); (b) stereonets of measured faults and extensional joints; (c) results of paleostress analysis (post-rift sequences). Equal area projection to lower hemisphere [Color figure can be viewed at wileyonlinelibrary.com]

In the post-rift sequences (Figure 2a,b) prevailing normal faults dip steeply to the ∼WNW or ESE bearing steeply ∼W plunging or ∼E to northeast (NE) steeply to moderately plunging slickensides, respectively. The subordinate faults dip steeply to ∼W (WSW) with slickensides plunging to the ∼W or have E (ENE) to W (WSW) trend with the prevailing oblique-slip pattern. Extensional joints (cracks) are mostly vertical, trending in ∼N (NNE)–S (SSW) or E (ESE)–W (WNW) directions.

2.3 | Geomorphological features

The morphological evolution of the MER is a result of the long-term interaction of tectonic, volcanic and climatic factors. The study area of the MER is characterized by a graben structure about 60 km wide with an average elevation of about 1600 m above sea level (a.s.l.) bounded by regional scale fault scarps separating the rift valley from the north-western Ethiopian Plateau and south-eastern Somalian Plateau with an average altitude of about 2500 m a.s.l. The MER floor forms a relatively flat landscape, partly segmented into small grabens and horsts divided by relatively steep straight scarps. The scarps form significant morpholineaments easily discernible from the ASTER digital elevation model (US Geological Survey, 2018; Figure 1). Post-rift Corbetti and Aluto volcanic centres (Fontijn et al., 2018; Hutchison et al., 2016; Rapprich et al., 2016) with an altitude of more than 2000 m a.s.l. are prominent landforms in the rift-valley. Due to active rifting, the landscape is modified by complex of surface processes such as water erosion and mass movements resulting in bad-land formation, slope instabilities and ground fissures (e.g., Asfaw, 1998; Billi 2003, Ayalew et al., 2004; Gebretsadik, 2014, Kycl et al., 2017, and references cited therein).

The erosional relicts of semi-conical crests of calderas are surrounded by numerous lakes situated into tectonically controlled endorheic depressions (e.g., Street, 1979; Chernet, 1982; Le Turdu et al., 1999; Rapprich et al., 2014.; Fontijn et al., 2018; McNamara et al., 2018). In general, the drainage pattern is characterized by gullies and narrow erosional valleys following joints and faults reflecting the overall uplift of the Somalian Plateau (e.g., Billi, 2015; Xue et al., 2018). The rivers have the character of ephemeral streams with high discharge fluctuation (Hroch et al., 2018a, 2018b; Rapprich et al., 2014) following the seasonal variation in precipitation. It suggests the erosional rate and controlling mechanisms could change significantly throughout the year and could lead to a rapid opening of ground fissures during the rainy seasons. Moreover, the faults and joints, forming preferential pathways and controlling the discharge could determine or influence the prevailing direction of newly opened ground fissures.

2.4 | Hydrogeology and climatic conditions

Most of the lithological types present in the MER rift floor could be considered permeable, in general. However, the homogeneity of hydrogeological parameters differs. The lacustrine and epiclastic deposits form shallow aquifers with high hydraulic conductivity (approximately 25 m/d according to Tenalem, 2001) due to the high porosity of the sediments. In contrast, the hydraulic conductivity of lava flows and ignimbrites is highly variable and closely related to joints and fault zones. While, for the compact rocks, this could be as low as 0.09 m/d the highly fractured and jointed rocks could have a hydraulic conductivity similar to the lacustrine sediments and form water bearing aquifers (Tenalem, 2001; Ayalew et al., 2004; Abiye, 2008).

The hydrogeological conceptual model of the area was described by Hroch et al. (2018a, 2018b). In general, the groundwater flow is parallel with the surface flow system. The direction being from highlands to the rift floor. On the rift floor, the groundwater flow is determined by the relative elevations between the individual sub-basin lakes. However, locally, the water regime could be influenced by major structural and tectonic features. This is evidenced by deep water circulation resulting in hot springs with a high yield (Hroch et al., 2018a, 2018b).

The climatic conditions of the study area are variable and mostly influenced by the altitude, partly also by the latitude. A subtropical highland variation of the oceanic climate, with mild summers and noticeably cooler winters, and a tropical wet and dry climate zone are both present.

The precipitation regimes correspond to zone A according to the classification by the National Meteorological Service Agency (1996) and it is characterized by four distinct seasons and bimodal precipitation patterns with two peaks, the first occurring in March–May and the second during August–November. The annual precipitation in the highlands can exceed 1.400 mm whilst on the rift floor it is 800 mm (Supporting Information Dataset S1). The mean annual temperature varies between 15 and 20°C.

A detailed description of annual precipitation, including data from meteorological stations, are included in the Supporting Information (Text Text S1, Figure S1 and Dataset S1). However, the most important fact for the study is the bimodal precipitation pattern leaving the area dry for most of the year and bearing a significant amount of rainfall within a short time causing the near surface sediments to become saturated with water.

3 | METHODS

Within the studied area (Figure 2a), both geological mapping and a field structural analysis on a scale of 1:200,000 and 1:50,000, according to conventional methods (Hanžl & Verner, 2018), were carried out from 2012 to 2018 as a part of Czech Development Aid (Czech Geological Survey, 2018). A part of this work was an assessment of the geological and lithological pattern with an emphasis on the ground fissure sites (Figures 1 and 2a).

The methods used were, initially, a detailed lithological, structural (the joints and faults could affect the evolution of fissures as well as the steeply inclined bedding) and geomorphological mapping, supported by a morphostructural analysis of a digital elevation model. The spatial evolution of ground fissures was studied using the temporal sequence of aerial photographs available at Google Earth. Next, several ground-fissure sites with different temporal evolution (to cover potentially different mechanisms of origin) were selected for detailed analysis. These included a laboratory determination of the geomechanical properties of soils and unconsolidated sediments (density, grain size, plasticity, water saturation, porosity, filtration coefficient) as they are considered to be the key factors controlling the erosional rate and stability of the ground fissures' vertical walls – the proportion, in volume and size, of individual particles and water saturation controls the internal stability of soils (Chang & Zhang, 2013). (In this study the term 'soil' is used in a geotechnical sense for all unconsolidated clastic deposits.) In addition, changes in the stress tensor affect the internal stability of soils as well (Richards & Reddy, 2012). Such changes are, typically, the result of changes in water saturation. However, they can be also induced by changes of the regional (tectonically induced) stress field. The latter affects the elastic properties (especially their azimuthal anisotropy). Therefore, shallow seismic measurements in two perpendicular directions (parallel and perpendicular to fissure direction) have been carried out to assess the anisotropy of the elastic properties, showing the predominant direction of lithological boundaries and, more importantly, weakened zones (joints and faults which serve as preferential water flow paths) determining subsequent erosion (e.g., Busby & Peart, 1997).

A total of 93 ground fissure sites were mapped (coordinates of the individual documentation points, sampling sites, seismic measurements, etc. with additional information can be found in Dataset S2 and in Figure 1). Two areas (southwest [SW] of Lake Awassa and SW of Lake Shala) were then selected for a detailed investigation (Figure 1). At seismic profile Sites 1 and 2 (Figure 1) geomechanical and petrological sampling was also carried out, at Site 4 all methods were applied (geophysics, geomechanics and lithological logging). In total, 24 simple ground fissures and more complex ground fissure systems were studied. A synthesis of the results obtained leads to an innovative model for ground fissure origin.

A detailed description of the methods used can be found in the Supporting Information, Text S2.

4 | RESULTS

4.1 | Lithological and structural characteristics

The ground-fissures were exclusively formed in the post-rift sequences such as unconsolidated pyroclastic deposits (unwelded pyroclastic fall deposits and ash-flows) commonly overlying weathered, more rigid rhyolitic ignimbrites and minor lava flows. These rocks reveal prevailing sub-horizontal to roughly ~N–SE or ~NNE–SSW gently dipping bedding planes defined by a planar preferred orientation of high-porosity fragments of volcanic glass or pumice and gently elongated micro-vesicles or micro-crystals. Rare, variously dipping flow-foliation is likely to reflect rhyolite lava-domes or the minor morphological heterogeneity of volcanic flows. Minor lacustrine sediments from the Holocene show scarce horizontal bedding. The exposed sections of the ground-fissures and sinkholes (Figure 3a) enable the overall characteristics of the lithological composition to be determined. From the lithological point of view, there is a common sequence of unconsolidated or poorly consolidated re-sedimented volcaniclastic, alluvial and lacustrine sediments or strongly weathered lava flows which overlie rigid (consolidated) lava flows or resistant, more consolidated, volcaniclastic rocks such as rhyolitic ignimbrites (Figures 3a and 4c). No significant amounts of salt, organic matter or traces of them were found. The prevailing part of the exposed sections is formed by unconsolidated volcaniclastic deposits (Figure 3a,b). These rocks are composed of a mixture of volcanic ash, pumice fragments (up to 43 cm in diameter), glass shards (rip-up obsidian up to 4 cm in diameter), and rock fragments (mainly rhyolite and trachyte lithoclasts up to 3 cm in diameter). Based on the emplacement mechanism and textural features, three types of irregularly alternating unconsolidated volcaniclastic deposits were distinguished: (a) a rhyolite to trachyte tephra, (b) a weathered ignimbrite and (c) epiclastic deposits. The bottom parts of the sections are usually formed by consolidated volcaniclastic deposits represented mainly by rhyolitic ignimbrites (Figure 3a, Sites 4 and 1068) and associated pyroclastic fall deposits. Their overall thickness remains unclear, consisting of numerous rigid, rhyolitic ignimbrite layers *c.* 1–3 m thick, often separated by narrow tephra or paleosol horizons. A detailed lithological description including microphotographs is available in Text S3 and Figure S2.

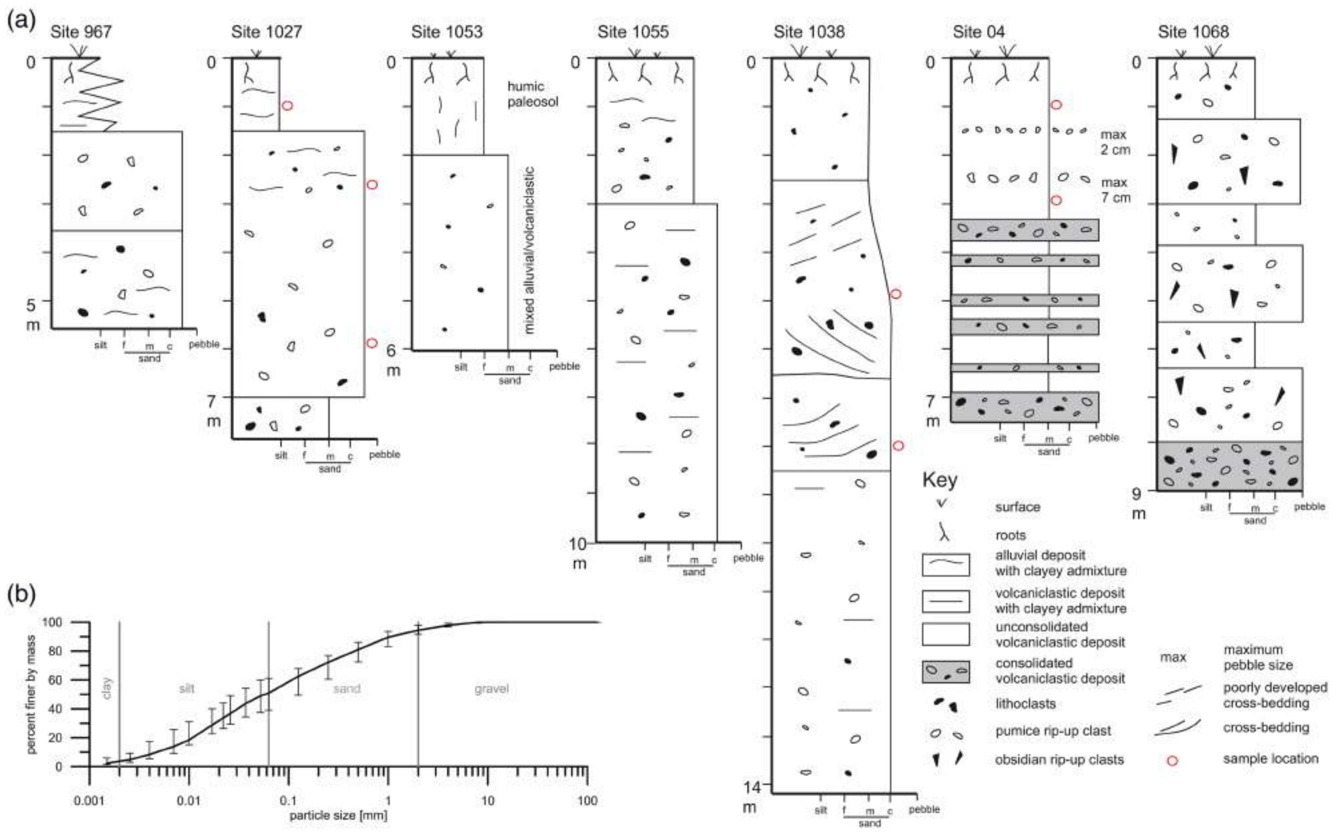

FIGURE 3 (a) Schematic lithological sections of ground fissures. For the location and additional description see Figure 1 and Dataset S2 in the Supporting Information. (b) Particle distribution curve of the sediments sampled. The curve represents a median value from all of the samples (16 samples in total), the error bars show the first and third quartile of the particular fraction. The locations and particle distribution of individual samples is included in the Datasets S2 and S3 in the Supporting Information [Color figure can be viewed at wileyonlinelibrary.com]

FIGURE 4 Field photographs of faults and main forms of ground-fissures: (a) east-southeast (ESE) moderately dipping normal fault, parallel with the main north-northeast–south-southwest (NNE–SSW) trending western rift escarpment (Ocholo Village, north of Arba Minch); (b) N (NNE)–S (SSW) trending normal faults in post-rift unconsolidated volcanoclastic deposits (Awassa-Sodo crossroad); (c) representative lithological profile of the ground fissure built by unconsolidated volcaniclastic deposits with rigid rhyolitic ignimbrite at the bottom; (d) intersection of principal N–S and subordinate E–W trending ground fissures with unstable steep walls parallel with regional faults; (e) linear N–S trending distribution of individual sinkholes and lenticular sinks; (f) NNE–SSW trending normal faults and associated sinkholes (Leku) [Color figure can be viewed at wileyonlinelibrary.com]

The results of the detailed geological and structural mapping around the ground fissure sites (for location see Figures 1 and 2a) show a clear spatial and orientation linkage between the regional normal faults and the mapped ground fissures (Figures 2a,c and 4b,c,d,f). Mapped faults are mostly steep having mostly ~N (NNW)–S (SSE) or ~NNE–SSW trends. Their slickensides plunge steeply to moderately to ~WNW (NW) or ~ENE (NE) bearing normal kinematics (Figure 2b, c). Subordinate ~ENE to WSW 'rift-perpendicular faults' reveal an oblique-slip pattern with prevailing left-lateral kinematics (Figure 2c). The principal axes of strain ellipsoid were identified based on a paleostress analysis of a consistent set of normal and oblique-slip faults (Figure 2c) cropping out nearby one of the ground fissures (Figures 1 and 2a). The results of paleostress analysis reveal the extension direction (σ1) trending ~WSW–ENE (azimuth 65°).

4.2 | Ground fissure and sinkhole characteristics

The ground-fissures (for location see Figures 1 and 2a) were documented mainly in the rift-floor environment where low-slope settings, mainly in flats or in shallow and widely opened depressions, with lower surface run-off occur. The following paragraph summarizes the most important general characteristics of the studied fissures.

A detailed description of the selected sites is available in Text S4.

Two forms of ground fissures were identified: (a) Linear ground fissures which are typically structures that are several metres to 20 m wide with depths of similar size as widths (the average depth to width ration observed was 1.35) and tens to hundreds of metres long (Figures 4d and 5). (For the dimensions of individual fissures, please refer to Dataset S2.) Most of them are part of the several kilometre long complex fissure structures, some showing the characteristic 'en-echelon' pattern (Figure 5) defined by Roering (1968). They form a single linear structure, or a multiple system of subparallel lines interconnected by perpendicular ones or step over. In some places, the closely spaced parallel structures are joined into wider zones affected by surface subsidence and side-wall collapse. Large fissures are initiated through the opening of a few elongated and aligned sinkholes. (b) Sinkholes, lenticular sinks and the domains of surface subsidence have steep side-walls, a circular or oval shape, which can be several metres in diameter, and have depths of up to 20 m (Figure 4e). These structures form in lines parallel to ground fissures and regional faults (Figures 4f and 6). The individual sinks, sinkholes and ground fissures are locally interconnected by underground pipes. Pipes were observed in nine ground fissure systems (from a total of 24 described, see Figure 7a–c), although it is supposed that the pipes are developed in most cases, but obliterated by subsequent collapse and sediment fill after collapse (see e.g., Figure 7d,e). Sometimes a row of small sinkholes (in the initial stages up to 1 m in diameter) can continue in the direction of the linear ground fissure and track the direction of the already formed pipe. This effect was observed, for example, at seismic Site 4.

The temporal evolution of ground fissures could be illustrated by the example of one of these fissures located SW of the Shala Lake (Figure 1). The description is based on the temporal sequence of orthophotographs – for the years 2013, 2016 and 2018 – available at Google Earth (2019).

In 2013 the ground-fissure had the character of a single and continuous SW–NE oriented fracture *c*. 470 m long. Two isolated sinkholes are identified in the south-western extension of the fissures (see Figure 5a).

The orthophotograph from 2016 detects the increasing size of older sinkholes and the propagation of a series of new cracks extending in the direction of the original crack. Also, a new isolated sinkhole *c*. 120 m away from the NE tip of the original ground fissure can be observed (see Figure 5b).

Interconnection of the individual sinkholes in the south-western part and the progradation of the ground fissure to the NE resulted in the formation of a multiple ground fissure system organized in an en-echelon pattern, which are apparent in the images from 2018 (see Figure 5c). Infilling of part of the original ground-fissure by sediment as the result of in-flow by a surface drainage system has also been detected.

4.3 | Geomechanical properties

The unconsolidated volcaniclastic deposits were classified as non-plastic silts or sands (11 and four specimens, respectively). None of the samples were uniform (from the particle-size point of view). The amount of clay particles is very low (below 10%) and, simultaneously, the amount of silt-size particles is high, leading to non-plasticity and internal instability in the soils (Figure 3b). All specimens were well graded, with rather flat portions of the grading curves in the range for silt-grain sizes and a very low amount of clay-size particles (Figure 3b). Therefore, going by grading alone, none of the soils is considered internally stable, as grading instability is most likely to occur in soils with gently inclined initial portions of grading curves (e.g., Kenney & Lau, 1985). All the undisturbed specimens had high porosities (50–63%) where high water permeability enables loss of the fine fraction, and hence further decreases the internal stability (Chang & Zhang, 2013), and a low or very low degree of saturation (4–76%; the samples were taken during the dry season). Although suction or water retention were not determined, it can be assumed that the soils exhibited very high suctions *in situ*. During the wet season, though, when the soils become saturated, they are prone to collapse and/or piping due to a decrease in effective stress.

4.4 | Seismic anisotropy measurements

The dispersion curves and calculated one-dimensional (1D) profiles for individual spreads are plotted and compared in Figures 8 and 9.

All fissure sites (Sites 1–4) exhibit distinct seismic anisotropy (more than 20%, Table 1) where seismic velocities in the direction parallel to the fissures is higher than in the perpendicular direction. In contrast, the reference site (Site 5) exhibits only low anisotropy (7%, Table 1) indicating a more homogeneous environment.

The anisotropy values from the ground fissure sites consistently show that S-wave velocities on the parallel profiles are higher than those on the perpendicular profiles. The high anisotropy values suggest either vertical (or sub-vertical) lithological boundaries (e.g., a steeply inclined bedding), or a significant effect from brittle tectonics (forming sets of parallel joints and faults). However, according to the geological and structural mapping, the bedding is generally horizontal or sub-horizontal, therefore the effect of anisotropy should be accounted to brittle tectonics forming weakened zones, with decreased horizontal stress and being more permeable to water. Such zones could be easily eroded, especially in sediments with a high silt/clay ratio, as described in the geomechanical sections.

The anisotropy at Site 5 (out of the ground fissure sites) was different from the fissure sites, the anisotropy value was 0.93, which means that S-wave velocities on the profile parallel with the axis of the rift were slightly lower than the velocities in the perpendicular direction. Nevertheless, the anisotropy ratio is low, close to one, which means that the velocities at this site are almost homogeneously distributed in the horizontal direction.

The high anisotropy values in this geological context suggest a significant preferential direction of weakened (more permeable) zones parallel to the rift axis.

5 | DISCUSSION

5.1 | Factors controlling ground fissures

Based on the new data and field observations from the MER, the main factors that can influence ground fissure formation are discussed (e.g., Sheng & Helm, 1998; Asfaw, 1998; Ayalew et al., 2004; Peng et al., 2018; Nikbakhti et al., 2017; Richards & Reddy, 2012; Bernatek-Jakiel & Poesen, 2018). All the ground fissures under study were formed suddenly by collapse, no hairline stages that slowly opened nor vertical displacements were observed or reported by local communities. In several cases it was possible to follow the continuation of the fissure by small isolated sinkholes aligned in the direction of the fissure (Figure 5), but no signs of vertical displacement or other

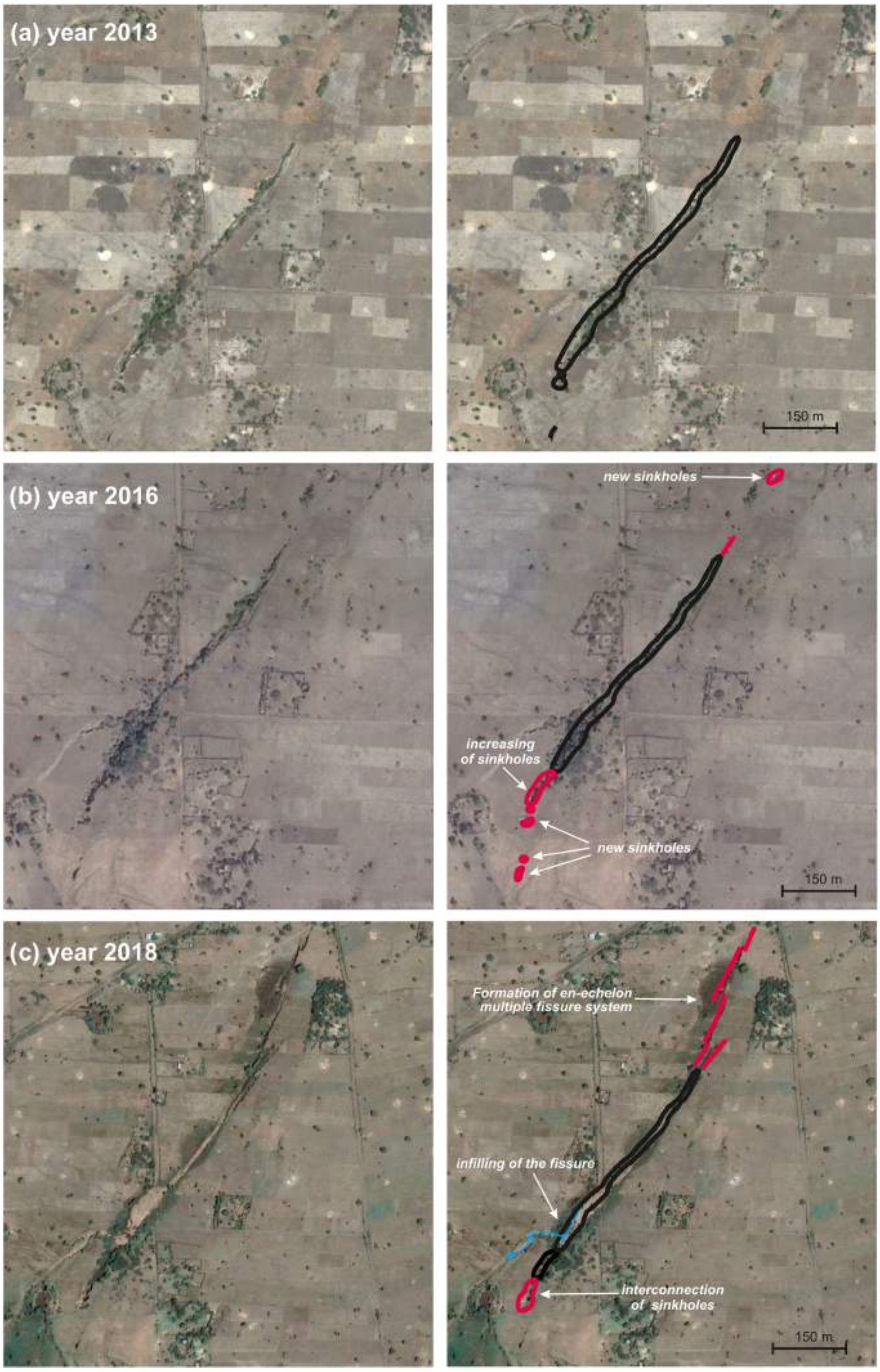

FIGURE 5 Temporal sequence of the orthophotographs from the Google Earth application reflecting geomorphological changes in ground-fissure formation: (a) year 2013, (b) year 2016 and (c) year 2018 [Color figure can be viewed at wileyonlinelibrary.com]

signs of fissuring. In addition, the temporal analysis of satellite images documents the gradual evolution of ground fissures, when, in their initial stage, the isolated sinkholes are formed and later they are interconnected to form a linear fissure by surface collapse.

All the ground fissures were developed in a highly porous and permeable environment of unconsolidated volcaniclastic deposits with a very low clay content. For these reasons we think that aquifer-system compaction and horizontal seepage stresses responsible for changes in the volume of material (e.g., Carpenter, 1993; Nikbakhti et al., 2017) do not have a significant effect on ground-fissure formation in the MER. Also, no significant amounts of salt, organic matter or traces of them were identified either, therefore their decay or dissolution (e.g., Ayalew et al., 2004) also cannot produce the ground fissures. In addition, the opening of ground fissures was not induced by earthquakes as the last large earthquake in the Awassa region (a moment magnitude of $MW = 4.29$) happened in January 2016 (Wilks et al., 2017) and many of the ground fissures postdate the earthquake. However, several geomorphological features corresponding to the piping mechanism (Bernatek-Jakiel & Poesen, 2018), such as underground pipes, minor depressions, sinkholes and blind gullies, were identified (for evidence see Figures 4 and 10). Therefore, and also in accordance with Farifteh and Soeters (1999), Atallah et al. (2015), Bernatek-Jakiel and Poesen (2018), and Wilson et al. (2018) it is assumed that piping is the major mechanism of ground fissure formation in the MER with a probable contribution from other factors which are discussed later.

In geotechnical engineering, several criteria are used in controlling or minimizing the detrimental effect of piping on the stability of earth structures subjected to seepage. Most commonly, they are based on the shape of the grading curve. In general, if the amount of the

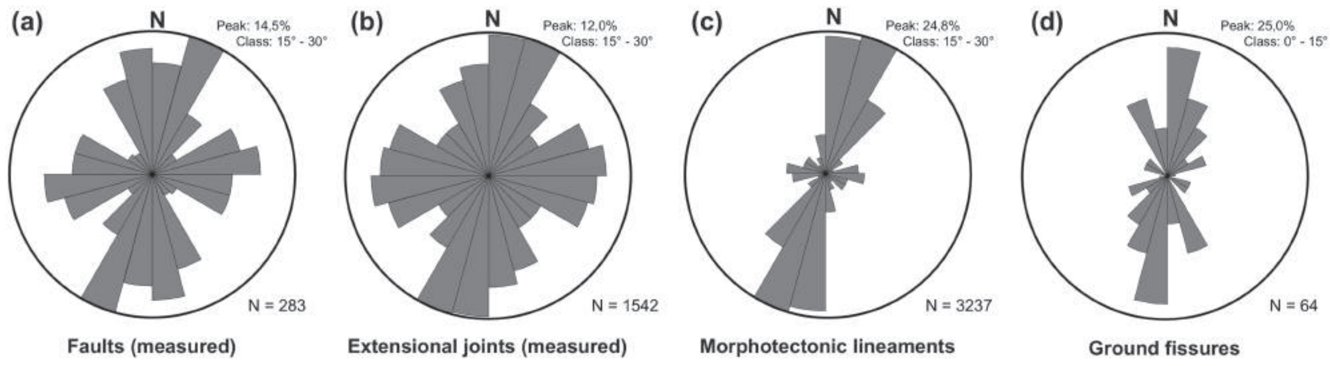

FIGURE 6 Field structural measurements and morphotectonic analysis (rose diagrams of strike directions): (a) normal faults; (b) extensional joints; (c) morphological lineaments (Figure 1) and (d) ground fissures

fine-grained fraction is too low, the coarse-grained fraction cannot prevent its loss due to seepage flow leading to soil instability (Chang & Zhang, 2013). Furthermore, for verifying/controlling the grading of the soils, there is a check as to whether the hydraulic gradients, or the seepage velocities, remain below a critical value (Terzaghi, 1943). For vertical upward flow of water Li and Fannin (2012) proposed a theoretical hydromechanical envelope in the plane of effective vertical stress. The effective stress, as the difference between the total stress and pore water pressure versus the hydraulic gradient, was defined by Terzaghi (1943).

Soil plasticity (liquid and plastic limits) is often also taken into account when assessing the possibility of piping. Richards and Reddy (2012), for example, showed that an admixture of highly plastic fines (namely montmorillonite) substantially increased the differential pressures required for inducing piping and that such highly plastic soils hydraulically failed during erosion by a concentrated leak in erosion channels. Furthermore, their paper experimentally confirms the influence of the mean effective stress on the initiation of piping: the increase in pore pressure (e.g., increased water saturation during the rainy season) and/or the reduction in confining stress (e.g., due to horizontal tension) lowers the critical seepage velocity needed for the onset of piping.

Furthermore, in addition to the basic properties of the soils (grading, non-plastic character) and to changes in the *in situ* state (water saturation), the occurrence of ground fissures and piping could also be partially attributed to the effective stress conditions. Decreased vertical stress due to horizontal tension (Richards & Reddy, 2012) demonstrated that a decrease of effective stress facilitated internal erosion. Thus, areas close to zones with decreased horizontal stress (e.g., zones weakened by horizontal extension and brittle tectonics) should be considered prone to erosion and piping. A similar effect – a decrease of stability with decreasing load – has been already described on sandstones by Bruthans et al. (2014).

The typical lithological environment in which ground fissures were identified is a sequence of unconsolidated volcaniclastic deposits, which underwent mechanical transport (fluvial transport or ash-fall) with a very high porosity (more than 50%) and very low clay content (2–8%, in maxima up to 15%; see Dataset S3). This unconsolidated sedimentary sequence overlies more rigid and less permeable strata such as rhyolitic ignimbrite or basalt lava flow (Figures 3a and 4c). In this specific geological environment, the accumulated rainfall can percolate down to the surface of the relatively impermeable underlying layer and effectively erode the bottom parts of the unconsolidated sediments. One important factor for the initial piping (sub-surface erosion) seems to be the size and content of the individual sedimentary or volcanic particles in the unconsolidated deposits (e.g., sand-content vs. clay-content). The lack of clay particles (mostly less than 10% from the bulk volume; Figure 3b) makes such deposits vulnerable to erosion due to reduced (internal) stability when saturated with water. Such deposits are considered to be prone to piping even under a low hydraulic gradient (e.g., Atallah et al., 2015). The clay-poor sediments could be effectively eroded when wet, especially in zones of low stress or reduced strength (e.g., Bruthans et al., 2014; Richards & Reddy, 2012) such as brittle tectonic zones (faults and joints). These zones of weakening are also predisposed path-ways for groundwater flow. In addition, the decreased hydraulic stability in unconsolidated sediments above the impermeable strata, mainly along the 'low-stress' tectonic structures (the principal extension in the horizontal direction), allows piping due to groundwater flow related to the heavy rainfall season.

In addition, our study revealed a clear spatial and orientation (trend) linkage between the ground fissures and regional tectonic structures, which is apparent by comparing the orientation trends of ground fissures, regional faults, morpholineaments and extensional joints across the study area (Figures 2 and 6) as well as field observations at individual sites. This fact demonstrates the importance of tectonic pattern where faults and tectonic joints are the most significant influencing factors for the origin of piping (sub-surface erosion) subsequently resulting in the formation of a ground fissure. This strongly resembles the earth fissures in Dali County (China) associated with extensional tectonic activity (Jia et al., 2020).

The results of the paleostress analysis on a consistent set of faults (Figure 2c) near the ground-fissures sites showed a major crustal extension in the ~ENE–WSW direction (azimuth 65°) which is comparable with several studies discussing the kinematics and paleostress conditions of the regional extension from the beginning of the rifting (*c.* 12 Ma) to the present. An early ~NW–SE oriented extension (Chorowicz, 2005) was later changed to an ~E–W direction (Bonini et al., 2005; Wolfenden et al., 2004). Alternatively, it is supposed a permanent ~E–W to ~ESE–WNW extension (e.g., Agostini et al., 2009; Erbello & Kidane, 2018) or an ~ENE (NE)–WSW (SW) oriented extension (Muluneh et al., 2014; Pagli et al., 2018) also identified in the post-rift volcanic sequences (from ~ 3 Ma to recent). Presumptive anticlockwise changes of the principal extension

FIGURE 7 Field photographs of successive stages of ground fissure formation: (a) isolated sinkhole in unconsolidated deposits and initial piping mechanism associated with sub-surface erosion (location); (b) isolated sinkholes interconnected by a pipe (Leku); (c) large-scale sinkhole and pipe in lower part (Boditi); (d) linear north–south (N–S) trending ground fissure formation associated with ceiling collapse (southwest of the town Awassa); (e) destruction of farmers facilities due to sudden collapse of pipe ceiling and ground fissure formation; (f) linear N–S trending ground fissure with unstable steep walls (Leku); (g) continuous erosion around the ground fissure forming deep gullies (Boditi); (h) later fluvial-dominated erosion and 'bad-land' formation (southwest of Awassa town) [Color figure can be viewed at wileyonlinelibrary.com]

direction (e.g., Muluneh et al., 2014; Wolfenden et al., 2004) may also have an influence on the overall ground fissure shape, often showing a partly asymmetric 'en-echelon' pattern (Figure 5).

The seismic surveys in the study area are consistent with the expectation of seismic anisotropy across the predominant orientation of the tectonic structures. The anisotropy measurements show that the S-wave velocities at the ground fissure sites are considerably higher in the direction parallel with the axis of the MER and hence along the strike of the tectonic structures. This fact not only implies that the stiff layers are affected by brittle tectonics (extensional joints

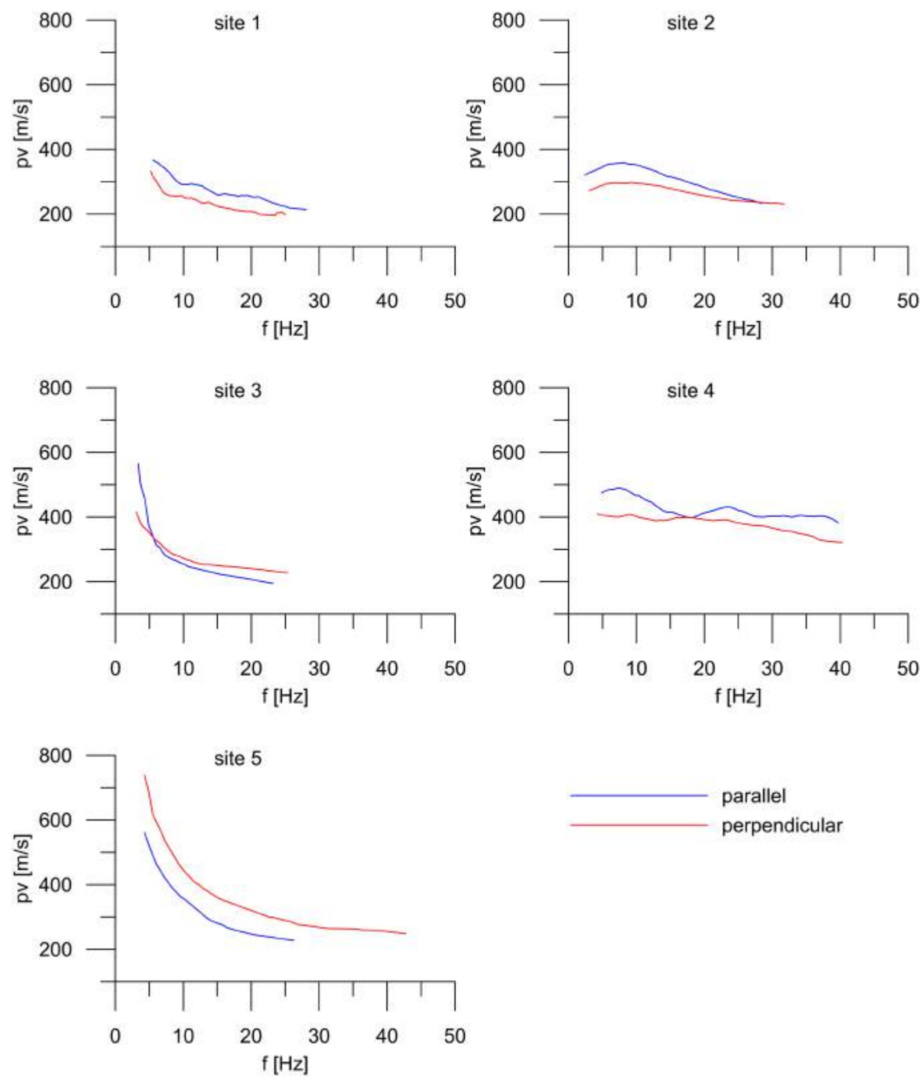

FIGURE 8 Dispersion of Rayleigh waves phase velocities (pv) for individual frequencies (*f*) determined for each of the measured seismic profiles and theoretical dispersions for the final one-dimensional models [Color figure can be viewed at wileyonlinelibrary.com]

and faults) due to the regional extension, but could also be used for mapping areas prone to future piping. The large difference of seismic wave velocities (this study shows more than 20% for S-waves) measured on profiles perpendicular to the main extension direction indicates severe jointing and, together with the lithological environment described earlier, predicts a high risk of ground fissure formation.

In contrast to other common geophysical field techniques used to map already existing pipes (e.g., electrical resistivity tomography and ground penetrating radar) (Anchuela et al., 2018; Bernatek-Jakiel & Kondracka, 2016; Shin et al., 2019) the seismic anisotropy measurements could indicate potentially endangered areas by finding zones prone to piping-favourable conditions (severe jointing and stiff layers). This phenomenon can occur even before the piping starts or whilst it is in its very early stages before the ceiling collapses. Therefore, it could be used for *sensu stricto* prediction of future occurrences in the region.

5.2 | Origin of ground fissures

Based on the discussion earlier, the following origin of ground fissures is proposed. In connection with the active ~ENE–WSW direction (azimuth 65°) rift-related extension and associated normal faulting, mechanical weakening and stress lowering occurs along the tectonic zones (Stage I.; Figures 4f and 10). Next, the groundwater flow erodes and expands the pipes in the unconsolidated sediments (Stage IIA.; Figures 7a,b and 10) and further propagates upwards through these sediments forming isolated sinkholes (Stage IIB; Figures 4e, 7a–c and 10). When the erosion exceeds the hydraulic stability of the sediments, the ceiling of the pipe eventually collapses to form the first ground fissures (Stage IIC; Figures 4d, 7d and 10). The collapse is sudden and often happens during or closely after a heavy rainfall period, which saturates the sediments and severely decreases their hydraulic stability (Figure 7e). The initial ground fissures are further interconnected by continuing erosion and increasing water flow forming deep gullies (Stage III; Figures 7f,g and 10). The subsequent erosion can result in 'bad-land' formation in topographic highs, or alternatively, depressions could be filled with water and sediments during fluvial-dominated erosion in topographic lows (Stage IV; Figures 7h and 10).

The proposed model presents an alternative scenario to the already published hypotheses on the origin of ground fissures in the MER, which emphasized an aseismic origin of the phenomena caused by an elastic strain due to groundwater level fluctuation (Ayalew et al., 2004) or solely connected to earthquake events (Asfaw, 1982) as both are not witnessed to have occurred prior to the onset of ground fissure emergence. Only one case from the 24 ground fissures described in this study is reported to have been modified by an earthquake (BO1 near Boditi).

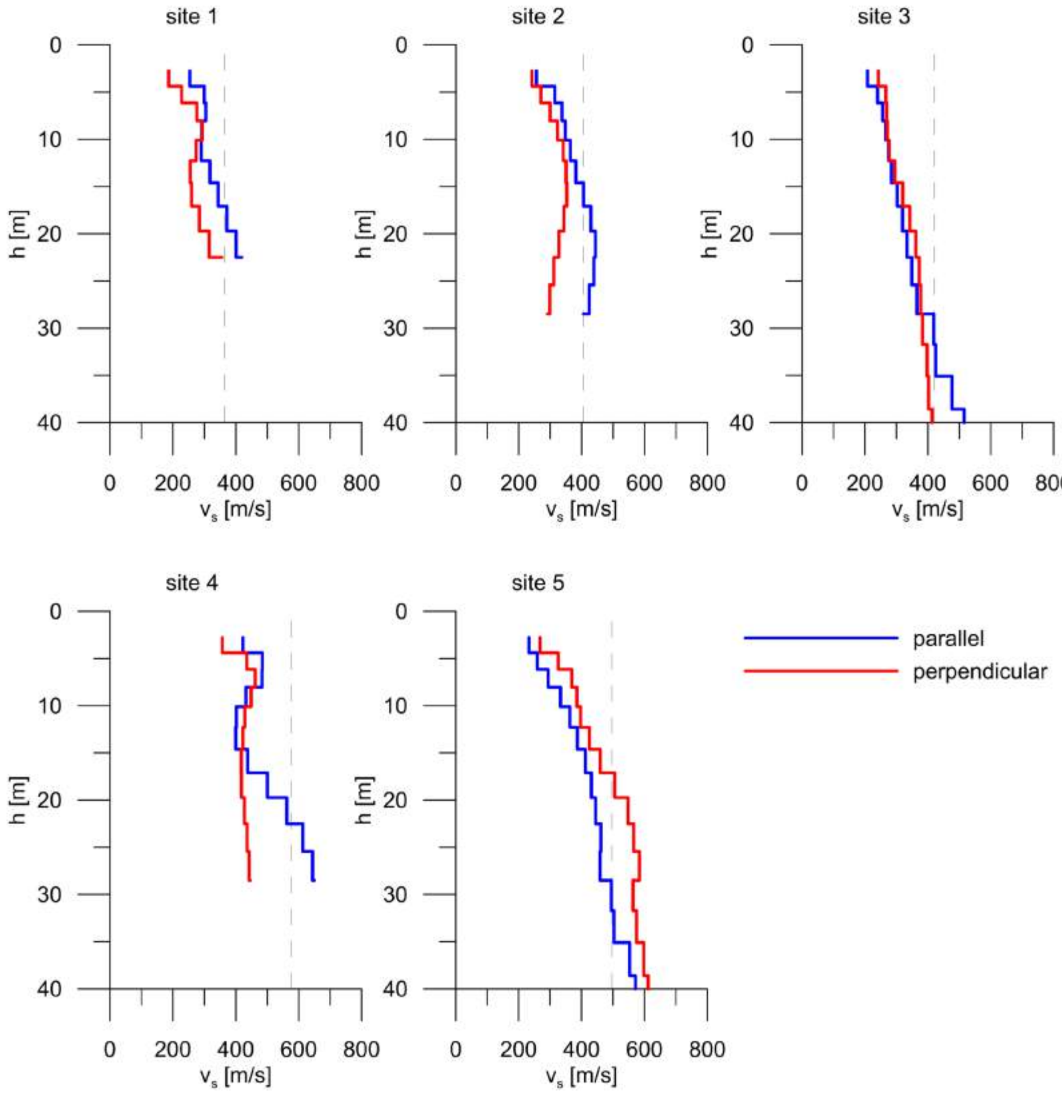

FIGURE 9 Calculated one-dimensional velocity distributions for individual ground fissure sites. The broken line shows the value of the threshold (the third quartile) [Color figure can be viewed at wileyonlinelibrary.com]

TABLE 1 The third quartile of S-wave velocities measured on the profile parallel to the course of the ground fissures or the axis of the Main Ethiopian Rift (MER) (Site 5) and the anisotropy value for each of the sites (the code in parenthesis references the geomorphological description)

	Latitude (°N)	Longitude (°E)	Elevation (m)	Third quartile of S-wave velocities (m/s)	Anisotropy
Site 1 (AW5)	7.022051	38.349276	1699	364.78	1.27
Site 2 (AW7)	7.005523	38.357770	1711	405.90	1.38
Site 3 (AW6)	7.004760	38.344560	1726	420.54	1.22
Site 4 (SH1)	7.378020	38.380995	1664	575.35	1.46
Site 5	7.335593	38.369207	1695	496.68	0.93

An anisotropy value larger than one indicates higher velocities in the direction parallel with the fissure.

5.3 | Comparison with other ground fissures

The case of the ground fissures from the MER are akin to the Type D – ground-fissures induced by the basal stretch fracture system with the coupling function of the exploitation of groundwater (Zang et al., 2019). They strongly resemble the ground fissures in the Shuanghuaishu Weihe Basin of China (Sanyuan County), where over 200 ground fissures have been reported (Peng et al., 2018). Although the origin is different there, the current locations of fissures are pre-determined by paleo-fissures, piping also plays an important role as well as the decrease in effective stress by horizontal extension. The fissures in, the Cenozoic rifting basin of the Weihe Basin develop in parallel to the underlying fault systems and in an active rift zone. The soft sediments of loess that make up the area affected by ground fissures, with their low cohesion and susceptibility to erosion, are, from the geomechanical point of view, similar to the pyroclastic deposits found in the plains of the MER hosting the ground fissures under study. Tectonic stress inferred from fault kinematics in the case of the Weihe Basin fissures, which is a NW–SE directed extensional regime in the upper crust (Deng et al., 1979; Jia et al., 2020), is well demonstrated to have initiated the NE–SW trending fissures following the underlying normal faults. The role of other factors is also

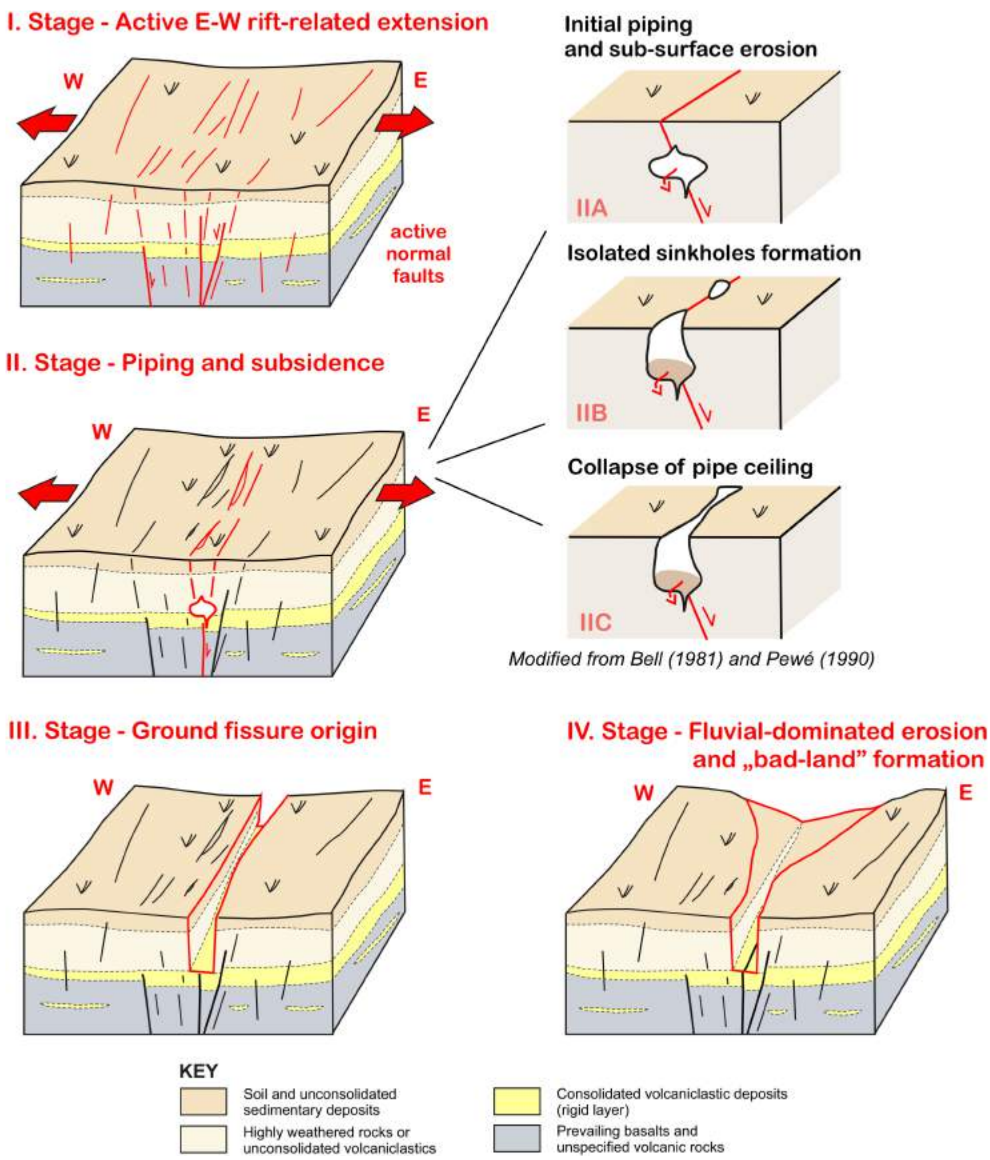

FIGURE 10 Interpretative blockdiagram showing individual stages of ground fissure formation [Color figure can be viewed at wileyonlinelibrary.com]

corroborated, including the heavy rainfall effect and the subsequent washing out of sediments under the surface resulting in the sudden collapse of the ground forming fissures (Peng et al., 2018). The role of the tectonic features, especially extensional joints and normal faults on predisposed sites that further develop into piping erosion and subsequently undergo sudden ceiling collapse and form ground fissures in the case of the studied fissures, is quite unequivocal.

6 | CONCLUSIONS

The specific conditions and factors leading to the origin of ground-fissures in the central and southern MER were concluded as follows (Figure 10):

a. The presence of active regional normal faults and associated extensional joints is an unequivocal prerequisite for the formation of ground-fissures (Stage I). The results of paleostress analysis on a consistent set of faults (Figure 2c) near the ground-fissures' sites showed a major crustal extension in the ~ENE–WSW direction (azimuth 65°), whereas the common 'en echelon pattern' of the ground-fissures is probably a result of the minor clockwise changes in the regional extension direction.
b. The study area is uniquely built by rigid and hydraulically impermeable rocks (e.g., rhyolitic ignimbrites of basalt lava flows) overlaid by relatively thick heterogeneous porous and permeable unconsolidated volcaniclastic deposits with a low amount of clay. As a consequence, the decrease of hydraulic stability above the relatively impermeable strata, mainly along the low-stress tectonic zones, initiates the piping mechanism and sub-surface erosion due to groundwater flow in relation to heavy rainfall periods (Stage IIA). The sub-surface erosion propagates upwards forming linearly distributed sinkholes parallel to the tectonic structures (Stage IIB) followed by the sudden collapse of the pipe ceiling (Stage IIC). Finally, the linear ground fissures are being formed (Stage III). After emerging on the surface, the ground fissures further expand laterally developing fluvial-dominated erosional valleys or the formation of 'bad-lands' (Stage IV).

Although the necessary clay-poor sediments are present in a large portion of the MER, evaluation of the intensity of jointing, which correlates with seismic anisotropy, and the presence of an impermeable layer could be used for mapping zones prone to piping. For such investigations, seismic measurements on two perpendicular profiles is proposed. If a large value of anisotropy is found (e.g., in our case S-wave anisotropy of more than 20% for ground-fissure sites), then the area should be considered prone to ground fissure formation. A thin impermeable layer might not be inferred from the surface wave profiles due to insufficient resolution but could be identified using standard geological techniques.

ACKNOWLEDGEMENTS

The research was funded by the Czech Development Agency in the framework of development project no. 281226/2018-ČRA 'Implementation of a Methodical Approach in Geological Sciences to Enhance the Quality of Doctoral Studies at the Addis Ababa University (Ethiopia)' (to K. Verner) and project no. 280614/2019-ČRA 'Ensuring Sustainable Land Management in Selected Areas of Ethiopia on the Basis of Geoscientific Mapping' (to K. Verner) and project Q45 Progress (Faculty of Science, Charles University, Prague). The authors thank the many colleagues from the Geological Survey of Ethiopia and Addis Ababa University (School of Earth Sciences) for their help in the acquisition, processing and interpretation of the data. The authors also gratefully acknowledge the Embassy of the Czech Republic in Addis Ababa for their support and Richard R. H. Withers for language revision.

CONFLICT OF INTEREST

None.

AUTHOR CONTRIBUTIONS

- J.V. was responsible for the conceptualization of the article, collected a part of the data, conducted the data analysis and drafted the article.
- K.V., K.M., T.H., D.B., L.M. and J.B. were responsible for a large part of the data collection. In particular, K.V. and L.M. for the structural geology part, K.M. for the sedimentology, T.H. for the geomorphology, D.B. for the igneous petrology and J.B. for the geomechanics. All of them significantly helped with writing and correcting the manuscript.
- M.K., F.L., M.Y. and B.K. contributed to the data collection and analysis.
- J.M. contributed to the idea that led to this article and helped write the manuscript.

DATA AVAILABILITY STATEMENT

Geophysical, geomechanical and meteorological data used in this study are available from https://doi.org/10.17632/stt8557n86.3.

ORCID

Jan Valenta https://orcid.org/0000-0002-3149-6067
Kryštof Verner https://orcid.org/0000-0002-9681-5380
Karel Martínek https://orcid.org/0000-0001-9857-8510

REFERENCES

Abiye, T.A. (2008) Environmental resources and recent impacts in the Awassa collapsed caldera, Main Ethiopian Rift. *Quaternary International*, 189(1), 152–162. Available from: https://doi.org/10.1016/j.quaint.2007.10.006

Agostini, A., Bonini, M., Corti, G., Sani, F. & Mazzarini, F. (2011) Fault architecture in the Main Ethiopian Rift and comparison with experimental models: implications for rift evolution and Nubia–Somalia kinematics. *Earth and Planetary Science Letters*, 301(3–4), 479–492. Available from: https://doi.org/10.1016/j.epsl.2010.11.024

Agostini, A., Corti, G., Zeoli, A. & Mulugeta, G. (2009) Evolution, pattern, and partitioning of deformation during oblique continental rifting: Inferences from lithospheric-scale centrifuge models. *Geochemistry, Geophysics, Geosystems*, 10, 1–11.

Anchuela, Ó.P., Frongia, P., Di Gregorio, F., Casas, A.M.S. & Pocoví, J.A. (2018) Internal characterization of embankment dams using ground penetrating radar (GPR) and thermographic analysis: A case study of the Medau Zirimilis Dam (Sardinia, Italy). *Engineering Geology*, 237, 129–139. Available from: https://doi.org/10.1016/j.enggeo.2018.02.015

Angelier, J. (1994) Fault Slip Analysis and Paleostress Reconstruction. In: Hancock, P.L. (Ed.) *Continental deformation*. Oxford: Pergamon Press, pp. 53–100.

Angelier, J., Tarantola, A., Valette, B. & Manoussis, S. (1982) Inversion of field data in fault tectonics to obtain the regional stress—I. Single phase fault populations: A new method of computing the stress tensor. *Geophysical Journal International*, 69(3), 607–621. Available from: https://doi.org/10.1111/j.1365-246X.1982.tb02766.x

Asfaw, L.M. (1982) Development of earthquake induced fissures. *Nature*, 286, 551553.

Asfaw, L.M. (1998) Environmental hazard from fissures in the Main Ethiopian Rift. *Journal of African Earth Sciences*, 27(3-4), 481–490. Available from: https://doi.org/10.1016/S0899-5362(98)00074-8

Assefa, E. & Bork, H.R. (2014) Deforestation and forest management in southern Ethiopia: Investigations in the Chencha and Arbaminch areas. *Environmental Management*, 53(2), 284–299. Available from: https://doi.org/10.1007/s00267-013-0182-x

Atallah, N., Shakoor, A. & Watts, C.F. (2015) Investigating the potential and mechanism of soil piping causing water-level drops in Mountain Lake, Giles County, Virginia. *Engineering Geology*, 195, 282–291. Available from: https://doi.org/10.1016/j.enggeo.2015.06.001

Ayalew, L., Yamagishi, H. & Reik, G. (2004) Ground cracks in Ethiopian Rift Valley: Facts and uncertainties. *Engineering Geology*, 75(3-4), 309–324. Available from: https://doi.org/10.1016/j.enggeo.2004.06.018

Barton, N. (2007) *Rock Quality, Seismic Velocity, Attenuation and Anisotropy*. London, UK: Taylor & Francis.

Bell, J. W. (1981) Subsidence in Las Vegas Valley: Nevada Bureau of Mines and Geology Bulletin 95, Nevada Bureau of Mines and Geology, Reno, NV, 84.

Bell, J. W., Price, J. G. & Mifflin, M. D. (1992) Subsidence-induced fissuring along preexisting faults in Las Vegas Valley, Nevada: Proceedings, Association of Engineering Geologists, 35th Annual Meeting, Los Angeles, CA, 66–75.

Benvenuti, M., Carnicelli, S., Ferrari, G. & Sagri M. (2005) Depositional processes in latest Pleistocene and Holocene ephemeral streams of the Main Ethiopian Rift (Ethiopia). In: Blum, M.D., Mariott, S.B., & Leclair, S.F. (Eds.) *Fluvial Sedimentology VII*. Special Publications of the International Association of Sedimentologists, 35, Blackwell Publishing, pp. 277–294.

Bernatek-Jakiel, A. & Kondracka, M. (2016) Combining geomorphological mapping and near surface geophysics (GPR and ERT) to study piping systems. *Geomorphology*, 274, 193–209. Available from: https://doi.org/10.1016/j.geomorph.2016.09.018

Bernatek-Jakiel, A. & Poesen, J. (2018) Subsurface erosion by soil piping: Significance and research needs. *Earth-Science Reviews*, 185, 1107–1128. Available from: https://doi.org/10.1016/j.earscirev.2018.08.006

Billi, P. (2015) *Landscapes and Landforms of Ethiopia*. Dordrecht: Springer.

Bonini, M., Corti, G., Innocenti, F., Manetti, P., Mazzarini, F., Abebe, T. & Pecskay, Z. (2005) Evolution of the Main Ethiopian Rift in the frame of Afar and Kenya rifts propagation. *Tectonics*, 24, 1–24.

Bruthans, J., Soukup, J., Vaculíková, J., Filippi, M., Schweigstillova, J., Mayo, A.L., *et al.* (2014) Sandstone landforms shaped by negative feedback between stress and erosion. *Nature Geoscience*, 7(8), 597–601. Available from: https://doi.org/10.1038/NGEO2209

Buriánek, D., Hroch, T., Verner, K., Megerssa, L., Martínek, K., Yakob, M., Haregot, A., Janderková, J., Šíma, J., Kryštofová, E., Valenta, J., Tadesse, E., Mosisa, A., Dalke, G., Legesse, F., Assefa, G., Pécskay, Z., Hejtmánková, P. & Krejčí Z. (2018) Explanatory notes to the thematic geoscientific maps of Ethiopia at a scale of 1: 50 000, Map Sheet 0638-C2 Dila, 1–103. Czech Geological Survey, Prague, Czech Republic.

Busby, J.P. & Peart, R.J. (1997) Azimuthal resistivity and seismic measurements for the determination of fracture orientations. In: McCann, D. M., Eddleston, M., Fenning, P.J. & Reeves, G.M. (Eds.) *Modern geophysics in Engineering Geology*, Geological Society Engineering Geology Special Publication No, Vol. 12. London, UK: The Geological Society, pp. 273–281.

Carpenter, M. C. (1993) Earth fissure movements associated with fluctuations in groundwater levels near the Picacho Mountains, south-central Arizona, 1980–84. US Geological Survey Professional Paper 497-H, US Geological Survey, Washington, DC; 40.

Chang, D.S. & Zhang, L.M. (2013) Extended internal stability criteria for soils under seepage. *Soils and Foundations*, 53(4), 569–583. Available from: https://doi.org/10.1016/j.sandf.2013.06.008

Chernet, T. (1982) *Hydrogeologic map of the lakes region (with memo)*. Addis Ababa, Ethiopia: Ethiopian Institute of Geological Surveys.

Chorowicz, J. (2005) The east African rift system. *Journal of African Earth Sciences*, 43(1-3), 379–410. Available from: https://doi.org/10.1016/j.jafrearsci.2005.07.019

Coubal, M., Adamovič, J., Málek, J. & Prouza, V. (2014) Architecture of thrust faults with alongstrike variations in fault-plane dip: anatomy of the Lusatian Fault, Bohemian Massif. *Journal of Geosciences*, 59, 183–208. Available from: https://doi.org/10.3190/jgeosci.174

Deng, Q.D., Zhang, Y.M., Xu, G.L. & Fan, F.T. (1979) On the tectonic stress field in China and its relation to plate movement. *Seismology and Geology*, 1(1), 11–22.

Ebinger, C.J., Yemane, T., Harding, D.J., Tesfaye, S., Kelley, S. & Rex, D.C. (2000) Rift deflection, migration, and propagation: Linkage of the Ethiopian and Eastern rifts, Africa. *Geological Society of America Bulletin*, 112(2), 163–176. Available from: https://doi.org/10.1130/0016-7606(2000)112<163:RDMAPL>2.0.CO;2

Ebinger, C.J., Yemane, T., Woldegabriel, G., Aronson, J.L. & Walter, R.C. (1993) Late Eocene-Recent volcanism and faulting in the southern Main Ethiopian Rift. *Journal of the Geological Society*, 150(1), 99–108. Available from: https://doi.org/10.1144/gsjgs.150.1.0099

Erbello, A. & Kidane, T. (2018) Timing of volcanism and initiation of rifting in the Omo-Turkana depression, southwest Ethiopia: Evidence from paleomagnetism. *Journal of African Earth Sciences*, 139, 319–329. Available from: https://doi.org/10.1016/j.jafrearsci.2017.12.031

Farifteh, J. & Soeters, R. (1999) Factors underlying piping in the Basilicata region, southern Italy. *Geomorphology*, 26, 219–251.

Fontijn, K., McNamara, K., Zafu Tadesse, A., Pyle, D.M., Dessalegn, F., Hutchison, W., *et al*. (2018) Contrasting styles of post-caldera volcanism along the Main Ethiopian Rift: Implications for contemporary volcanic hazards. *Journal of Volcanology and Geothermal Research*, 356, 90–113. Available from: https://doi.org/10.1016/j.jvolgeores.2018.02.001

Gaždová, R., Kolínský, P., Vilhelm, J. & Valenta, J. (2015) Combining surface waves and common methods for shallow geophysical survey. *Near Surface Geophysics*, 13(1), 19–32. Available from: https://doi.org/10.3997/1873-0604.2014039

Gebretsadik, Z.M. (2014) Watershed degradation and erosion in Hawassa-Zuria district. *Journal of Flood Risk Management*, 7(2), 118–127. Available from: https://doi.org/10.1111/jfr3.12033

Hanžl, P. & Verner, K. (2018) *Basic principles of geological and thematic mapping*. Czech Geological Survey & Geological Survey of Ethiopia. Available from: http://www.geology.cz/etiopie-2018/outputs/manual/basic-principles-of-geological-and-thematic-mapping.pdf

Hayward, N.J. & Ebinger, C.J. (1996) Variations in the along-axis segmentation of the Afar Rift system. *Tectonics*, 15(2), 244–257. Available from: https://doi.org/10.1029/95TC02292

Holzer, L.T. (1984) Ground failure induced by groundwater withdrawal from unconsolidated sediment. In: Holzer, L.T. (Ed.) *Man Induced Land Subsidence, Reviews in Engineering Geology*, Vol. 6. Boulder, Colorado: The Geological Society of America, pp. 67–105.

Hroch, T., Megerssa, L., Buriánek, D., Verner, K., Martínek, K., Mihret, Y., Janderková, J., Šíma, J., Kryštofová, E., Gebremariyam, H., Tadesse, E., Legesse, F., Valenta, J., Pécskay, Z. & Hejtmánková P. (2018a) Explanatory notes to thematic geoscientific maps of Ethiopia at a scale of 1: 50,000, Map sheet 0638-A2 Leku. Czech Geological Survey, Prague, Czech Republic.

Hroch, T., Megerssa, L., Buriánek, D., Verner, K., Martínek, K., Yakob, M., Ali, Y., Tadesse, E., Legesse, F., Hejtmánková, P. & Krejčí Z. (2018b) Geological map at a scale of 1: 50,000, Map Sheet 0638-A2 Leku. Czech Geological Survey, Prague, Czech Republic.

Hutchison, W., Pyle, D.M., Mather, T.A., Yirgu, G., Biggs, J., Cohen, B.E., *et al*. (2016) The eruptive history and magmatic evolution of Aluto volcano: new insights into silicic peralkaline volcanism in the Ethiopian rift. *Journal of Volcanology and Geothermal Research*, 328, 9–33. Available from: https://doi.org/10.1016/j.jvolgeores.2016.09.010

IUSS Working Group WRB. (2015) World Reference Base for Soil Resources 2014, update 2015International soil classification system for naming soils and creating legends for soil maps. World Soil Resources Reports No. 106. FAO, Rome.

Jia, Z., Lu, Q., Peng, J., Qiao, J., Wang, F., Wang, S. & Zhao, J. (2020) Analysis and comparison of two types of ground fissures in Dali County in the Weihe Basin, China. *Environmental Earth Sciences*, 79(1), 1–15.

Kazmin, V., Seife, M.B., Nicoletti, M. & Petrucciani, C. (1980) Evolution of the northern part of the Ethiopian Rift. *Atti Convegni Lincei*, 47, 275–291.

Kenney, T.C. & Lau, D. (1985) Internal stability of granular filters. *Canadian Geotechnical Journal*, 22(1), 215–225. Available from: https://doi.org/10.1139/t85-029

Kycl, P., Rapprich, V., Verner, K., Novotný, J., Hroch, T., Mišurec, J., *et al*. (2017) Tectonic control of complex slope failures in the Ameka River Valley (Lower Gibe Area, central Ethiopia): Implications for landslide formation. *Geomorphology*, 288, 175–187. Available from: https://doi.org/10.1016/j.geomorph.2017.03.020

Laury, R.L. & Albriton, C.C. (1975) Geology of Middle Stone Age Archaeological Sites in the Main Ethiopian Rift Valley. *Geological Society of America Bulletin*, 86(7), 999–1011. Available from: https://doi.org/10.1130/0016-7606(1975)86<999:GOMSAA>2.0.CO;2

Le Turdu, C., Tiercelin, J.J., Gibert, E., Travi, Y., Lezzar, K.-E., Richert, J.-P., *et al*. (1999) The Ziway–Shala lake basin system, Main Ethiopian Rift: Influence of volcanism, tectonics, and climatic forcing on basin formation and sedimentation. *Palaeogeography, Palaeoclimatology, Palaeoecology*, 150(3–4), 135–177. Available from: https://doi.org/10.1016/S0031-0182(98)00220-X

Li, M. & Fannin, R.J. (2012) A theoretical envelope for internal instability of cohesionless soil. *Géotechnique*, 62(1), 77–80. Available from: https://doi.org/10.1680/geot.10.T.019

Málek, J., Fischer, T. & Coubal, M. (1991) Computation of regional stress tensor from small scale tectonic data. *Publications of the Institute of Geophysics. B*, M-15, 235, 77–92.

McNamara, K., Cashman, K.V., Rust, A.C., Fontijn, K., Chalié, F., Tomlinson, E.L. & Yirgu, G. (2018) Using lake sediment cores to improve records of volcanism at Aluto volcano in the Main Ethiopian Rift. *Geochemistry, Geophysics, Geosystems*, 19(9), 3164–3188. Available from: https://doi.org/10.1029/2018GC007686

Moges, A. & Holden, N.M. (2008) Estimating the rate and consequences of gully development, a case study of Umbulo catchment in Southern Ethiopia. *Land Degradation & Development*, 19(5), 574–586. Available from: https://doi.org/10.1002/ldr.871

Mohr, P., Mitchell, J.G. & Raynolds, R.G.H. (1980) Quaternary volcanism and faulting at O'A Caldera, central Ethiopian Rift. *Bulletin of Volcanology*, 43(1), 173–189. Available from: https://doi.org/10.1007/BF02597619

Muluneh, A.A., Cuffaro, M. & Doglioni, C. (2014) Left-lateral transtension along the Ethiopian Rift and constrains on the mantle-reference plate motions. *Tectonophysics*, 632, 21–31. Available from: https://doi.org/10.1016/j.tecto.2014.05.036

Ngecu, W.M. & Nyambok, I.O. (2000) Ground subsidence and its socio-economic implications on the population: a case study of the Nakuru area in Central Rift Valley, Kenya. *Environmental Geology*, 39(6), 567–574. Available from: https://doi.org/10.1007/s002540050468

Nikbakhti, O., Hashemi, M., Banikheir, M. & Khabbazi, B.A. (2017) Geoenvironmental assessment of the formation and expansion of earth fissures as geological hazards along the route of the Haram-to-Haram Highway, Iran. *Bulletin of Engineering Geology and the Environment*, 77(4), 1421–1438. Available from: https://doi.org/10.1007/s10064-017-1019-2

Pacheco-Martínez, J., Hernandez-Marín, M., Burbey, T.J., González-Cervantes, N., Ortíz-Lozano, J.Á., Zermeño-De-Leon, M.E. & Solís-Pinto, A. (2013) Land subsidence and ground failure associated to groundwater exploitation in the Aguascalientes Valley, México. *Engineering Geology*, 164, 172–186. Available from: https://doi.org/10.1016/j.enggeo.2013.06.015

Pagli, C., Yun, S.H., Ebinger, C., Keir, D. & Wang, H. (2018) Strike-slip tectonics during rift linkage. *Geology*, 47, 31–34.

Park, B.C., Miller, R.D. & Xia, J. (1999) Multichannel analysis of surface waves. *Geophysics*, 64(3), 800–808. Available from: https://doi.org/10.1190/1.1444590

Peng, J., Wang, F., Cheng, Y. & Lu, Q. (2018) Characteristics and mechanism of Sanyuan ground fissures in the Weihe Basin, China. *Engineering Geology*, 247, 48–57. Available from: https://doi.org/10.1016/j.enggeo.2018.10.024

Rapprich, V., Hroch, T., Málek, J., Malík, J. & Verner, K. (2014) Geohazard map of Dila sheet NB 37–6 at scale 1:250,000. Czech Geological Survey/Aquatest/Geological Survey of Ethiopia, Prague, Czech Republic/ Addis Ababa, Ethiopia.

Rapprich, V., Žáček, V., Verner, K., Erban, V., Goslar, T., Bekele, Y., *et al.* (2016) Wendo Koshe pumice: the latest Holocene silicic explosive eruption product of the Corbetti volcanic system (southern Ethiopia). *Journal of Volcanology and Geothermal Research*, 310, 159–171. Available from: https://doi.org/10.1016/j.jvolgeores.2015.12.008

Richards, K.S. & Reddy, K.R. (2012) Experimental investigation of initiation of backward erosion piping in soils. *Géotechnique*, 62(10), 933–942. Available from: https://doi.org/10.1680/geot.11.P.058

Roering, C. (1968) The geometrical significance of natural en-echelon crack-arrays. *Tectonophysics*, 5(2), 107–123. Available from: https://doi.org/10.1016/0040-1951(68)90084-X

Saria, E., Calais, E., Stamps, D.S., Delvaux, D. & Hartnady, C.J.H. (2014) Present-day kinematics of the East African Rift. *Journal of Geophysical Research – Solid Earth*, 119(4), 3584–3600. Available from: https://doi.org/10.1002/2013JB010901

Schumann, H.H. & Poland, J.F. (1970) Land subsidence, earth fissures and groundwater withdrawal in south-central Arizona, USA. In: Tison, L.J. (Ed.) *Land Subsidence*. Tokyo, Japan: International Association of Hydrological Sciences, pp. 295–302.

Sheng, Z. & Helm, D. (1998) Multiple steps of earth fissuring caused by ground-water withdrawal. In Borchers, J. (Ed.) *Land subsidence case Studies and Current Research: Proceedings of the Dr. Joseph F. Poland Symposium on Land Subsidence*. Assoc Eng Geol Special Publication no 8. Star Publishing company, pp. 149–154.

Shin, S., Park, S. & Kim, J. (2019) Time-lapse electrical resistivity tomography characterization for piping detection in earthen dam model of a sandbox. *Journal of Applied Geophysics*, 170, 103834. Available from: https://doi.org/10.1016/j.jappgeo.2019.103834

Stamps, D.S., Calais, E., Saria, E., Hartnady, C., Nocquet, J.M., Ebinger, C. J. & Fernandes, R.M. (2008) A kinematic model for the East African Rift. *Geophysical Research Letters*, 35(5), L05304. Available from: https://doi.org/10.1029/2007GL032781

Street, F.A. (1979) *Late Quaternary lakes in the Ziway–Shala Basin, Southern Ethiopia*. 457.

Tenalem, A. (2001) Numerical groundwater flow modeling of the central Main Ethiopian Rift lakes basin. *Ethiopian Journal of Science*, 24, 167–184.

Terzaghi, K. (1943) *Theoretical soil mechanics*. Chichester, UK: John Wiley & Sons.

Verner, K., Megerssa, L., Hroch, T., Buriánek, D., Martínek, K., Mihret, Y. & Hejtmankova P. (2018) Explanatory notes to the thematic geoscientific maps of Ethiopia at a scale of 1:50,000: Map Sheet 0637-D3 Arba Minch. Czech Geological Survey/Geological Survey of Ethiopia, Prague, Czech Republic/ Addis Ababa, Ethiopia. 112.

Viste, E. & Sorteberg, A. (2013) Moisture transport into the Ethiopian highlands. *International Journal of Climatology*, 33(1), 249–263. Available from: https://doi.org/10.1002/joc.3409

Wilks, M., Ayele, A., Kendall, J.M. & Wookey, J. (2017) The 24th January 2016 Hawassa earthquake: Implications for seismic hazard in the Main Ethiopian Rift. *Journal of African Earth Sciences*, 125, 118–125. Available from: https://doi.org/10.1016/j.jafrearsci.2016.11.007

Williams, F.M., Williams, M.A.J. & Aumento, F. (2004) Tensional fissures and crustal extension rates in the northern part of the Main Ethiopian Rift. *Journal of African Earth Sciences*, 38(2), 183–197. Available from: https://doi.org/10.1016/j.jafrearsci.2003.10.007

Wilson, G.V., Wells, R., Kuhnle, R., Fox, G. & Nieber, J. (2018) Sediment detachment and transport processes associated with internal erosion of soil pipes. *Earth Surface Processes and Landforms*, 43(1), 45–63. Available from: https://doi.org/10.1002/esp.4147

Wolfenden, E., Ebinger, C., Yirgu, G., Deino, A. & Ayale, D. (2004) Evolution of the northern Main Ethiopian rift: birth of a triple junction. *Earth and Planetary Science Letters*, 224(1-2), 213–228. Available from: https://doi.org/10.1016/j.epsl.2004.04.022

Xue, L., Alemu, T., Gani, N.D. & Abdelsalama, M.G. (2018) Spatial and temporal variation of tectonic uplift in the southeastern Ethiopian Plateau from morphotectonic analysis. *Geomorphology*, 309, 98–111. Available from: https://doi.org/10.1016/j.geomorph.2018.02.025

Yismaw, A., Mitiku, B., Tsadik, T., Beyene, B., Dure, T., Edris, M., Burusa, G., Wenduante, M., Yehualashet, E., Abdulahid, T., Alemu, T., Haro, W. & Ashenafi, S. (2015) Geology, geochemistry and gravity survey of Dila Map Sheet. Geological Survey of Ethiopia, Addis Ababa, Ethiopia, 49.

Zang, M., Peng, J. & Qi, S. (2019) Earth fissures developed within collapsible loess area caused by groundwater uplift in Weihe watershed, northwestern China. *Journal of Asian Earth Sciences*, 173, 364–373. Available from: https://doi.org/10.1016/j.jseaes.2019.01.034

Zenebe, B., Agonafir, M., Teshome, M., Taye, M., Bekele, M., Edris, M., Burusa, G. & Yehualashet, E. (2012) Geology, Geochemistry and Gravity Survey of the Hosaina area. Memoir No 36. Geological Survey of Ethiopia, Addis Ababa, Ethiopia,

WEB REFERENCES

Czech Geological Survey. (2018) http://www.geology.cz/etiopie-2018

Google Earth. (2019) https://earth.google.com/web accessed 27 January 2020.

US Geological Survey. (2018) ASTER and SRTM Digital Elevation Models. https://earthexplorer.usgs.gov accessed 2018.

SUPPORTING INFORMATION

Additional supporting information may be found in the online version of the article at the publisher's website.

How to cite this article: Valenta, J., Verner, K., Martínek, K., Hroch, T., Buriánek, D., Megerssa, L.A. et al. (2021) Ground fissures within the Main Ethiopian Rift: Tectonic, lithological and piping controls. *Earth Surface Processes and Landforms*, 46 (15), 3158–3174. Available from: https://doi.org/10.1002/esp.5227

Appendix 5

Nat. Hazards Earth Syst. Sci., 21, 3465–3487, 2021
https://doi.org/10.5194/nhess-21-3465-2021

Natural Hazards and Earth System Sciences
Open Access
EGU

Main Ethiopian Rift landslides formed in contrasting geological settings and climatic conditions

Karel Martínek[1,2], Kryštof Verner[2,3], Tomáš Hroch[2], Leta A. Megerssa[3,2], Veronika Kopačková[2], David Buriánek[2], Ameha Muluneh[4], Radka Kalinová[3], Miheret Yakob[5], and Muluken Kassa[4]

[1]Institute of Geology and Palaeontology, Faculty of Science, Charles University, Albertov 6, Prague 12843, Czech Republic
[2]Czech Geological Survey, Klárov 3, 11821 Prague, Czech Republic
[3]Institute of Petrology and Structural Geology, Faculty of Science, Charles University, Albertov 6, Prague 12843, Czech Republic
[4]School of Earth Sciences, Addis Ababa University, Arat Kilo, 1176 Addis Ababa, Ethiopia
[5]Geological Survey of Ethiopia, P.O. Box 2302, Addis Ababa, Ethiopia

Correspondence: Karel Martínek (karel.j.martinek@gmail.com)

Received: 18 December 2020 – Discussion started: 18 January 2021
Revised: 20 September 2021 – Accepted: 7 October 2021 – Published: 16 November 2021

Abstract. The Main Ethiopian Rift (MER), where active continental rifting creates specific conditions for landslide formation, provides a prospective area to study the influence of tectonics, lithology, geomorphology, and climate on landslide formation. New structural and morphotectonic data from central Main Ethiopian Rift (CMER) and southern Main Ethiopian Rift (SMER) support a model of progressive change in the regional extension from NW–SE to the recent E(ENE)–W(WSW) direction, driven by the African and Somali plates moving apart with the presumed contribution of the NNE(NE)–SSW(SW) extension controlled by the Arabian Plate. The formation and polyphase reactivation of faults in the changing regional stress field significantly increase the rocks' tectonic anisotropy, slope, and the risk of slope instabilities forming.

According to geostatistical analysis, areas prone to landslides in the central and southern MER occur on steep slopes, almost exclusively formed on active normal fault escarpments. Landslide areas are also influenced by higher annual precipitation, precipitation seasonality, vegetation density, and seasonality. Deforestation is also an important predisposition because rockfalls and landslide areas typically occur on areas with bushland, grassland, and cultivated land cover.

A detailed study on active rift escarpment in the Arba Minch area revealed similar affinities as in a regional study of MER. Landslides here are closely associated with steep, mostly faulted, slopes and a higher density of vegetation. Active faulting forming steep slopes is the main predisposition for landslide formation here, and the main triggers are seismicity and seasonal precipitation. The Mejo area situated on the uplifting Ethiopian Plateau 60 km east of the Great Rift Valley shows that landslide occurrence is strongly influenced by steep erosional slopes and a deeply weathered Proterozoic metamorphic basement. Regional uplift, accompanied by rapid headward erosion forming steep slopes together with unfavourable lithological conditions, is the main predisposition for landslide formation; the main triggers here are intense precipitation and higher precipitation seasonality.

1 Introduction

Slope instabilities, including mainly landslides, rockfalls, and debris flows are usually influenced by key factors such as slope, bedrock lithology and rock fabric anisotropy, active tectonics and seismicity, type and grade of weathering, climatic conditions, vegetation cover, land use, and human activity. Links between these factors and the formation of landslides and rockfalls are complex (e.g. Abebe et al., 2010; Meinhardt et al., 2015). Geomorphic indices have been used to decipher links between landform and tectonics in several studies (Ayalew and Yamagishi, 2004; Ayalew et al., 2004). However, the influence of other factors on slope instabilities

Published by Copernicus Publications on behalf of the European Geosciences Union.

is unclear and a matter of current debate (e.g. Asfaw, 2007; Temesgen et al., 1999; Vařilová et al., 2015; Woldearegay, 2013). In general, ongoing discussions on the formation of slope instabilities in an active rift setting state either tectonics, climate, or anthropogenic activity as being triggering factors, depending on the characteristic conditions at the particular locality (e.g. Mancini et al., 2010; Peduzzi, 2010; Wotchoko et al., 2016). Other studies also conclude that lithology and precipitation are the main landslide controlling factors (e.g. Kumar et al., 2019, and references therein). Geomorphic indices, such as slope, aspect, hypsometric integral, the stream length gradient index, or river incision rates, are capable of detecting landform responses to tectonics (Ayalew and Yamagishi, 2004; Gao et al., 2013), but studies showing slope instabilities having a direct link to active tectonics are relatively rare (Chang et al., 2018, and references therein). Other studies also conclude that lithology and precipitation are the main landslide controlling factors (e.g. Kumar et al., 2019, and references therein).

Central and southern parts of the Main Ethiopian Rift (MER), which belong to the northern part of the East African Rift System (EARS), form a relatively narrow, slowly spreading extensional zone with a humid, strongly seasonal climate. The rift valley is significantly drier in comparison to the more humid rift flanks and plateau. There is a thick sequence of unconsolidated, often strongly weathered, volcaniclastic deposits cropping out in grabens on steep tectonic slopes or occasionally also on moderately elevated areas. Such a complex environment is an excellent natural laboratory to study the interplay of factors influencing various types of slope instabilities as they form in different geological and geomorphic conditions. Active extensional tectonism has a strong influence on the present-day morphology, but there are also important variations in climatic parameters (annual precipitation and seasonality); moreover, a population explosion in the last few decades has led to extensive deforestation, overgrazing, and dramatic changes in land cover and land use, which all may have significant importance in landslide formation (FAO, 2001; Janetos and Justice, 2000; Gessesse, 2007; Gete and Hurni, 2001; Melese, 2016).

This multidisciplinary study is focused on evaluating the landslide distribution in the central and southern MER. A combination of the results of geological, geohazard, and structural mapping, with remotely sensed data, and climatic, vegetation, and land use indicators is assessed using geostatistical methods. The discussion of the main factors influencing the formation of landslides in the regional scale in the central and southern MER and also on a detailed scale in the Mejo and Arba Minch areas in the southern part of the MER is the main focus of this study. In the regional-scale study, the direct link to tectonics is clear, so a large data set of new field structural data from this area is given. The situation in detailed scale studies in Mejo and Arba Minch is more complex. These two areas have contrasting styles of tectonic setting and varying lithological and climatic conditions, i.e. the Mejo landslide area is more humid, located on the eastern plateau, 60 km east of the rift valley, and dominated by highly weathered Proterozoic basement rocks, while the Arba Minch landslide area is situated directly on the western rift escarpment, with active tectonism and seismicity, and dominated by Tertiary volcanic rocks (Fig. 1). In both areas, slope failures are closely associated with steep slopes, but these are generated by very different processes, i.e. either active rift normal faulting or deep headward river erosion of the uplifting rift flank. The anthropogenic influence is also discussed, but only locally, because the relevant data for a thorough geostatistical evaluation are, unfortunately, missing.

2 Geological and geohazard setting

2.1 Geology and tectonics of the studied area

The overall geological pattern of southern Ethiopia includes a basement formed by metamorphic rocks of the Neoproterozoic age, which have been overlain by widespread volcanic sequences ranging from pre-rift Cenozoic volcanism to the Main Ethiopian Rift (MER) associated volcanism (Bonini et al., 2005; Hayward and Ebinger, 1996; Woldegabriel et al., 2000). The Precambrian rocks exposed in southern Ethiopia constitute the most southern part of the Arabian–Nubian Shield (ANS), which includes several terrane assemblages (for a review, see Fritz et al., 2013, and references therein). The ANS is an assemblage of juvenile low-grade volcano–sedimentary rocks and associated plutons and ophiolite traces with ages between ~ 890 and 580 Ma (Fritz et al., 2013). The Main Ethiopian Rift (MER) is an active intracontinental rift bearing the magma-dominated extension of the African (Nubian), Somali, and Arabian lithospheric plates (e.g. Acocella, 2010; Agostini et al., 2011). Of the MER reflecting temporally and spatially different stages of regional extension and volcanic activity, the following three segments have been defined (e.g. Hayward and Ebinger, 1996; Muluneh et al., 2014): (a) the northern Main Ethiopian Rift (NMER), (b) the central Main Ethiopian Rift (CMER), and (c) the southern Main Ethiopian Rift (SMER; see Fig. 1). In the southern part of the MER, the current rate of $\sim$ E–W oriented extension between the African and Somali plates amounts to 5.2 ± 0.9 mm per year (Saria et al., 2014).

The volcanic activity in the studied parts of the CMER (Hossana area) and SMER (Dilla area) could be divided into three major episodes (Bonini et al., 2005; Corti, 2009; Hayward and Ebinger, 1996). The Eocene to Oligocene pre-rift volcanic products (~ 45 to 27 Ma) comprise mainly tholeiite to alkaline basalt lava flows and the associated volcaniclastic deposits (Amaro–Gamo Basalts), with the presence of rhyolite ignimbrites (Shole Ignimbrites) and minor trachytes (Burianek et al., 2018; Verner et al., 2018c, d). The Miocene syn-rift volcanic products (~ 22 to 8 Ma) are represented by basalts, felsic volcanites, and volcaniclastic rocks (rhyolite lava, minor ignimbrites, trachyte lava flows, and related pyroclastic deposits) belonging mainly to the Getra and Kele sequences, including Mimo trachyte (Bonini et al., 2005; Ebinger et al., 1993, 2000). These two events were followed by a period of drastically low volcanism, except for a small eruption of peralkaline pantelleritic ignimbrites intercalated with minor basaltic lava flows in the areas beyond the rift escarpments (Bonini et al., 2005; see also Fig. 4). Subsequently, the products of Pleistocene to Holocene post-rift volcanic activity ($\sim$ 1.6–0.5 Ma) are bimodal volcanites and volcanoclastic rocks such as, for example, massive Nech Sar basalts, rhyolites, strongly welded rhyolitic ignimbrites, and other pyroclastic deposits (Ebinger et al., 1993). A typical example of post-rift volcanic activity in the southern CMER is the lower Pleistocene formation of unconsolidated pyroclastic deposits on the rift floor (e.g. Corbetti volcanic system; Rapprich et al., 2014), which was consequently disturbed by tectonic movements and erosion.

The complex fault pattern of the MER (interference of SSW(SW)–NNE(NE), N–S, and WNW(W)–ESE(E) trending faults) has been attributed to various mechanisms of contrasting hypothesis (for a review, see Abate et al., 2015; Erbello and Kidane, 2018), including (a) the pure extension orthogonal to the rift, (b) a right lateral NW–SE to the NNW–ESE transtension continuously transferred to sinistral oblique rifting as a result of an E–W regional extension, (c) a constant NE(ENE)–SW(WSW) trending extension, (d) a constant extension in the NW–SE direction, and (e) a constant E–W to ESE–WNW extension.

2.2 Geohazards in the central and southern MER

Active extensional tectonics and the intense volcanism associated with the East African Rift System (e.g. Agostini et al., 2011; Chorowicz, 2005) represent one of the main reasons for frequent hazardous geological phenomena in the Main Ethiopian Rift (MER). Characteristic rift-related morphology, seasonal climatic conditions, and inappropriate human interference in the landscape create suitable conditions for hazardous geological processes. Endogenous risk factors such as earthquakes, volcanism, and post-volcanic phenomena are closely related with tectonics in this area. The geomorphology is highly variable across the MER and is mainly the result of volcanic and tectonic events with the associated erosional and depositional processes (Billi, 2015).

Notable geohazard features across and along the MER range from intense erosion to slope-instability-related mass wasting processes, including rockfalls and debris flows up to shallow and deep-seated landslides, all with immense costs in terms of casualty and infrastructure loss (Abebe et al., 2005; Ayalew, 1999; Hearn, 2018). Landslides are rather more common in the highlands of Ethiopia. The most affected regions are the Blue Nile Gorge (Ayalew and Yamagishi, 2004; Gezahegn and Dessie, 1994; JICA and GSE, 2012; Tadesse, 1993), the Dessie area and the highlands surrounding Ambassel and Woldia (Ayenew and Barbieri, 2005; Fubelli et al., 2008), the Simien highlands, particularly western and central Tigray, the Sawla and Bonga areas of southern Ethiopia (Lemessa et al., 2000) and the MER margins of the western and eastern escarpment (Kycl et al., 2017; Rapprich and Eshetu, 2014; Rapprich et al., 2014; Temesgen et al., 2001), the surroundings of Finchewa, and the Debre Libanos and the Mugher locality (Zvelebil et al., 2010). On the western escarpment of the MER, a vast and recurrent landslide is notable close to the town of Debre Sina at the locality of Yizeba Weyn in central Ethiopia (Kropáček et al., 2015).

Other common geological hazards that recurrently appear in the area are ground fissures in various sectors along the rift floor, for example, north of the Fentale area in the northern MER (Williams et al., 2004) and various localities in the central MER segment (Asfaw, 1982, 1998; Ayalew et al., 2004) which often transform into deep and long gully systems (Billi and Dramis, 2003). Persistent seismic tremors, usually of lower magnitudes, are apparently located in the entire rift floor (e.g. Wilks et al., 2017). Particular clusters and source zones have been identified in Ethiopia, with those being (1) the western plateau margin, (2) the central Afar, (3) the Aisha block, (4) the Ankober area, (5) the central Main Ethiopian Rift, and (6) the southwestern Main Ethiopian Rift (Ayele, 2017). Nevertheless, historical high-magnitude earthquake records have also been reported (Asfaw, 1992; Gouin, 1975, 1979; Wilks et al., 2017). An updated probabilistic seismic hazard analysis and zonation has since been recently carried out with seismotectonic source zones constrained from recent studies for the Horn of Africa with reference to the East African Rift Valley (Ayele, 2017).

In addition to the seismic tremors, volcanism is also of apparent risk. Among the recent events are the Nabro Volcano in 2011 in the far northern part of the Afar Triangle (Goitom et al., 2015) and the Debahu rifting and volcanic dyke swarm intrusion events in 2005 (Ayele et al., 2007, 2009). These two events each triggered major alarms significant enough to warrant flight diversions (in the case of the Nabro Volcano) across the region and the temporary displacement of local people (e.g. Goitom et al., 2015).

3 Methods and data

Field geological, structural, geomorphological, and engineering geological mapping were conducted to acquire geological, tectonic, geomorphological, and rock mechanic properties (rock mass strength) characteristics.

3.1 Geotechnical data

Rock mass strength is obtained from the engineering geological map of the Hossana map sheet (Yekoye et al., 2012) and Dilla map sheet (Habtamu et al., 2012). The maps are

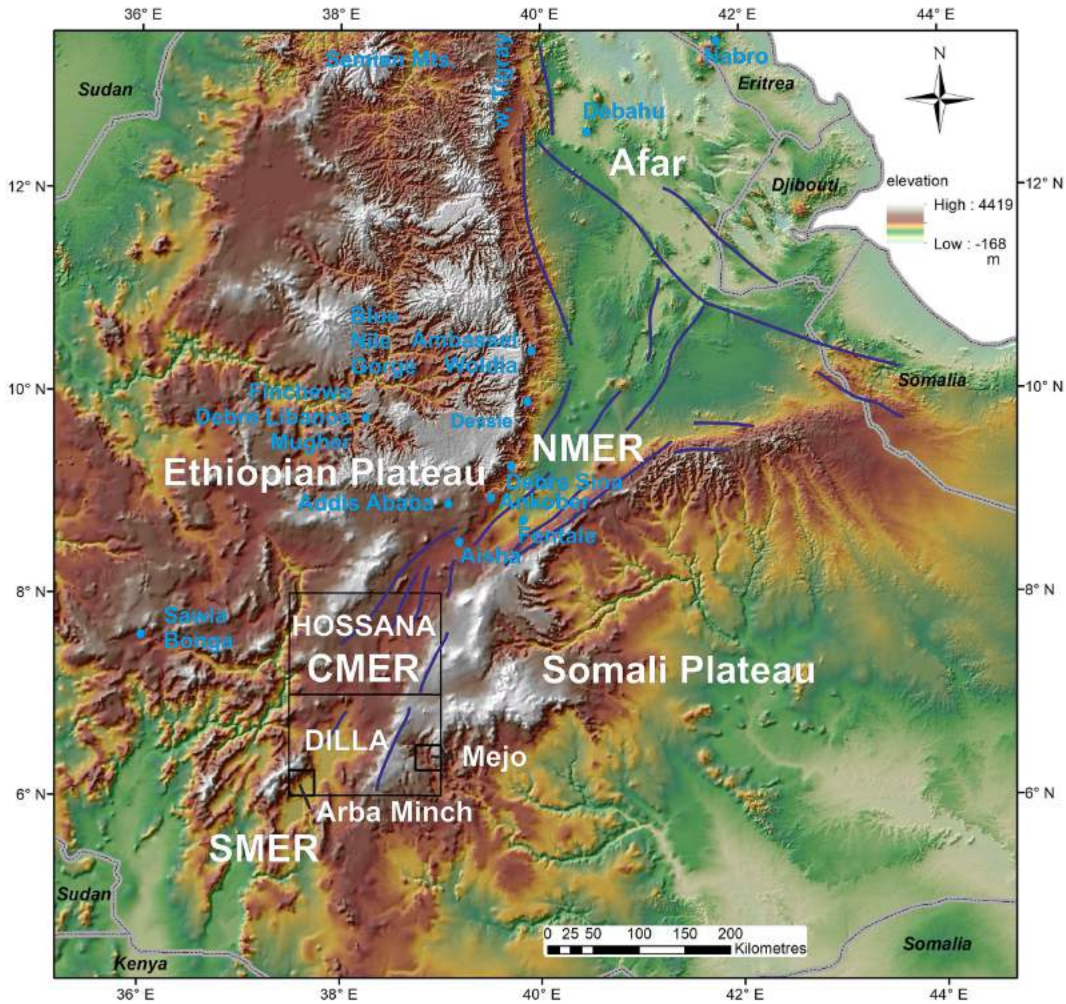

Figure 1. The Hossana and Dilla areas in the central and southern part of the Main Ethiopian Rift (MER). The location of the NMER (northern MER), CMER (central MER), SMER (southern MER), Mejo, and Arba Minch case study areas are also indicated. The blue lines represent major fault zones. Digital elevation models ASTER DEM and SRTM3, with a resolution of 30 m, were used (USGS EROS Archive; NASA LP DAAC).

prepared based on extensive and multiple types of field data to classify the lithological units into ranks of strength class as very low, low, medium, high, and very high rock mass strength units. These classifications are based on multiple criteria evaluations determined from field documentation, including intact rock strength, discontinuity conditions, and degree of weathering. The intact rock strength determination is made either by Schmidt hammers or testing representative irregular samples under the point load tester, and the results are normalized to the standard size of samples, as recommended by International Society for Rock Mechanics (ISRM, 1985) to IS_{50} reference strength. The discontinuity condition is determined by considering the spacing, aperture, and discontinuity surface roughness and overall geometry. The degree of weathering, on the other hand, is determined qualitatively on the bases of the criteria set out in British Standard (BS 5930; 1981) from various outcrops in the region.

3.2 Climatic data

The precipitation data were obtained from the national database that was set up by the Centre for Development and Environment (CDE), University of Bern, Switzerland in the 1990s for all of Ethiopia. Since the beginning, the data set has been upgraded with additional information layers, but the data set released as version I on a single CD-ROM, which has mean monthly precipitation data of the major settlement areas with information on the temporal coverage of recorded years, has been used in this study (Centre for Development and Environment, 1999). Precipitation point data (Centre for Development and Environment, 1999) were averaged (annual and for each month), and then the spatial distribution over the areas of interest were interpolated using the inverse distance weighted (IDW) method. Nevertheless, the precipitation seasonality index could not be calculated due to data inhomogeneities, where only some stations have a recording period of more than 20 years but often less than 5 years. In order to calculate a seasonality index, 30 years continuity is required. Therefore, precipitation seasonality was evaluated using standard deviation among particular monthly precipitations and by wet (July and August) and dry season (December and January) differences. Monthly averages of all available data were considered for the calculations.

3.3 Remote sensing data and morphotectonic analysis

ASTER DEM (digital elevation model), SRTM3, and Landsat 7 ETM+ were used for morphotectonic analysis, the normalized difference vegetation index (NDVI) based on Modis (Terra Modis, U.S. Geological Survey (USGS) eMODIS Africa 10 d composite), and land use/land cover data available from the USGS (https://earthexplorer.usgs.gov/; last access: 15 October 2019; U.S. Geological Survey, 2017) were also evaluated. MODIS scenes from January (peak of dry season) and August (peak of wet season) 2016 were used for the vegetation assessment.

The main approach for the morphotectonic analysis followed that used by Dhont and Chorowicz (2006, and references therein). The main aim was to use DEM imagery to interpret the largest neotectonic structures in the central and southern MER regions. Single-directional and multi-directional shaded reliefs and an elevation-coloured ASTER DEM image (Fig. 3) was generated using ArcMap 10.6 (http://www.esri.com; last access: 5 November 2019). This DEM constitutes the basis for morphotectonic analysis at the regional scale. The faults mapped can be considered as being the main neotectonic faults because they have a prominent expression in the morphology. In some cases, they form asymmetric ranges, with one side corresponding to breaks in slope or scarps by the displacement of Pleistocene and Neogene lithological boundaries or by the occurrence of straight lines of kilometres to several tens of kilometres in length. The images were compared with field geological mapping data to distinguish the scarps formed by active faults from those formed by differential erosion of contrasted lithology.

The emplacement of volcanoes, which are abundant in study area, can also be related to tectonic structures such as tension fractures or open faults. Small volcanoes arranged along the straight lines or linear clusters of adjacent volcanoes were also interpreted as being linear structures. The result of the interpretation is called linear indices, which mostly represent active faults (normal and normal-oblique slip), but because of uncertainties in detailed lithology in some areas and a lack of field verification in some cases, the linear indices may also represent prominent fracture zones and, in exceptional cases, also lithological boundaries. To avoid such uncertainties, an independent evaluation of the geomorphology by numerical methods was carried out. For an evaluation of the main tectonic indications of the CMER and SMER, morphotectonic analysis was carried out at a regional scale of 1 : 250 000 (presented in Sect. 4.1 and 4.4), while case studies of Mejo and Arba Minch were evaluated on a detailed scale of 1 : 50 000 (Sect. 4.5). Linear indices are referred to as lineaments hereafter in the text and figures.

In addition to a visual interpretation of lineaments, a quantitative technique – morphometry – was also employed to analyse landforms in a quantitative manner. This technique uses numerical parameters such as slope, surface curvature, and convexity to extract morphological and hydrological objects (e.g. stream networks and landforms) from DEM (Fisher et al., 2004; Pike, 2000; Wood, 1996). Landforms and lithological units reflect also different geotechnical properties (e.g. rock strength and degree of weathering) so they can be identified by these numerical methods. Various studies have been carried out to link morphometry with fluvial erosion, tectonics and diverse geomorphological conditions, and volcanic activity (Altin and Altin, 2011; Bolongaro-Crevenna et al., 2005; Ganas et al., 2005; Kopačková et al., 2011; Rapprich et al., 2010). Morphometric maps were constructed utilizing Wood's algorithm based on Shuttle Radar Topography Mission (SRTM) DEM data (30 m pixel resolution). First, the topographic slope and the maximum and minimum convexity values were derived on a pixel-by-pixel basis. The variation in these parameters was quantified for each pixel with respect to neighbouring pixels (in orthogonal directions). Second, based on a set of tolerance rules, morphometric classes were defined for each pixel, i.e. ridge, channel, plane, peak, pit, and pass (Wood, 1996). Wood's (1996) algorithm allows the relief to be parameterized by setting different values for the tolerance of the topographic slope and convexity. In this study, the slope tolerance of 3.0 and convexity tolerance of 0.02 were used for the best fit.

4 Results and interpretations

The results of the regional study of morphotectonics, morphometric and field structural analysis, slope failure mapping, and a geostatistical evaluation of the relationships between tectonic, lithological, and surface conditions and the occurrence of the landslides are presented here. Also, a more detailed evaluation is finally carried out, taking two case study sites at the Mejo (on MER eastern shoulder) and Arba Minch (western MER escarpment) areas which have a contrasting geological and climatic setting across the MER.

4.1 Morphotectonic and morphometric analysis

Shaded relief maps, derived from DEMs with NW, N, and NE illumination, and multidirectional shaded relief maps were used as a base map for morphotectonic interpretation. After carrying out the first stage of a visual interpretation of the lineaments, the second stage was carried out on the automated/numerical morphology base map, which helped uncover some important lineaments with a not-so-prominent morphological expression. Based on a comparison with geological maps, lineaments representing lithological boundaries, without the evidence of faults, were removed during the third stage. Thus, the interpreted lineaments mostly represent present-day active faults, fault zones, important fracture zones and, possibly, also shear zones (if there are any) which are manifested in morphology. Moreover, older faults with a prominent lithological contrast can be expressed in morphology. The interpretation was made on a scale of 1 : 250 000, so only the lineaments considered to represent a main fault or other tectonic zones have been mapped.

A combination of a visual morphotectonic interpretation, based on DEMs (Fig. 2) and an interpretation on morphometric landforms (Fig. 3), was used to map lineaments. The study area is characterized by a predominance of NNE–SSW-oriented lineaments mostly representing the major normal faults of the rift valley. The central and northern parts of the study area represent a relatively wider rift zone with extension spread over a larger area, while the southern part is narrower with steeper topographic gradients and more prominent vertical displacements on the faults. The subordinate population of lineaments, mostly perpendicular to the strike of the rift, has an E–W to WNW trend, while also showing vertical displacement.

4.2 Tectonics

The primary fabrics in rift-related volcanic deposits and lava flows are defined by the planar-preferred orientation of rock-forming minerals, micro-vesicles or micro-crystals and elongated mineral grains, lithic fragments, or stretched and welded pumice fragments. With the exception of the lateral parts of lava flows or volcanic centres, these planar fabrics are predominantly flat-lying or dip gently to ∼ SSW or E. In addition, a large amount of fault structures associated to the ∼ NNE–SSW trending MER dip predominantly steeply to ∼ ESE in the western part of the rift and to ∼ WNW along its eastern margin. The main ∼ NNE–SSW trending faults also form a prominent escarpment and other morphological features of the MER (Figs. 4a, 5). These faults are associated with fault lineation (slickensides) plunging steeply to moderately to ∼ SE (in the western escarpment) or to ∼ NW (in the eastern escarpment), both bearing exclusively normal kinematic indicators (Fig. 6a–c). There are two subordinate sets of fault structures that appear to be synchronous with the main ∼ NNE–SSW faults that are mostly perpendicular, WNW(W)–ESE(E) trending normal faults with predominantly NNW plunging slickensides, or steeply ∼ NNW dipping normal faults (Fig. 5a). Relatively younger or newly reactivated ∼ NNW(N)–SSE(S) trending faults which are oblique by ∼ 20–30° to the main fault system were mapped mainly in the central part of the rift valley (Figs. 2, 5a). In addition, ∼ NNW–ESE, ∼ NE-SW, and ∼ WSW–ENE trending strike-slip faults, with a gently prevailing right-lateral kinematic pattern, were identified across the studied area (Figs. 2, 5b). In the spatial context of large volcanic centres (e.g. Wobitcha, Duguna Fango, and Awassa caldera; Fig. 2) the caldera-related ring faults were found to have a curved asymmetric shape, mostly parallel to the caldera rim. These faults predominantly dip steeply to moderately inward to the centre of the caldera. Extensional joints occur in three distinct sets with a ∼ N–S, NNE–SSW, and E(WNW)–W(ESE) trend (Fig. 5c).

4.3 Areas prone to slope instabilities

The principal feature of the MER is the graben bounded by normal faults. The drainage network is largely controlled by tectonic activity and lithological variation. Parts of grabens form endorheic depressions are filled by temporal lakes. The area is climatically highly variable; the average amounts of annual rainfall vary from 500 mm in the Gibe and Omo gorges to 2600 mm on the escarpments and the adjacent highlands. The mean annual temperature is about 20 °C (Yekoye et al., 2012; Habtamu et al., 2012; Rapprich and Eshetu, 2014; Rapprich et al., 2014).

Slope failures, erosion, floods, and the occurrence of ground fissures are the most common geological hazards investigated in the Hossana and Dilla areas. Landslides, debris flows, and rockfalls represent common exogenous hazards distributed mainly on the fault scarps (Figs. 2 and 7a). The subsidence of the rift floor and consequent uplift of the highland lead to isostatic disequilibrium resulting in intensive headward erosion and slope processes. Most of the slope instabilities represent deep-seated complex fossil slumps or translational or rotational slides (Fig. 7b) that host reactivated smaller landslides and debris flows which are triggered by adverse anthropogenic practices (road construction, deforestation, and overgrazing) or river undercutting (Fig. 7e, f). The landslides develop in the succession of competent volcanic rocks – basalts and welded ignimbrites intercalated by highly weathered pyroclastics and horizons of palaeosoils – following the slip zone of these landslides. The steep slopes of the highly decomposed volcanic rocks due to columnar jointing are subject to toppling and rockfalls.

Rare lateral spread, with typical horst and graben features at the head, have been encountered in the complex unwelded ignimbrites and unconsolidated pyroclastic deposits, with horizons of palaeosoils following the slip zone of this landslide (Fig. 7c). Topographic depressions with a higher degree of saturation are often noted to have the long-term effect of triggering landslides and debris flow on the slopes below them (Fig. 7d, f). More detailed descriptions of slope instabilities in the Mejo and Arba Minch areas are given in Sect. 4.5 and in Figs. 9 and 11.

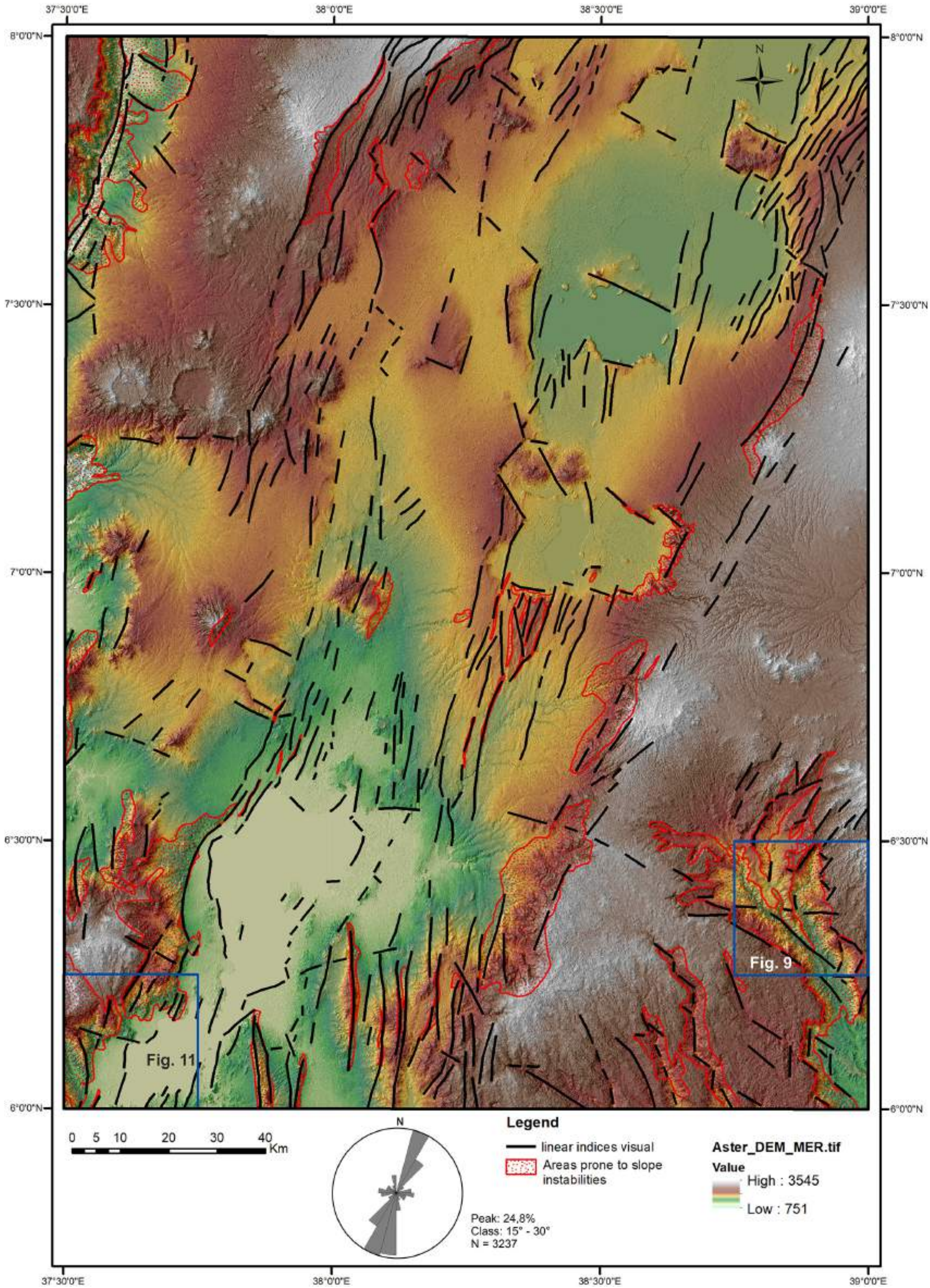

Figure 2. DEM (colour elevation map on multidirectional shaded relief) of the Dilla and Hossana areas, with visually interpreted linear indices and the distribution of their strikes in a rose diagram. The locations of the Mejo (Fig. 9) and Arba Minch (Fig. 11) detailed study areas are also shown (see Sect. 4.5). Digital elevation models ASTER DEM and SRTM3, with a resolution of 30 m, were used (USGS EROS Archive; NASA LP DAAC).

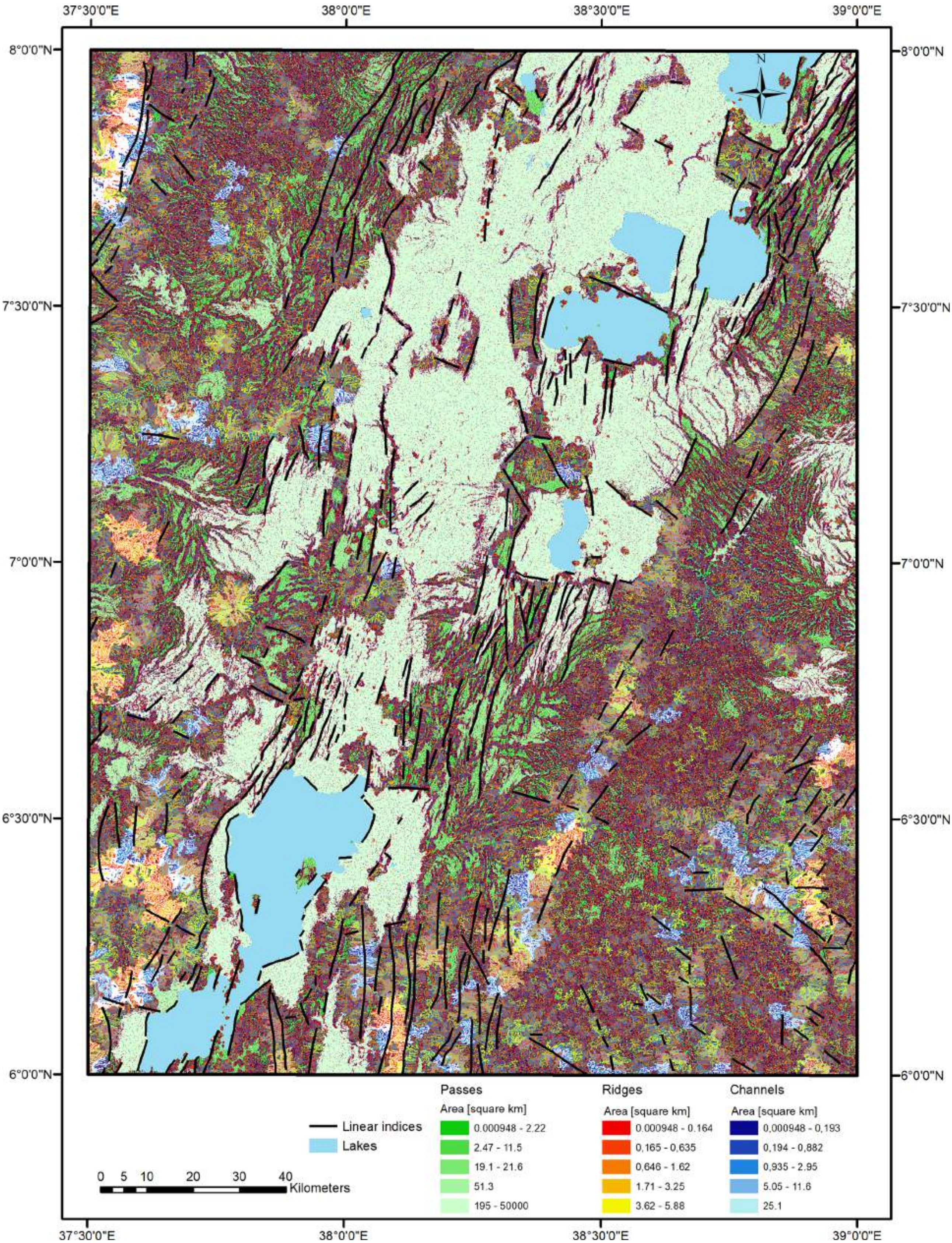

Figure 3. Morphotectonic analysis of the Dilla and Hossana areas based on morphometry. Linear indices show only the lines which are in accordance with both the visual interpretation of the DEM and the morphometry.

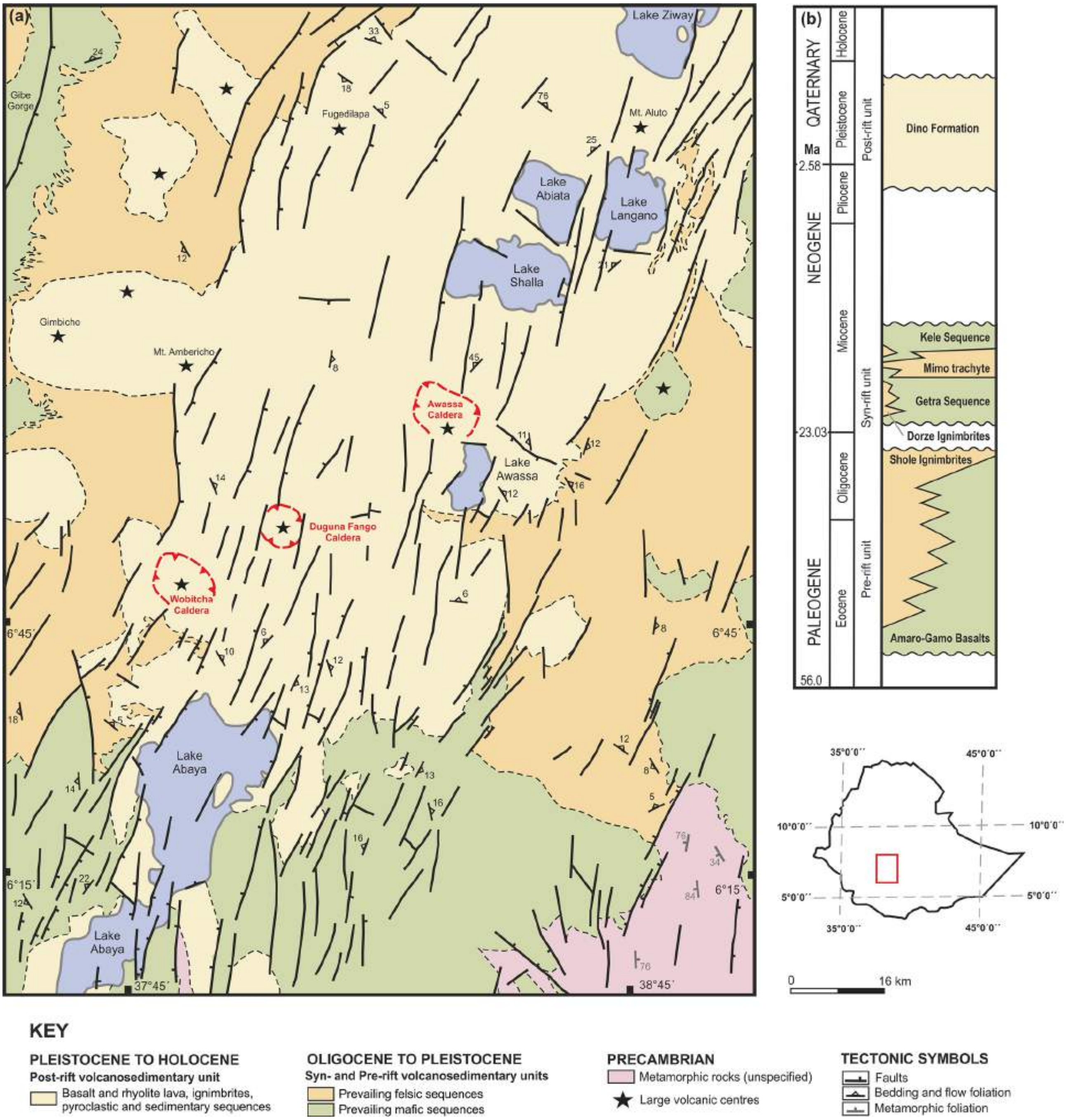

Figure 4. **(a)** Simplified geological map of the southern part of the Main Ethiopian Rift (Hossana and Dilla areas). **(b)** Schematic stratigraphic chart of the Main Ethiopian Rift (Dilla and Hossana areas). Compiled using unpublished geological maps (1 : 250 000; Geological Survey of Ethiopia).

4.4 Statistical analysis

Statistical analysis was carried out to better understand the influence of various surface processes and conditions (precipitation, vegetation, slope, and land cover) and geological parameters (rock mass strength, proximity of faults, and lineaments) on the formation of landslides and rockfalls. However, anthropogenic factors could not be evaluated statistically because the relevant data are not available. This section refers to regional mapping on a 1 : 250 000 scale, where areas prone to geohazards rather than particular geohazards were mapped. The results should be interpreted in this light.

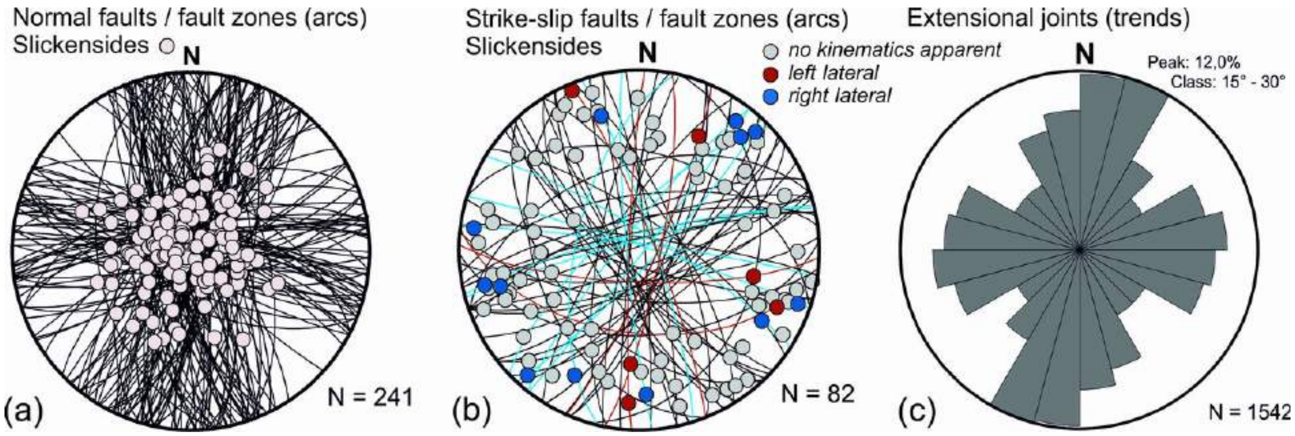

Figure 5. Field structural measurements of faults (equal area projection to the lower hemisphere) and extensional joints (rose diagram) from the southern part of the Main Ethiopian Rift (Hossana and Dilla areas).

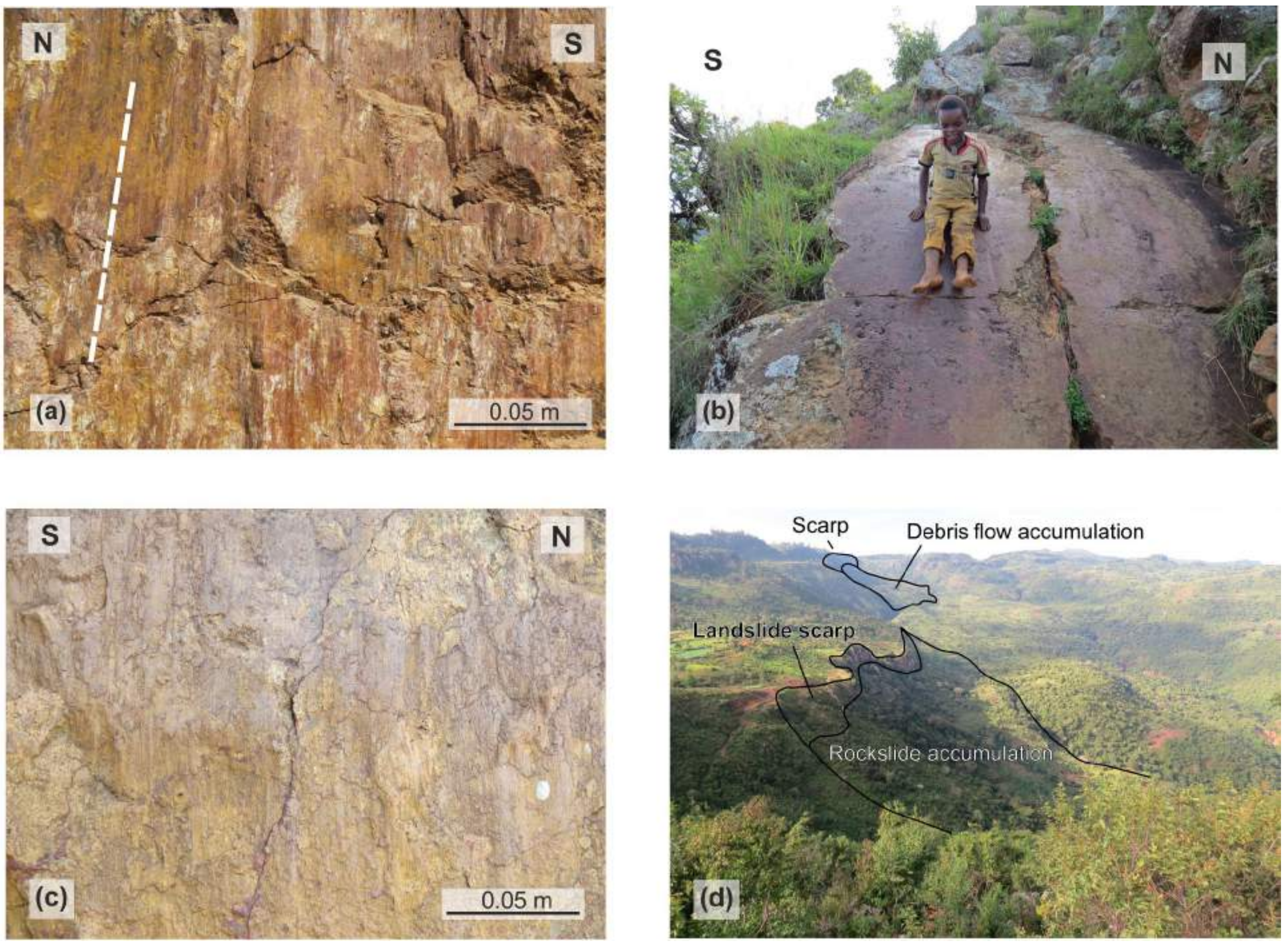

Figure 6. Field photographs. **(a)** Steeply dipping, N–S oriented fault plane, with steeply plunging slickensides and normal kinematic indicators (west of Dilla; eastern rift escarpment). **(b)** ESE moderately dipping normal fault, parallel with the main NNE–SSW trending western rift escarpment (Ocholo village; north of Arba Minch). **(c)** Steeply dipping, N–S oriented fault plane, with steeply plunging slickensides and normal kinematic indicators (Mejo plateau; ca. 60 km east of the main rift valley). **(d)** Rockslide and debris flow on normal fault slope north of Arba Minch.

Figure 7. Field photographs of various types of geohazards in MER (Hossana and Dilla areas). **(a)** Toppling and subsequent rockfall of welded ignimbrites in the crown of a deep-seated landslide situated close to a fault scarp in the western highland area (Dilla area; NW of Arba Minch). **(b)** Large landslide in Dilla area (5 km SW of Mejo). **(c)** Tilted blocks of deep-seated landslide southwest of Awassa. **(d)** Undrained depression in the deep-seated fossil landslide east of Dilla. **(e)** Tension cracks in the crown of a shallow landslide reactivated by road construction (west of Arba Minch). **(f)** Recent debris flow accumulation below the road construction in the landslide area west of Mejo.

4.4.1 Descriptive statistics

For the purposes of descriptive statistics, the rock mass strength (RMS) was coded as follows: very high RMS (VHRMS) is equal to 7, high RMS (HRMS) is equal to 6, medium RMS (MRMS) is equal to 5, low RMS (LRMS) is equal to 4, very low RMS (LRMS) is equal to 3, soils are equal to 2, and lacustrine deposits are equal to 1. A significant correlation between RMS and slope and most precipitation parameters was found (see Table 1). More wet and seasonal areas occur on steeper slopes formed by stronger (less weathered) rocks. Most of the steep slopes in the study area are active normal fault escarpments. Another interesting statistically significant correlation is shown by slope, and most of the precipitation parameters and the NDVI of the dry period. Steeper slopes and higher altitudes attract clouds and precipitation, while flat lowlands allow clouds to pass by without precipitation. Significant correlations can also be found within various precipitation parameters, within selected vegetation parameters, and also between these two groups (precipitation and vegetation), which was supposed. No significant correlation was found between the proximity of faults and lineaments (expressed by faults and lineaments density) and other parameters. It seems to be an independent variable very suitable for further geostatistical evaluation. There is a high density of faults and lineaments in areas where faults and lineaments of different strikes cross; these areas do not necessarily have higher slopes. For other tectonic parameters, such as faults and lineament proximity, it is difficult to calculate by conventional correlation; hence, they are evaluated geostatistically in the following sections.

4.4.2 Geostatistics

The mean values of various geological, tectonic, climatic, vegetation, and land use factors were calculated for each landslide polygon area. The normalized difference vegetation index (NDVI) is adopted from MODIS images of 2016, while the density of lineaments is expressed as $\times 10^6$. The Kernel Density tool (under Spatial Analyst Tools/Density in ArcGIS 10.6) was used to evaluate the faults and lineaments density in MER on a scale of 1 : 250 000 (see Table 2). The proximity to tectonic features is expressed in terms of the percentage area of a particular geohazard within a particular buffer zone (500 m and 1 km buffer).

Most landslides and rockfalls form on steeper slopes close to faults and in areas with higher lineament density. Rockfalls are formed on steeper slopes than landslides (Table 2; see also see Figs. 2, 9, and 11), but slope factor has higher importance for the formation of landslides (in comparison to other factors; see Fig. 8). Rockfalls typically occur in areas receiving lower precipitation. Most of them occupy areas with grassland and, to a lesser extent, also on cultivated land and bush land cover. Higher vegetation seasonality is also found to coincide well with rockfall occurrences. There is a

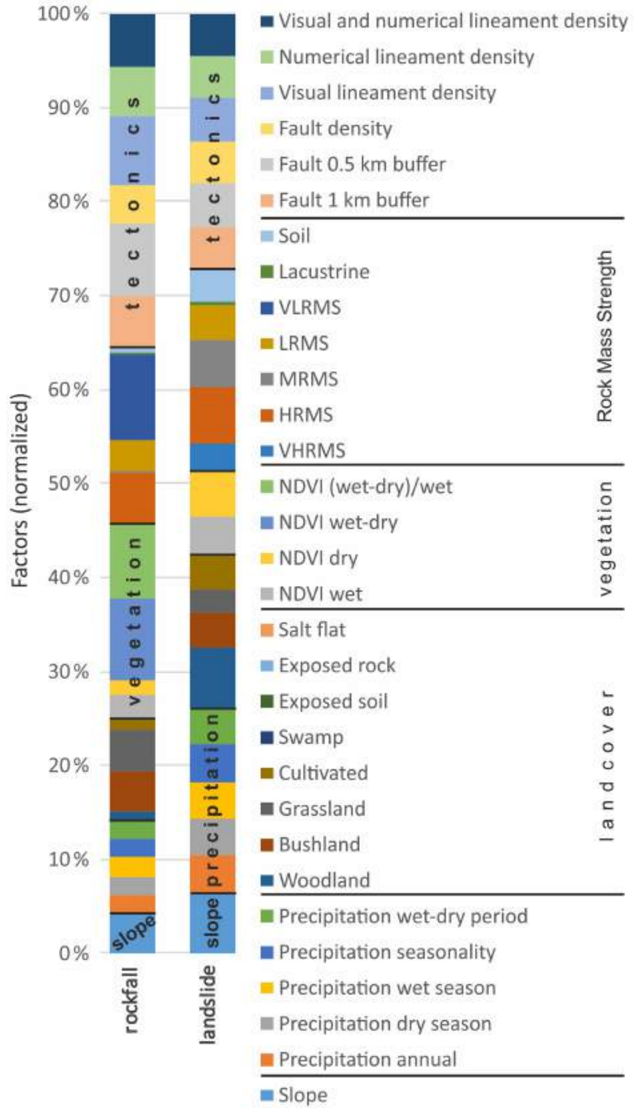

Figure 8. Plot of mean values of particular factors occurring across landslides and rockfalls polygons normalized to the mean value for the whole area. Diagram shows the relative importance of each factor.

high vegetation difference between the dry season (January) and the rainy season (August; see Table 2). This is probably because fault escarpment vegetation, which grows in difficult conditions on steep rocky slopes, is more sensitive to precipitation seasonality. The low, very low, and high rock mass strength class probably influence the occurrence of rockfalls (see Table 2 and Fig. 8) but not medium rock mass strength. Probably because hard rocks are jointed, and then rockfalls with big blocks occur, these polygons also include slope deposits, classified as low to very low RMS, while landslides are formed in areas with higher precipitation and higher precipitation seasonality. Woodland, bushland, grassland, and cultivated areas with higher vegetation density and low vege-

Table 1. Correlation matrix of the selected factors controlling distribution of geohazards in the MER area. The number of samples is 153, and the critical value for correlation coefficient (R) at the 95 % significance level is 0.195. A statistically significant (95 %) R is in bold.

	RMS	Slope	Precipitation					NDVI			Faults and lineaments
			Annual	Dry period	Wet period	Seasonality	Wet–dry period	Wet period	Dry period	Wet–dry period	density
RMS	1.00	**0.44**	**0.49**	0.17	**0.43**	**0.58**	**0.39**	0.10	0.07	−0.01	0.13
Slope	0.44	1.00	**0.37**	0.11	**0.25**	**0.37**	**0.22**	0.16	**0.24**	−0.12	−0.11
Precipitation annual	0.49	0.37	1.00	**0.61**	**0.47**	**0.73**	**0.35**	**0.28**	**0.37**	−0.16	−0.14
Precipitation dry period	0.17	0.11	0.61	1.00	−0.11	−0.01	**−0.27**	0.14	**0.41**	**−0.29**	−0.18
Precipitation wet period	0.43	0.25	0.47	−0.11	1.00	**0.80**	**0.99**	0.15	**−0.39**	**0.44**	0.06
Precipitation seasonality	0.58	0.37	0.73	−0.01	0.80	1.00	**0.77**	**0.20**	0.06	0.07	0.03
Precipitation wet–dry period	0.39	0.22	0.35	−0.27	0.99	0.77	1.00	0.12	**−0.44**	**0.47**	0.09
NDVI wet period	0.10	0.16	0.28	0.14	0.15	0.20	0.12	1.00	0.16	**0.46**	−0.05
NDVI dry period	0.07	0.24	0.37	0.41	−0.39	0.06	−0.44	0.16	1.00	**−0.80**	−0.10
NDVI wet–dry period	−0.01	−0.12	−0.16	−0.29	0.44	0.07	0.47	0.46	−0.80	1.00	0.06
Faults and lineaments density	0.13	−0.11	−0.14	−0.18	0.06	0.03	0.09	−0.05	−0.10	0.06	1.00

tation seasonality are found to have an affinity with landslide occurrences. The entire range of rock mass strength classes (low, medium, and high) occur in areas of landslides.

4.5 Case studies – Mejo and Arba Minch areas

We selected two areas with contrasting lithological, tectonic, climatic, and vegetation settings and a similar size and morphology of landslides and rockfalls for a detailed study. The study areas correspond with 1 : 50 000 mapping (for the location of the map sheets, see Fig. 2).

4.5.1 Mejo site

Geological and climatic setting

The Mejo study area is located 60 km east of the main rift valley on the upland plateau of the southeastern flank of the MER. The Gambelto and Genale rivers draining the area southeast of Somalia form a typical morphology, with deeply incised N–S trending valleys in the central part and volcanic plateaus along the southwestern and eastern margin (Fig. 9). These volcanic plateaus attain an elevation slightly above 2000 m a.s.l. (above sea level) in the east and around 2100 m a.s.l. in the southwest. Neoproterozoic medium-grade metamorphic rocks crop out mainly in the deeper part of the valleys below the altitude of ca. 1900 m, and the deepest parts reach below 1000 m a.s.l. Thus, the area has a prominent topography with an altitude difference of more than 1000 m; the average slope in the area is more than 14°. The overlaying volcanic deposits are of the Eocene to Pleistocene age (Verner et al., 2018a, d). The local climate is humid, the annual precipitation is $\sim$ 1200 to $\sim$ 1550 mm (average 1393 mm) and highly seasonal, usually with two peaks corresponding to April–May and August–October, with more than 125 mm monthly average rainfall, while the rest of the months have a monthly average rainfall of slightly more than 40 mm. The difference between the average wet (July and August) and dry season (December and January) is 310 mm (Centre for Development and Environment, 1999). Vegetation cover is dense (NDVI values are almost double compared to the Arba Minch area) and moderately seasonal (see Table 3). Due to intense weathering, the area is dominated by rocks with low and medium mass strengths. The dominant land cover is woodland and bushland and cultivated areas form up to 25 % of the area.

The area is formed by the following two units: (i) a metamorphic basement consisting of foliated biotite orthogneiss with minor lenses of amphibolites outcropped in the lower parts of the slope and the bottom of valleys. The orthogneiss is moderately to strongly weathered, and the lenses of amphibolites have higher intact strength with a lower degree of weathering. The foliation of metamorphic rocks is often oriented downslope, parallel with the topography of the instable slopes. (ii) The volcanic complex overlying the metamorphic basement is formed by a roughly 500 m thick succession of basalt and trachybasalt massive lava flows and intercalations of palaeosols, fine basaltic scoria layers, and epiclastic deposits up to 2 m thick. The lava flows are moderately to strongly weathered with high fissured permeability, and the pyroclastic layers, palaeosols, and strongly weathered horizons with a high content of clay minerals may form semi-horizontal barriers for water movement resulting in higher plasticity and a reduction in permeability (Verner et al., 2018a, d).

Faults

Most of the fault structures were identified in the complex of metamorphic rocks without evidence of young reactivation. The youngest faults and fault zones belonging to the East African Rift System are rare and have no significant effect on the overall tectonic pattern of the area. These minor faults dip steeply to $\sim$ E or $\sim$ W, bearing well-developed steeply plunging slickensides and normal kinematics. The minor subordinate set of normal faults have a $\sim$ W (WNW) to E (ESE) trend. The fault displacement is relatively low

Table 3. Mean values for each geohazard polygon area compared to the overall area of Mejo and Arba Minch, respectively. Values that are in bold and underlined are highly above average, while bold values are above average.

Geohazard/factor		Precipitation				P. seasonality		Vegetation		V. seasonality		Rock mass strength					Tectonics				Land use				
		Slope (°)	Annual (mm)	Dec + Jan (dry) (mm)	Jul + Aug (wet) (mm)	Monthly (1)	Wet–dry (mm)	NDVI wet (Aug)	NDVI dry (Jan)	NDVI Aug–Jan	(Aug–Jan)/Aug (%)	VHRMS (%)	HRMS (%)	MRMS (%)	LRMS (%)	Lacustrine (%)	1 km buffer (%)	0.5 km buffer (%)	Faults density	Lineaments density	Woodland (%)	Bushland (%)	Grassland (%)	Cultivated (%)	Water (%)
Mejo	Landslide and debris flow	**17.6**	1335	46	346	75	300	**6303**	**7278**	**−975**	−0.15	2.06		**31.7**	**60.8**	5.4	50.9	27	33.8	**58**	**72**	3		**26**	
	Whole area	14.2	1393	47	357	78	310	5548	6421	−874	−0.16	7.89		**28.3**	**41.9**	**22**	61.5	36	33.6	34	**53**	**19**	3.1	**24.8**	
Arba	Landslide and rockfall	**14.9**	1070	60	188	45	128	**5361**	**6412**	**−1051**	−0.20			**42.7**	**56.7**	0.6	**97.1**	**68**	**67.0**	**78**		**30**		**70**	
Minch	Whole area	9.8	1068	59	189	46	130	3051	3909	−858	−0.28		3.01	**21.2**	**49.5**	**26**	68.8	44	43.6	51	1.14	**19.2**		**51.2**	**28.4**

Table 2. Mean values for each geohazard polygon area compared to the whole area of Hossana and Dilla. NDVI calculated from MODIS images (https://earthexplorer.usgs.gov/; last access: 20 June 2018; U.S. Geological Survey, 2017), and the lineaments density is $\times 10^6$. The proximity of tectonics is expressed in the percentage area of the particular geohazard within the buffer. Values that are in bold and underlined are highly above average, while bold values are above average, and values in italic are below average.

Geohazard/factor		Precipitation			P. seasonality		Vegetation		V. seasonality		Rock mass strength							Tectonics		Lineaments density				Land use						
	Slope (°)	Annual (mm)	Dec + Jan (dry) (mm)	Jul + Aug (wet) (mm)	Monthly (1)	Wet–dry (mm)	NDVI wet (Aug)	NDVI dry (Jan)	NDVI Aug–Jan	(Aug–Jan)/Aug (%)	VHRMS (%)	HRMS (%)	MRMS (%)	LRMS (%)	VLRMS (%)	Lacustrine (%)	Soil (%)	Within 1 km buffer	Within 0.5 km buffer	Faults	Visual	Numerical	Vis. and num.	Woodland (%)	Bushland (%)	Grassland (%)	Cultivated (%)	Swamp (%)	Exposed soil (%)	Water (%)
Rockfall	**17.2**	*1041*	44	312	54	268	**5412**	*3149*	**2263**	42	0	**27**	3	**40**	**25**	1	3	**88**	**66**	**155**	**341**	**227**	**227**	8	**18**	**48**	**21**	1	0	4
Landslide	**15.6**	**1248**	**51**	**351**	**66**	**300**	**5296**	**5510**	*-214*	−4	4	**18**	**38**	**26**	0	1	12	43	24	**97**	**131**	**111**	**108**	**38**	9	**16**	**37**	0	0	
Whole area	9.0	1172	48	333	61	285	4868	4297	571	12	5	11	28	26	6	11	13	36	19	82	103	95	88	22	9	24	36	1	1	6

across the area, reaching a maximum of 100 m in the vertical section (Verner et al., 2018a, d). The prominent morphology, with up to 1000 m deeply incised valleys, is made almost solely by erosion caused by the Neogene uplift.

Landslides and rockfalls

A large and deep-seated complex landslide area occurs in the slope of the eastern banks of the Gambelto valley. The landslide areas vary in length from several hundred metres to 4 km, with a width of up to 2 km (see Fig. 9). The landslide complexes are characterized by amphitheatre (horseshoe)-shaped edges of the main scarps and reach up to 200 m high and have 50 to 100 m high minor scarps. Commonly, tilted blocks, endorheic depressions, and a number of springs have also been noted in the landslide zone. Reactivated parts are characterized by small-scale (tens to hundreds of metres) and shallow-seated debris flows, slumps, and rockfalls accompanied by the subsidence of surface, cracks, or curved tree trunks, which were observed close to the new road construction.

Most landslides are fossil and inactive. The preservation of colluvial deposits is limited, while, in the depressed domain and the arched accumulation area of the landslide, they are covered by boulders and blocks. The morphology of the main and minor scarps is relatively sharp, and the accumulation zone is strongly modified by erosional processes with a smooth and undulating topography, an absence of a hummocky landscape and traverse ridges. Most of the reactivated parts are represented by small-scale and shallow-seated failures triggered by the poor design of local road construction.

Statistical evaluation

The mean values of the same factors as for the Hossana and Dilla areas (see Sect. 4.4.2) were also calculated for each landslide and rockfall polygon area in the case of the Mejo site. The same calculations and symbology as in Table 2 was used for most parameters, but faults and lineaments data were adopted from more detailed studies at a scale of 1 : 50 000 (Verner et al., 2018a, b, c, d), and the faults and lineaments density is calculated by a Line Density tool (ArcGIS 10.6.; Spatial Analyst Tools) and expressed as $\times 10^2$. Here the landslides and debris flows are situated in areas with much higher slopes compared to the overall study area (see Fig. 10 and Table 3). They are also formed in areas with a higher vegetation density and medium and low RMS. Landslide and debris flow areas have a much higher density of lineaments. They are also dominantly vegetated by woodlands, and cultivated areas are a minor land cover. Precipitation distribution does not show any significance; it can be due to the poor spatial resolution of the precipitation data. The same applies for the Arba Minch area.

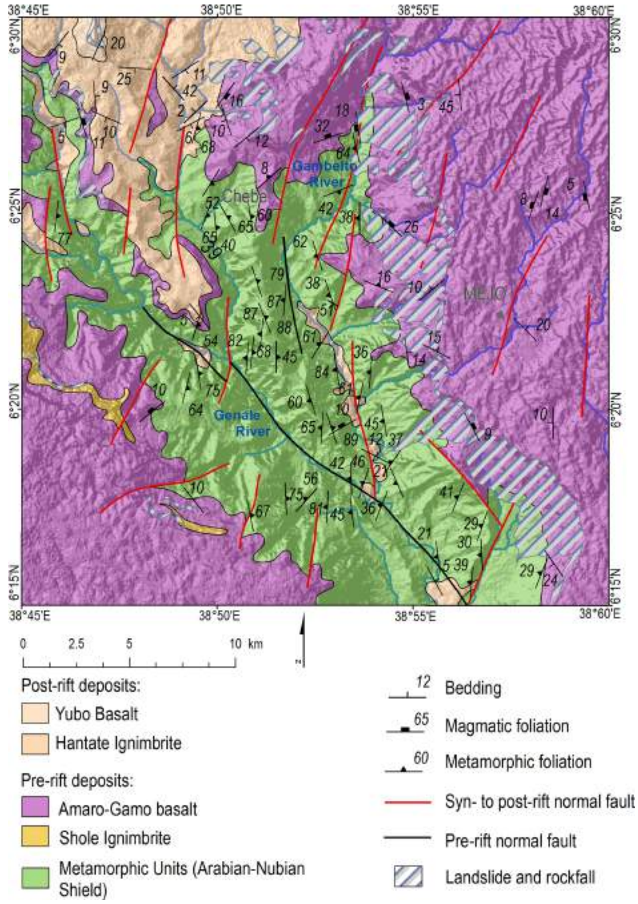

Figure 9. Geological and tectonic map of the Mejo site, with landslides and rockfalls indicated. For the location, see Fig. 2.

4.5.2 Arba Minch site

Geological and climatic setting

The Arba Minch study area is located directly in the main rift valley on the western normal fault escarpment. The total displacement of the syn- and post-rift normal faults is more than 1500 m. The average slope in the area is less than 10° because a large part of the area is covered by Abaya Lake (see Fig. 11). The area is less humid compared to Mejo, with an average annual precipitation of 1068 mm, and precipitation is moderately seasonal; the difference between the wet and dry season is 130 mm. But significant variations in precipitation have been recorded in apical parts of mountain ridges, such as Chencha, attaining, on average, an altitude of 2700 m a.s.l., with 1390 mm of rainfall, whereas, in the low-lying plains, with an average elevation of about 1200 m a.s.l. around the city of Arba Minch, the precipitation fluctuates around 780 mm (Centre for Development and Environment, 1999). Vegetation cover is moderate and moderately seasonal (see Table 3). Rocks with low and medium mass strengths and lacustrine deposits dominate the area. The dominant land

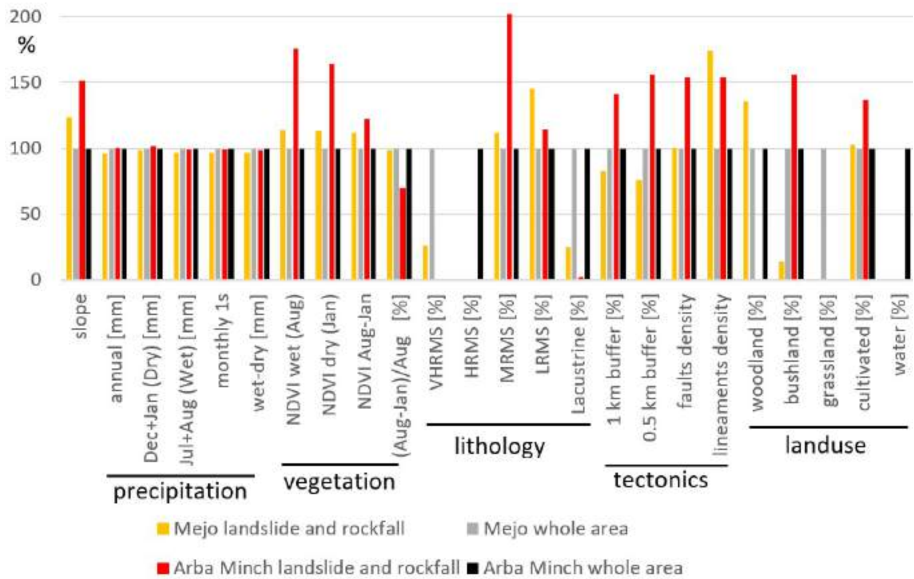

Figure 10. Plot of mean values of particular factors occurring across merged polygons of landslides and rockfalls normalized to the mean value for the overall area. Mejo and Arba Minch sites evaluated separately.

cover type is cultivated areas (from up to 51 %); bushland and water surface are also abundant types. The area is characterized by the lower Eocene to Pleistocene volcanic and volcaniclastic rocks, which are a product of episodic eruptions. They mostly have a bimodal composition, with alternating basic volcanic rocks and acidic pyroclastic rock intercalations (Verner et al., 2018b, c).

Faults

The prevailing faults are mostly parallel to the axis of the MER, forming the area's prominent morphological features. These major normal faults dip steeply to ESE or SE and trending NNE–SSE. Moreover, subordinate normal faults were identified, predominantly steeply inclined faults trending WNW–ESE, which are perpendicular to the prevailing rift parallel normal faults. Fault displacement is relatively high across the area, reaching a minimum of 1000 m, forming prominent morphology with an altitude difference of up to 1500 m between the plateau and graben floor.

Landslides and rockfalls

The slope failures are located in the western steep fault scarps separating the bottom of the rift valley with Abaya Lake, representing a local erosional base at an elevation of 1200 m a.s.l. and the western highland with an undulating landscape at an elevation of between 2000 and 2400 m a.s.l. The scarps are often modified by deep-seated slope failures. The lower parts of the slopes form moderately weathered basalts and trachybasalt, with minor pyroclastic fall layers of volcanic ash reaching up to 2 m in thickness and a reddish palaeosol up to 30 cm thick. The ridges and upper parts are formed from welded ignimbrites with minor rhyolitic ash fall deposits and palaeosol horizons. Volcanic rocks are variably affected by intense fracturing, jointing, and mega-tectonic fault systems. Basalts and trachybasalts are with a higher degree of weathering, while the welded ignimbrites with common columnar jointing are more resistant. The volcanic units have fissured permeability. Mainly the ignimbrites represent rocks with high permeability; on the other hand, the highly weathered basalt, the intercalation of fine grained pyroclastics, and palaeosol horizons could form hydrogeological horizontal barriers because of the high content of clay minerals. Most of the landslides are represented by deep-seated complex slope deformations including toppling, rockfall, rockslide, rotational landslides, and debris flows. These slope failures appear to be currently stable; the morphology is modified by subsequent exogenous processes as in the Mejo area. Only several small-scale active landslides triggered by river erosion and human intervention were observed.

Statistical evaluation

The mean values of the same factors as for the Mejo site were also calculated for each landslide and rockfall polygon area at the Arba Minch site. Here the landslides and rockfalls are situated in areas with much higher slopes compared to the overall study area (see Fig. 10 and Table 3). There is a much higher density of faults and lineaments close to faults. They are also formed in areas with much higher vegetation density and medium and low RMS. Landslide and rockfall areas are also dominantly covered by cultivated areas, with woodlands taking a minor role.

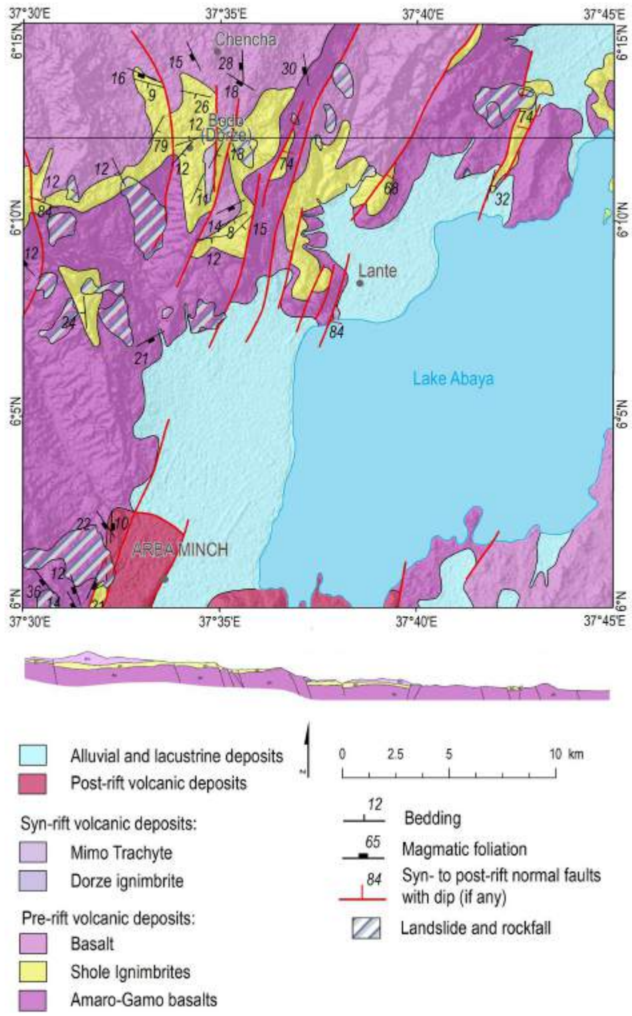

Figure 11. Geological and tectonic map of the Arba Minch site, with landslides and rockfalls indicated. For the location, see Fig. 2.

5 Discussion

The results discussed in the first subsection refer to regional mapping, where larger areas prone to geohazards rather than particular geohazards were mapped. Then, in the following subsections, there is a discussion of the detailed study of two areas (Arba Minch and Mejo) with contrasting lithological, tectonic, climatic, and vegetation settings and a similar size and morphology of landslides and rockfalls.

5.1 Main Ethiopian Rift (Hossana and Dilla area)

The progressive changes in the palaeostress regime during the active continental extension and faulting in the MER (e.g. Corti et al., 2018; Zwaan and Schreurs, 2020) increase the tectonic anisotropy of rocks and slope instabilities along major and subordinate fault escarpments, which have a pronounced effect on the genesis and formation of landslides. Several tectonic models explain the kinematics and palaeostress conditions of the regional extension/transtension from the beginning of the rifting (ca. 12 Ma) to the present (for the review, see Zwaan and Schreurs, 2020). Some models suppose continuous a NW–SE oriented extension (e.g. Chorowicz, 2005) in the early phase, which later changed to its current E–W direction (Bonini et al., 2005; Wolfenden et al., 2004). Alternatively, other models also assume a permanent E–W to ESE–WNW oriented extension (e.g. Agostini et al., 2009; Erbello and Kidane, 2018).

Proximity to faults and lineaments has a strong influence on the occurrence of areas prone to rockfalls and landslides in tectonically active areas worldwide (e.g. Chang et al,, 2018; Kumar et al., 2019, and references therein). According to statistical analysis, in the MER, both rockfalls and landslide areas typically occur on areas with steep slopes, close to faults and with a higher density of faults and lineaments. The latter parameter also reflects faults and fracture zone intersections and, according to geostatistic evaluation (Table 2), is more important for the formation of rockfalls than landslides. Rockfalls also show a much higher affinity to the proximity of faults. Most of them are normal faults associated with fissures opening during weathering, which initiates later rockfalls.

Rockfall areas occur in areas with lower precipitation, while, for landslides, high precipitation and high precipitation seasonality are typical. It correlates well with high vegetation density and low vegetation seasonality, which are found to have strong affinity with landslide occurrences. Thus, precipitation does not seem to be an important factor for rockfall formation but is important for landslides. It is probably because rockfalls are mapped on fault escarpments close to the rift valley, which is more dry, but they are initiated upslope at the edge of the plateau, where precipitation is higher.

Rockfalls and landslide areas occur in areas with bushland, grassland, and cultivated land cover. It leaves deforestation as one of the possible triggering factors. They also occur in areas with a wide range of rock mass strength classes (very low, low, medium, and high), so lithology and intensity of weathering do not seem to be an important triggering factor.

In the large area of the MER, the vast majority of slope instabilities is located on active normal fault escarpments (Fig. 12). This is a major natural triggering factor for rockfalls, while for landslides there is also the important influence of higher precipitation, precipitation seasonality, and vegetation density and vegetation seasonality.

5.2 Arba Minch case study

According to geostatistical analysis, the slope instabilities here, mostly landslides and rockfalls, are situated in areas with much steeper slopes, a much higher density of faults and lineaments, and are close to major faults. The majority of the large-scale slope instabilities of this area are strongly

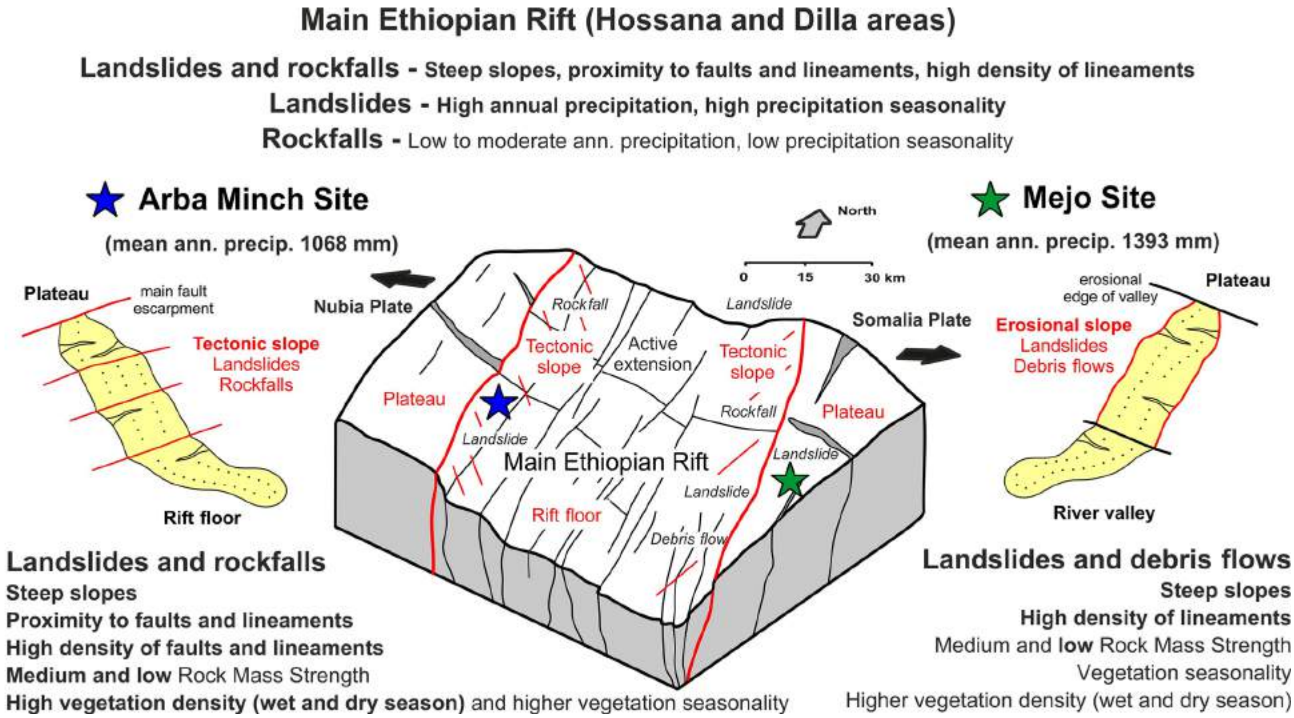

Figure 12. Sketch diagram summarizing the main factors controlling the formation and distribution of particular slope failures in the MER and in the Arba Minch and Mejo study sites.

associated with active tectonic morphological features characterized by straight fault scarps with triangular facets, large downthrown blocks, parallel sets of erosional valleys and asymmetrical ridges with SSW–NNE trending. These features are associated with active normal faults having large displacements (total vertical displacement of the western rift escarpment is more than 1500 m). Slope instabilities are also formed in areas with a much higher vegetation density and medium and low RMS. Volcanic rocks are variably affected by intense fracturing along faults; these zones are often altered, which lowers the slope stability of the rock environment. Alteration is also enhanced by more intense water–rock interactions – most springs are located on fault zones (Arba Minch means “forty springs”). Precipitation was not confirmed as an important factor.

The Arba Minch area is seismically active. According to the catalogue of earthquakes of the United States Geological Survey (USGS), several earthquakes have been documented around Abaya Lake since 1973 with magnitudes between 4 and 6 (U.S. Geological Survey, Earthquake Hazards Program, 2017). This active tectonic is also documented by young faults affecting Quaternary volcanic rocks and sediments outcropped around the town of Arba Minch (Verner et al., 2018b, c).

5.3 Mejo case study

Geostatistical analysis revealed that landslides and debris flows here are situated in areas with steep slopes. The geomorphology of the area is almost unaffected by local faults parallel with the rift valley; evidence of young faulting as displacement of the Pleistocene and Holocene rocks and straight fault scarps with triangular facets has not been observed. The steep slopes are formed and strongly modified by an intensive headward erosion. The incision of the valley as a result of a lowered erosional level and highland uplift could be the driving factor for the slope instability in the case of the Mejo area. Geomorphic proxies and the thickness of flood basalts suggest that the more tectonically active southeastern escarpment of the CMER and SMER (where the Mejo site is situated) are experiencing a relatively higher rate of tectonic uplift compared to the southeastern escarpment of the northern MER and the Afar Triangle (Xue et al., 2018; Sembroni et al., 2016). This can also be noted from the Eocene–Oligocene–Miocene basalts base (35–26 My) occurring in Arba Minch at an elevation of around 1050 m a.s.l., compared to their occurrence at a much higher elevation in Mejo at around 1900 m a.s.l. (Verner et al., 2018a, b, c, d).

Another factor causing the decrease in slope stability could be the following local lithological properties (dominance of medium and low RMS characteristic for slope instabilities in the area): (i) frequent intercalations of palaeosols with a high content of clay minerals and low permeability, or (ii) a strongly weathered metamorphic basement with foliation often concordant with the landscape, forming a very weak lithological environment, which is favourable for slope processes. No young volcanic features and products have been observed; the probability of earthquakes related to volcanic eruptions is very low in the Mejo area, where the nearest earthquakes were recorded 60 km NW of the study area.

5.4 Comparison of the Arba Minch and Mejo sites

Landslides at both sites are similar from a geomorphological point of view, i.e. old, stabilized, and smoothed by erosion. The estimated age of landslides is Plio-Pleistocene, maybe even older, and uplift dates minimally last several mega-annums (Ma), i.e. approximately the same interval plus the Holocene, so, in both cases, it concerns long-term evolution. Young reactivations are very localized and mostly due to human activity. Both study areas have seasonal humid climates with a prominent summer (mid-June to mid-September) rain season, but the Mejo study area, which is situated 90 km east of Arba Minch, 60 km out of the main rift valley on the uplifting plateau, is more humid. In the Mejo area. the mean annual rainfall is 30 % higher (1393 mm) compared to Arba Minch (1068 mm); most of the precipitation difference falls in the rainy season, while, during the dry months, the precipitation at both localities is comparable (Table 3).

Steep slopes associated with active faulting and hydrogeological conditions favouring rock alterations along these zones are probably the main predisposition for the formation of slope instabilities in Arba Minch. Seasonal precipitation and seismic events could be triggering factors.

The combination of a deeply weathered Proterozoic basement and steep slopes formed by intense headward erosional processes due to relatively rapid uplift could represent the main predisposition for creating favourable conditions for landslide evolution in Mejo (Fig. 12). Triggers of slope instabilities are probably more intense precipitation and higher precipitation seasonality.

6 Conclusions

Active continental rifting has a distinct effect on the formation of landslides. The formation, superposition, and polyphase reactivation of fault structures in the changing regional stress field increase the tectonic anisotropy of rocks and increase the risk of slope instabilities forming. The new structural data from the CMER and SMER support a model of progressive change in the orientation of the regional extension from NW–SE to the recent E(ENE)–W(WSW) direction driven by the African and Somali plates moving apart, with the presumable contribution of the NNE(NE)–SSW(SE) extension controlled by the Arabian Plate.

An evaluation at the regional scale of the central and southern MER demonstrates that areas prone to slope instabilities, mainly landslides and rockfalls, occur on steep slopes, which were almost exclusively formed on active normal fault escarpments. Landslide areas are also significantly influenced by higher annual precipitation, higher precipitation seasonality, and vegetation density and seasonality, while rockfalls have an affinity to vegetation seasonality only. Landslide areas occur on slopes at higher altitudes with higher precipitation and vegetation density, but large parts of the study area are on the rift floor, which is more dry, scarcely vegetated, very flat, and without landslides, while dense vegetation cannot develop on rockfalls occupying very steep rocky and blocky fault escarpments. Deforestation is also an important predisposition because rockfalls and landslides typically occur in areas with bushland, grassland, and cultivated land cover.

Different geological, geomorphological, and climatic conditions can lead to the formation of similar types of slope instabilities. A detailed study on active rift escarpment in the Arba Minch area revealed similar affinities as in the regional study of MER. Slope instabilities here are closely associated with steep, mostly faulted, slopes and a higher density of vegetation. Active faulting, forming steep slopes, is the main predisposition for landslide formation here, and the main triggers could be seismicity and seasonal precipitation.

While the detailed study situated in the Mejo area on the uplifting Ethiopian Plateau 60 km east of the rift valley shows that the occurrence of slope instabilities is strongly influenced by steep erosional slopes and the deeply weathered Proterozoic metamorphic basement, landslides here are often formed in areas densely fractured and with foliation concordant with topography. Regional uplift, accompanied by rapid headward erosion forming steep slopes together with unfavourable lithological conditions, is the main predisposition for landslide formation; the main triggers can be intense precipitation and higher precipitation seasonality. Triggers for young landslides are also very probably human activity and erosion, but the relevant data are lacking for a thorough evaluation and only occasional observations support this conclusion.

Data availability. Data are available upon request from the corresponding author.

Author contributions. KM prepared the paper, with contributions from all co-authors, and performed morphotectonic study, remote sensing data processing and analysis, statistic and geostatistical analysis and part of the field geological mapping. KV was responsible for the structural analysis and part of the field geological mapping. TH performed the geohazard mapping and analysis. LAM contributed with climatic and engineering geology data and did part of the field geohazard mapping. VK performed morphometric analysis. DB carried out part of the field geological mapping and provided information on rock lithologies. AM contributed to structural analysis, RK helped with the preparation of the paper, and MY (with MK) did important parts of the field mapping.

Competing interests. The authors declare that they have no conflict of interest.

Disclaimer. Publisher's note: Copernicus Publications remains neutral with regard to jurisdictional claims in published maps and institutional affiliations.

Acknowledgements. We thank our many colleagues from the Geological Survey of Ethiopia and Addis Ababa University (School of Earth Sciences), for their help in the acquisition, processing and interpretation of the data, and especially Aberash Mosisa and Wubayehu Dessalegn Sallile. Many thanks to Richard Withers, for the English proofreading. The paper was enhanced by valuable comments from the editor, Filippo Catani, and two anonymous referees.

Financial support. The research has been funded by the Czech Development Agency in the framework of a development project (project no. 281226/2018-Č RA – "Implementation of a Methodical Approach in Geological Sciences to Enhance the Quality of Doctoral Studies at the Addis Ababa University (Ethiopia)" – and project 15 no. 280614/2019-Č RA – "Ensuring Sustainable Land-Management in Selected Areas of Ethiopia on the Basis of Geoscientific Mapping" – with both grants being awarded to Kryštof Verner) and project Q45 Progress (Faculty of Science, Charles University, Prague).

Review statement. This paper was edited by Filippo Catani and reviewed by two anonymous referees.

References

Abate, M., Nyssen, J., Steenhuis, T. S., Moges, M. M., Tilahun, S. A., Enku, T., and Adgo, E.: Morphological changes of Gumara River channel over 50 years, upper Blue Nile basin, Ethiopia, J. Hydrol., 525, 152–164, https://doi.org/10.1016/j.jhydrol.2015.03.044, 2015.

Abebe, T., Manetti, P., Bonini, M., Corti, G., Innocenti, F., Mazzarini, F., and Pecskay, Z.: Geological map (scale 1 : 200 000) of the northern main Ethiopian rift and its implication for the volcano-tectonic evolution of the rift, Geological Society of America, Boulder, Colorado, Maps and Charts series, MCH094, 2005.

Abebe, B., Dramis, F., Fubelli, G., Umer, M., and Asrat, A.: Landslides in the Ethiopian highlands and the Rift margins, J. Afr. Earth Sci., 56, 131–138, https://doi.org/10.1016/j.jafrearsci.2009.06.006, 2010.

Acocella, V.: Coupling volcanism and tectonics along divergent plate boundaries: Collapsed rifts from central Afar, Ethiopia, Geol. Soc. Am. B., 122, 1717–1728, https://doi.org/10.1130/B30105.1, 2010.

Agostini, A., Corti, G., Zeoli, A., and Mulugeta, G.: Evolution, pattern, and partitioning of deformation during oblique continental rifting: Inferences from lithospheric-scale centrifuge models, Geochem. Geophys. Geosyst., 10, 1–11, https://doi.org/10.1029/2009GC002676, 2009.

Agostini, A., Bonini, M., Corti, G., Sani, F., and Manetti, P.: Distribution of Quaternary deformation in the central Main Ethiopian Rift, East Africa, Tectonics, 30, 4010, https://doi.org/10.1029/2010TC002833, 2011.

Altin, T. B. and Altin, B. N.: Development and morphometry of drainage network in volcanic terrain, Central Anatolia, Turkey, Geomorphology, 125, 485–503, https://doi.org/10.1016/j.geomorph.2010.09.023, 2011.

Asfaw, L. M.: Development of earthquake-induced fissures in the Main Ethiopian Rift, Nature, 297, 393–395, https://doi.org/10.1038/297393a0, 1982.

Asfaw, L. M.: Seismic risk at a site in the East African rift system, Tectonophysics, 209, 301–309, https://doi.org/10.1016/0040-1951(92)90038-8, 1992.

Asfaw, L. M.: Environmental hazard from fissures in the Main Ethiopian Rift, J. Afr. Earth Sci., 27, 481–490, https://doi.org/10.1016/S0899-5362(98)00074-8, 1998.

Asfaw, L. M.: Integrated approach to the study of geohazards with application in southern Afar, J. Afr. Earth Sci., 48, 237–244, https://doi.org/10.1016/j.jafrearsci.2006.08.006, 2007.

Ayalew, L.: The effect of seasonal rainfall on landslides in the highlands of Ethiopia, B. Eng. Geol. Environ., 58, 9–19, https://doi.org/10.1007/s100640050065, 1999.

Ayalew, L. and Yamagishi, H.: Slope failures in the Blue Nile basin, as seen from landscape evolution perspective, Geomorphology, 57, 95–116, https://doi.org/10.1016/S0169-555X(03)00085-0, 2004.

Ayalew, L., Yamagishi, H., and Reik, G.: Ground cracks in Ethiopian Rift Valley: facts and uncertainties, Eng. Geol., 75, 309–324, https://doi.org/10.1016/j.enggeo.2004.06.018, 2004.

Ayele, A.: Probabilistic seismic hazard analysis (PSHA) for Ethiopia and the neighboring region, J. Afr. Earth Sci., 134, 257–264, https://doi.org/10.1016/j.jafrearsci.2017.06.016, 2017.

Ayele, A., Jacques, E., Kassim, M., Kidane, T., Omar, A., Tait, S., Nercessian, A., de Chabalier, J. B., and King, G.: The volcano–seismic crisis in Afar, Ethiopia, starting September 2005, Earth Planet. Sc. Lett., 255, 177–187, https://doi.org/10.1016/j.epsl.2006.12.014, 2007.

Ayele, A., Keir, D., Ebinger, C., Wright, T. J., Stuart, G. W., Buck, W. R., Jacques, E., Ogubazghi, G., and Sholan, J.: September 2005 mega-dike emplacement in the Manda-Harraro nascent oceanic rift (Afar Depression), Geophys. Res. Lett., 36, L20306, https://doi.org/10.1029/2009GL039605, 2009.

Ayenew, T. and Barbieri, G.: Inventory of landslides and susceptibility mapping in the Dessie area, northern Ethiopia, Eng. Geol., 77, 1–15, https://doi.org/10.1016/j.enggeo.2004.07.002, 2005.

Billi, P.: Geomorphological landscapes of Ethiopia, in: Landscapes and Landforms of Ethiopia, Springer, Dordrecht, 3–32 pp., https://doi.org/10.1007/978-94-017-8026-1_1, 2015.

Billi, P. and Dramis, F.: Geomorphological investigation on gully erosion in the Rift Valley and the northern highlands of

Ethiopia, Catena, 50, 353–368, https://doi.org/10.1016/S0341-8162(02)00131-5, 2003.
Bolongaro-Crevenna, A., Torres-Rodríguez, V., Sorani, V., Frame, D., and Ortiz, M. A.: Geomorphometric analysis for characterizing landforms in Morelos State, Mexico, Geomorphology, 67, 407–422, https://doi.org/10.1016/j.geomorph.2004.11.007, 2005.
Bonini, M., Corti, G., Innocenti, F., Manetti, P., Mazzarini, F., Abebe, T., and Pecskay, Z.: Evolution of the Main Ethiopian Rift in the frame of Afar and Kenya rifts propagation, Tectonics, 24, 1–24, https://doi.org/10.1029/2004TC001680, 2005.
British Standard BS5930: Code of Practice for Site Investigations, British Standards Institution (BSI), London, 147 pp., 1981.
Burianek, D., Hroch, T., Verner, K., Megerssa, L., Martinek, K., Yakob, M., Haregot, A., Janderkova, J., Sima, J., Krystofova, E., Valenta, J., Tadesse, E., Mosisa, A., Dalke, G., Legesse, F., Assefa, G., Pecskay, Z., Hejtmankova, P., and Krejci, Z.: Explanatory notes to thematic geoscientific maps of Ethiopia at a scale of 1 : 50 000, Map Sheet 0638-C2 Dila, Czech Geological Survey, Prague, 103 pp., 2018.
Centre for Development and Environment: Ethio GIS CD-ROM Database file system, University of Bern, Switzerland, 1999.
Chang, K.-J., Chan, Y.-C., Chen, R.-F., and Hsieh, Y.-C.: Geomorphological evolution of landslides near an active normal fault in northern Taiwan, as revealed by lidar and unmanned aircraft system data, Nat. Hazards Earth Syst. Sci., 18, 709–727, https://doi.org/10.5194/nhess-18-709-2018, 2018.
Chorowicz, J.: The east African rift system, J. Afr. Earth Sci., 43, 379–410, https://doi.org/10.1016/j.jafrearsci.2005.07.019, 2005.
Corti, G.: Continental rift evolution: From rift initiation to incipient break-up in the Main Ethiopian Rift, East Africa, Earth-Sci. Rev., 96, 1–53, https://doi.org/10.1016/j.earscirev.2009.06.005, 2009.
Dhont, D. and Chorowicz, J.: Review of the neotectonics of the Eastern Turkish–Armenian Plateau by geomorphic analysis of digital elevation model imagery, Int. J. Earth Sci., 95, 34–49, https://doi.org/10.1007/s00531-005-0020-3, 2006.
Ebinger, C. J., Yemane, T., Woldegabriel, G., Aronson, J. L., and Walter, R. C.: Late Eocene-Recent volcanism and faulting in the southern Main Ethiopian Rift, J. Geol. Soc., 150, 99–108, https://doi.org/10.1144/gsjgs.150.1.0099, 1993.
Ebinger, C. J., Yemane, T., Harding, D. J., Tesfaye, S., Kelley S., and Rex D. C.: Rift deflection,migration, and propagation: Linkage of the Ethiopian and Eastern rifts, Africa, Geol. Soc. Am. B., 112, 163–176, https://doi.org/10.1130/0016-7606(2000)112<163:RDMAPL>2.0.CO;2, 2000.
Erbello, A. and Kidane, T.: Timing of volcanism and initiation of rifting in the Omo-Turkana depression, southwest Ethiopia: Evidence from paleomagnetism, J. Afr. Earth Sci., 139, 319–329, https://doi.org/10.1016/j.jafrearsci.2017.12.031, 2018.
FAO, Food and Agriculture Organization: Global Forest Resources Assessment 2000: Main Report, FAO Forestry Paper 140, Rome, Italy, https://doi.org/10.1016/S0264-8377(03)00003-6, 2001.
Fisher, P., Wood, J., and Cheng, T.: Where is Helvellyn? Fuzziness of multi-scale landscape morphometry, Transactions of the Institute of British Geographers, 29, 106–128, https://doi.org/10.1111/j.0020-2754.2004.00117.x, 2004.
Fritz, H., Abdelsalam, M., Ali, K. A., Bingen, B., Collins, A. S., Fowler, A. R., Ghebreab, W., Hauzenberger, C. A., Johnson, P. R., Kusky, T. M., and Macey, P.: Orogen styles in the East African Orogen: a review of the Neoproterozoic to Cambrian tectonic evolution, J. Afr. Earth Sci., 86, 65–106, https://doi.org/10.1016/j.jafrearsci.2013.06.004, 2013.
Fubelli, G., Abebe, B., Dramis, F., and Vinci, S.: Geomorphological evolution and present-day processes in the Dessie Graben (Wollo, Ethiopia), Catena, 75, 28–37, https://doi.org/10.1016/j.catena.2008.04.001, 2008.
Ganas, A., Pavlides, S., and Karastathisa, V.: DEM-based morphometry of range-front escarpments in Attica, central Greece, and its relation to fault slip rates, Geomorphology, 65, 301–319, https://doi.org/10.1016/j.geomorph.2004.09.006, 2005.
Gao, M., Zeilinger, G., Xu, X., Wang Q., and Hao, M.: DEM and GIS analysis of geomorphic indices for evaluating recent uplift of the northeastern margin of the Tibetan Plateau, China, Geomorphology, 190, 61–72, https://doi.org/10.1016/j.geomorph.2013.02.008, 2013.
Gessesse, D.: Forest Decline in South Central Ethiopia Extent, history and process. Doctoral dissertation. Department of Physical Geography and Quaternary Geology. Stockholm University, Sweden, 2007.
Gete, Z. and Hurni, H.: Implications of Land Use and Land Cover dynamics for mountain resource degradation in the northwestern Ethiopian highlands, Mt. Res. Dev., 21, 184–191, https://doi.org/10.1659/0276-4741(2001)021[0184:IOLUAL]2.0.CO;2, 2001.
Gezahegn, A. and Dessie, T.: Report on Engineering geophysical investigation of the Blue Nile basin for rerouting of the main road, Ethiopian Institute of Geological Survey, Addis Ababa, 1994.
Goitom, B., Oppenheimer, C., Hammond, J. O., Grandin, R., Barnie, T., Donovan, A., Ogubazghi, G., Yohannes, E., Kibrom, G., Kendall, J. M., and Carn, S. A.: First recorded eruption of Nabro volcano, Eritrea, 2011, B. Volcanol., 77, 85, 2015.
Gouin, P.: Kara Kore and Serdo epicenters: relocation and tectonic implications, B. Geophys. Obs., 15, 15–25, 1975.
Gouin, P.: Earthquake history of Ethiopia and the Horn of Africa, International Development Research Centre, Ottawa, Canada, 1979.
Habtamu, E., Ermiyas, F., Tutan, N., and Tsigehana, T.: Engineering Geological Map of Dila Sheet at scale of 1:250,000 scale (NB 37-6), Geological Survey of Ethiopia, Addis Ababa, 2012.
Hayward, N. J. and Ebinger, C. J.: Variations in the along-axis segmentation of the Afar Rift system, Tectonics, 15, 244–257, https://doi.org/10.1029/95TC02292, 1996.
Hearn, G. J.: Slope hazards on the Ethiopian road network, Q. J. Eng. Geol. Hydrogeol., 52, 295–311, 2018.
ISRM, International Society of Rock Mechanics Commission on Testing Methods: Suggested method for determining point load strength, Int. J. Rock Mech. Min. Sci. Geomech., 22, 51–60, https://doi.org/10.1016/0148-9062(85)92985-7, 1985.
Janetos, A. C. and Justice, C. O.: Land covers global productivity: a measurement strategy for the NASA programme, Int. J. Remote Sens., 21, 1491–1512, https://doi.org/10.1080/014311600210281, 2000.
JICA and GSE: The Project for Developing Countermeasures against Landslides in the Abay River Gorge, technical report, Japan International Cooperation Agency and Geological Survey of Ethiopia, Addis Ababa, 348 pp., 2012.
Kopačková, V., Rapprich, V., Sebesta, J., and Zelenkova, K.: Slope dependent morphometric analysis as a tool contributing to re-

construction of volcano evolution, In Earth and environmental sciences, InTech, https://doi.org/10.5772/29466, 2011.

Kropáček, J., Vařilová, Z., Baroň, I., Bhattacharya, A., Eberle, J., and Hochschild, V.: Remote sensing for characterisation and kinematic analysis of large slope failures: Debre sina landslide, main ethiopian rift escarpment, Remote Sens., 7, 16183–16203, https://doi.org/10.3390/rs71215821, 2015.

Kumar, V., Gupta, V., and Sundriyal, Y. P.: Spatial interrelationship of landslides, litho-tectonics, and climate regime, Satluj valley, Northwest Himalaya, Geol. J., 54, 537–551, https://doi.org/10.1002/gj.3204, 2019.

Kycl, P., Rapprich, V., Verner, K., Novotný, J., Hroch, T., Mišurec, J., Eshetu, H., Haile, E. T., Alemayehu, L., and Goslar, T.: Tectonic control of complex slope failures in the Ameka River Valley (Lower Gibe Area, central Ethiopia): Implications for landslide formation, Geomorphology, 288, 175–187, https://doi.org/10.1016/j.geomorph.2017.03.020, 2017.

Lemessa, G., Asfaw, B., Mamo, S., and Ashenafi, S.: Mass movement hazards assessment on Betto and Sawla sub sheet of Goffa district, North Omo Zone, Southern Nations Nationalities and People's Regional State, technical Report, Geological Survey of Ethiopia, Addis Ababa, 2000.

Mancini, F., Ceppi, C., and Ritrovato, G.: GIS and statistical analysis for landslide susceptibility mapping in the Daunia area, Italy, Nat. Hazards Earth Syst. Sci., 10, 1851–1864, https://doi.org/10.5194/nhess-10-1851-2010, 2010.

Meinhardt, M., Fink, M., and Tünschel, H.: Landslide susceptibility analysis in central Vietnam based on an incomplete landslide inventory: Comparison of a new method to calculate weighting factors by means of bivariate statistics, Geomorphology, 234, 80–97, https://doi.org/10.1016/j.geomorph.2014.12.042, 2015.

Melese, S. M.: Effect of land use land cover changes on the forest resources of Ethiopia, International Journal of Natural Resource Ecology and Management, 1, 51, https://doi.org/10.11648/j.ijnrem.20160102.16, 2016.

Muluneh, A. A., Cuffaro, M., and Doglioni, C.: Left-lateral transtension along the Ethiopian Rift and constrains on the mantle-reference plate motions, Tectonophysics, 632, 21–31, https://doi.org/10.1016/j.tecto.2014.05.036, 2014.

Peduzzi, P.: Landslides and vegetation cover in the 2005 North Pakistan earthquake: a GIS and statistical quantitative approach, Nat. Hazards Earth Syst. Sci., 10, 623–640, https://doi.org/10.5194/nhess-10-623-2010, 2010.

Pike, R. J.: Geomorphomery-diversity in quantitative surface analysis, Prog. Phys. Geogr., 24, 1–20, https://doi.org/10.1177/030913330002400101, 2000.

Rapprich, V. and Eshetu, H.: Geological hazards and engineering geology maps of Dilla NB 37-6, Czech Development Agency, Czech Geological Survey, Geological Survey of Ethiopia, Addis Ababa, 2014.

Rapprich, V., Erban, V., Fárová, K., Kopačková, V., Bellon, H., and Hernandez, W.: Volcanic history of the Conchagua Peninsula (eastern El Salvador), J. Geosci., 55, 95–112, https://doi.org/10.3190/jgeosci.069, 2010.

Rapprich, V., Nida, D., and Bizuye, Y.: Geological hazards and engineering geology maps of Hossana NB 37-2, Czech Development Agency, Czech Geological Survey, Geological Survey of Ethiopia, Addis Ababa, 2014.

Saria, E., Calais, E., Stamps, D. S., Delvaux, D., and Hartnady, C. J. H.: Present-day kinematics of the East African Rift, J. Geophys. Res.-Sol. Ea., 119, 3584–3600, https://doi.org/10.1002/2013JB010901, 2014.

Sembroni, A., Faccenna, C., Becker T. W., Molin, P., and Abebe, B.: Long-term, deep-mantle support of the Ethiopia-Yemen Plateau, Tectonics, 35, 69–488, https://doi.org/10.1002/2015TC004000, 2016.

Tadesse, T.: Recent landslide and resulting damages in the Blue Nile River Gorge and its tributaries, Eastern Gojam Zone, Technical Report, Geological Survey of Ethiopia, Addis Ababa, 1993.

Temesgen, B., Umer, M., Asrat, A., Berakhi, O., Ayele, A., Francesco, D., and Demissie, M.: Landslide hazard on the slopes of Dabicho Ridge, Wondo Genet area: the case of June 18, 1996 event, SINET: Ethiopian Journal of Science, 22, 127–140, 1999.

Temesgen, B., Mohammed, M. U., and Korme, T.: Natural hazard assessment using GIS and remote sensing methods, with particular reference to the landslides in the Wondogenet area, Ethiopia, Phys. Chem. Earth Pt. C, 26, 665–675, https://doi.org/10.1016/S1464-1917(01)00065-4, 2001.

U.S. Geological Survey: Earthquake Hazards Program, Advanced National Seismic System (ANSS), Comprehensive Catalogue of Earthquake Events and Products: Various, https://doi.org/10.5066/F7MS3QZH, 2017.

Vařilová, Z., Kropáček, J., Zvelebil, J., Šťastný, M., and Vilímek, V.: Reactivation of mass movements in Dessie graben, the example of an active landslide area in the Ethiopian Highlands, Landslides, 12, 985–996, https://doi.org/10.1007/s10346-015-0613-2, 2015.

Verner, K., Megerssa, L., Buriánek, D., Martínek, K., Hroch, T., Yakob, M., Haregot, A., Bewketu, H., Mosisa, A., Dalke, G., Hejtmánková, P., and Krejčí, Z.: Geological map at a scale of 1 : 50 000, Geological and thematic maps at a scale of 1:50,000 for Mejo, Leku, Arba Minch and Dila areas, SNNPR, Ethiopia. Czech Geological Survey, Prague, Map Sheet 0638-D2 Mejo, 2018a.

Verner, K., Megerssa, L., Hroch, T., Buriánek, D., Martínek, K., Gebremariyam, H., Tadesse, E., Legesse, F., Nisra, E., Abateneh, B., Hejtmánková, P., and Krejčí, Z.: Geological map at a scale of 1 : 50 000, Geological and thematic maps at a scale 1 : 50 000 for Mejo, Leku, Arba Minch and Dila areas, SNNPR, Ethiopia, Czech Geological Survey, Prague, Map Sheet 0637-D3 Arba Minch, 2018b.

Verner, K., Megerssa, L., Hroch, T., Buriánek, D., Martínek, K., Janderková, J., Šíma, J., Kryštofová, E., Gebremariyam, H., Tadesse, E., Legesse, F., Nisra, E., Abateneh, B., Assefa, G., Valenta, J., Pécskay, Z., Hejtmánková, P., and Krejčí, Z.: Explanatory notes to the thematic geoscientific maps of Ethiopia at a scale of 1 : 50 000, Czech Geological Survey, Prague, Map Sheet 0637-D3 Arba Minch, 2018c.

Verner, K., Megerssa, L., Hroch, T., Buriánek, D., Martínek, K., Yakob, M., Haregot, A., Janderková, J., Šíma, J., Kryštofová, E., Valenta, J., Bewketu, H., Mosisa, A., Dalke, G., Assefa, G., Pécskay, Z., Hejtmánková, P., and Krejčí, Z.: Explanatory notes to the thematic geoscientific maps of Ethiopia at a scale of 1 : 50 000, Czech Geological Survey, Prague, Map Sheet 0638-D2 Mejo, 2018d.

Wilks, M., Ayele, A., Kendall, J. M., and Wookey, J.: The 24th January 2016 Hawassa earthquake: Implications for seismic hazard in the Main Ethiopian Rift, J. Afr. Earth Sci., 125, 118–125, https://doi.org/10.1016/j.jafrearsci.2016.11.007, 2017.

Williams, F. M., Williams, M. A. J., and Aumento, F.: Tensional fissures and crustal extension rates in the northern part of the Main Ethiopian Rift, J. Afr. Earth Sci., 38, 183–197, https://doi.org/10.1016/j.afrearsci.2003.10.007, 2004.

Woldearegay, K.: Review of the occurrences and influencing factors of landslides in the highlands of Ethiopia: With implications for infrastructural development, Momona Ethiopian Journal of Science, 5, 3–31, https://doi.org/10.4314/mejs.v5i1.85329, 2013.

Woldegabriel, G., Heiken, G., White, T. D., Asfaw, B., Hart, W. K., and Renne, P. R.: Volcanism, tectonism, sedimentation, and the paleoanthropological record in the Ethiopian Rift System, Special papers-Geological Society of America, 83–99, 2000.

Wolfenden, E., Ebinger, C., Yirgu, G., Deino, A., and Ayale, D.: Evolution of the northern Main Ethiopian rift: birth of a triple junction, Earth Planet. Sc. Lett., 224, 213–228, https://doi.org/10.1016/j.epsl.2004.04.022, 2004.

Wood, J. D.: The geomorphologic characterization of digital elevation models, PhD Thesis, University of Leicester, UK, 1996.

Wotchoko, P., Bardintzeff, J. M., Itiga, Z., Nkouathio, D. G., Guedjeo, C. S., Ngnoupeck, G., Dongmo, A., and Wandji, P.: Geohazards (Floods and Landslides) in the Ndop Plain, Cameroon volcanic nine, Open Geosci., 8, 429–449, https://doi.org/10.1515/geo-2016-0030, 2016.

Xue, L., Alemu, T., Gani, N. D., and Abdelsalama, M. G.: Spatial and temporal variation of tectonic uplift in the southeastern Ethiopian Plateau from morphotectonic analysis, Geomorphology, 309, 98–111, https://doi.org/10.1016/j.geomorph.2018.02.025, 2018.

Yekoye, B., Yewubinesh, B., and Debebe, N.: Engineering Geological Map of Hosaina sheet (NB 37-2) at scale of 1 : 250 000, Geological Survey of Ethiopia, Addis Ababa, 2012.

Zvelebil, J., Šíma, J., and Vilímek, V.: Geo-risk management for developing countries – vulnerability to mass wasting in the Jemma River Basin, Ethiopia, Landslides, 7, 99–103, https://doi.org/10.1007/s10346-009-0191-2, 2010.

Zwaan, F. and Schreurs, G.: Rift segment interaction in orthogonal and rotational extension experiments: Implications for the large-scale development of rift systems, J. Struct. Geol., 140, 1–17, https://doi.org/10.1016/j.jsg.2020.104119, 2020.

Attachment I

Geological map of Mejo map sheet at a scale of 1:50,000

SET OF GEOSCIENCE MAPS OF ETHIOPIA AT SCALE 1 : 50,000

GEOLOGICAL MAP

Editors: K. Verner, L. Megerssa

Subsheet 0638-D2 Mejo

LITHOSTRATIGRAPHIC SCHEME

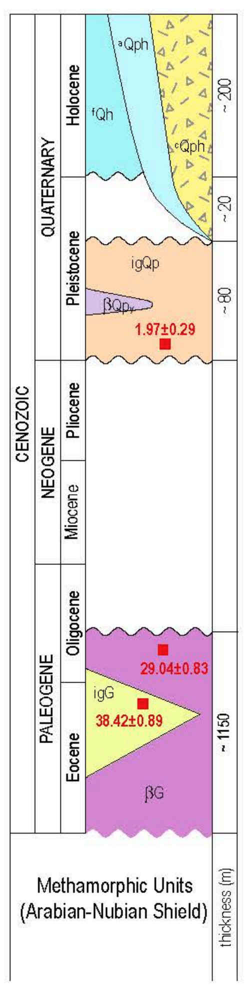

Quarternary sediments

Fluvial sediments fQh

Alluvial sediments aQph

Colluvial sediments cQph

Post-rift volcanic deposits

Yubo Basalt βQp_y

Hantate Ignimbrite: welded to unwelded rhyolitic ignimbrite igQp

Pre-rift volcanic deposits

Shole Ignimbrite: rhyolitic ignimbrite and minor rhyolite igG

Basalt βG

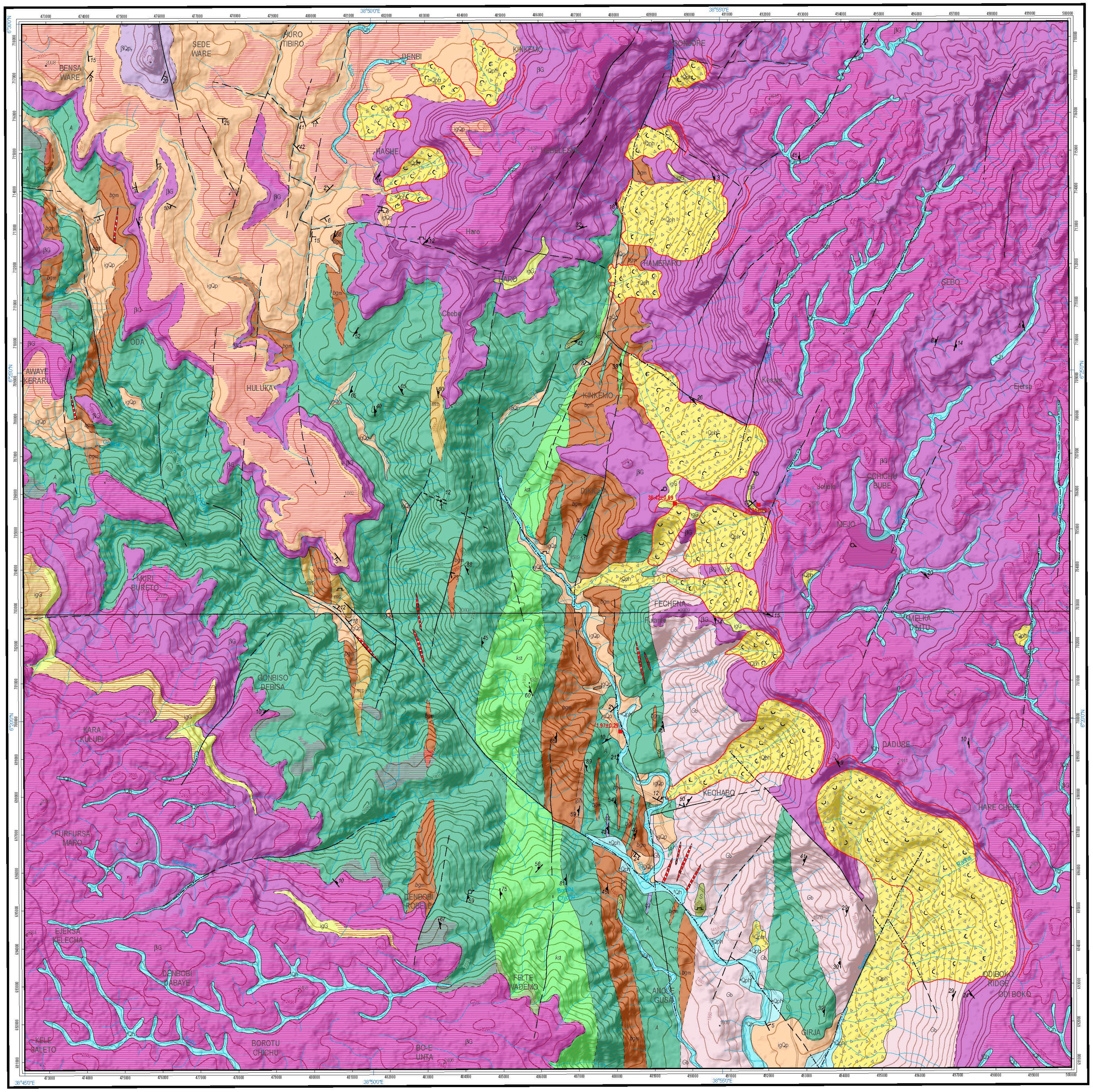

SCHEME OF GEOLOGICAL UNITS

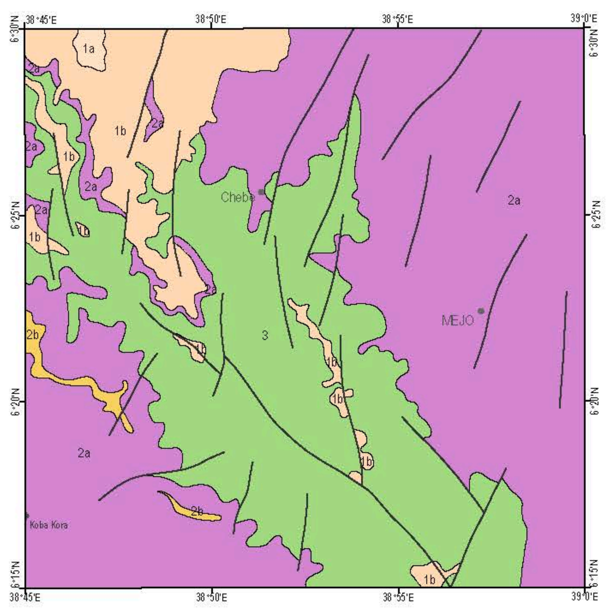

1 : 250,000

1 Post-rift deposits
- 1a Yubo Basalt
- 1b Hantate Ignimbrite

2 Pre-rift deposits
- 2a Amaro-Gamo Basalt
- 2b Shole Ignimbrite

3 Metamorphic Units (Arabian-Nubian Shield)

SCHEME OF DMR AND REGIONAL FAULTS

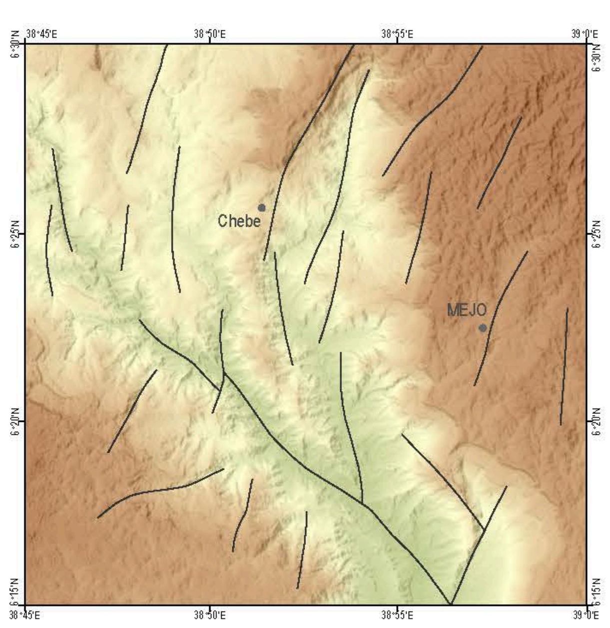

1 : 250,000

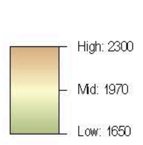

LEGEND

Quarternary sediments
CENOZOIC
QUATERNARY
Holocene

1. fQh — Fluvial sediments

Pleistocene–Holocene

2. aQph — Alluvial sediments
3. cQph — Colluvial sediments

Post-rift volcanic deposits
Pleistocene

4. βQp_y — Yubo Basalt
5. igQp — Hantate Ignimbrite: welded to unwelded rhyolitic ignimbrite

Pre-rift volcanic deposits
PALEOGENE
Eocene–Oligocene

6. igG — Shole Ignimbrite: rhyolitic ignimbrite and minor rhyolite
7. βG — Amaro–Gamo Basalt: basalt to trachybasalt with minor basaltic pyroclastic deposits

Southern Ethiopian Shield
NEOPROTEROZOIC

8. Quartz vein
9. S — Serpentinite and metagabbro
10. kst — Talc-tremolite and chlorite schist
11. A — Amphibolite
12. Gb — Biotite orthogneiss
13. ph — Biotite-muscovite phyllite
14. bgm — Biotite to muscovite-biotite paragneiss
15. qz — Quartzite
16. ms — Sericite schist
17. Lithological boundary observed
18. Lithological boundary inferred
19. Significant unconformity (only in lithostratigraphic scheme)
20. Normal fault observed
21. 74 — Normal fault observed with dip and slickensides
22. Normal fault inferred
23. Normal fault obscured
24. Mylonitization
25. 14 — Bedding
26. 41 — Magmatic foliation
27. 39 — Metamorphic foliation
28. 12 — Fold axis
29. Alluvial fan
30. Landslide
31. Main landslide scarp
32. Regolith (deeply weathered rock)
33. Quarry
34. Spring
35. 1–2 Cross-section line
36. 2,34±0.61 — K-Ar dating (Ma - megaannum)

MAP SHEET INDEX

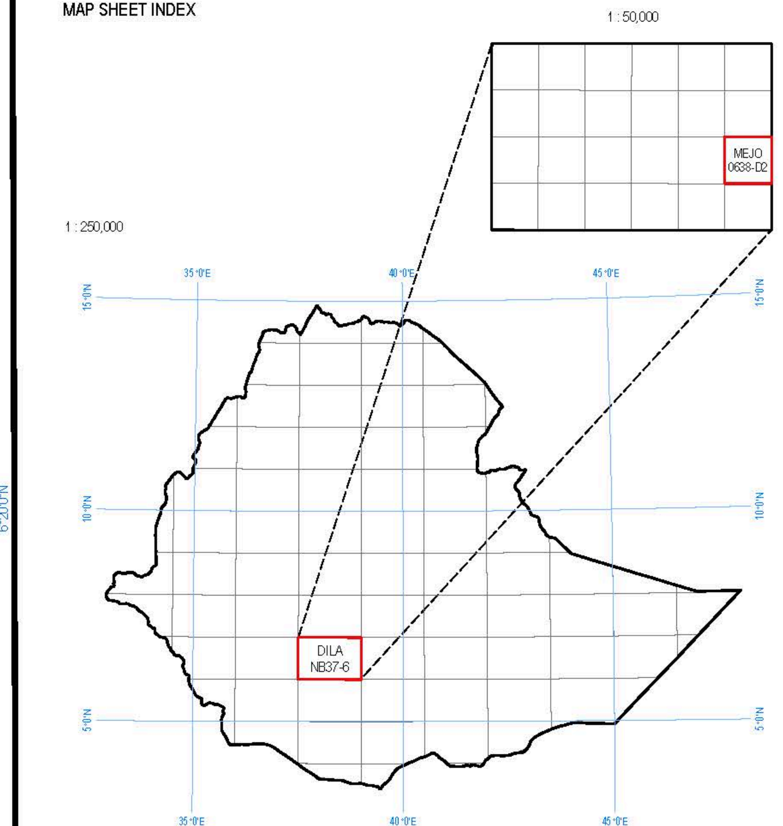

Set of Geoscience Maps of Ethiopia at Scale 1 : 50,000
Geological map of Mejo subsheet
Collaborators: Buriánek D., Hroch T., Martínek K., Yakob M., Haregot A., Bewketu H., Mosisa A., Balke G., Hejtmánková P., Krejčí Z.
Digital cartography: Krejčí Z., Hejtmánková P.

Kilometers — Miles

1 : 50,000
Contour interval: 50 meters

Coordinate system:
Blue numbers: longitude & latitude
Black numbers: UTM - zone 37 in meters
Projection: Transverse Mercator
Ellipsoid, Datum: Clarke 1880, Adindan
Topography derived from Ethiopia 1 : 50,000 scale maps Ministry of Land Reform and Administration (Thematic and Mapping Department)

CZECH REPUBLIC DEVELOPMENT COOPERATION

CZECH GEOLOGICAL SURVEY

aquatest

GEOLOGICAL CROSS-SECTION

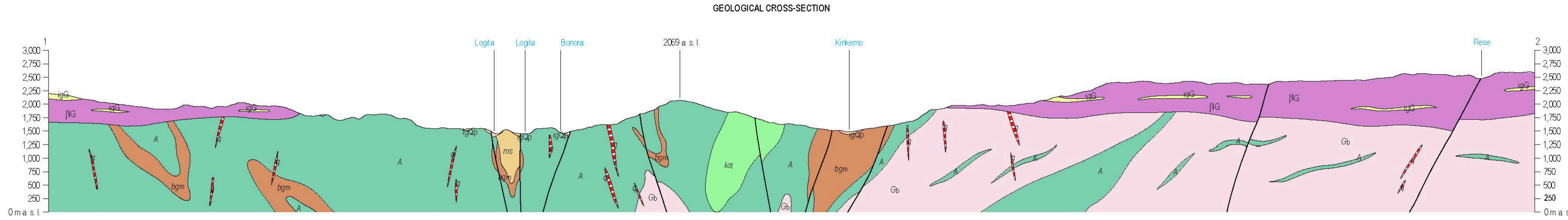

Cross-section with no vertical exaggeration

Attachment II

Geological map of Arba Minch map sheet at a scale of 1:50,000

SET OF GEOSCIENCE MAPS OF ETHIOPIA AT SCALE 1 : 50,000

GEOLOGICAL MAP

Editors: Kryštof Verner, Leta Megerssa

Sheet 0637-D3 Arba Minch

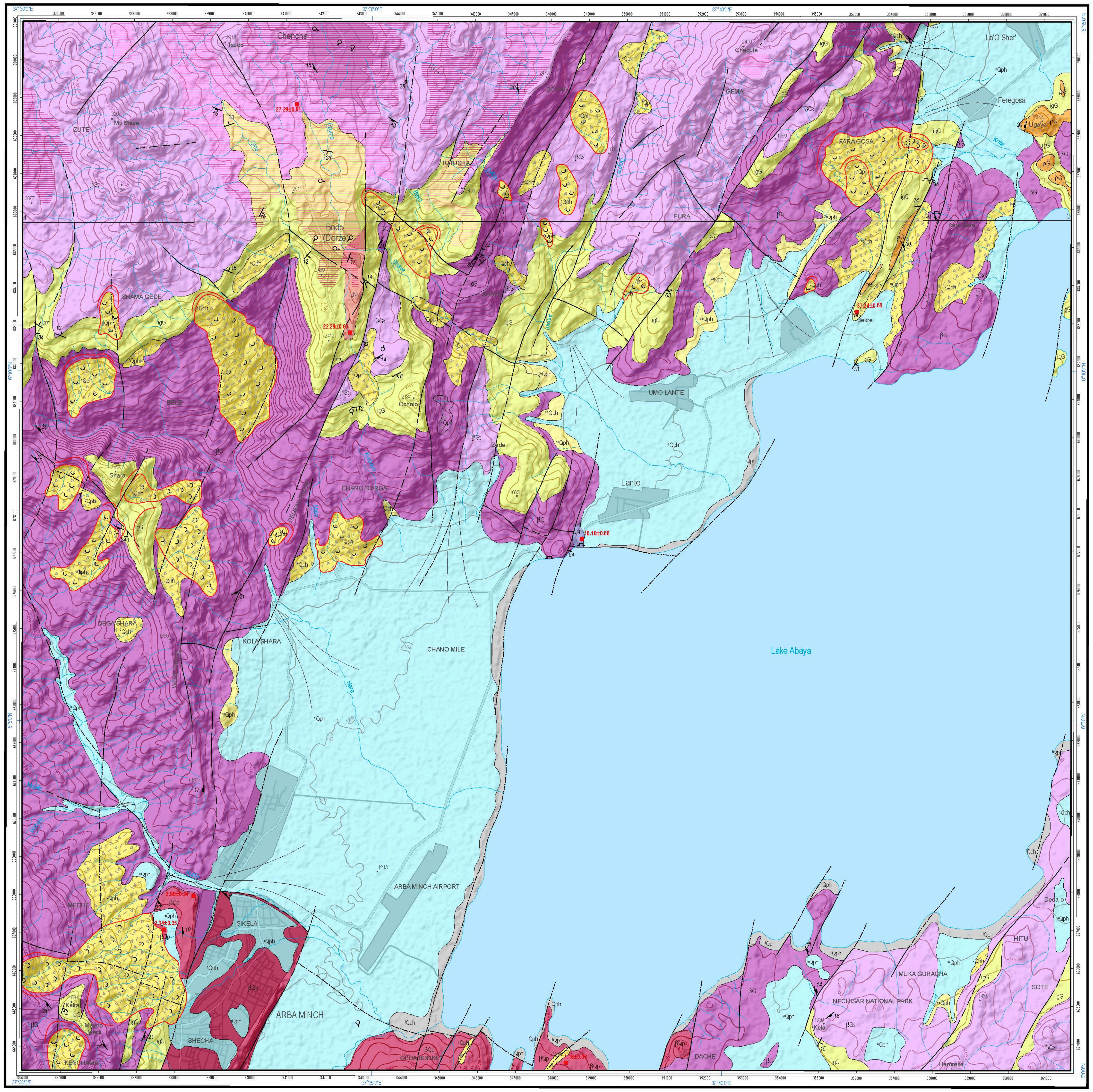

LITHOSTRATIGRAPHIC SCHEME

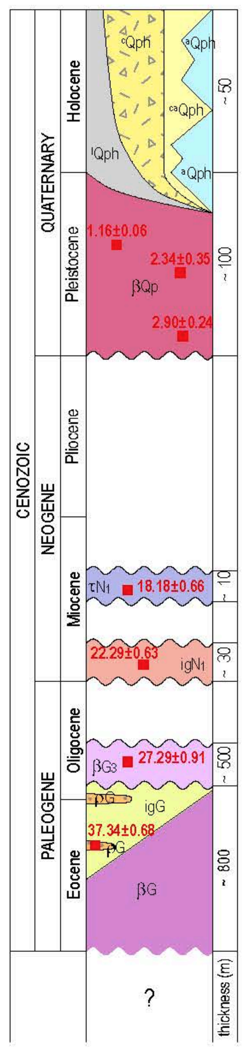

Quaternary sediments

Lacustrine sediments ^{l}Qph

Alluvial sediments ^{a}Qph

Colluvial to alluvial sediments ^{ca}Qph

Colluvial sediments ^{c}Qph

Post-rift volcanic deposits

Nech-Sar Basalt: basalt and pyroclastic deposits βQp

Syn-rift volcanic deposits

Mimo Trachyte τN_1

Dorze Ignimbrite igN_1

Pre-rift volcanic deposits

Basalt βG_3

Shole Ignimbrite: rhyolitic ignimbrite and minor rhyolite igG

Ugayo Rhyolite: rhyolite with subordinate ignimbrite ρG

Amaro–Gamo Basalt: basalt to trachybasalt with minor basaltic pyroclastic deposits βG

SCHEME OF GEOLOGICAL UNITS

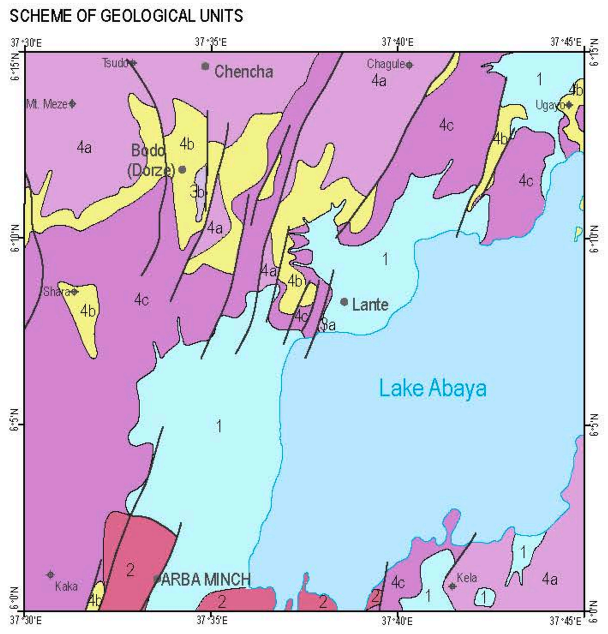

1 : 250,000

1 Alluvial and lacustrine deposits
2 Post-rift volcanic deposits
3 Syn-rift volcanic deposits:
3a Mimo Trachyte
3b Dorze Ignimbrite
4 Pre-rift volcanic deposits:
4a Basalt
4b Shole Ignimbrite
4c Amaro-Gamo Basalt

SCHEME OF DMR AND REGIONAL FAULTS

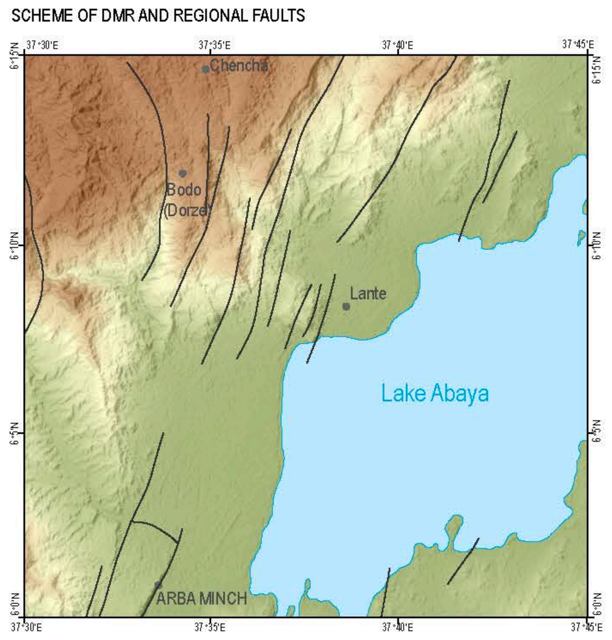

1 : 250,000

High: 3207
Mid: 1975
Low: 1171

LEGEND

Quaternary sediments
CENOZOIC
QUATERNARY
Pleistocene–Holocene

1 ^{l}Qph Lacustrine sediments
2 ^{a}Qph Alluvial sediments
3 ^{ca}Qph Colluvial to alluvial sediments
4 ^{c}Qph Colluvial sediments

Post-rift volcanic deposits
Pleistocene

5 βQp Nech-Sar Basalt: basalt and pyroclastic deposits

Syn-rift volcanic deposits
NEOGENE
Miocene

6 τN_1 Mimo Trachyte
7 igN_1 Dorze Ignimbrite

Pre-rift volcanic deposits
PALEOGENE
Oligocene

8 βG_3 Basalt

Eocene–Oligocene

9 igG Shole Ignimbrite: rhyolitic ignimbrite and minor rhyolite
10 ρG Ugayo Rhyolite: rhyolite with subordinate ignimbrite
11 βG Amaro–Gamo Basalt: basalt to trachybasalt with minor basaltic pyroclastic deposits

12 Lithological boundary observed
13 Lithological boundary inferred
14 Significant unconformity (only in lithostratigraphic scheme)
15 Normal fault observed
16 Normal fault observed with dip and slickensides
17 Normal fault inferred
18 Normal fault obscured
19 Bedding
20 Magmatic foliation
21 Alluvial fan
22 Landslide
23 Main landslide scarp
24 Regolith (deeply weathered rock)
25 Quarry
26 Spring
27 Cross-section line
28 2.34±0.61 K-Ar dating (Ma - megaannum)

MAP SHEET INDEX

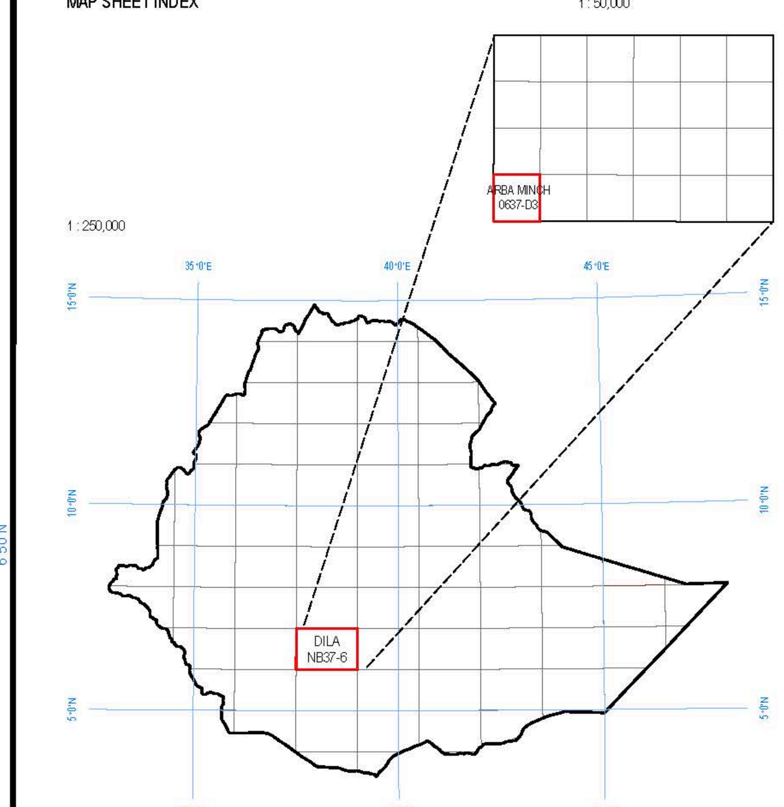

Set of Geoscience Maps of Ethiopia at Scale 1 : 50,000
Geological map of Arba Minch subsheet
Collaborators: Hroch T., Buriánek D., Martínek K., Gebremariam H., Tadesse E., Legesse F., Nisra E., Abateneh B., Hejtmánková P., Krejčí Z.
Digital cartography: Krejčí Z., Hejtmánková P.

N

Kilometers: 1 0 1 2 3 4

Miles: 1 0 1 2

1 : 50,000

Contour interval: 50 meters

Coordinate system:
Blue numbers: longitude & latitude
Black numbers: UTM - zone 37 in meters
Projection: Transverse Mercator
Ellipsoid, Datum: Clarke 1880, Adindan
Topography derived from Ethiopia 1 : 50,000 scale maps Ministry of Land Reform and Administration (Thematic and Mapping Department)

CZECH REPUBLIC DEVELOPMENT COOPERATION

CZECH GEOLOGICAL SURVEY

aquatest

GEOLOGICAL CROSS-SECTION

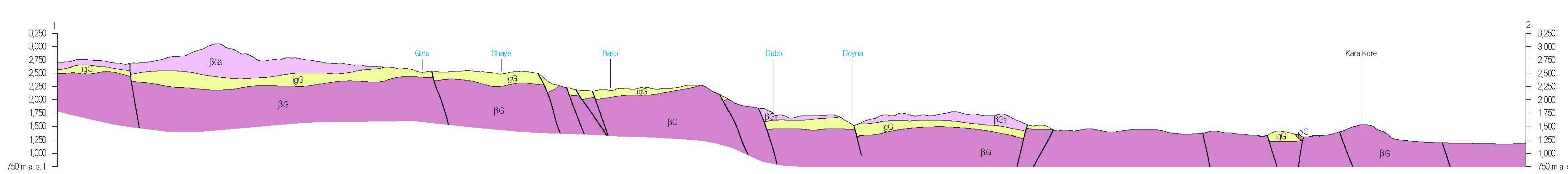

Cross-section with no vertical exaggeration

Attachment III
Geological map of Leku map sheet at a scale of 1:50,000

SET OF GEOSCIENCE MAPS OF ETHIOPIA AT SCALE 1 : 50,000

GEOLOGICAL MAP

Editor: Tomáš Hroch

Subsheet 0638-A2 Leku

LITHOSTRATIGRAPHIC SCHEME

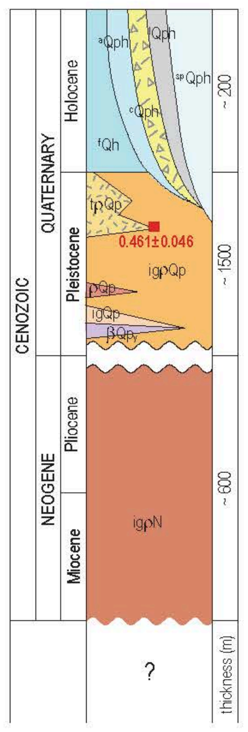

Quarternary sediments

Lacustrine sediments ^{l}Qph

Alluvial sediments ^{a}Qph

Colluvial sediments ^{c}Qph

Post-rift volcanic deposits

Hawasa Ignimbrite: rhyolitic ignimbrite with subordinate pyroclastic deposits $ig\rho Qp$

Hawasa Pyroclastic Deposits: pyroclastic deposits with subordinate ignimbrite $t\rho Qp$

Boricha Rhyolite ρQp

Yubo Basalt βQp_y

Hantate Ignimbrite: welded to unwelded rhyolitic ignimbrite $igQp$

Syn-rift volcanic deposits

Ignimbrite - only in geological cross-section and litostratigrafic scheme $ig\rho N$

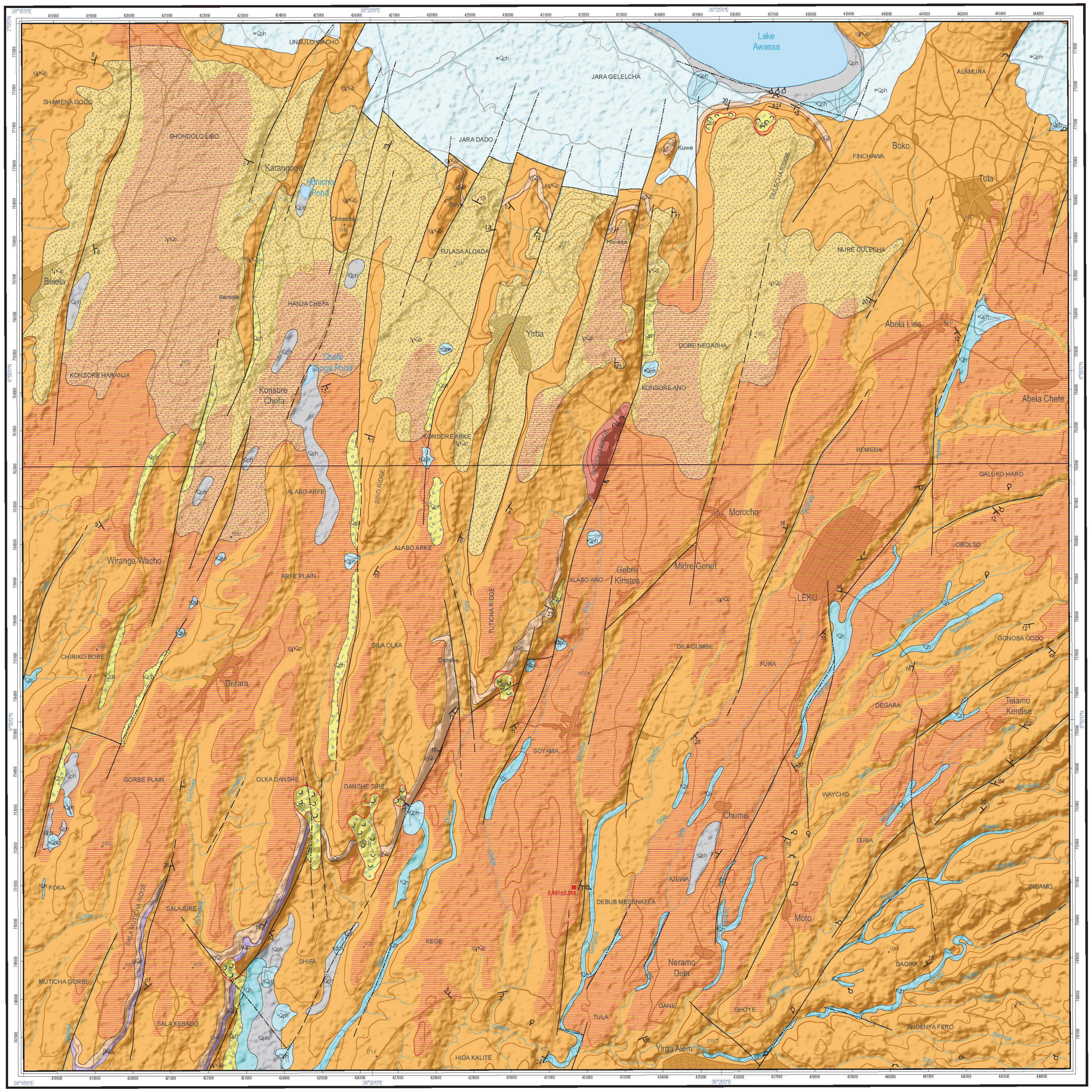

LEGEND

Quarternary sediments

CENOZOIC

QUATERNARY

Holocene

1 ^{f}Qh Fluvial sediments

Pleistocene–Holocene

2 ^{l}Qph Lacustrine sediments

3 ^{a}Qph Alluvial sediments

4 ^{sp}Qph Polygenetic sediments (resedimented pyroclastics, alluvial and lacustrine sediments)

5 ^{c}Qph Colluvial sediments

Post-rift volcanic deposits

Pleistocene

6 $ig\rho Qp$ Hawasa Ignimbrite: rhyolitic ignimbrite with subordinate pyroclastic deposits

7 $t\rho Qp$ Hawasa Pyroclastic Deposits: pyroclastic deposits with subordinate ignimbrite

8 ρQp Boricha Rhyolite

9 βQp_y Yubo Basalt

10 $igQp$ Hantate Ignimbrite: welded to unwelded rhyolitic ignimbrite

Syn-rift volcanic deposits

NEOGENE

Miocene–Pliocene

11 $ig\rho N$ Ignimbrite - only in geological cross-section and litostratigrafic scheme

12 Lithological boundary observed

13 Lithological boundary inferred

14 Significant unconformity (only in lithostratigraphic scheme)

15 Normal fault observed

16 74 Normal fault observed with dip and slickensides

17 Normal fault inferred

18 Normal fault obscured

19 14 Bedding

20 Alluvial fan

21 Landslide

22 Main landslide scarp

23 Regolith (deeply weathered rock)

24 Quarry

25 Spring

26 1 2 Cross-section line

27 2,34±0.61 K-Ar dating (Ma - megaannum)

MAP SHEET INDEX

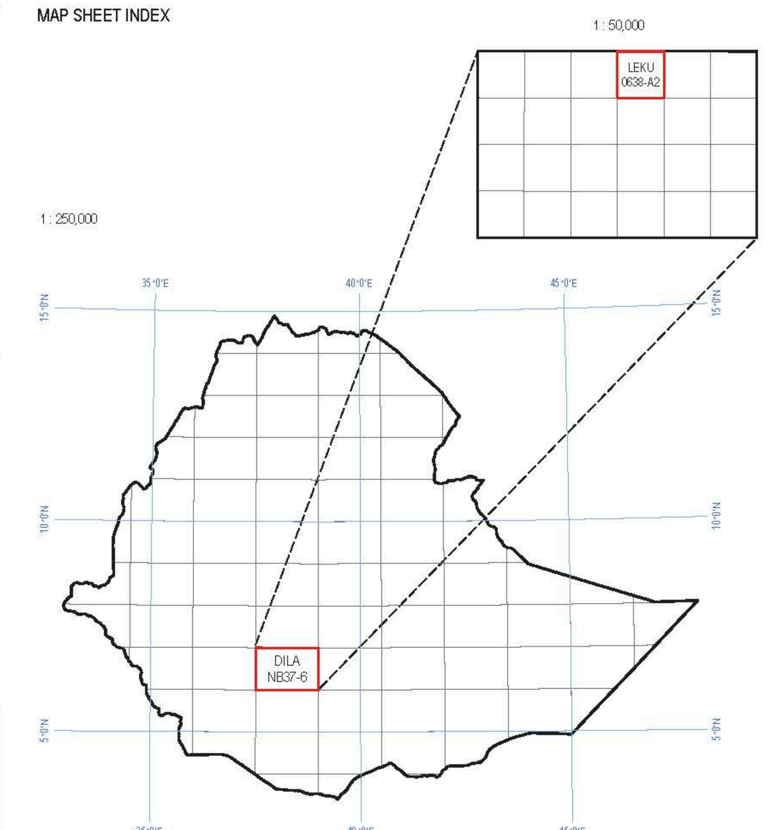

SCHEME OF GEOLOGICAL UNITS

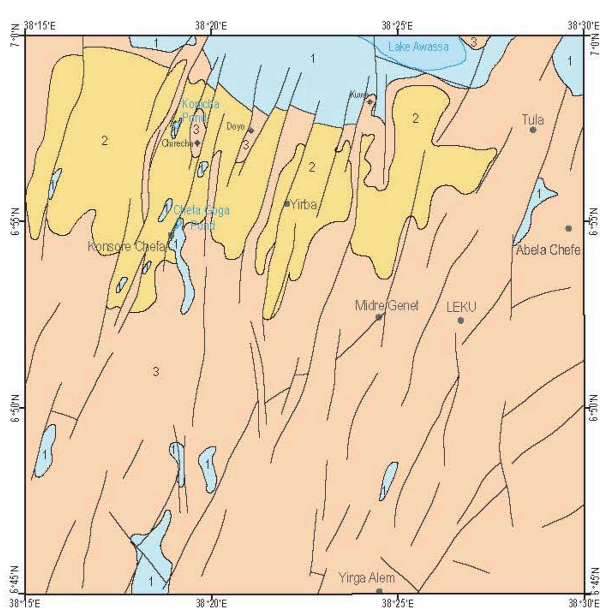

1 : 250,000

1 Alluvial, colluvial, polygenetic and lacustrine deposits

2 Pyroclastic deposits

3 Post-rift volcanic deposits of Dino formation

SCHEME OF DMR AND REGIONAL FAULTS

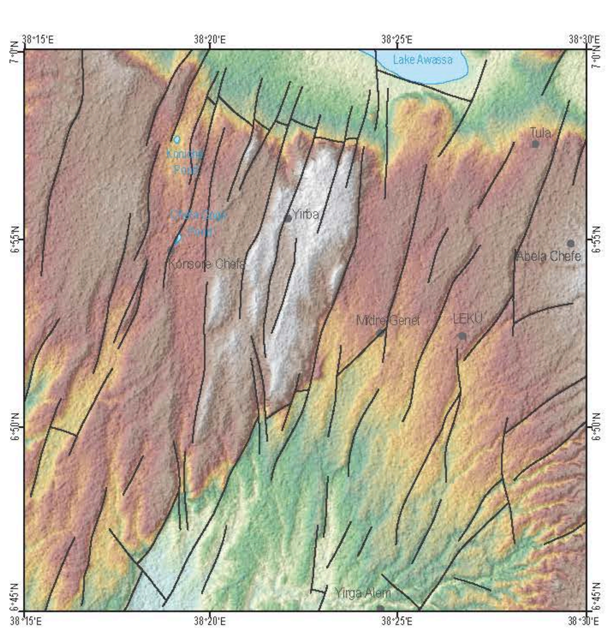

1 : 250,000

High: 2083

Mid: 1846

Low: 1614

Set of Geoscience Maps of Ethiopia at Scale 1 : 50,000
Geological map of Leku subsheet
Collaborators: Verner K., Megerssa L., Buriánek D., Martínek K., Mihret Y., Yechale A., Krejčí Z., Hejtmánková P.
Digital cartography: Krejčí Z., Hejtmánková P.

N

Kilometers

Miles

1 : 50,000

Contour interval: 50 meters

Coordinate system:
Blue numbers: longitude & latitude
Black numbers: UTM - zone 37 in meters
Projection: Transverse Mercator
Ellipsoid, Datum: Clarke 1880, Adindan
Topography derived from Ethiopia 1 : 50,000 scale maps Ministry of Land Reform and Administration (Thematic and Mapping Department)

CZECH REPUBLIC DEVELOPMENT COOPERATION

CZECH GEOLOGICAL SURVEY

aquatest

GEOLOGICAL CROSS-SECTION

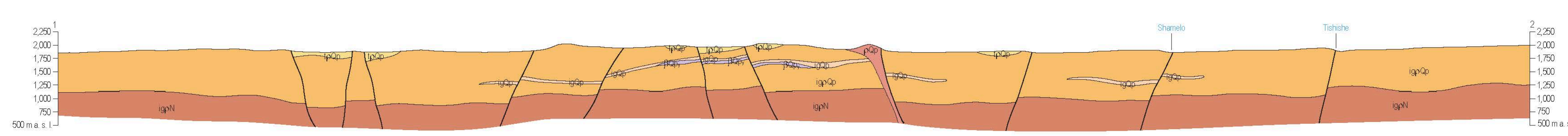

Cross-section with no vertical exaggeration

Attachment IV

Geological map of Dila map sheet at a scale of 1:50,000

SET OF GEOSCIENCE MAPS OF ETHIOPIA AT SCALE 1 : 50,000

GEOLOGICAL MAP

Editor: David Buriánek

Subsheet 0638-C2 Dila

LITHOSTRATIGRAPHIC SCHEME

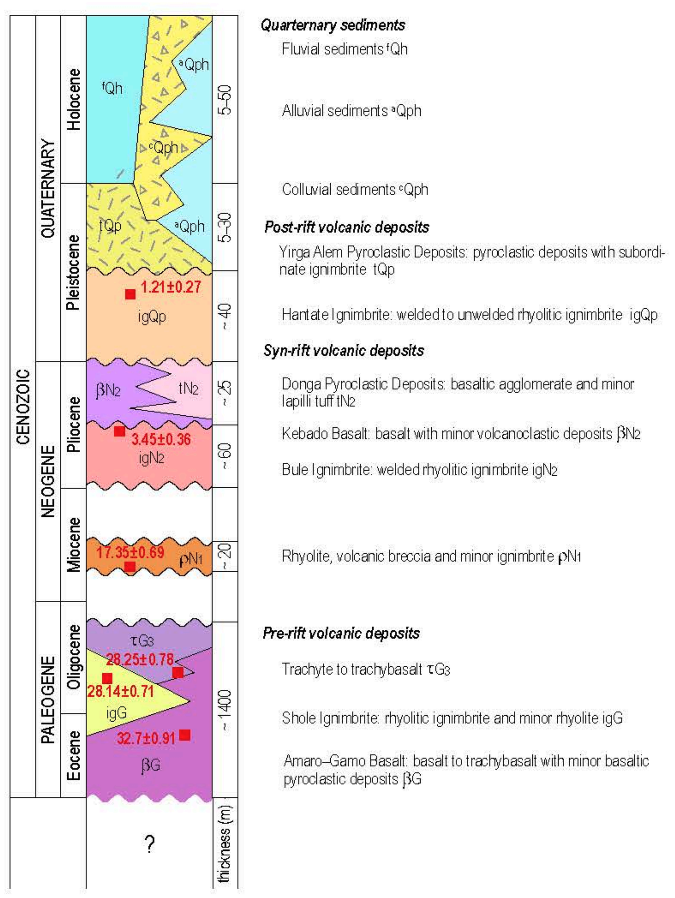

SCHEME OF GEOLOGICAL UNITS

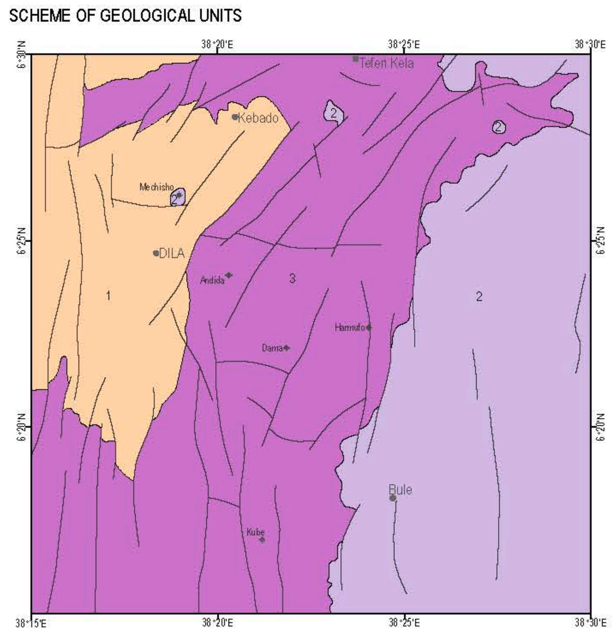

1 : 250,000

1 Post-rift volcanic deposits
2 Syn-rift volcanic deposits
3 Pre-rift volcanic deposits

SCHEME OF DMR AND REGIONAL FAULTS

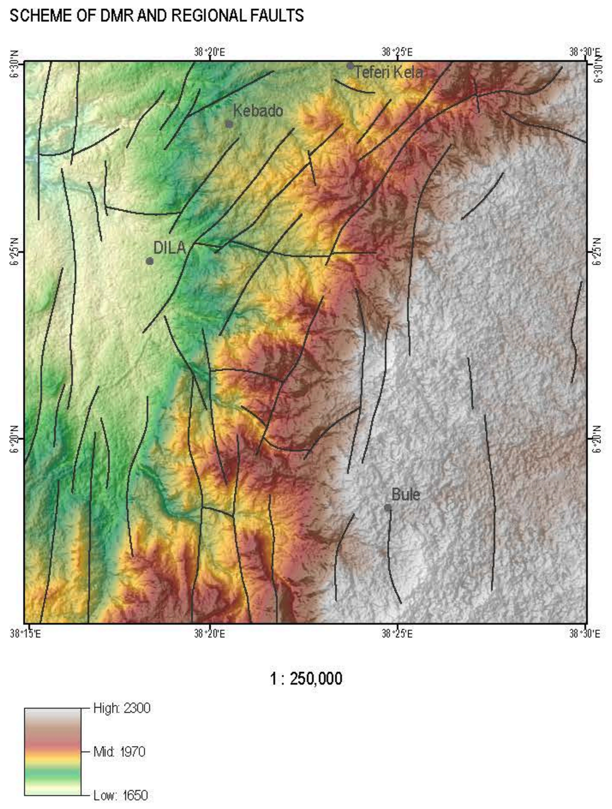

1 : 250,000

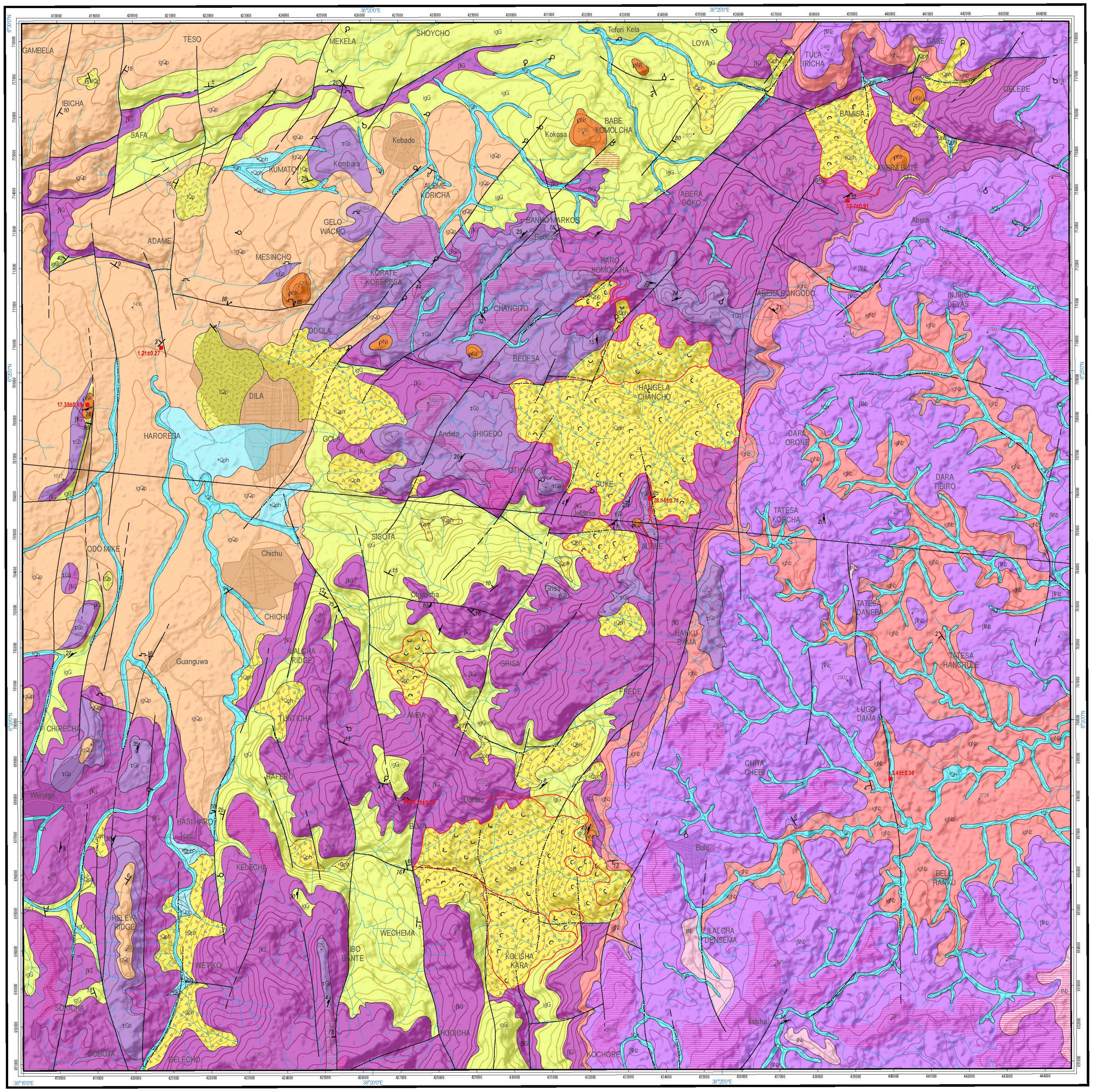

Set of Geoscience Maps of Ethiopia at Scale 1 : 50,000
Geological map of Dila subsheet
Collaborators: Verner K., Hroch T., Martínek K., Megerssa L., Yakob M., Haregot A., Balke G., Mosisa A., Krejčí Z., Hejtmánková P.
Digital cartography: Krejčí Z., Hejtmánková P.

Kilometers

Miles

1 : 50,000

Contour interval: 50 meters

Coordinate system:
Blue numbers: longitude & latitude
Black numbers: UTM - zone 37 in meters
Projection: Transverse Mercator
Ellipsoid, Datum: Clarke 1880, Adindan
Topography derived from Ethiopia 1 : 50,000 scale maps Ministry of Land Reform and Administration (Thematic and Mapping Department)
Tematic content © Czech Geological Survey and Geological Survey of Ethiopia, 2018

LEGEND

Quarternary sediments
CENOZOIC
QUATERNARY
Holocene

1 fQh Fluvial sediments

Pleistocene–Holocene

2 aQph Alluvial sediments
3 cQph Colluvial sediments

Post-rift volcanic deposits
Pleistocene

4 tQp Yirga Alem Pyroclastic Deposits: pyroclastic deposits with subordinate ignimbrite
5 igQp Hantate Ignimbrite: welded to unwelded rhyolitic ignimbrite

Syn-rift volcanic deposits
NEOGENE
Pliocene

6 tN2 Donga Pyroclastic Deposits: basaltic agglomerate and minor lapilli tuff
7 βN2 Kebado Basalt: basalt with minor volcanoclastic deposits
8 igN2 Bule Ignimbrite: welded rhyolitic ignimbrite

Miocene

9 ρN1 Rhyolite, volcanic breccia and minor ignimbrite

Pre-rift volcanic deposits
PALEOGENE
Oligocene

10 τG3 Trachyte to trachybasalt

Eocene–Oligocene

11 igG Shole Ignimbrite: rhyolitic ignimbrite and minor rhyolite

12 βG Amaro–Gamo Basalt: basalt to trachybasalt with minor basaltic pyroclastic deposits

13 Lithological boundary observed
14 Lithological boundary inferred
15 Significant unconformity (only in lithostratigraphic scheme)
16 Normal fault observed
17 Normal fault observed with dip and slickensides
18 Normal fault inferred
19 Normal fault obscured
20 Bedding
21 Magmatic foliation
22 Alluvial fan
23 Landslide
24 Main landslide scarp
25 Regolith (deeply weathered rock)
26 Quarry
27 Spring
28 Cross-section line
29 3.45±0.36 K-Ar dating (Ma - megaannum)

MAP SHEET INDEX

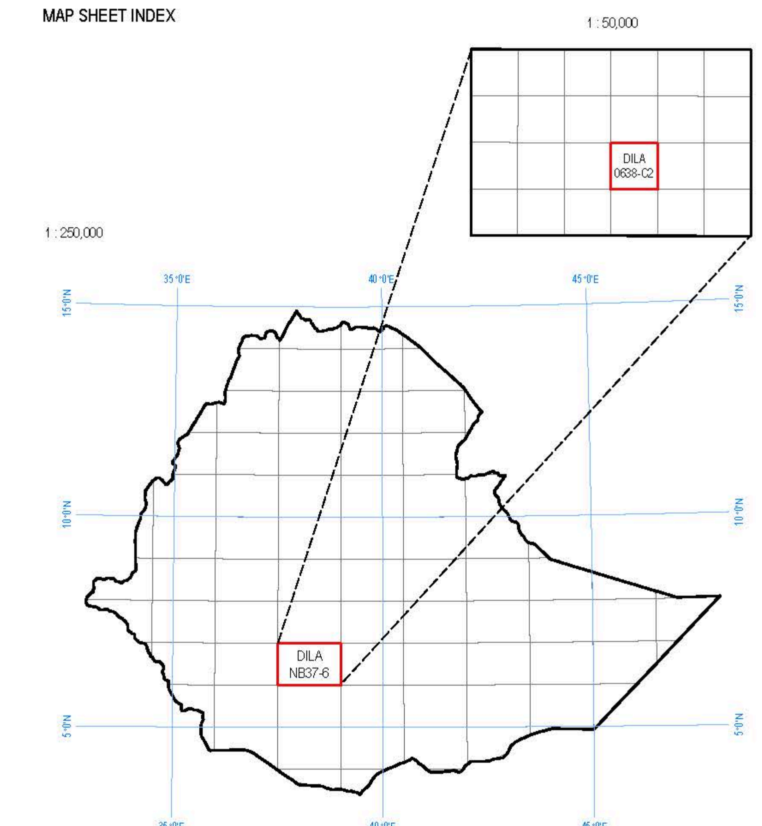

CZECH REPUBLIC
DEVELOPMENT COOPERATION

CZECH GEOLOGICAL SURVEY

aquatest

GEOLOGICAL CROSS-SECTION

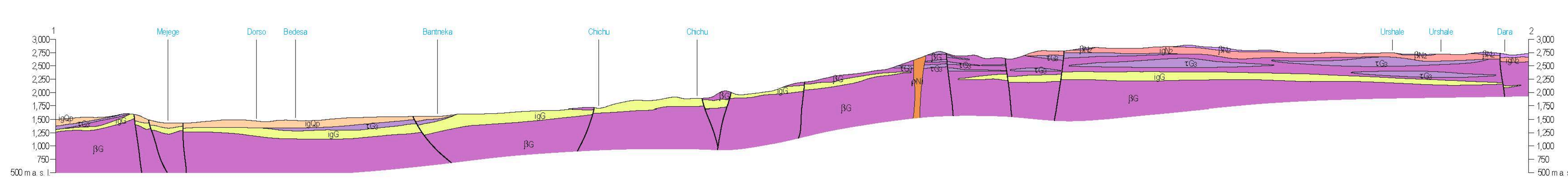

Cross-section with no vertical exaggeration